6-2015

Exploration of Stimulus Current Energy Reduction and Bifurcation Dynamics in Conductance-Based Neuron Models Using Optimal Control Theory

Michael E. Ellinger

Western Michigan University, mike.ellinger@gmail.com

Recommended Citation

Ellinger, Michael E., "Exploration of Stimulus Current Energy Reduction and Bifurcation Dynamics in Conductance-Based Neuron Models Using Optimal Control Theory" (2015). *Dissertations*. 583.
https://scholarworks.wmich.edu/dissertations/583

Exploration of Stimulus Current Energy Reduction and Bifurcation Dynamics in Conductance-Based Neuron Models Using Optimal Control Theory

by

Michael E. Ellinger

A dissertation submitted to the Graduate College
in partial fulfillment of the requirements
for the degree of Doctor of Philosophy in Engineering
Electrical and Computer Engineering
Western Michigan University
June 2015

Dissertation Committee:

Damon A. Miller, Ph.D., Chair
John W. Gesink, Ph.D.
Melinda E. Koelling, Ph.D.
Cindy L. Linn, Ph.D.
Frank L. Severance, Ph.D.

Exploration of Stimulus Current Energy Reduction and Bifurcation Dynamics in Conductance-Based Neuron Models Using Optimal Control Theory

Michael E. Ellinger, Ph.D.

Western Michigan University, 2015

Hodgkin-Huxley type conductance-based models can simulate the effect of time-varying injected stimulus currents on the neuron membrane voltage. The dynamics simulated by these model types enables investigation of the biophysical basis of neuronal activity which is fundamental to higher level function. Broadened understanding the basis of nervous system function could lead to development of effective treatment for related diseases, disorders, and the effects of trauma. In this dissertation, optimal control is used with conductance-based neuron models to develop a "Reduced Energy Input Stimulus Discovery Method." Within the method, an objective function balances two competing criteria: tracking a reference membrane voltage resulting from a stimulus current and reducing the squared input stimulus current 'energy' of that stimulus current. The technique enables computation of optimal input current stimuli that provide differing emphasis on either reference membrane potential tracking or input stimulus current energy reduction. Differences between mathematically optimal and reference stimulus-response signal pairs serve as a source of investigation for furthering understanding of neural dynamics. The method is applied to investigations including four fundamental bifurcation types in a reduced-order, conductance-based neuron model as well as the classical Hodgkin-Huxley model. Experimental feasibility of the approach is demonstrated by applying optimal current stimuli to neurons of the leech *Hirudo verbana* using single cell intracellular stimulation and recording techniques with sharp microelectrodes. Applicability may include finding reduced energy current stimuli for treatment of neurological diseases and prosthesis control.

Acknowledgements

Although my name is on the cover of this document, its creation would not have been possible without the amazing support and encouragement I have received along the way.

I have a truly heroic wife and two exceptional sons who love me with a grace and freedom. My extended family, especially my sister, have been instrumental in supporting us as a family as we have juggled schedule constraints.

At Western Michigan University, I have been surrounded by tremendous faculty and staff. My advisor Dr. Damon Miller is a trustworthy and generous advisor who has allowed himself to be consistently available for my questions and encouragement. Dr. Frank Severance is a true teacher and lifelong learner who was my inspiration for attending graduate school. Dr. John Gesink served as chair of the Electrical and Computer Engineering Department at WMU during most of my time as a graduate student, and I am grateful for his vision and dedication. Dr. Melinda Koelling is a gifted and patient mathematician, and I am thankful for her insights and commitment to our research group. In addition to her technical contributions, Dr. Koelling brings an exceptional relational dynamic to the group which fundamentally changes how we interact as a group and how we perceive the research community.

Key faculty in the Department of Biological Sciences include Dr. John Jellies, Dr. Cindy Linn, Dr. John Spitsbergen, and fellow graduate student Sr. John-Mary Vianney. Every experience that I have had with the Department of Biological Sciences, and the Neuroscience Journal Club, has been one of exceptional support. They have been generous with their laboratory equipment, supplies, time, knowledge and energy.

Funding for continued research and completion of my degree has been provided by the NASA Michigan Space Grant Consortium, the Western Michigan University Graduate Student Research Fund, and Parker Hannifin Corporation, my employer during the latter portion of this degree.

Michael E. Ellinger

Contents

List of Tables

List of Figures

1 Introduction

Neurons are cells which are highly specialized for rapid development of electrical membrane potentials [8][9, p. 3]. Selective permeability of the cellular membrane to positively and negatively charged ions enables neurons to generate electrical signals that encode information essential for organism function at many levels, from sensing to muscle control. Thus encoding and processing of information enables the nervous system to play its fundamental role in interactions between an organism and the environment in which it lives.

Deficiencies or disorders of the nervous system can greatly impair abilities of an organism to perform tasks critical for life and health. Examples of neurological diseases include Alzheimer's and Parkinson's. Disorders such as epilepsy and effects of trauma are further examples of impairments to nervous system function.

A broad range of approaches have been utilized to further understanding of the nervous system and develop methods for prevention and treatment of neurological diseases. One approach is to investigate the biophysical basis of neuronal activity which is fundamental to higher level function. The pioneering work of Hodgkin and Huxley is foundational to all biophysically derived neuron models [10, p. 41]. Furthermore, convergence of computational neuroscience with control theory has produced increased interest in studying how the ranges of dynamical behavior vary in response to changes in various parameters. These bifurcations of neuron dynamics are fundamental properties of individual neurons [10, p. 2][1, p. xv].

Within this dissertation, single cells are modeled using conductance-based Hodgkin-Huxley type models. Optimal control theory, which provides a mathematical framework for minimization of performance objectives, is used to develop a "Reduced Energy Input Stimulus Discovery Method," that enables computation of optimal input stimuli which balance reduced squared integral 'energy' of the input stimulus against accurate tracking of a desired membrane potential [2, 3]. Nonlinear neuron dynamics are investigated for four bifurcation types considered to be fundamental to neurocomputational properties of neurons [1], as a precursor. Differences between optimal and reference stimulus-response signal pairs provides insight into neuron function.

The relationship between energy efficient input stimuli and development of a desired time-varying neural membrane response is relevant to neural prostheses and electrical stimulation therapies involved in spinal cord and Parkinson's treatments [11, 12, 13]. In these cases, chronic over-stimulation is problematic, and decreased energy input stimuli improves longevity of implanted devices and reduces damage to associated tissues [14, 15].

Various toxins and pharmacological blockers have long been used in electrophysiological studies due to their impact on ion channel function and neural responses [8, 16]. Model-based tracking of neural signals, including membrane potential, has been shown to be an effective tool for studying the effect of toxins or pharmaceuticals on neuron function, and estimating changes in model parameters [17, 18, 10].

The method presented within this dissertation has several advantages when considering applicability of theoretical methods 'at the bench.' All simulations presented have been performed on a personal laptop computer with simulation times sufficient to enable computation and application of optimal input stimulus currents within a single experimental preparation. Furthermore, measurement and stimulation of the signals required for the computation and application method does not require continuous feedback of neuron states [14].

When speaking of the present state of the art, one researcher states that "implementation of this research program is still a pipe dream," lamenting the separation of experimental neurobiologists and practitioners of theoretical computational neuroscience [1, p. 20]. The framework presented within this dissertation takes into account the theoretical system dynamics underpinning neural system functionality and exhibits characteristics favorable for experimental application at the rig [14]. The method published within this dissertation, along with its broadly extensible paradigm, is intended to be a step toward realization of the "pipe dream".

1.1 Dissertation Overview

Analysis and optimal control of nonlinear system dynamics in conductance-based Hodgkin-Huxley type neuron models enables discovery of reduced energy input stimuli. In this section an overview of topics necessary for development of the "Reduced Energy Input Stimulus Discovery Method" is provided [2, 3].

1.1.1 Neuron Modeling

Understanding conductance-based models is essential when studying single neuron dynamics, or networks of a small number of neurons, and the Hodgkin-Huxley model is foundational to all biophysically-based models [1, p. 320][10, p. 41]. All models considered within this dissertation are conductance-based models of the Hodgkin-Huxley formalism.

Scope is a primary decision encountered when modeling any dynamical process, and consequently neuronal models exist at every level, from individual ion channels to organism behavior. Theoretical and experimental research pertinent to individual ion channels has developed alongside whole cell approaches [8, p. 33][16]. As scope increases, simplified models are often employed to investigate behavior in networks of neurons. In some cases action potentials, or spikes, are treated as atomic events where timing of the event is the only concern [19]. In other cases, it is assumed that the neuron is in a repetitive spiking mode, and phase models can be used to explore delay times and frequency characteristics of the neural response [11, 20]. In other cases large scale simulations are created without sacrificing the fidelity of conductance-based models, necessitating the use of supercomputers [21, 22].

The family of conductance-based models utilized within this dissertation represent a range of complexity from minimal, second-order models to a sixth-order model experimentally validated in the research literature [1, 17]. Scope of the models is limited such that all simulations presented can be performed on a personal laptop computer with reasonable simulation times. When taken as a group, the family of models facilitates analysis in lower-dimensional cases, and incorporates more complex neural dynamics in the higher-dimensional models.

For further details on the biophysical basis of neuronal signals or their modeling within this dissertation, reference Chapter 2.

1.1.2 Nonlinear Systems Analysis and Bifurcation Dynamics

Considering bifurcation dynamics of system fixed points in neuronal models, in addition to the electrophysiological properties of individual cells, is essential for understanding the computational properties of the neuron [1]. Attempts to precisely estimate values for model parameters in isolation, without considering the composite nonlinear dynamics of the model, often results in the need for "fine tuning" to reproduce the dynamics of the neuron type under investigation [1, p. 7].

A framework for investigation of system dynamics is presented in Chapter 3 which includes determining the number and location of system fixed points, classification of system fixed points, and examination of bifurcation type, based in large part on [1]. Using this framework, the "Reduced Energy Input Stimulus Discovery Method" is introduced that finds optimal stimulation currents that can track a reference membrane potential [2, 3].

The framework is applied to reduced-order conductance-based neuron models for discovery of reduced energy input stimuli in Chapter 4. These models are conducive to geometric analysis techniques due to their low-dimension, but have sufficient fidelity to demonstrate the four bifurcation types fundamental to neural behavior [1, 6].

Higher-order models allow incorporation of a greater range of dynamical behavior, but are not as readily analyzed. Information related to system fixed points and dynamics is not as readily analyzed graphically [3]. The classical Hodgkin-Huxley model is examined in Chapter 5 and results from a six-dimensional conductance-based model have been previously published in [3].

1.1.3 Optimal Control

Through optimization of different performance objectives, previous research has demonstrated the utility of applying optimal control theory to neuronal models. Within this dissertation, optimal control theory is used to study a family of conductance-based neuron models from an energy efficiency perspective. While energy efficiency of the nervous system has been studied for a variety of reasons [23, 24, 25, 26], development of an objective function which balances two competing criteria, tracking a reference membrane voltage and reducing the squared input stimulus current (input current ‘energy’) enables discovery of optimal stimulus signals [2, 3]. A set of optimal input stimuli can be computed for any given reference membrane voltage by adjusting the user prescribed balance between emphasis of accurately tracking the reference signal and reducing the input current energy.

Any difference between the reference membrane voltage and the membrane voltage generated by the optimal input stimulus signal is tracking error. In contrast, differences between the originally applied input stimulus current and the optimal input current is a source of investigation for furthering understanding of neural dynamics.

It is well known that many biological systems operate in an oscillatory manner which is often represented by phase models [27]. Optimal control has been applied to phase models for computing input stimulus signals to alter spike timing, including causing a neuron to spike at a prescribed time [28], maximizing neuron firing rate [11], or breaking unwanted synchronization of neural activity [11, 29]. The technique presented in this dissertation has also been extended for application to phase models [30]. Tracking and control of neural dynamics and model parameter estimation in conductance-based neuron models was studied in [31] using Kalman filter-based technique.

Chapter 3 further develops details of the control objective and methodology used within this dissertation. Chapters 4 and 5 present results from application of the technique to a family of conductance-based neuron models.

1.1.4 Experimental Feasibility

A preliminary feasibility study has been conducted via single cell intracellular stimulation and recording using sharp microelectrodes. Recordings were taken from P and N-cell types in mid-body segment ganglia of the leech *Hirudo verbana.*

Based on the known properties of P-cells, a saddle-node on invariant circle (SNIC) bifurcation type was selected for the model. A non-smooth square stimulus pulse of sufficient amplitude to generate an action potential was applied to the cell of interest. The amplitude and duration of the square wave was used as a reference for scaling the theoretically computed optimal input stimulus signals. A family of optimal input stimulus signals, with increasing emphasis on reduced input stimulus energy, was then applied to the same neuron. The cell fired action potentials in response to the optimal input stimuli, validating experimental feasibility of the approach. Results from application of optimal input stimuli to an N-cell are also presented.

Further details regarding the experimental preparation, signal processing, and preliminary data from the feasibility study is presented in Chapter 6.

1.1.5 Dissertation Structure

The dissertation proceeds as follows. The biophysical basis of signals in an individual neuron, and associated mathematical models used, are presented in Chapter 2. Chapter 3 incorporates conductance-based neuronal models, analysis of bifurcation dynamics, and optimal control theory into a framework for investigation of energy efficiency in modeled individual neurons. The framework will serve as a template for theoretical simulations presented in Chapters 4 and 5. Chapter 4 demonstrates applicability of the method to a reduced-order Hodgkin-Huxley type model capable of producing the four bifurcations deemed essential for most neural computational properties [1]. Chapter 5 applies the method to the classical Hodgkin-Huxley model. Chapter 6 provides an initial demonstration of experimental applicability of the method with single cellular stimulation and recording via sharp microelectrodes. Conclusions are presented in Chapter 7.

2 Neuron Modeling

This section provides an overview of the biophysical basis of neural signals pertinent to this dissertation and an introduction to electronic circuit and dynamical system models. Reviewing these topics together provides a context to relate relevant properties of neuronal excitable membranes to the electronic circuit models and dynamical systems which model them.

All models considered in this dissertation are conductance-based, Hodgkin-Huxley type neuron models. Neurons are modeled as isopotential entities, with membrane potential represented by a single voltage. The family of models examined consists of a reduced-order, two-dimensional model, the classical four-dimensional Hodgkin-Huxley model and a six-dimensional model. Other means of neuron modeling including phase models and stochastic techniques are not considered here.

This section begins with an overview of the biophysical basis of selected neural signals in Section 2.1. Fundamental concepts of ion channel conductance and equilibrium potential are explained and incorporated into a circuit model which describes resting membrane potential in terms of concentration gradients and relative permeability of multiple ionic species. Variation of the relative permeability of ionic species is shown to sway the resting membrane potential toward the equilibrium potential of the ionic species with the greatest permeability, allowing for rapid modulation of membrane potential through primarily passive means.

The classical Hodgkin-Huxley model is examined in Section 2.2. Specifically, the circuit model developed in Section 2.1 is extended to incorporate injected current stimulus signals and capacitive properties of the cell membrane. Inclusion of ion channel dynamics relates the representative circuit to the classical Hodgkin-Huxley model, a dynamical system of equations.

Section 2.3 provides a cursory overview of a reduced-order, two-dimensional model which is based on the classical Hodgkin-Huxley.

Section 2.4 highlights the quandary of parameter estimation when seeking to apply results in models to experimental preparations.

2.1 Biophysical Basis of Neural Signals

Neurons are exceptionally functionally and morphologically diverse. A working definition of a neuron is a cell which is highly specialized for rapid communication of information over varying distance through rapid modulation of membrane voltage [8].

This section provides an overview of the biophysical basis of selected neural signals. For a thorough review, see [8]. Some figures and text within this section were previously presented in [5].

2.1.1 Excitable Membranes

Chemical concentrations can vary greatly at different locations within a living organism, and are often different than those which are necessary to sustain life inside a cell. Cellular membranes enable the interior of a cell to consist of a different chemical composition than the environment in which it resides. The majority of the cellular membrane is composed of a lipid bilayer. Lipids consist of a hydrophilic head region, which is attracted to aqueous solutions, and long hydrophobic tails, which are repelled from them [32]. Due to these fundamental properties lipids naturally form micelles (Figure 1a) and lipid bilayers (Figure 1b) when placed in aqueous solutions [32].

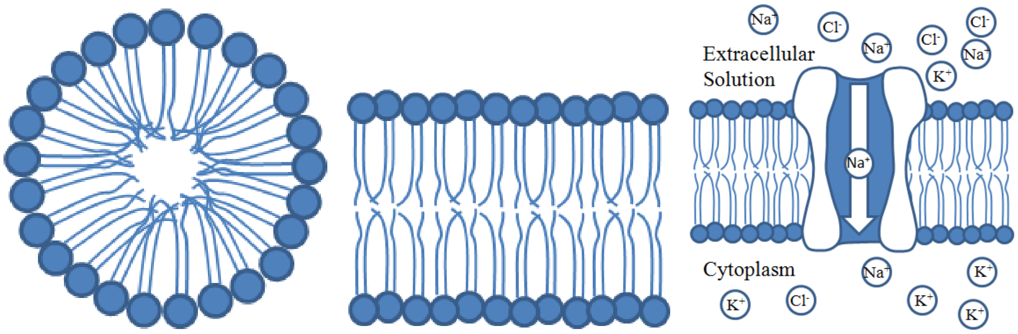

(a) (b) (c)

Figure 1: Lipid formations, directly from [5]

In addition to a lipid bilayer the excitable cell membrane of a neuron contains membranespanning proteins (Figure 1c) called ion channels. Ion channels are often selectively permeable to specific ionic species and are capable of opening and closing in response to membrane voltage or ligands, which are ions that selectively bind to receptors [8]. Although ion channels control the permeability of the cell membrane to various ions, the driving force for the movement of ions into or out of the cell is an electro-chemical gradient created by differing ion concentrations and electromagnetic forces related to membrane voltage and ion valence.

In addition to the passive flow of ions according to their electro-chemical gradient, neurons also have active transport mechanisms for moving ions across the cell membrane against their gradient. The sodium-potassium pump is an example of active transport, using energy from hydrolysis of ATP to transport sodium and potassium ions against their respective electro-chemical gradients [8, p. 62].

Through selective permeability of embedded ion channels and energy consuming processes for active transport of ions, a cell is able to maintain a consistent internal environment which is distinct from the extracellular solution [32].

2.1.2 Resting Potential

Many essential factors combine for generation of an electrical potential across the cell membrane. As described in Section 2.1.1, a concentration gradient exists between the cytoplasm and the extracellular solution and ions diffuse across the membrane with different relative permeability. Additionally, the cell must remain in osmotic balance and both interior and exterior solutions must both be electrically neutral [8]. Based on these biophysical properties, this subsection describes the equations which enable calculation of ion specific equilibrium potentials and the resting membrane potential for a cell.

2.1.2.1 Nernst Equation

Both diffusion and electromotive forces act upon ions, to influence their movement between the cytoplasm inside the cell membrane and the extracellular solution. Diffusion forces equilibrate concentration gradients across the membrane. The electromotive force acts with respect to the membrane potential and ion valence.

Consider a cell with a negative resting potential V_m, as illustrated in Figure 2. Since potassium is at a higher concentration inside the cell, diffusion drives potassium out of the cell, depicted by the arrow on the left. Due to the negative membrane potential positively charged potassium ions are driven into the cell by the electromagnetic force, depicted by the arrow on the right.

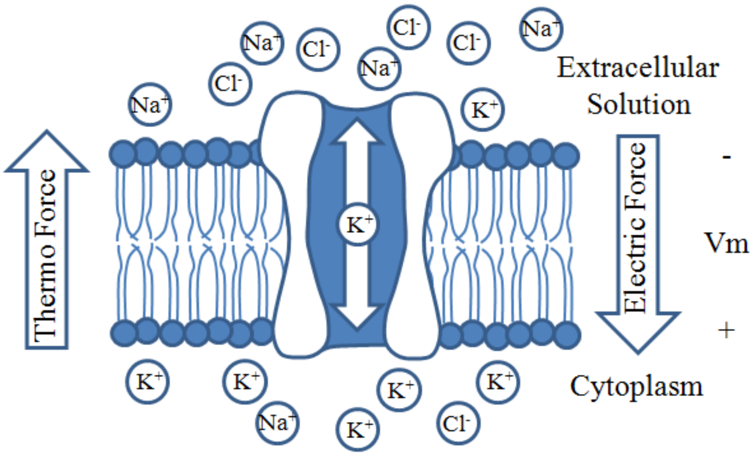

Figure 2: Depiction of forces acting on a potassium ion, directly from [5]

There is a membrane voltage at which the diffusion force will be equal to the electromagnetic force. That voltage is defined as the equilibrium potential for that specific ion, often designated as E_{ion}, and can be calculated using the Nernst equation [8]

$$E_{ion} = \frac{RT}{zF} \ln \frac{[ionic\ concentration]_{extracellular}}{[ionic\ concentration]_{intracellular}} = 58 * \log \frac{[ion]_{ext}}{[ion]_{int}} \text{ mV} \tag{1}$$

where $[ion]_{ext}$ and $[ion]_{int}$ are the external and internal ion concentrations, respectively.

Originally formulated by Walther Nernst, equation (1) computes the equilibrium potential according to the universal gas constant (R), absolute temperature (T), ion valence (z), Faraday's constant (F), and ionic concentration gradient across the membrane [16, 8]. The constant value of 58 is computed at room temperature ($20°C$) for univalent positive ions ($z = 1$).

The equilibrium potential for each ionic species is significant since it indicates the voltage at which the net ionic current across the membrane, I_{ion}, will be equal to zero. Using Ohm's law and the equilibrium potential defined by the Nernst equation, the relationship between membrane voltage V_m and ionic current I_{ion} is

$$I_{ion} = g_{ion}(V_m - E_{ion}) \tag{2}$$

where g_{ion} is the ion specific conductance.

As early as 1902, long before it was possible to actually measure the resting potential of a cell, Julius Bernstein, in his famous hypothesis, recognized that membrane potential was the result of unequal distribution of potassium [8]. Specifically, Bernstein hypothesized that if the cell was permeable to potassium alone, then the resting potential must be equal to the equilibrium potential of potassium, as calculated by the Nernst equation [8]. By the time Hodgkin and Huxley were performing their experiments on the giant axon of *Loligo* in the early 1950s, scientists believed that the cell membrane of a neuron was typically permeable to more than one ionic species, thus the Nernst equation was unable to accurately predict the resting membrane potential of a cell.

2.1.2.2 Goldman-Hodgkin-Katz Equation

Derivation of the equation, which is able to predict the electric potential of a cell membrane permeable to more than one ionic species, was discovered independently by Goldman, Hodgkin, and Katz [8]. As an example, the resting membrane potential for a cell which is permeable to only sodium, potassium, and chloride is calculated using the GHK equation as

$$V_m = \frac{g_K E_K + g_{Na} E_{Na} + g_{Cl} E_{Cl}}{g_K + g_{Na} + g_{Cl}} = 58 * \log \frac{p_K[K]_{ext} + p_{Na}[Na]_{ext} + p_{Cl}[Cl]_{int}}{p_K[K]_{int} + p_{Na}[Na]_{int} + p_{Cl}[Cl]_{ext}} \text{ mV} \tag{3}$$

where $[K]$, $[Na]$, and $[Cl]$ are ionic concentrations.

Due to the opposite ionic valence, the interior and exterior concentration values for chloride are transposed compared to those of sodium and potassium . Also, the units of the GHK equation produce a membrane potential which is in millivolts. When written in terms of permeability and concentration gradients, it is helpful to think of the GHK equation as a Nernst equation with multiple terms weighted by the relative permeability of each ionic species.

The GHK equation is often modeled by an electric circuit, in which a parallel branch of the circuit is associated with each conductance term. Often sodium, potassium, and chloride have the most significant impact on resting membrane potential. Remaining currents, if included, are often lumped in the model as ‘leak currents’, resulting in an additional term to the equation.

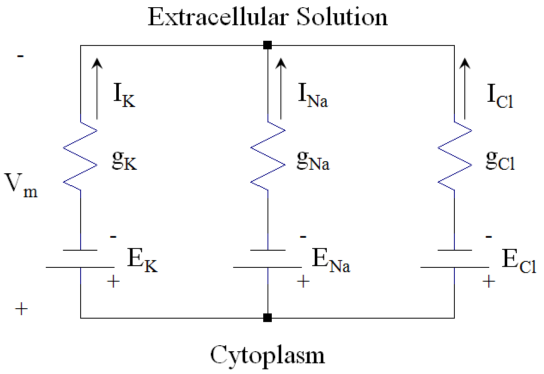

Figure 3: Circuit model of a neuron membrane

The circuit model of Figure 3 corresponds to the terms of GHK equation (3), neglecting any additional leak currents. Summing the ion species specific currents, Kirchoff’s current law yields

$$I_K + I_{Na} + I_{Cl} = 0. \tag{4}$$

Using Ohm’s law each conductance is substituted using equation (2) yielding

$$g_K(V_m - E_K) + g_{Na}(V_m - E_{Na}) + g_{Cl}(V_m - E_{Cl}) = 0. \tag{5}$$

Rearranging terms and solving for V_m reproduces the GHK equation (3)

$$V_m = \frac{g_K E_K + g_{Na} E_{Na} + g_{Cl} E_{Cl}}{g_K + g_{Na} + g_{Cl}}. \tag{6}$$

Breaking out individual terms of the equation as in [33] produces equation (7), highlighting the resting membrane potential V_m as the weighted average of equilibrium potentials for each permeant ion

$$V_m = \frac{g_K}{g_T} E_K + \frac{g_{Na}}{g_T} E_{Na} + \frac{g_{Cl}}{g_T} E_{Cl} \tag{7}$$

where $g_T = g_K + g_{Na} + g_{Cl}$.

One potentially confusing aspect of the circuit model as commonly presented in other sources is that the battery polarity in the circuit model schematic is often reversed for any ion with a negative equilibrium potential [33]. Polarity of the equilibrium potentials is discussed further in Section 2.1.2. For this section it is noted that the polarity of the battery for all equilibrium potentials will be oriented in the same direction, in contrast to the classical presentation of the circuit model.

2.1.3 Action Potential

The circuit model in Figure 3 depicts the cell at rest. Static values for each equilibrium potential, conductance, and associated ionic concentrations enable computation of the membrane resting potential via equation (3). Generation of an action potential requires introduction of dynamics to the circuit model.

As discussed in Section 2.1.1, a cell is able to regulate membrane potential through selective permeability of embedded ion channels and as well as active transport mechanisms [32]. Yet, active transport mechanisms generally constitute less than 10% of the resting membrane potential [8, p. 88]. Furthermore, net ionic movement across the membrane during an action potential is minuscule in terms of the overall ionic concentration in either the cytoplasm or extracellular solution [8, p. 93]. Thus ionic concentrations can be considered constant.

Therefore, it is correct to heavily emphasize ion channel dynamics as the essential component in both resting membrane potential and action potential generation.

In fact, a significant contribution of the work of Hodgkin and Huxley involved quantifying activation and inactivation dynamics of ion channel populations as described in Section 2.2.2. For now, consider each resistor in Figure 3 as a variable. The conductance for each ion channel can vary according to membrane potential, ligand binding, or another characteristic of the cell or environment.

Since the overall membrane potential is a result of each equilibrium potential, weighted by the relative permeability of the membrane to each ionic species, any increase in permeability to a specific ion will sway the membrane potential toward the equilibrium potential of that ion. As an example, consider the following equilibrium potentials, representative of a typical mammalian cell [8]:

$$E_K = 58 * \log \frac{[K]_{ext}}{[K]_{int}} = 58 * \log \frac{[10]_{ext}}{[165]_{int}} = -70.61\,\text{mV}; \tag{8}$$

$$E_{Na} = 58 * \log \frac{[Na]_{ext}}{[Na]_{int}} = 58 * \log \frac{[175]_{ext}}{[20]_{int}} = 54.64\,\text{mV; and} \tag{9}$$

$$E_{Cl} = 58 * \log \frac{[Cl]_{int}}{[Cl]_{ext}} = 58 * \log \frac{[4]_{int}}{[97]_{ext}} = -80.31\,\text{mV}. \tag{10}$$

Resting membrane potential can be computed for the hypothetical cell using the GHK equation (3). Assuming relative permeability values of $p_K = 5.0$, $p_{Na} = 0.0005$, and $p_{Cl} = 0.5$ the membrane potential is computed according to equation (11) as

$$\begin{aligned} V_m &= 58 * \log \frac{p_K K_{ext} + p_{Na} Na_{ext} + p_{Cl} Cl_{int}}{p_K K_{int} + p_{Na} Na_{int} + p_{Cl} Cl_{ext}}, && (11) \\ &= 58 * \log \frac{(5.0)[10]_{ext} + (0.0005)[175]_{ext} + (0.5)[4]_{int}}{(5.0)[165]_{int} + (0.0005)[20]_{int} + (0.5)[97]_{ext}} = -71.02\,\text{mV}. && (12) \end{aligned}$$

Presently the resting membrane potential is closest to the equilibrium potential of potassium. This is the result of potassium having the highest relative permeability. If the relative permeability of sodium increases to $p_{Na} = 50$ in response to some input stimulus, the resting membrane potential is forced toward the equilibrium potential of sodium. Since the equilibrium potential of sodium is equal to 54.64 mV, as computed in equation (9), this results in an increased membrane potential, often referred to as depolarization of the membrane, computed as

$$V_m = 58 * \log \frac{(5.0)[10]_{ext} + (50)[175]_{ext} + (0.5)[4]_{int}}{(5.0)[165]_{int} + (50)[20]_{int} + (0.5)[97]_{ext}} = 38.97\,\text{mV}. \tag{13}$$

The increase in sodium permeability is due to a portion of the population of sodium channels opening, allowing sodium ions to flow into the cytoplasm according to their concentration gradient. These computations exemplify how the resting membrane potential can be varied toward any of the equilibrium potentials through primarily passive means. An amazing aspect of cellular neurobiology is the efficiency with which neurons maintain the environment necessary for continued life of the cell. Much of what the cell requires is achieved using existing energy gradients [8]. During the time course of an action potential the conductance of populations of ion channels change in a concerted fashion to produce the stereotypical waveform commonly known as an action potential or ‘spike.’

A stereotypical description of the signal cascade leading to generation of a classical action potential begins at the dendritic arbor. Depending on their function, dendrites respond to different types of stimulus, including touch, heat, light, or the presence of chemicals. The stimulus produces a response in the dendrite which influences the probability that ion channels will open or close. Changes in the state of the ion channels produces a localized change in membrane potential. If the inputs from the dendrites arrive close enough to each other in time and position at the cell body, they create momentary positive feedback when voltage gated sodium channels open in response to the stimulus. Positively charged sodium ions flow into the cell through the opened sodium channels, raising the membrane voltage further still. Elevated membrane voltage in turn causes more sodium channels to open, with the net effect resulting in the rising phase of a stereotypical action potential.

Potassium channels are voltage gated as well, but respond more slowly than sodium channels. When potassium channels open, positively charged potassium ions flow out of the cell into the extracellular solution according to their concentration gradient, reducing the membrane voltage. Although potassium channel activation is slower than sodium channels, potassium channel activation is persistent. Sodium channels are inactivated in the presence of a positive membrane voltage. This results in a reduction in the sodium conductance, and the net membrane voltage begins to move toward the equilibrium potential of potassium. Thus, the persistent potassium current, simultaneous with inactivation of the sodium current, accounts for the falling phase and undershoot of membrane voltage beyond the resting potential [8]. Figure 11 on page 26 portrays a classical action potential as generated by the Hodgkin-Huxley model.

The generalized behavior of a hypothetical neuron is able to qualitatively describe the form of a classical action potential, but greater detail is required to understand more quantitative features of a spike. Continuous time waveforms demonstrating the quantitative values for each conductance according to Hodgkin-Huxley dynamics, along with corresponding ionic currents and membrane voltage, will be explored in Section 2.2.2.

2.2 Classical Hodgkin-Huxley Model

In late 1951 and early 1952 Alan Hodgkin and Andrew Huxley published a series of articles which mathematically and experimentally characterized the squid axon action potential in terms of ionic concentrations and variable membrane permeability [34, 35, 36, 37, 38]. Using a mathematical model, coupled with experimental application of feedback amplifiers and voltage clamp techniques, Hodgkin and Huxley were able to quantify the role of individual ionic species during an action potential within the giant axon of *Loligo*. Their work was, in many ways, the culmination of centuries of work centered on understanding the “nervous impulse” and earned the Nobel Prize in Physiology or Medicine in 1963 [19, p. 2][39].

Since its publication, the Hodgkin-Huxley model has been studied and used from numerous perspectives. The original model has been extended to account for neural dynamics found in different experimental preparations [40, 17]. It has been reduced, demonstrating that simplified models can accurately describe neural behavior from a dynamical systems perspective [1]. It has been used to study energy efficiency of neural tissues [23]. It can exhibit chaotic behavior [41] and has been combined with optimal control techniques [2, 3, 31]. Even though its continued relevance has been questioned, the model still remains as a foundation of neuron electrophysiology [42].

For the purposes of research presented in this dissertation, the Hodgkin-Huxley model has two important characteristics. First, it has been shown that using the Hodgkin-Huxley formalism as a starting point, a reduced model of two dimensions can exhibit the four bifurcations fundamental to most neural behavior with proper selection of parameter values [1]. Second, it is a biophysically-derived model. That is, model parameters are clearly related to properties of the cell membrane commonly measured 'on the rig' by electrophysiologists.

2.2.1 Equivalent Circuit Model

It is common practice to model the electrical properties of neurons, with an equivalent circuit model. The giant axon of *Loligo*, as originally modeled by Hodgkin and Huxley, was determined to consist primarily of three currents: a voltage gated potassium current, a voltage gated sodium current, and a leak current [1, p. 37]. Specifically, the initial upswing in membrane voltage was quantifiably related to the influx of a rapid, transient sodium current, with a decrease in membrane voltage related to a slower, persistent potassium current [8]. Capacitive properties of the membrane are also accounted for in the model, resulting in an equivalent circuit model depicted in Figure 4. Each branch consists of a battery, set to the equilibrium potential for that ionic species, and a conductance which can be dynamic or Ohmic. The membrane voltage V_m is across the parallel branches.

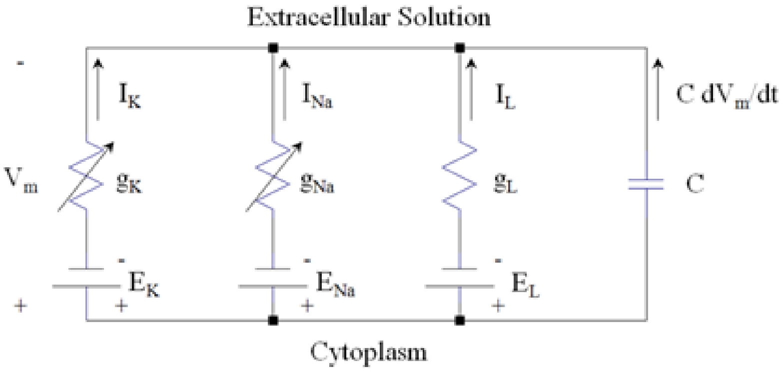

Figure 4: Circuit model of a neuron membrane with membrane capacitance

Beginning with summation of the defined currents via Kirchoff's Current Law, analysis of the model produces

$$I_K + I_{Na} + I_L + C\dot{V} = 0. \tag{14}$$

Substitution of each ionic conductance and equilibrium potential via equation (2) yields

$$g_K(V_m - E_K) + g_{Na}(V_m - E_{Na}) + g_L(V_m - E_L) + C\dot{V} = 0. \tag{15}$$

Another parallel branch can be added to the circuit to account for an injected current, which may be used by electrophysiologists to stimulate neural activity and tease out neuron dynamics.

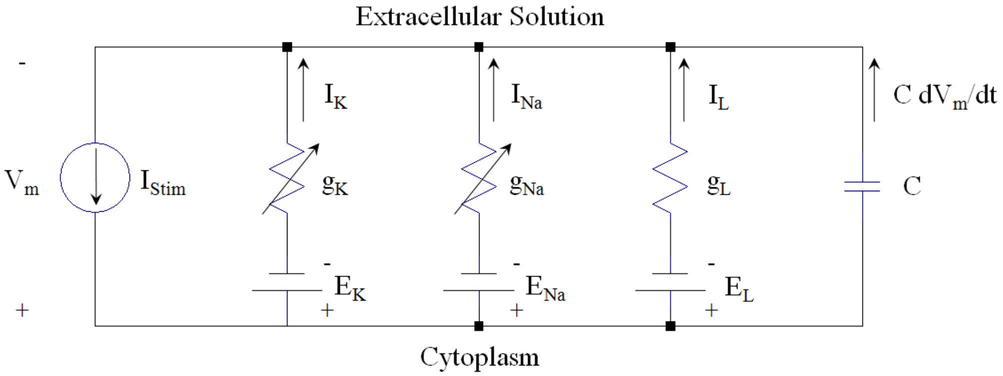

Figure 5: Circuit model of a neuron membrane with injected current stimulus

As drawn, the injected current is opposite in sign as compared to the ionic currents, resulting in

$$g_K(V_m - E_K) + g_{Na}(V_m - E_{Na}) + g_L(V_m - E_L) + C\dot{V} = I_{Stim}. \tag{16}$$

Rearranging terms produces

$$C\dot{V} = I_{Stim} - g_K(V_m - E_K) - g_{Na}(V_m - E_{Na}) - g_L(V_m - E_L). \tag{17}$$

Equation (17) very closely resembles the equation for membrane voltage from the Hodgkin-Huxley model, but ion channel dynamics neglected. Ion channel dynamics associated with changes in potassium and sodium conductance were modeled by Hodgkin and Huxley using gating variables, n, m, and h. Adding activation and inactivation variables reproduces the Hodgkin-Huxley equation for membrane voltage results in

$$C\dot{V} = I_{Stim} - g_K n^4(V_m - E_K) - g_{Na} m^3 h(V_m - E_{Na}) - g_L(V_m - E_L). \tag{18}$$

Originally Hodgkin and Huxley accounted for negative equilibrium potentials by reversing battery polarity in the circuit model. While this inconsistency has been addressed by researchers in some cases, the convention of reversing the battery of any ion with a negative equilibrium potential has persisted in literature [33]. From a historical and biophysical perspective there are a number of salient features of the model which must be maintained. When the membrane voltage is equal to the equilibrium potential of an ionic species, as calculated by the Nernst equation, the net ionic current is equal to zero [8]. It is advantageous to retain the original form of the Hodgkin-Huxley equations rather than alter the polarity of the equilibrium potential on a term by term basis. The simplest means of achieving these goals is to avoid reversing the battery in the circuit model, and orient all equilibrium potentials polarities in the same direction. The neuron circuit model equations used here are consistent with the passive sign convention.

2.2.2 Hodgkin-Huxley Equations

The Hodgkin-Huxley model, as originally published, consists of a nonlinear system of four differential equations [1, p. 37][38]. State variables are the neuron membrane voltage (V), a potassium activation variable (n), a sodium activation variable (m), and a sodium inactivation variable (h).

The Hodgkin-Huxley model is

$$C\dot{V} = I_{Stim} - g_K n^4(V_m - E_K) - g_{Na} m^3 h(V_m - E_{Na}) - g_L(V_m - E_L), \tag{19}$$

$$\dot{n} = \alpha_n(V)(1 - n) - \beta_n(V)n, \tag{20}$$

$$\dot{m} = \alpha_m(V)(1-m) - \beta_m(V)m, \text{ and} \tag{21}$$

$$\dot{h} = \alpha_h(V)(1-h) - \beta_h(V)h. \tag{22}$$

Equations correspond to the circuit diagram in Figure 5. The constants C, g_K, g_{Na}, and g_L are cell membrane capacitance and maximal conductances for potassium and sodium and the leak term conductance, respectively. Nernst equilibrium potentials are represented by the constants E_K, E_{Na}, and E_L. The injected stimulus current, I, can be a constant value, step, pulse, ramp, or other waveform. Nonlinear, voltage dependent modulation of specific ionic conductance values is accomplished via dimensionless gating variables n, m, and h.

The potassium current is considered to have four activation gates. The sodium current has three activation gates and one inactivation gate. Presence of the inactivation gate is what causes the sodium current to be transient. The number of activation or inactivation gates is accounted for in the equations by the exponent on each term (i.e. n^4, m^3, and h) [1]. Gating variables are not to be confused with conformal state of ion channels. See [1, p. 33] for a discussion of activation and inactivation gates.

From a physical perspective activation increases the probability of an ion channel opening while deactivation decreases the probability of a channel opening [8]. Thus, conductance of both potassium and sodium increases in response to increased membrane potential due to the activation variables n and m, respectively. Inactivation describes a state where ion channel activation is inhibited even though the activating stimulus may be present [8, p. 28]. Inactivation of sodium channels in the response to positive membrane voltage due to inactivation variable h causes a reduction in sodium conductance.

Values for all gating variables are bounded between zero and one. As the value for a gating variable approaches one the associated conductance approaches the maximal conductance for associated ionic species. For example, as the value for n approaches one the term $g_K n^4$ approaches g_K, which is aptly named the maximal conductance for potassium. Likewise, the term m^3h modulates the conductance of sodium.

The leak current is Ohmic, or constant, and is therefore represented by a constant conductance, g_L.

Functions denoted by $\alpha(V)$ and $\beta(V)$ describe the rate at which associated ion channels transition between open and closed states. The functions for α and β, which depend only on membrane potential, are:

$$\alpha_n(V) = 0.01\frac{10 - V}{\mathrm{e}^{\frac{10-V}{10}} - 1}; \tag{23}$$

$$\beta_n(V) = 0.125\mathrm{e}^{-\frac{V}{80}}; \tag{24}$$

$$\alpha_m(V) = 0.1\frac{25 - V}{\mathrm{e}^{\frac{25-V}{10}} - 1}; \tag{25}$$

$$\beta_m(V) = 4\mathrm{e}^{-\frac{V}{18}}; \tag{26}$$

$$\alpha_h(V) = 0.07\mathrm{e}^{-\frac{V}{20}}; \text{ and} \tag{27}$$

$$\beta_n(V) = \frac{1}{\mathrm{e}^{\frac{30-V}{10}} + 1}. \tag{28}$$

It is now common practice to present differential equations for gating variables in terms of their steady-state value and time constant. Thus, equations (20) through (22) can be rewritten as

$$\dot{n} = \frac{n_\infty(V) - n}{\tau_n(V)}, \tag{29}$$

$$\dot{m} = \frac{m_\infty(V) - m}{\tau_m(V)}, \text{ and} \tag{30}$$

$$\dot{h} = \frac{h_\infty(V) - h}{\tau_h(V)}. \tag{31}$$

Equations of the form shown in (29) through (31) can be found for each gating variable by a substitution, where

$$n_\infty(V) = \frac{\alpha_n(V)}{\alpha_n(V) + \beta_n(V)}, \text{ and} \tag{32}$$

$$\tau_n(V) = \frac{1}{\alpha_n(V) + \beta_n(V)}. \tag{33}$$

Similar substitutions can be performed to solve for steady-state values and time constants of m and h.

When written in terms of steady-state values and time constants interpretation of gating variable effects is simplified. For any given membrane potential, V, the gating variable will converge to the steady-state value, given sufficient time. The speed with which it converges is governed by its time constant, τ.

In Figures 6 through 8, steady-state values for gating variables have been plotted, along with their associated functions α and β.

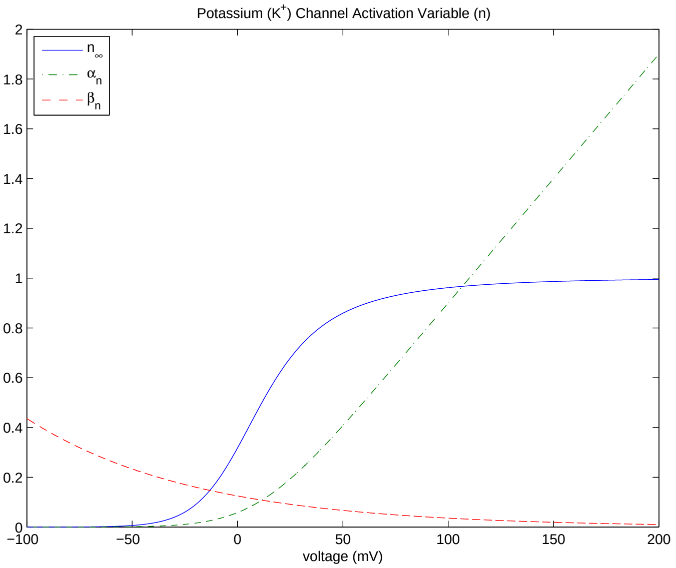

Figure 6: Potassium channel activation variable, n

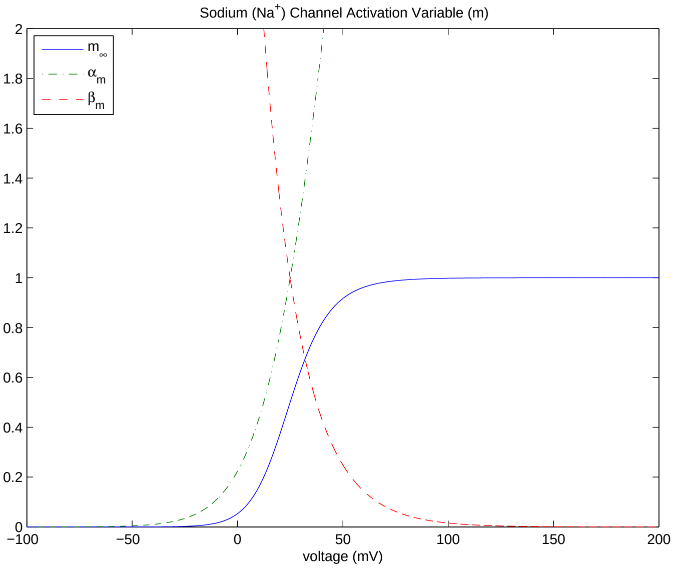

Figure 7: Sodium channel activation variable, m

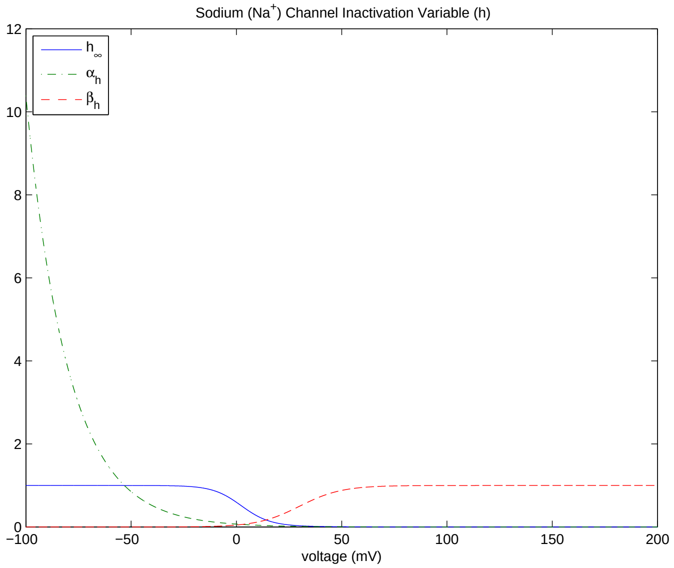

Figure 8: Sodium channel inactivation variable, h

Although the form of potassium ($n_\infty(V)$) and sodium ($m_\infty(V)$) steady-state values is similar, the functions α and β are much steeper for sodium. Furthermore, since there is an inactivation variable for the sodium current (h), the current is only transiently present where as the potassium current is persistent [8]. The steady-state values for n, m, and h are plotted on a single axis in Figure 9 for comparison, with corresponding time constants plotted in Figure 10.

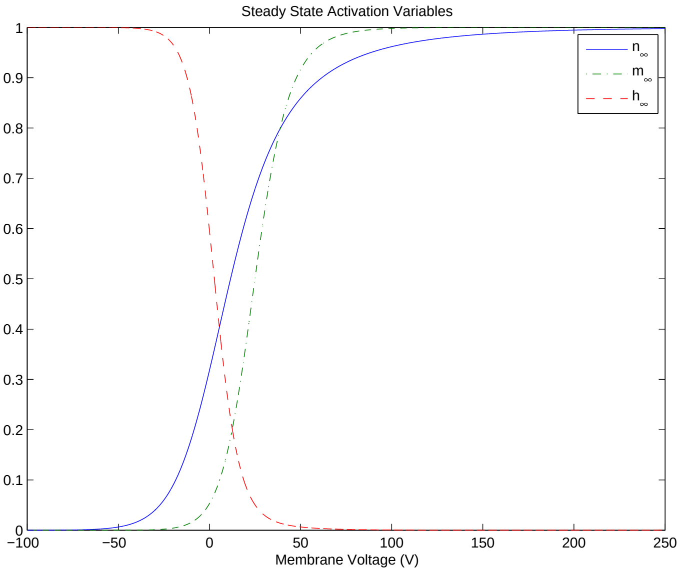

Figure 9: Steady-state activation variables

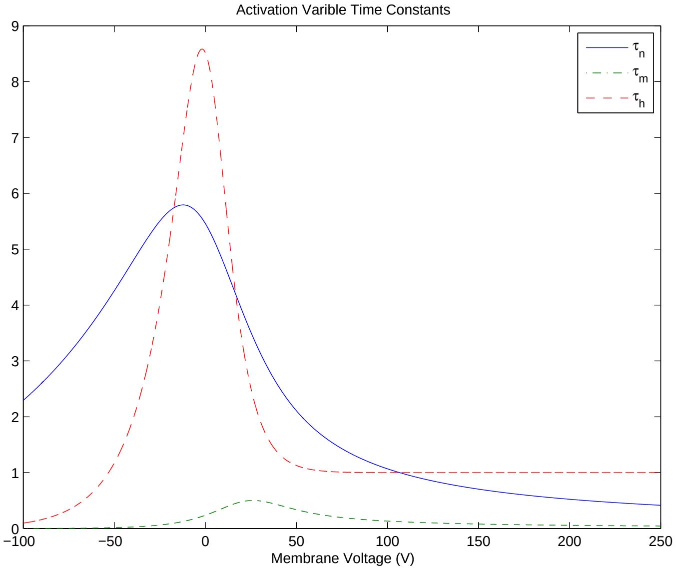

Figure 10: Activation variable time constants

From the perspective of time constant alone it is readily apparent why the sodium current is called “fast” as compared to the potassium current. The activation variable of the sodium current is approximately an order of magnitude faster than that of potassium. This aspect of the classical Hodgkin-Huxley model is exploited to provide a reduced-order approximation of model behavior, as described in Section 2.3.

Thus, in the original Hodgkin-Huxley model, rates at which ion channels are opening and closing are functions of membrane voltage, as modeled by functions α and β for each ionic species. These functions drive activation and inactivation variables which modulate conductance of a given ion channel between zero and its maximal conductance. At any point in time the ionic current is a product of the conductance and the difference between membrane potential and the Nernst equilibrium potential for the given ionic species. Summation of the ionic currents enables computation of the membrane voltage.

An elegant means of portraying this relationship is through time aligned plots of the described signals. Figure 11, after [1, p. 40], depicts both a subthreshold perturbation, as well as an action potential generated by the classical Hodgkin-Huxley model described in this section.

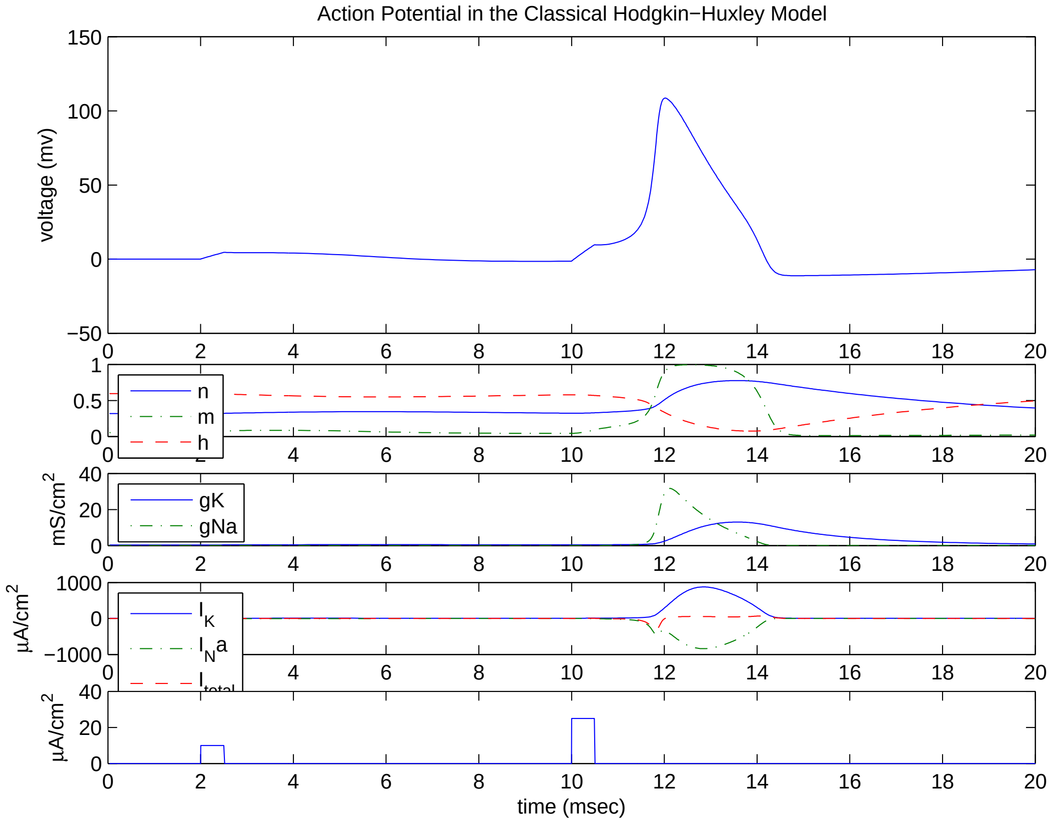

Figure 11: Hodgkin-Huxley model action potential, after [1, p. 40]

As shown in Figure 11, the originally published parameters shifted the resting membrane potential to zero volts [38][1, p. 37]. It is now common practice to have the resting membrane potential of the model align with the experimentally observed resting membrane potential.

2.3 Reduced-Order Hodgkin-Huxley Model

The fact that the described Hodgkin-Huxley model is inherently a dynamical system was not lost on researchers at the time of its publication. Notably, Richard Fitzhugh quickly embraced studying neural models from a dynamical systems point of view, proving as early as 1955 that neither threshold or all-or-none spikes are properties of the Hodgkin-Huxley model, and publishing a simplified model in 1961 [1]. Since that time, the computational neuroscience community has continued to explore neuronal dynamics from a variety of perspectives, including phase plane analysis and simplified neuron models. More recently, Eugene Izhikevich has published a book dedicated to furthering study of neuroscience from a dynamical systems perspective, claiming that most neurocomputational properties can be related to four fundamental bifurcation types [1].

Furthermore, these four fundamental bifurcation types can be exhibited by a second-order simplification of the original Hodgkin-Huxley model. Reduction to two dimensions enables phase plane analysis and simplifies visualization of system dynamics. The reduced neuron model described in [1, p. 133] is

$$C\dot{V} = I - g_K n(V - E_K) - g_{Na} m_\infty(V)(V - E_{Na}) - g_L(V - E_L), \tag{34}$$

$$\dot{n} = \frac{n_\infty(V) - n}{\tau(V)}. \tag{35}$$

The basis for reducing the dimensionality of the original model lies in the difference in the time scale between sodium and potassium activation variables described in Section 2.2.2. Since the sodium channel dynamics are significantly faster than those of the potassium channel, considering them instantaneous introduces very little error to the model as a whole [1, p. 133].

As described in Chapter 4, with proper selection of parameters, this reduced-order model can exhibit the four bifurcation types of interest, and is an excellent means of exploring neurocomputational dynamics.

2.4 Model Parameter Estimation

A goal of system modeling is to determine variables which influence the behavior of interest so that the simulation environment produces results that match observed data to the degree required. In practice, it is often difficult or impossible to accurately quantify all variables of interest. Furthermore, increasing model fidelity is often at odds with computational efficiency or simplified mathematical analysis. Agreement between behavior of the model and the original organism must be established, determining the domain of applicability of the model [43].

This section investigates philosophies for deriving parameter values that are as accurate as possible while producing models with behavior that can be deemed equivalent to the biological neuron it represents. Section 2.4.1 describes techniques for quantifying specific model parameters. Section 2.4.2 describes methods for verifying the model has correct bifurcation dynamics at the system level.

2.4.1 Empirically Derived Parameter Values

When determining parameter values for conductance-based models, researchers often employ a combination of pharmacological and electrical techniques. Pharmacological blockers with known effect on specific ion channels are used to determine the type and number of ionic currents present [1, p. 6]. Specific stimulation profiles are then used to characterize the dynamics of the populations of ion channels.

While researchers have success modeling neuron behavior in this way, a number of limitations, practical and theoretical, complicate the task. For instance, effects of some pharmacological blockers are irreversible (e.g. tetrodotoxin (TTX)). Furthermore, many electrophysiological techniques, such as intracellular recording, greatly limit the future viability of an experimental preparation, prohibiting long term trials. Thus, it is usually not possible to experimentally characterize all parameters of interest within a single trial or preparation and then perform the experiment of interest.

Some progress has been made using continuous time techniques for estimating model parameters more accurately [44]. Optimal state estimation is also used to overcome practical limitations related to variable measurement or reduced trial size [10]. Yet, at the root of system modeling and simulation of neural systems is the inherent variability of the system, and researchers are forced to rely on a combination of theoretical and experimental techniques.

The prevailing opinion is that behavior of interest must be characterized over a statistically significant sample of trials within the environment or organism of interest, or as close as possible. Any results from *In vitro* or simulated environments must be characterized in terms of their relationship to the original system behavior before they can be accepted as valid. Some of the difficulties encountered are well documented in [1, p. 6]. The necessity of a coherent systems-based approach is also advocated in [10].

2.4.2 Bifurcation Dynamics

An approach for producing neuron models which are more likely to produce behavior equivalent to the neuron under investigation is outlined in [1, p. 20]. Emphasis is placed on correct system dynamics over, or in addition to, correct parameter values. The approach is analogous to that advocated by Poincare for nonlinear system analysis in the late 1800s [6, p. 2]. The resulting analysis, both in the case of Poincare and Izhikevich is a geometric one.

The approach advocated by Izhikevich begins with qualitative system dynamics such as bifurcation type, and progresses through description of necessary kinetics [1, p. 20]. The approach can be thought of as a top-down modeling methodology, beginning with simple questions regarding neuron dynamics, rather than a bottom-up approach beginning with individual parameter values. For example, the most fundamental questions highlighted by the Izikevich paradigm revolve around the presence/absence of sub-threshold oscillations, and coexistence of resting and spiking states [1, p. 14].

Under the proposed research paradigm, a tight-knit, multi-disciplinary understanding is required. The capabilities and limitations of each facet of the research approach must be understood, with a common vocabulary to unite the work done in simulation with that accomplished experimentally at the rig.

3 Methods and Analysis

This section describes techniques used for nonlinear analysis and optimal control of mathematical models used throughout this dissertation. The techniques and methods provided in this section are a set of tools to aid in understanding, troubleshooting, and increasing execution efficiency of mathematical neuron models. This section presents a consistent framework for varying inputs and parameters of conductance-based Hodgkin-Huxley type models.

The framework considered here for nonlinear analysis and optimal control of neuron models is depicted in Figure 12. The process has the following steps: define the neuron model, determine the location of system fixed points, classify behavior of the fixed points, determine fixed point bifurcation types, and perform optimal control of the neuron model. Following the framework eases initial implementation and investigation of neuron models and selection of their parameters.

In Chapter 4, a set of reduced-order, two-dimensional models are analyzed. Two-dimensional phase space is readily graphed, providing opportunities to graphically present the number, location, and stability of fixed points, as well as the shape of limit cycle attractors. A two-dimensional phase space enables use of simplified analysis techniques for fixed point location and classification. These techniques (fixed point location via nullclines and fixed point classifier) are presented in the left-hand column of Figure 12 and are described in Sections 3.1.1.1 and 3.1.2.1. By modifying one or more parameters of the second-order model, a range of system behavior can be considered, including the four fundamental bifurcation types that underlay many neurocomputational properties [1, p. 17].

When higher dimensional models are considered, such as the fourth-order system in Chapter 5 and sixth-order system studied in [3], graphical portrayal of the phase space or classification of system fixed points is impeded. For the higher-order models, alternative techniques are utilized for locating and classifying system fixed points, depicted in the right-hand column of Figure 12 and described in Sections 3.1.1.2 and 3.1.2.2. For the considered models, a single function $f(v)$ is derived, the roots of which provide the location of system fixed points, thereby avoiding the need to graphically portray high dimension phase space.

Fixed point behavior can often be classified based on the values of the eigenvalues.

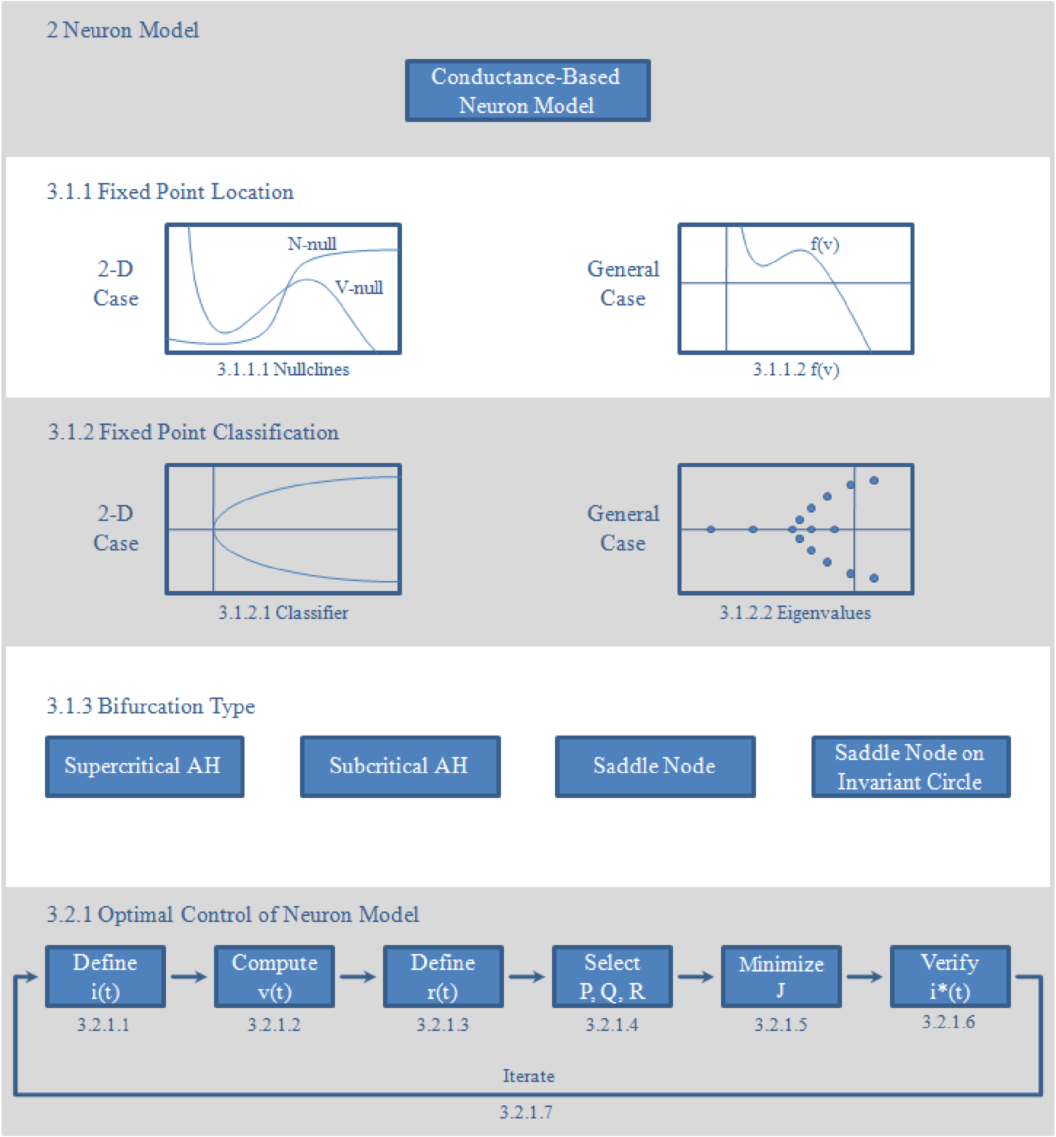

Figure 12: Framework for nonlinear analysis and optimal control of neuron models

Once the nonlinear system is characterized, an optimal control technique can be used to investigate differences between an originally applied input current stimulus and optimal input stimulus currents computed as the result of a user-selected balance between the input current 'energy' and the tracking error between the achieved and original membrane voltages.

Following Figure 12 from top to bottom, neuron models used within this dissertation were described in Chapter 2. Within this chapter, Section 3.1 describes the nonlinear analysis methods employed within this dissertation in further detail and Section 3.2 describes the developed optimal control technique and its application. Section 3.3 highlights specific application level nuances which are employed for efficiency of computation or troubleshooting purposes.

3.1 Nonlinear Systems Analysis Primer

It is often impossible to analytically solve all but the most trivial of nonlinear systems. As a result, the analysis of nonlinear systems typically involves analysis of system dynamics using numerical techniques [6, p. 2]. For a thorough review of nonlinear system analysis techniques see [6]. This section will describe techniques for locating, classifying, and determining bifurcation types of system fixed points for mathematical models considered in this dissertation.

3.1.1 Fixed Point Location

An important starting point for analysis of system dynamics is to determine the number and location of system fixed points. Fixed points, or equilibria, are locations in the phase space where the rate of change for all system states is zero.

When it is not possible to solve the system of equations analytically, a number of methods exist for determining approximate fixed point location [6]. Two such techniques will be presented in this section. In both cases, the technique results in an approximate location of the system fixed point which will be used as the initial condition for a numerical solver, $fsolve$, which is part of the library of functions within MATLAB®, to provide a more accurate estimate.

The first method, applicable to second-order systems, consists of plotting and looking for intersections of the nullclines. Nullclines are the set of points where the differential equation for one of the state variables is equal to zero [6]. For a second-order system, the nullclines indicate the areas in the phase space where movement is either purely vertical or purely horizontal. This technique is described in Section 3.1.1.1.

A second method, described in 3.1.1.2, is extensible to higher-order systems, and involves solving for roots of a derived function, $f(v)$ [3]. Plotting the nullclines in the two dimensional phase space and finding the roots of $f(v)$ are redundant tasks, and only one technique is typically used for analysis based on the order of a given model. Both techniques will be described to provide a means of developing intuition for understanding dynamics of higher-order systems where graphical representation is not possible.

Geometric analysis of the phase space via intersection of the nullclines, in conjunction with associated time domain plots, is preferable when possible since this facilitates both qualitative and quantitative understanding. Solving for roots of $f(v)$ is a more general approach, applicable to the entire family of models considered in this dissertation; however, this method provides little information other than approximate location of system fixed points. Plotting $f(v)$ does not provide any information regarding specific trajectories, and interpretation of the system dynamics is easily lost in the generality of the approach. Thus, the second-order system of Section 4.2.1 will be analyzed using both the two dimensional phase plane and $f(v)$ to develop an intuitive grasp of system dynamics. This will facilitate interpretation of higher-order results back to the neurocomputational properties as they relate to system bifurcation type as presented in [1].

3.1.1.1 Location of System Equilibria Using Nullclines

To find nullclines for the second-order Hodgkin-Huxley model of Section 2.3, each state derivative is set equal to zero, and solved for n [1, p. 92]:

$$\dot{V} = 0 \Rightarrow n = \frac{I - g_{Na} m_{\infty}(v)(v - E_{Na}) - g_L(v - E_L)}{g_K(v - E_K)}\text{; and} \tag{36}$$

$$\dot{n} = 0 \Rightarrow n = n_{\infty}(v) = \frac{1}{1 + \mathrm{e}^{\left(\frac{V_n - v}{k_n}\right)}}. \tag{37}$$

The resulting curves can then be plotted on the phase plane, sweeping V through the applicable range of membrane potential values.

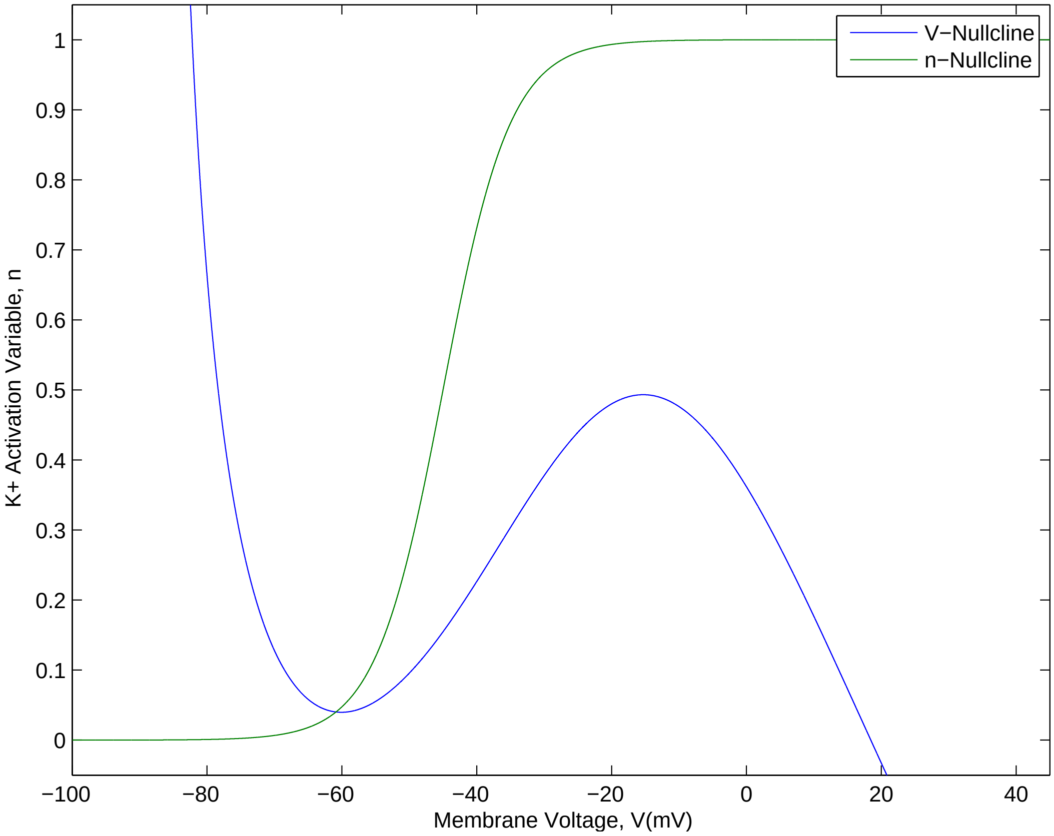

Figure 13: Example reduced-order Hodgkin-Huxley model nullclines

From the plot an approximate value for each state variable at the fixed point location can be deduced directly. For example, the curves plotted in Figure 13 intersect at $V \approx -61\,\text{mV}$, $n \approx 0.07$. These values can be used as initial conditions to compute a numerical solution for the location of the system fixed point.

Additionally, equation (36) reveals that changing the injected current I results in a shift in the V-nullcline. Due to the term $g_K(V - E_K)$ in the denominator, and its dependence on membrane potential, the V-nullcline does not shift in a purely vertical fashion. As seen in Figure 23 of Section 4.2.1.1.1, changes in the injected current result in changes of the system fixed point location. Equation (37) shows that the n-nullcline is dependent on only the membrane potential, V, with no shape or position change as the injected current is varied.

3.1.1.2 Location of System Equilibria Using $f(v)$

To find $f(v)$ for the second-order Hodgkin-Huxley model of Section 2.3, $\dot{n}$ is set equal to zero and solved for n. The result is back-substituted into the equation for $\dot{V}$. This function, designated $f(v)$, is

$$f(v) = \frac{I - g_K n_\infty(V)(V - E_K) - g_{Na} m_\infty(V)(V - E_{Na}) - g_L(V - E_L)}{C} \tag{38}$$

and roots of the function correspond to fixed points of the system.

The derived function $f(v)$ can then be plotted by sweeping V through the applicable range of membrane potential values, as shown in Figure 14.

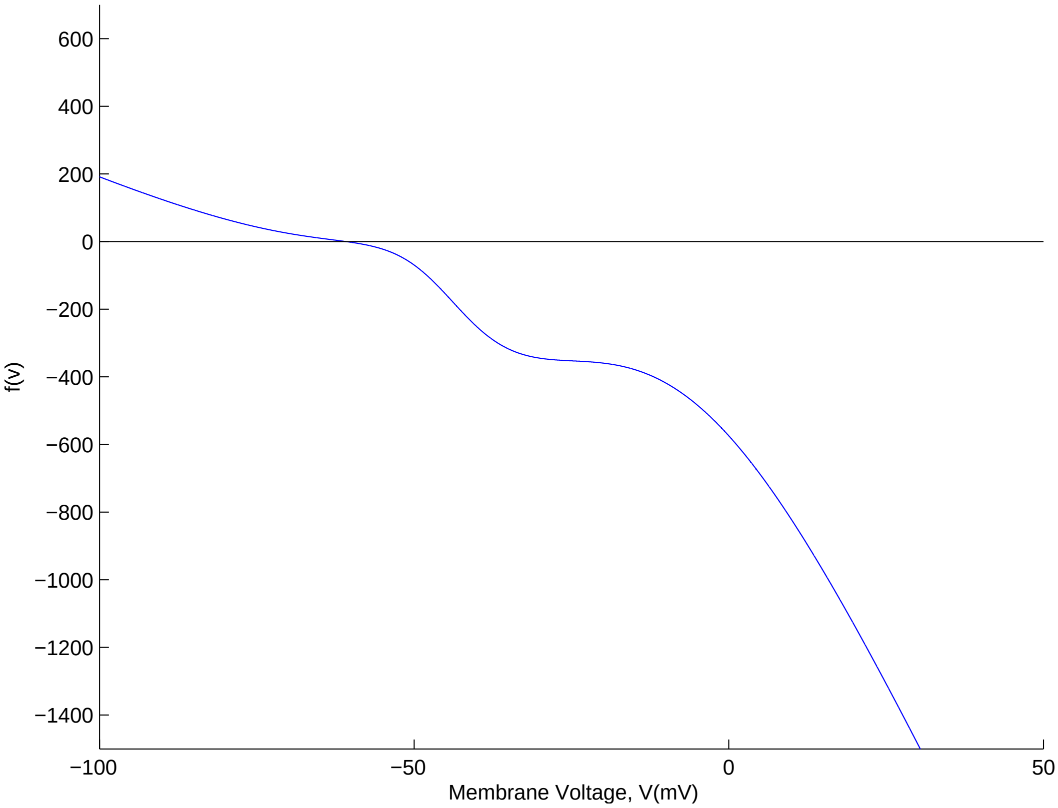

Figure 14: Example reduced-order Hodgkin-Huxley model $f(v)$

From the plot an approximate value for the equilibrium potential of the system fixed point can be deduced by estimating the voltage at which $f(v)$ is equal to zero. The approximate equilibrium potential can then be used to compute the approximate value of n by substituting value for V into $n_\infty(V)$, producing an estimate of the fixed point. Notice in Figure 13 the value for n can be estimated from the phase plane graphically, where Figure 14 does not provide a graphical indication of the value for n.

Like the V-nullcline in Figure 13, $f(v)$ is shifted vertically with changes in the injected stimulus. Additionally, the shape of the plot is informative of the possible number of fixed points for any value of I [3]. In Figure 14, since $f(v)$ is monotonic, it is directly observable that no value of I will result in more than one system fixed point.

3.1.1.3 Results Comparison

The intersection of the nullclines in Figure 13 and the root of $f(v)$ in Figure 14 approximate the same equilibrium membrane potential. That is, the two techniques produce the same result. Plotting the nullclines in the two dimensional phase space and finding the roots of $f(v)$ are redundant tasks with different benefits for system analysis.

The n-V phase plane enables plotting system trajectories and approximation of equilibrium values for both n and V directly; however, plotting the phase space, which is easy to draw in two dimensions, can become more complicated in three dimensions, and is difficult or impossible to portray graphically in high dimensional space. It is also not immediately clear from Figure 13 how many fixed points the system will have for all values of I.

Finding the roots of $f(v)$ is a more general method for determining the number and approximate location of fixed points as the dimensionality of the system increases, and the results can be displayed on a single plot. It is a fortunate consequence that the structure of conductance-based models often results in a straightforward calculation of $f(v)$ which depends only on membrane potential. However, the plot for $f(v)$ does not enable plotting system trajectories, and back-substitution of the approximate equilibrium potential is required for approximation of the system fixed point.

When these two techniques are used together, it becomes possible to understand system dynamics in the framework of [1], and to interpret applicable neurocomputational properties for higher-order models.

3.1.2 Fixed Point Classification

Once the location of a fixed point has been computed, it can be classified according to behavior of system trajectories in its immediate vicinity. Following the technique presented in [6, pp. 137, 150], the phase plane will be linearized in the region surrounding the fixed point using the system Jacobian. Eigenvalues of the Jacobian are indicative of local stability of the system fixed point, depending on their value. As shown in Figure 12, two techniques will be described for analyzing results of the linearized system. Once classification has been achieved by linearization of the system of equations, it is essential to verify the localized behavior of the linear system is equivalent to the original nonlinear system for both techniques.

As described in Section 3.1.2.1, for two-dimensional systems, it is possible to classify stability and localized behavior on a single diagram [6, p. 137]. A parallel method, described in Section 3.1.2.2, consists of examining the locus of eigenvalues as the injected current is varied. The classification diagram is explicit and informative, but limited to use in second-order systems. The locus of eigenvalues can be generated for a higher-order system, but requires interpretation for relating results to the neural computational properties identified in [1]. For instance, stability requires the real part of all eigenvalues to be negative, and oscillation requires eigenvalues with complex conjugate pairs.

3.1.2.1 Fixed Point Classification for Two-Dimensional Systems

Once the location of the system fixed points has been determined, they can be classified according to local stability. Properties of the nonlinear system can then be related to neurocomputational properties of the model. For example, in the context of neuron models a stable fixed point indicates a stable resting membrane potential of the cell. Local dynamics also provide details for confirming neurocomputational properties such as the presence of subthreshold oscillations [1].

Following [6, p. 150], linearization of the system proceeds by substitution of the fixed point, plus a small perturbation, into the system of equations. If higher-order terms are neglected, linearization of the second-order Hodgkin-Huxley model of Section 2.3 yields

$$\begin{bmatrix} \dot{V} \\ \dot{n} \end{bmatrix} = \begin{bmatrix} \frac{\partial f_1}{\partial V} & \frac{\partial f_1}{\partial n} \\ \frac{\partial f_2}{\partial V} & \frac{\partial f_2}{\partial n} \end{bmatrix} \begin{bmatrix} V \\ n \end{bmatrix} \tag{39}$$

where $\dot{V} = f_1()$, $\dot{n} = f_2()$, and the matrix of partial derivatives comprise the Jacobian matrix. Values for state variables, in this case V and n, as well as the corresponding injected current value, are substituted into the Jacobian, allowing computation of eigenvalues. Eigenvalues of the linearized system, evaluated at the location of a fixed point, are indicative of expected qualitative system behavior and stability of the linear system in the vicinity of the fixed point.

It should be noted that classification of the fixed point via linearization is not always robust. The question remains as to whether linear system with neglected higher-order terms accurately approximates the original nonlinear system. According to the Hartman-Grobman theorem, the phase plane for a nonlinear system near a hyperbolic fixed point is topologically equivalent to the linearized system in the neighborhood of the fixed point [6, p. 155][1, p. 103]. A fixed point is hyperbolic when the Jacobian does not have eigenvalues which are equal to zero or with real parts equal to zero [6, 1].

In the context of the fixed point classification diagram, fixed points which exist within the regions corresponding to saddle points, nodes, and spirals constitute hyperbolic fixed points. In these regions classification of fixed points of the linearized system accurately represent classification of fixed points of the original, nonlinear system.

For cases where the classification lies on the borderline between two regions, classification of fixed points for the linearized system are not guaranteed to be topologically equivalent to those of the nonlinear system, and higher-order terms must be taken into account. These cases correspond to the bifurcation point of the system [1, p. 103].

After computing eigenvalues for the linearized system in the vicinity of the fixed point for each injected current value, the trace (τ) and determinant (Δ) for each fixed point is

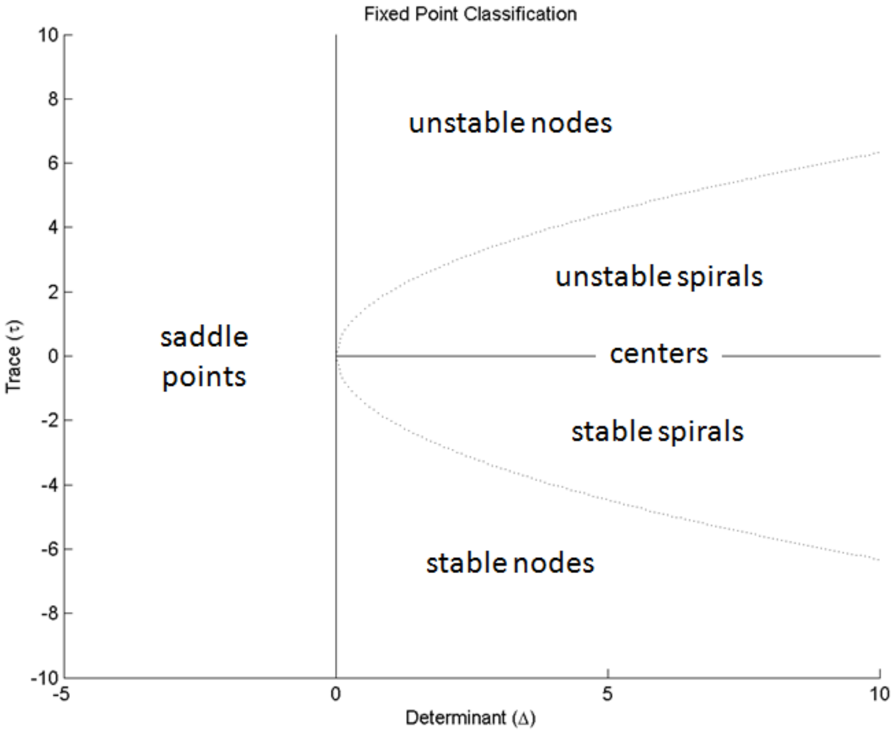

Figure 15: Graphical fixed point classification, after [6]

calculated as described in [6]. Namely,

$$\tau = \lambda_1 + \lambda_2 \tag{40}$$

and

$$\Delta = \lambda_1 * \lambda_2 \tag{41}$$

where λ_1 and λ_2 are the eigenvalues of the linearized two dimensional system of equations. Classification of each fixed point is represented on the classification diagram by a single point. This process must be carried out for each injected current value under investigation. The result is a set of points plotted on top of the fixed point classification diagram with one point representing each injected current value as shown in Figure 25 of Chapter 4.

The goal of fixed point classification is to determine the range of injected current levels which elicit qualitatively different behavior from the model (i.e. rest, subthreshold oscillation, repetitive spiking). The boundaries between those ranges are levels of injected current which cause the system fixed point to undergo bifurcation. Determining values for these boundaries allows proper selection of injected current stimulus values for application of the optimal control to the neuron model.

If a specific level of injected current produces a fixed point which is classified as an unstable spiral, and another level of injected current produces a fixed point which is classified as a stable spiral then, by continuity, the fixed point undergoes a bifurcation for some value of injected current in between these two values. Again, Figure 25 of Chapter 4 provides an example. For $I = 10\,\mu\text{A/cm}^2$ the fixed point is classified as a stable spiral, and for $I = 20\,\mu\text{A/cm}^2$ the fixed point is classified as an unstable spiral. By continuity, at some value in between these two injected current levels, the system fixed point undergoes a bifurcation.

Classification of the system fixed point according to Figure 15 provides two important pieces of information for interpretation of system dynamics. First, the stability of the fixed point is determined. Any fixed point which has a negative trace (τ) and positive determinant (Δ) is stable. A fixed point with a negative determinant or positive trace is unstable. Second, any fixed point which is classified as a spiral exhibits oscillation. The existence of subthreshold oscillations allows categorization of the neural model as a resonator according to the classification scheme of [1, p. 14]. Further investigation is required to determine the coexistence of repetitive spiking and resting states.

3.1.2.2 Fixed Point Classification for Higher-Order Systems

Examination of eigenvalues of the Jacobian is also informative of stability and behavior of the system in the immediate vicinity of a system fixed point for a higher-order system. Analysis proceeds along the same lines as Section 3.1.2.1. First the Jacobian is calculated, and values for the system fixed point and injected current level are substituted into the linearized system. Eigenvalues are then calculated and plotted on the complex plane rather than computing the trace and determinant.

As in Section 3.1.2.1, so long as none of the eigenvalues are zero valued, or have real parts equal to zero, the linearized system is topologically equivalent to the original nonlinear system by the Hartman-Grobman theorem [6, p. 155][1, p. 103]. If any eigenvalues are equal to zero, or have real parts equal to zero, the fixed point is not hyperbolic, and higher-order terms must be taken into account to determine if the linear system accurately represents the original nonlinear system.

If all eigenvalues exist on the left hand plane with negative real parts, the fixed point is stable. If any eigenvalue has a positive real part the fixed point is unstable. Furthermore, if all eigenvalues exist on the real axis the system will not exhibit local oscillation. Eigenvalues which exist in complex conjugate pairs are indicative of a system which will oscillate.

To create a locus of eigenvalues this process is repeated for each injected current value I. When eigenvalues transition from the left to right hand plane loss of stability is indicative of a bifurcation of the fixed point. Likewise, when eigenvalues break away or collapse to the real axis, a qualitative change in system dynamics has occurred related to the ability of the system to oscillate.

3.1.2.3 Results Comparison

Using the fixed point classification diagram of [6] or the eigenvalues of the Jacobian allows determination of fixed point stability, including the presence of oscillatory behavior. Classification of the system fixed point must be carried out for each fixed point of the system, at every injected current value. Depending on the order of the model only one of these techniques is typically used for any given analysis.

Classification of the fixed point according to the scheme presented in [6] aligns nicely with the neurocomputational properties in [1], but is limited to two dimensional systems. The results from plotting eigenvalues on the complex plane are not limited to two dimensional systems, but require further interpretation for relating the results to [1].

Thus the results from both techniques will be presented for a two-dimensional model in Chapter 4 to demonstrate interpretation of the resulting data.

3.1.3 Bifurcations

To select appropriate injected current values, and properly classify neurocomputational properties, it is essential to know the approximate injected current value at which a bifurcation of the system fixed point occurs, and what type of bifurcation the fixed point undergoes. In fact, determination of bifurcation types are the primary means of identifying the neurocomputational properties of the neuron or neuron model under investigation [1].

Information gleaned in the analysis process thus far provides an approximation of the value at which the bifurcation occurs. For the purposes of this dissertation, it will not be necessary to determine the exact value at which the bifurcation occurs. It will be sufficient to understand the type of bifurcation and the approximate bifurcation point.

Section 3.1.3.1 will describe the method for determining bifurcation type, and Section 3.1.3.2 will describe methods for determining bifurcation value where required.

3.1.3.1 Bifurcation Type

For conductance-based neuron models considered in this dissertation the primary goal is to determine which of the four primary bifurcations identified in [1] have occurred. The four bifurcation types are saddle-node, saddle-node on an invariant circle, supercritical Andronov-Hopf, and subcritical Andronov-Hopf. A number of criteria, both empirical and theoretical, will be presented in this section for determination of the bifurcation type exhibited by a system fixed point.

Identification of the bifurcation type can be made by answering two questions regarding qualitative neural activity [1]. Does the neuron, or neuron model, exhibit subthreshold oscillations? Does the neuron, or neuron model, demonstrate coexistence of resting and repetitive spiking states? Answering these two questions relates observed properties of the neural dynamics (i.e. integrator, resonator, bistability, or monostability) to the type of bifurcation the system dynamics undergo (i.e. saddle-node, saddle-node on invariant circle (SNIC), subcritical Andronov-Hopf, or supercritical Andronov-Hopf). Additionally, rigorous definition of bifurcation criteria can be investigated when required [1].

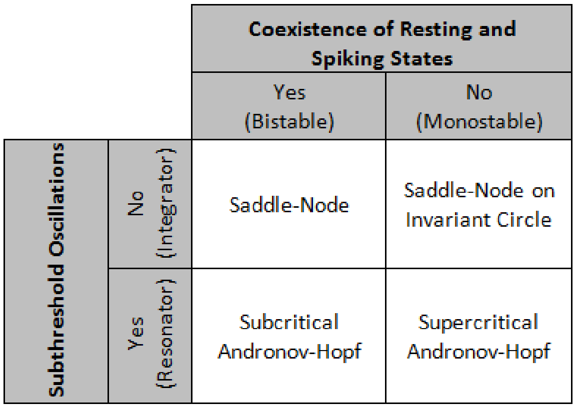

		Coexistence of Resting and Spiking States	
		Yes (Bistable)	No (Monostable)
Subthreshold Oscillations	No (Integrator)	Saddle-Node	Saddle-Node on Invariant Circle
	Yes (Resonator)	Subcritical Andronov-Hopf	Supercritical Andronov-Hopf

Table 1: Determination of Bifurcation Type, after [1, p. 14, 229-230]

Using theoretical information from the analysis presented in Sections 3.1.2.1 and 3.1.2.2, it is possible to determine if a neuron is capable of subthreshold oscillations directly. For two-dimensional systems, classification of a system fixed point as a spiral is indicative of the ability to produce subthreshold oscillations. For higher-order systems the presence of complex conjugate eigenvalue pairs is indicative of a neuron model which is capable of oscillation. Models capable of subthreshold oscillation are defined as resonators and likely undergo Andronov-Hopf bifurcation types. Also, occurrence of either Andronov-Hopf bifurcation type results in a change in stability of a system fixed point. Thus, a change in stability of a system fixed point is also indicative of an Andronov-Hopf bifurcation.

Models which cannot oscillate are defined as integrators and likely undergo saddle-node bifurcation types. In terms of the classification diagram for two-dimensional systems presented in Section 3.1.2.1, a saddle-node can be identified based on a negative valued determinant. A fixed point which undergoes an Andonov-Hopf bifurcation will have a positive determinant and be classified as a node or spiral. Using the technique presented in Section 3.1.2.2 for higher-order systems, a fixed point which is a saddle-node consists of one stable, and one unstable eigenvalue. Also, saddle-node bifurcation types always result in creation or disappearance of a pair of fixed points via coalescence [1]. Therefore, any system which exhibits a saddle-node bifurcation of either type will gain or lose a pair of fixed points.

Thus, observation of subthreshold oscillations enables classification of neural dynamics between integrators (saddle-node) and resonators (Andronov-Hopf). Determination of the exact bifurcation type among the four classes described in [1, p. 14] then depends on whether or not there is a coexistence of resting and spiking states. When resting and repetitive spiking states exist simultaneously, the neural dynamics are referred to as bistable due to the presence of a stable fixed point along with a stable limit cycle attractor.

As shown in Figure 15, saddle-node and subcritical Andronov-Hopf bifurcation types are bistable and saddle-node on invariant circle and supercritical Aronov-Hopf bifurcation types are monostable.

The most recognizable trait when there is a coexistence of resting and spiking states is hysteresis. By applying a ramp current which increases above the bifurcation point and then ramps back to zero, the presence of hysteresis behavior can be tested. If the repetitive spiking ceases when the injected current returns to zero the neuron is likely monostable. Another empirical test which can be conducted 'at the rig' or in simulation is to apply transient injected current pulses. If it is possible to change the behavior of neural dynamics between rest and repetitive spiking with appropriately timed transient injected current pulses the neuron is likely bistable [1].

It is noteworthy that distinction between supercritical and subcritical Andronov-Hopf bifurcation types can be made through application of different levels of injected current. If the action potential amplitude is able to be modulated by the level of injected current it is a supercritical bifurcation type. Otherwise it is a subcritical Andronov-Hopf bifurcation [1, p. 12].

3.1.3.2 Bifurcation Value

If required, it is often possible to compute a numerical solution for the bifurcation value using the information provided by the analysis method outlined in this section.

A saddle-node bifurcation occurs for the injected current value at which the one stable and one unstable fixed point coalesce. A numerical solution for the point at which the two equilibria are equal is indicative of the bifurcation value. A fixed point exhibits an Andonov-Hopf bifurcation when the real part of the eigenvalues are equal to zero as the fixed point changes stability. A numerical solution for the bifurcation point can be developed using this criteria.

3.2 Optimal Control Primer

Optimal control theory provides a framework for mathematical optimization of system performance according to a selected objective function. Given a mathematical model of the system dynamics, an objective function is developed either to maximize a performance index or minimize a system cost [45, p. 1]. The technique developed in this dissertation uses an objective function which balances two competing criteria: tracking accuracy and input ‘energy’ usage. For a thorough review of optimal control see [46].

The objective function described has been previously published in two different forms [2, 3]. As published in [2], the objective function consists of three independently weighted terms: a P-term, which is the squared error between a reference membrane voltage and actual membrane voltage at the end of the interval of interest; a Q-term, which is the squared error between a reference membrane voltage and actual membrane voltage over the interval of interest; and lastly, an R-term, which is the squared amplitude of the injected current (input current ‘energy’), that is,

$$J[i(t)] = \frac{P}{2}[v(T) - r(T)]^2 + \frac{Q}{2}\int_0^T [v(t) - r(t)]^2 dt + \frac{R}{2}\int_0^T [i(t)]^2 dt. \tag{42}$$

Choosing values of P and Q which are large compared to R results in a solution for $i(t)$ which minimizes error between the desired reference signal, $r(t)$, and the actual membrane voltage, $v(t)$. This solution will however often require an injected current $i(t)$ with a higher ‘energy’ in comparison to optimal currents with lower weighting on P and Q. Conversely, selecting a value of R which is large in relation to P and Q results in a reduced amount of injected current ‘energy’, likely at the expense of increased differences between $r(t)$ and $v(t)$.

In most cases, the value chosen for P and Q are equal since both terms relate to the difference between the desired and actual membrane voltage. However, since P specifically penalizes error at the end of the time interval, the objective function can be used to investigate optimal injected current for generation of an action potential at a specified time, where the end of the simulation interval, T, is chosen to align with the peak of an action potential, $v(t)$ [2]. In this case, intermediate values of the membrane voltage are unimportant ($Q = 0$), and P should be large in comparison to R.

Since the P-term specifies a value for the membrane potential at the end of the time interval, and the signals of interest are functions of continuous time, T, optimal control problems of this form are called Continuous-Time, Final State Fixed, Optimal Controllers [46].

Although the criteria of interest (tracking accuracy and 'energy' usage) were not changed, two modifications were made to the objective function as published in [3]. The P-term was removed, and the method for specifying Q and R was modified. The objective function, as published in [3] is

$$J[i(t)] = \frac{1-\alpha}{2}\int_0^T [v(t) - r(t)]^2 dt + \frac{\alpha}{2}\int_0^T [i(t)]^2 dt. \tag{43}$$

With the objective function defined in equation (43), adjusting the balance between tracking accuracy and input 'energy' requires changing only a single variable, α. As α is increased, 'energy' efficiency is emphasized. As α is decreased, tracking accuracy is improved. Choosing a value for α within the range $\alpha \in (0, 1]$ balances these two competing criteria.

The objective function (43) enables varying a single variable over a given range to balance two competing aspects of system performance; however, the fixed final state implementation of equation (42) provides the capability of investigating action potential timing. Within this dissertation an objective function in the form of equation (42) will be used.

The Hamilton associated with equation (42) for the two-dimensional case is

$$\begin{aligned}H(v,n,\lambda_1,\lambda_2) &= \frac{Q}{2}[v(t)-r(t)]^2+\frac{R}{2}[i(t)]^2\\&+\frac{\lambda_1(t)}{C}[i(t)-g_{Na}m_\infty(v)(v(t)-E_{Na})-g_Kn(t)(v(t)-E_K)-g_L(v(t)-E_L)]\\&+\frac{\lambda_2(t)}{\tau}[n_\infty(v)-n(t)]\end{aligned} \tag{44}$$

where λ_1 and λ_2 are the co-state variables. Following [46, p. 134], the "Continuous Nonlinear Optimal Controller with Function of Final State Fixed" yields

$$\begin{aligned}\dot{v} &= \frac{\partial H}{\partial \lambda_1}\\&= \frac{1}{C}[i(t)-g_{Na}m_\infty(v)(v(t)-E_{Na})-g_Kn(t)(v(t)-E_K)-g_L(v(t)-E_L)]\end{aligned} \tag{45}$$

$$\dot{n} = \frac{\partial H}{\partial \lambda_2} = \frac{1}{\tau}[n_\infty(v)-n(t)] \tag{46}$$

$$\begin{aligned}\dot{\lambda}_1 = -\frac{\partial H}{\partial v} &= -Q(v(t)-r(t))\\&+\frac{\lambda_1(t)}{C}[g_{Na}m_\infty(v)+g_Kn(t)+g_L+g_{Na}(v(t)-E_{Na})\frac{\partial m_\infty(v)}{\partial v}]\\&-\frac{\lambda_2(t)}{\tau}\frac{\partial n_\infty(v)}{\partial v}\end{aligned} \tag{47}$$

$$\dot{\lambda}_2 = -\frac{\partial H}{\partial n} = \frac{g_K}{C}\lambda_1(t)(v(t)-E_K)+\frac{\lambda_2(t)}{\tau} \tag{48}$$

with boundary conditions

$$v(0) = v_0 \tag{49}$$

$$n(0) = n_0 \tag{50}$$

$$\lambda_1(T) = P(v(T)-r(T)) \tag{51}$$

$$\lambda_2(T) = 0 \tag{52}$$

The input stimulus current $i(t)$ can be removed by substitution using the stationarity condition. Using the stationarity condition,

$$\frac{\partial H}{\partial i} = Ri(t) + \frac{\lambda_1(t)}{C} = 0, \tag{53}$$

and solving for $i(t)$ yields

$$i(t) = -\frac{1}{RC}\lambda_1(t). \tag{54}$$

The derivatives in equation (47) are

$$\frac{\partial m_\infty(v)}{\partial v} = \frac{1}{k_m}\frac{\mathrm{e}^{\left(\frac{V_m - v}{k_m}\right)}}{\left(1+\mathrm{e}^{\left(\frac{V_m - v}{k_m}\right)}\right)^2} \tag{55}$$

$$\frac{\partial n_\infty(v)}{\partial v} = \frac{1}{k_n}\frac{\mathrm{e}^{\left(\frac{V_n - v}{k_n}\right)}}{\left(1+\mathrm{e}^{\left(\frac{V_n - v}{k_n}\right)}\right)^2} \tag{56}$$

Solving the boundary value problem (BVP) of equations (45) through (48), resulting from the system dynamical model of equations (34) and (35) and objective function (42), yields $v(t)$, $n(t)$, $\lambda_1(t)$, and $\lambda_2(t)$ specific to the selected balance of tracking error and 'energy' according to P, Q, and R along with initial conditions. The optimal input stimulus current, designated $i^*(t)$, can be computed via equation (54). A range of injected current waveforms, $i(t)$, and weighting coefficients, P, Q, and R, form the basis of an investigation into neuron dynamics.

This section continues with a high level overview of the technique in Section 3.2.1 with example results in Section 3.2.2.

3.2.1 Technique Overview

The developed optimal control technique is a general method that enables investigation of mathematical optimality between the input provided and the output produced. In general, an arbitrary signal could be chosen for the reference signal $r(t)$ (constant, step function, sine wave, etc.). Since the model under investigation is a nonlinear neuron model certain waveforms are of particular interest. Specifically, signals of interest include perturbations from the resting potential with subthreshold oscillations, single action potentials, and repetitive spiking. Furthermore, it is especially informative to relate these signals to injected stimuli traditionally applied ‘at the bench’ by electrophysiologists.

More pragmatically, considering the nonlinear, highly sensitive dynamics of the mathematical models under investigation it also greatly increases the likelihood and efficiency of convergence of numerical methods when the typical domain and behavior of the model is taken into account. One method, for example, involves using a membrane voltage generated by the model as the reference voltage.

Table 2 outlines a series of steps for computation of a reduced ‘energy’ input stimulus.

1. Select an arbitrary $i(t)$ over an interval $[0, T]$ and initial conditions $v_0 = v(0)$ and $n_0 = n(0)$ (often set to resting values).
2. Compute the resulting membrane voltage, $v(t)$, produced by the mathematical model.
3. Use the computed membrane voltage, $v(t)$, from step 2 as the reference signal, $r(t)$.
4. Select values for the weighting coefficients P, Q, and R to reflect the desired balance between tracking error and injected current stimulus ‘energy’.
5. Minimize the corresponding objective function using a two point boundary value problem solver to find $i^*(t)$ [46, 47].
6. Verify the optimal current found in step 5 by computing the membrane voltage, $v^*(t)$, resulting from application of $i^*(t)$ to the mathematical model.

Table 2: Reduced Energy Input Stimulus Discovery Method, adapted from [2, 3]

In practice, a family of results is generated by iterating on steps 4 through 6 of Table 2 for different values of P, Q, and R. Values of P, Q, and R are selected to represent a spectrum of results, with emphasis ranging from tracking accuracy to input stimulus ‘energy’ reduction.

Next a different input signal can be selected, often either a step input of different amplitude or a ramp input, and the entire process repeated.

Although the objective function (43) selected emphasizes a relationship between the reference and actual membrane voltage, no relationship is specified with respect to the initial injected stimulus current $i(t)$ and the optimal current $i^*(t)$. In fact, examination of the differences between the original input current $i(t)$ and the optimal input current $i^*(t)$ provides insight into neuron model function.

As demonstrated in Chapter 4, the described method is effective in producing reduced 'energy' input stimuli for a range of conductance-based, Hodgkin-Huxley type models, with a variety of reference signals and weighting coefficient values.

Further description of each step of the process outlined in Table 2 is provided below.

3.2.1.1 Selecting an Input Current and Initial Conditions

Often it is desirable to select initial conditions as close to resting values as possible. This reduces transients at the beginning of the time interval. Large transients, or even action potentials, can result from initial conditions which are too far from the resting values.

A good method for determining initial conditions is to perform step 2 of Table 2 with quiescent input current, that is $I = 0$. If the simulation interval is long enough all transients should decay, and the values for all state variables at the end of the simulation can be used as initial conditions to prevent transients.

The process of selecting an input current is informed by the process described in Section 3.1. Of special interest are values of the input current at which bifurcations of the fixed point occur as described in Section 3.1.3.

For example, as published in [2], the fixed point of the reduced-order Hodgkin-Huxley model undergoes a supercritical Andronov-Hopf bifurcation at $I \approx 14.66\,\mu\text{A/cm}^2$. As a result, values of $I = 10\,\mu\text{A/cm}^2$ and $I = 35\,\mu\text{A/cm}^2$ were chosen for constant input currents. This demonstrated the qualitatively different behavior of the model.

3.2.1.2 Compute the Membrane Potential Waveform

Once initial conditions and a stimulus waveform have been selected, it is possible to compute the time varying membrane potential, $v(t)$. Using the MATLAB® routine *ode*45, computation of $v(t)$ is generally a straight-forward process which is not computationally intensive; however, properly defining tolerances of the solution is essential. Further details on this topic are presented in Section 3.3.1.

3.2.1.3 Define the Reference Signal

In general, steps 3.2.1.1 and 3.2.1.1 could be ignored and any arbitrary signal could be used as the reference signal in this step. In the case of neuron models, there are two reasons why these steps are important.

First, the models are inherently nonlinear and numerically sensitive. Forcing the model to track an arbitrary reference signal $r(t)$ is outside the applicable domain for some or all of the state variables, often resulting in non-convergence of the numerical optimization techniques. Furthermore, neurons have specific behaviors of interest, such as action potentials or subthreshold oscillations, which are difficult to specify arbitrarily.

Consequently, it is often useful to use the model itself to generate a membrane potential, $v(t)$ with characteristics of interest and to set the reference signal $r(t)$ equal to $v(t)$.

3.2.1.4 Select Weighting Coefficient Values

Understanding the system dynamics and impact of optimal control will require a spectrum of values, with emphasis ranging from tracking accuracy to input stimulus ‘energy’ reduction. Yet it is often the simulations with extreme emphasis on one of the two criteria which are the most sensitive and time intensive to run. A good starting point is to set $P = Q = 100$ and $R = 1$. Once a baseline understanding of the execution efficiency and results are understood, more extreme values can be investigated.

3.2.1.5 Minimize the Objective Function

Computation of the optimal stimulus input current, $i^*(t)$, for the selected reference signal $r(t)$ and weighting coefficients P, Q, and R consists of minimizing the defined objective function by solving a two point boundary value problem (BVP) [46]. An essential tool for computing the numerical solution is a collocation-based boundary value problem solver such as *bvp4c* in MATLAB® [47]. Boundary value problem solvers based on the shooting method have been ineffective with the neuron models used in this dissertation. Further details on this topic are presented in Section 3.3.3.

The numerical solution to the two point boundary value problem consists of a set of points that approximate the time varying solution to each state and costate of the system. The optimal input current and resulting membrane potential are part of the resulting solution.

3.2.1.6 Verify the Optimal Input Current

One method to verify the computed optimal input current is repeat step 2, applying $i^*(t)$ as described in Section 3.2.1.2. After simulating the system, verify the membrane potential generated by *ode*45 is approximately equal to that generated by *bvp*4*c*.

3.2.1.7 Iterate

After generating results as described by Table 2, it is often necessary to change the values of the weighting coefficients and repeat steps 4 through 6. Once a spectrum of results have been produced, it can be informative to select a new input current, $i(t)$, as defined in step 1, and repeat the entire process again, creating another spectrum of results.

Generating results for all of the qualitatively different system behaviors, as determined through the analysis process of Section 3.1, provides insight into neural model function.

As described in [3], a higher level simulation was written which automated the process. By choosing a range of values for α and running the simulation, a spectrum of results is produced. The numerical solution for each successful run was provided to *bvp*4*c* as the initial approximation of the solution for the next value of α. Automated adaptation of α was a more efficient means of simulating the system, and also included the ability to adapt changes in α based on the convergence of numerical algorithms. This also resulted in more convergent solutions than choosing values arbitrarily.

3.2.2 Example Results

Example results will be generated to demonstrate the Reduced Energy Stimulus Discovery Method. The results presented in this section mirror plots presented in [2, 3].

Section 3.2.2.1 proceeds by demonstrating the method when selecting a constant input current, and Section 3.2.2.2 uses a ramp input current.

3.2.2.1 Example 1: Constant Input Current Stimulus

3.2.2.1.1 Step 1: Select a stimulus current waveform $i(t)$ and initial conditions

For this example, a constant value stimulus input current is selected that is below the bifurcation value. As published in [2], the system fixed point undergoes a bifurcation at $I \approx 14.66\,\mu\text{A/cm}^2$, so the selected input current of $i(t) = 10\,\mu\text{A/cm}^2$ produces damped, subthreshold oscillations.

Previous simulations with quiescent input current have enabled identification of resting values for the membrane potential, V, and the gating variable, n, which will be used as initial conditions. In this example $v_0 \approx -60.86\,\text{mV}$ and $n_0 \approx 0.04$.

3.2.2.1.2 Step 2: Compute the membrane voltage $v(t)$ produced by the model

Using $ode45$, the constant value input current selected in step 1 was applied to the model to produce the time varying membrane voltage pictured in Figure 16.

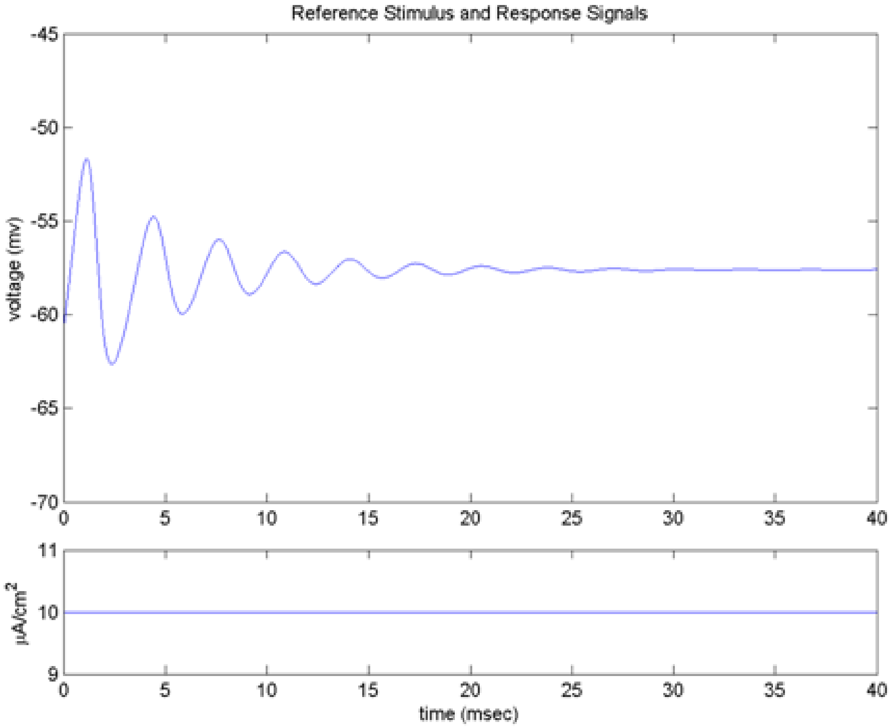

Figure 16: Constant stimulus current and reference membrane voltage signals

3.2.2.1.3 Step 3: Use the computed membrane voltage $v(t)$ as the reference signal $r(t)$

In the simulation, the set of points constituting the numerical solution for the membrane potential $v(t)$ was set equal to the reference signal $r(t)$.

3.2.2.1.4 Step 4: Select values for the weighting coefficients P, Q, and R

Values were selected for P, Q, and R which reflect an emphasis on reducing tracking error between the reference signal and resulting membrane potential. Weighting coefficients which relate to tracking accuracy were set to $P = 100$ and $Q = 100$ and the coefficient which emphasizes reduced input 'energy' was set to $R = 1$.

3.2.2.1.5 Step 5: Minimize the corresponding objective function

Using *bvp4c*, the two point boundary value problem was solved numerically, producing the optimal input current $i^*(t)$ and the resulting time varying membrane voltage $v^*(t)$ pictured in Figure 17. For comparison the reference signals are also included in Figure 17.

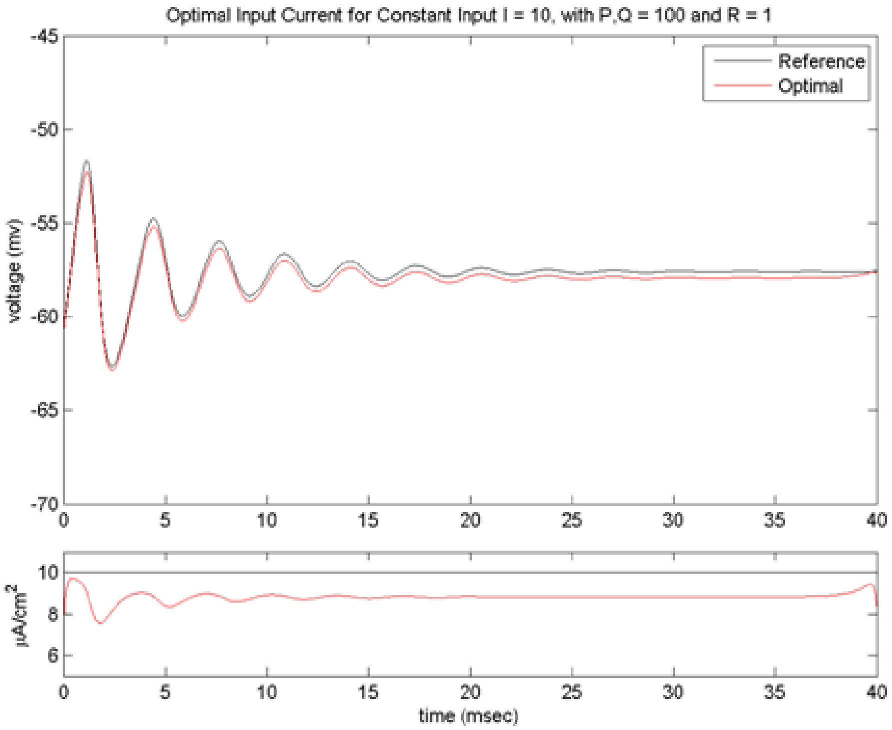

Figure 17: Comparison of reference and optimal signals for a constant stimulus

3.2.2.1.6 Step 6: Verify the optimal current $i^*(t)$ found in step 5 by computing the membrane voltage

For verification purposes, the optimal input current $i^*(t)$ computed in step 5 is applied to the original model using *ode*45. The resulting membrane potential $v^*(t)$ is plotted in Figure 18, along with the membrane potential computed by *bvp4c*. Figure 18 shows that these two signals plot directly on top of one another, qualitatively verifying the numerical solution.

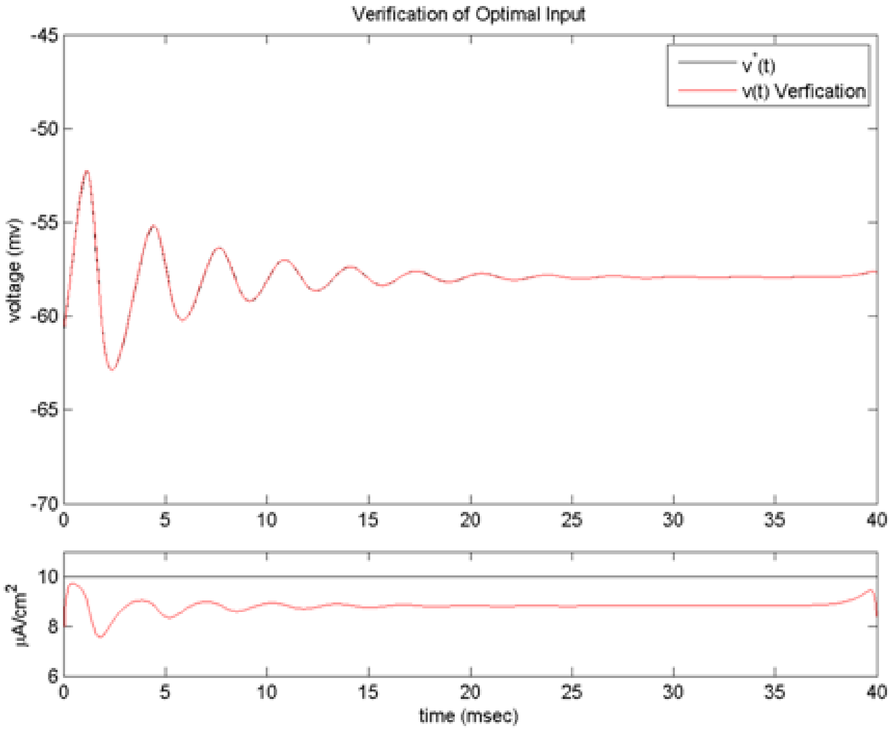

Figure 18: Verification of optimal input current for a constant stimulus

As a result of the process, a stimulus current input has been computed with a lower 'energy' content than the originally applied constant current of $I = 10\,\mu\text{A/cm}^2$. Figure 17 shows that initial weighting coefficient values provide a noticeable reduction in stimulus input energy with minimal tracking error. If improved tracking accuracy is desired, steps 4 through 6 can be repeated with increased P and Q. If a further reduction in stimulus input energy is required, steps 4 through 6 can be repeated with a larger value for R.

3.2.2.2 Example 2: Ramp Input Current Stimulus

3.2.2.2.1 Step 1: Select a stimulus current waveform $I(T)$ and initial conditions

For this example, a ramp stimulus input current is selected which increases through the bifurcation value. The system fixed point undergoes a bifurcation at $I \approx 14.66\,\mu\text{A/cm}^2$, so the final value of the ramp input current of $I \approx 46\,\mu\text{A/cm}^2$ produces a spike [2].

As in Section 3.2.2.1, initial conditions of $v_0 \approx -60.86\,\text{mV}$ and $n_0 \approx 0.04$ eliminate transients at the beginning of the simulation interval.

3.2.2.2.2 Step 2: Compute the membrane voltage $v(t)$ produced by the model

Using *ode*45, the ramp input current selected in step 1 was applied to the model, producing the time varying membrane voltage pictured in Figure 19.

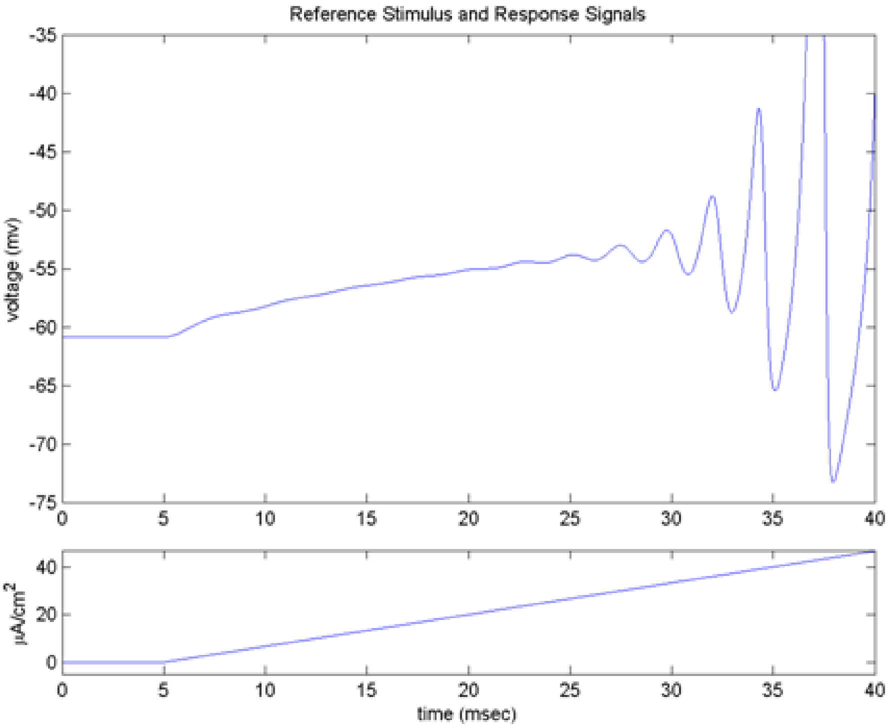

Figure 19: Ramp stimulus current and reference membrane voltage signals

3.2.2.2.3 Step 3: Use the computed membrane voltage $v(t)$ as the reference signal $r(t)$

In the simulation, the set of points constituting the numerical solution for the membrane potential $v(t)$ was set equal to the reference signal $r(t)$.

3.2.2.2.4 Step 4: Select values for the weighting coefficients P, Q, and R

In this example, weighing coefficients values are $P = 100$, $Q = 100$, and $R = 1$. This choice reflects an emphasis on reducing tracking error between the reference signal and resulting membrane potential because P and Q are both greater than R.

3.2.2.2.5 Step 5: Minimize the corresponding objective function

Using *bvp4c*, the two point boundary value problem was solved numerically to produce the optimal input current $i^*(t)$ and the resulting time varying membrane voltage $v^*(t)$ pictured in Figure 20. For comparison the reference signals are included in Figure 20.

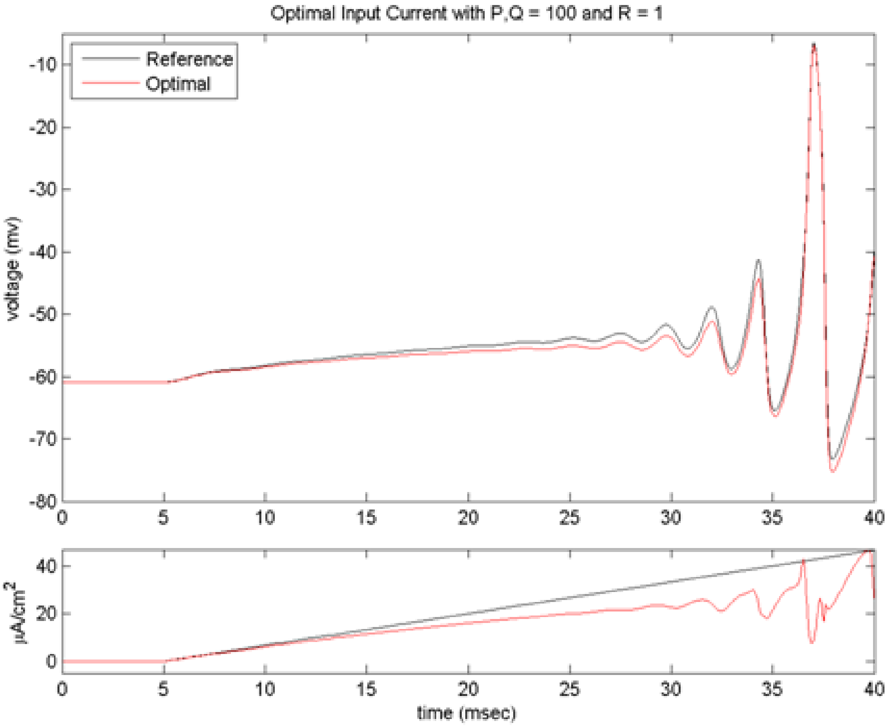

Figure 20: Comparison of reference and optimal signals for a ramp stimulus

3.2.2.2.6 Step 6: Verify the optimal current $i^*(t)$ found in step 5 by computing the membrane voltage

For verification purposes, the optimal input current $i^*(t)$ computed in step 5 is applied to the original model using *ode*45. The membrane potential is plotted in Figure 21, along with the resulting membrane potential $v^*(t)$ computed by *bvp4c*. Figure 21 shows that these two signals plot directly on top of one another, qualitatively verifying the numerical solution.

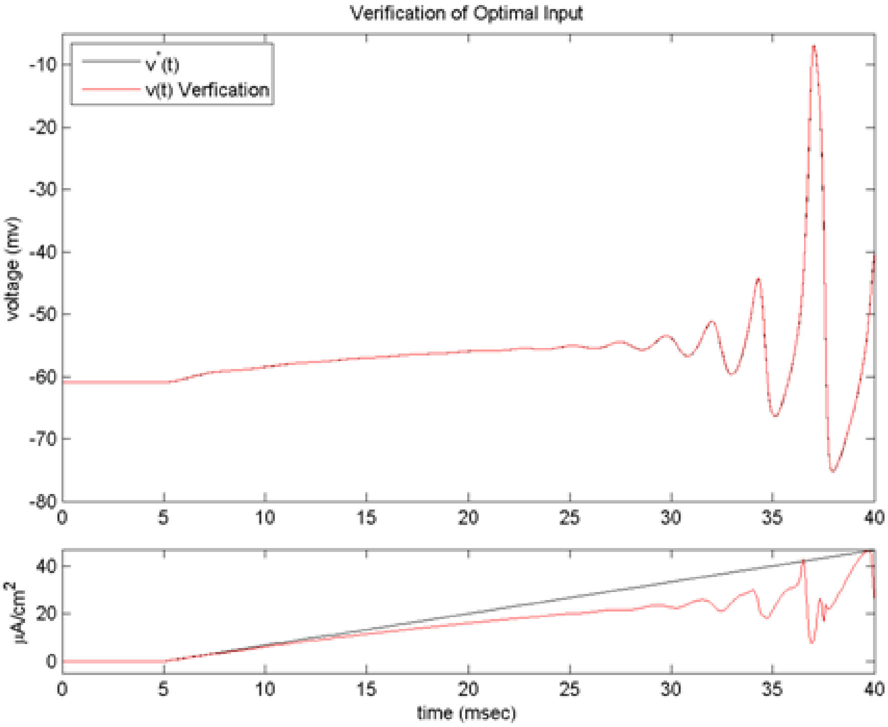

Figure 21: Verification of optimal input current for a ramp stimulus

As a result of the process, a stimulus current input has been computed with a lower ‘energy’ content than the originally applied ramp current. Figure 20 shows that initial weighting coefficient values provide a noticeable reduction in stimulus input energy with minimal tracking error. If improved tracking accuracy is desired, steps 4 through 6 can be repeated with values for P and Q increased. If a further reduction in stimulus input energy is required, steps 4 through 6 can be repeated with a larger value for R.

3.3 Numerical Considerations

This section contains implementation level nuances that increase likelihood of convergence of numerical algorithms and improve execution efficiency. Topics in this section are presented in order of importance.

3.3.1 *ode*45 Settings and Tolerances

All conductance-based, Hodgkin-Huxley type models in this dissertation are amenable to standard ordinary differential equation solvers. Numerical solutions were computed in MATLAB®using *ode*45 with execution times on the order of one minute.

However, low tolerances are required of *ode*45 solutions to enable convergence of bvp4c calculations. The MATLAB®routine *odeset* was used to apply relative tolerance and absolute tolerance settings of 10^{-13}. Default values for relative and absolute tolerance settings are 10^{-3} and 10^{-6}, respectively.

Although these low tolerances did not provide qualitative differences in the corresponding numerical solution, they were required for successful computation by *bvp*4*c*. This observation indicates numerical sensitivity of the solutions using the *bvp*4*c* routine.

3.3.2 Initial Solution Estimation

Use of the *bvp*4*c* routine requires initial estimates of the solution for each variable. It is possible to provide either constant valued, or time varying estimates of the solution. Both likelihood of convergence and execution efficiency were improved when *bvp*4*c* was provided with continuous-time estimates of the solution over the time interval.

Following the steps provided in Table 2 produces a series of values for all states of the original differential equations based on the numerical solution computed by *ode*45. The MATLAB®subroutine *interp*1 was then used to allow interpolation at any time within the given interval.

Due to the structure of the optimal control problem, each state of the original differential equations requires a co-state, doubling the dimension of the problem. For each costate variable, a constant valued guess was set equal to zero.

3.3.3 Choice of Boundary Value Problem Solver

MATLAB®includes routines which implement both the *bvp*4*c* and *bvp*5*c* formulas for solving boundary value problems for ordinary differential equations. An extension to these techniques has been published, providing implementation in the form of a MATLAB®subroutine, *bvp*5*c* [48]. The routines included within the MATLAB®environment can be used interchangeably without modification to function parameters.

3.3.4 Vectorization

Many operations within MATLAB®can be written in the form of iterative, loop-based operations or in terms of matrix or vector operations. Although loop-based code is common to most programming languages, writing code to take advantage of optimization within MATLAB®via vectorization of code can greatly improve execution efficiency [49].

Efficiency gains are especially prevalent in subroutines called repeatedly by *ode*45 or *bvp*4*c*. Specifically, vectorization of code related to the ordinary differential equations utilized by *bvp*4*c* provides a significant reduction in the number of function calls required. A flag must be set using *bvpset* to inform the MATLAB®environment that the code is optimized for vectorization [50]. In practice, these routines are called thousands, or hundreds of thousands of times, and larger simulation runs can last in the range of 20 minutes.

Use of the MATLAB®Profiler greatly assists optimization of program execution [51]. It is informative to run the same simulation with the vecorization flag both true and false to verify the reduction in execution time and number of function calls.

4 Reduced-Order Hodgkin-Huxley Models

This chapter applies the nonlinear analysis and optimal control techniques depicted in Chapter 3, Figure 12 to the reduced-order, Hodgkin-Huxley type neuron model defined in Section 2.3.

Reduced-dimensionality, as compared to the classical Hodgkin-Huxley model, facilitates analysis since two-dimensional phase space is readily graphed. With proper selection of parameter values, the chosen model is able to produce the four fundamental bifurcation types that underlay many neurocomputational properties [1, p. 17].

Section 4.1 defines the neuron model, provides derivation of the system nullclines, and defines the Hamiltonian with associated state and co-state equations. Since the form of the model and objective function remain unchanged within this chapter, the derivations of Section 4.1 are common to all four bifurcation types presented in Section 4.2. Section 4.2 demonstrates applicability of the defined optimal control techniques to supercritical Andronov-Hopf, subcritical Andronov-Hopf, saddle-node, and saddle-node on invariant circle bifurcation types in Sections 4.2.1 through 4.2.4, respectively.

4.1 Model Definition

Following Chapter 3, Figure 12, this section corresponds to the first row of the figure, definition of the conductance-based neuron model. This includes definition of the reduced-order, Hodgkin-Huxley model, and all symbolic equations required for nonlinear analysis and optimal control techniques.

4.1.1 Reduced-Order Hodgkin-Huxley Type Model Definition

Following [1], the reduced-order, Hodgkin-Huxley model consists of a persistent potassium current, transient sodium current, ohmic leak current, injected stimulus current, and cellular membrane capacitance. Presented as Figure 5 in Chapter 2, an equivalent circuit for the neuron model is reproduced here for completeness.

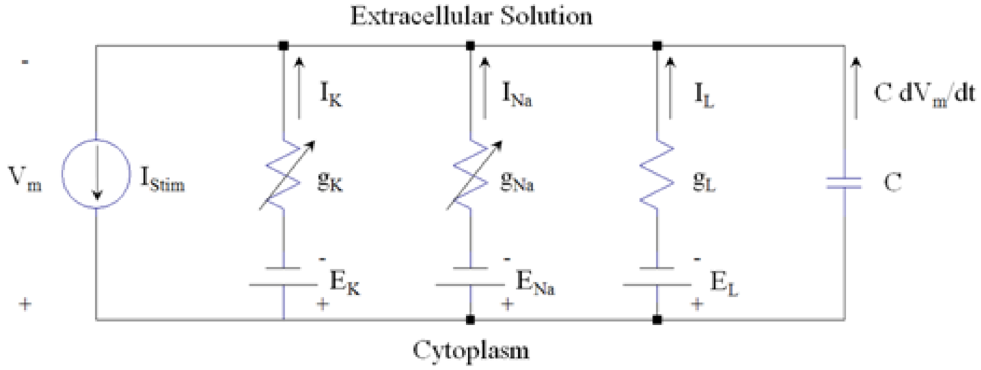

Figure 22: Equivalent circuit of a reduced-order conductance-based neuron model

Differential equations for the reduced-order, Hodgkin-Huxley model are

$$C\dot{V} = I - g_K n(V - E_K) - g_{Na} m_\infty(V)(V - E_{Na}) - g_L(V - E_L) \tag{57}$$

$$\dot{n} = \frac{(n_\infty(V) - n)}{\tau(V)} \tag{58}$$

where

$$m_\infty(V) = \frac{1}{1 + \mathrm{e}^{\left(\frac{V_m - v}{k_m}\right)}} \tag{59}$$

$$n_\infty(V) = \frac{1}{1 + \mathrm{e}^{\left(\frac{V_n - v}{k_n}\right)}}. \tag{60}$$

Modulation of potassium and sodium conductance values is achieved using gating variables n and m_∞, respectively. System dynamics can be modified to produce four fundamental bifurcations of the system fixed point(s) by changing constant valued parameters in equations (57) through (60). Parameter values to achieve the four bifurcation types under investigation are provided in Table 3 [1].

After defining the qualitative system behavior via model parameters, the injected current stimulus is used to cause bifurcations of the system fixed point.

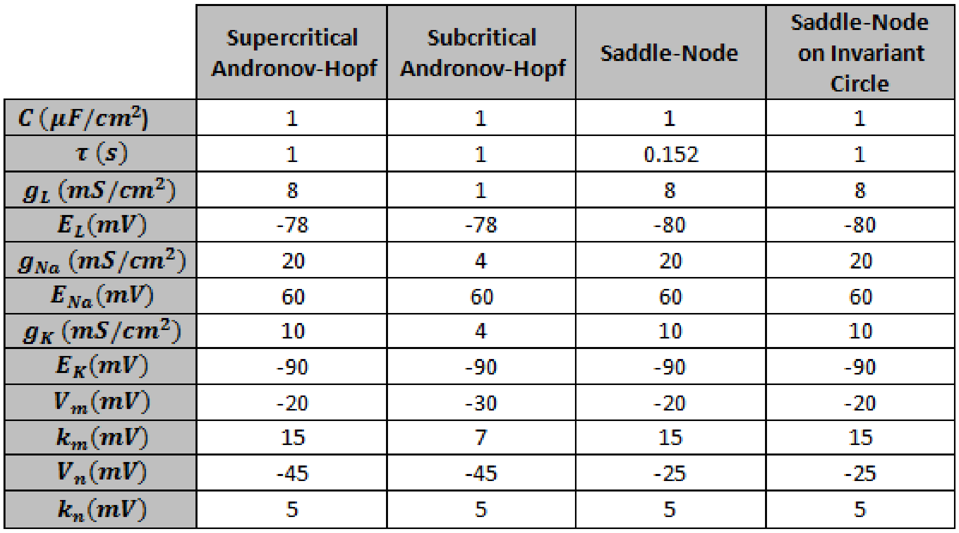

	Supercritical Andronov-Hopf	Subcritical Andronov-Hopf	Saddle-Node	Saddle-Node on Invariant Circle
$C\ (\mu F/cm^2)$	1	1	1	1
$\tau\ (s)$	1	1	0.152	1
$g_L\ (mS/cm^2)$	8	1	8	8
$E_L(mV)$	-78	-78	-80	-80
$g_{Na}\ (mS/cm^2)$	20	4	20	20
$E_{Na}(mV)$	60	60	60	60
$g_K\ (mS/cm^2)$	10	4	10	10
$E_K(mV)$	-90	-90	-90	-90
$V_m(mV)$	-20	-30	-20	-20
$k_m(mV)$	15	7	15	15
$V_n(mV)$	-45	-45	-25	-25
$k_n(mV)$	5	5	5	5

Table 3: Model parameters [1]

4.1.2 Fixed Point Location

As described in Sections 3.1.1.1 and 3.1.1.2, two methods are used within this dissertation to compute the location of system fixed points. For two-dimensional models equations for nullclines are derived and plotted. Intersections of the nullclines indicate the location of a system fixed point. For higher-dimensional models the form of conductance-based models enable derivation of a function $f(v)$, the roots of which are indicative of fixed points. In Section 4.2.1 both methods will be utilized to demonstrate their equivalence. For the remaining three bifurcation types in Sections 4.2.2 through 4.2.4, only the intersection of system nullclines will be used.

4.1.2.1 Derivation of Nullclines

To solve for nullclines of the two-dimensional, reduced-order, Hodgkin-Huxley model set each differential equation equal to zero

$$0 = \left(\frac{1}{C}\right)(I - g_K n(V - E_K) - g_{Na} m_\infty(V)(V - E_{Na}) - g_L(V - E_L)) \tag{61}$$

$$0 = \frac{(n_\infty(V) - n)}{\tau(V)} \tag{62}$$

The nullclines are obtained by solving equations (61) and (62) for n, yielding

$$n = \frac{1}{Cg_K(V - E_K)}(I - g_{Na}m_\infty(V)(V - E_{Na}) - g_L(V - E_L)) \tag{63}$$

$$n = n_\infty(V) \tag{64}$$

where $m_\infty(V)$ and $n_\infty(V)$ are described by equations (59) and (60).

Equation (63) is the v-nullcline, representing purely vertical motion on the (v, n) phase plane. Equation (64) is the n-nullcline, representing purely horizontal motion on the (v, n) phase plane. Each injected current value I will produce a different curve for the v-nullcline. The n-nullcline does not depend on the injected current, as shown in equation (64), and thus will not change as a function of stimulus current I. An appropriate set of injected current values will be determined for each bifurcation type to demonstrate the qualitatively different behaviors of the system for each set of parameters in Table 3.

4.1.2.2 Derivation of $f(v)$

As an alternative means to find fixed point locations, the form of equations (57) and (58) make it possible to derive a single function, $f(v)$, the roots of which are system fixed points. The function $f(v)$ is obtained by setting $dotn = 0$, and solving for n as shown in equation (64). The result is substituted into equation (63) yielding

$$f(v) = \left(\frac{1}{C}\right)(I - g_K n_\infty(V - E_K) - g_{Na}m_\infty(V)(V - E_{Na}) - g_L(V - E_L)) \tag{65}$$

with $m_\infty(V)$ and $n_\infty(V)$ described by equations (59) and (60), respectively. The function $f(v)$ will be plotted for each injected current value, with the roots of the function indicating the location of the system fixed point.

4.1.3 System Linearization

Once the number and location of system fixed points has been determined, they can be classified according to their localized behavior. Classification of system fixed points proceeds as described in Section 3.1.2, beginning with linearization of the phase plane using the system Jacobian [6].

For the two-dimensional model under investigation the Jacobian is

$$\begin{bmatrix} \dot{V} \\ \dot{n} \end{bmatrix} = \begin{bmatrix} \frac{\partial f_1}{\partial V} & \frac{\partial f_1}{\partial n} \\ \frac{\partial f_2}{\partial V} & \frac{\partial f_2}{\partial n} \end{bmatrix} \begin{bmatrix} V \\ n \end{bmatrix} \tag{66}$$

where $\dot{V} = f_1()$, $\dot{n} = f_2()$, and

$$\frac{\partial f_1}{\partial V} = \left(\frac{1}{C}\right)\left(-g_L - g_{Na}\left(\frac{1 + \mathrm{e}^{\left(\frac{v_m - V}{k_m}\right)} + \frac{V}{k_m}\mathrm{e}^{\left(\frac{v_m - V}{k_m}\right)}}{\left(1 + \mathrm{e}^{\left(\frac{v_m - V}{k_m}\right)}\right)^2} - \frac{\mathrm{e}^{\left(\frac{v_m - V}{k_m}\right)}}{k\left(1 + \mathrm{e}^{\left(\frac{v_m - V}{k_m}\right)}\right)^2}\right) - g_K n\right) \tag{67}$$

$$\frac{\partial f_1}{\partial n} = -g_K V + g_K E_K \tag{68}$$

$$\frac{\partial f_2}{\partial V} = \frac{1}{\tau(V)}\left(\frac{\mathrm{e}^{\left(\frac{v_n - V}{k_n}\right)}}{k\left(1 + \mathrm{e}^{\left(\frac{v_n - V}{k_n}\right)}\right)^2}\right) \tag{69}$$

$$\frac{\partial f_2}{\partial n} = -\frac{1}{\tau(V)} \tag{70}$$

As described in Sections 3.1.2.1 and 3.1.2.2, two methods are used within this dissertation for classification of behavior in the immediate vicinity of system fixed points. Both methods utilize the linearized system produced by the Jacobian. Values from Table 3 for the model parameters, the injected current value, and the location of the system fixed point are substituted into the Jacobian, allowing computation of eigenvalues.

For second-order systems, the eigenvalues of the Jacobian are used to compute the trace and determinant for each injected current value, and they are plotted on the classification diagram. For higher-order models, the eigenvalues for each injected current value are plotted on the complex plane. In Section 4.2.1 both methods will be utilized to demonstrate their equivalence. In Sections 4.2.2 through 4.2.4 only the fixed point classification diagram will be used.

4.1.4 Objective Function Definition

The objective function, previously published in [2], is

$$J[i(t)] = \frac{P}{2}(v(T) - r(T))^2 + \frac{Q}{2}\int_0^T (v(t) - r(t))^2 dt + \frac{R}{2}\int_0^T (i(t))^2 dt. \tag{71}$$

A user prescribed balance between tracking error and minimization of ‘energy’ is used in the computation of the optimal input current $i^*(t)$. Making P and Q large with respect to R penalizes differences between the chosen reference signal $r(t)$ and the computed membrane voltage $v(t)$, resulting in a solution which emphasizes tracking accuracy. Conversely, a large value for R, in comparison to P and Q, emphasizes a solution which seeks to minimize the ‘energy’ content of $i^*(t)$, likely at the expense of reduced agreement between reference and membrane potential signals.

The Hamilton associated with equation (71) is

$$\begin{aligned} H(v, n, \lambda_1, \lambda_2) = {} & \frac{Q}{2}(v(t) - r(t))^2 + \frac{R}{2}(i(t))^2 \\ & + \frac{\lambda_1(t)}{C}(i(t) - g_K n(t)(v(t) - E_K) - g_{Na} m_\infty(v)(v(t) - E_{Na}) - g_L(v(t) - E_L)) \\ & + \frac{\lambda_2(t)}{\tau}(n_\infty(v) - n(t)) \end{aligned} \tag{72}$$

where λ_1 and λ_2 are the co-state variables. Following [46, p. 134], the “Continuous Nonlinear Optimal Controller with Function of Final State Fixed” yields

$$\begin{aligned} \dot{v} &= \frac{\partial H}{\partial \lambda_1} \\ &= \frac{1}{C}[i(t) - g_{Na} m_\infty(v)(v(t) - E_{Na}) - g_K n(t)(v(t) - E_K) - g_L(v(t) - E_L)] \end{aligned} \tag{73}$$

$$\dot{n} = \frac{\partial H}{\partial \lambda_2} = \frac{1}{\tau}[n_\infty(v) - n(t)] \tag{74}$$

$$\begin{aligned}\dot{\lambda}_1 = -\frac{\partial H}{\partial v} &= -Q(v(t) - r(t)) \\ &\quad + \frac{\lambda_1(t)}{C}[g_{Na}m_\infty(v) + g_K n(t) + g_L + g_{Na}(v(t) - E_{Na})\frac{\partial m_\infty(v)}{\partial v}] \\ &\qquad - \frac{\lambda_2(t)}{\tau}\frac{\partial n_\infty(v)}{\partial v}\end{aligned} \tag{75}$$

$$\dot{\lambda}_2 = -\frac{\partial H}{\partial n} = \frac{g_K}{C}\lambda_1(t)(v(t) - E_K) + \frac{\lambda_2(t)}{\tau} \tag{76}$$

with boundary conditions

$$v(0) = v_0 \tag{77}$$

$$n(0) = n_0 \tag{78}$$

$$\lambda_1(T) = P(v(T) - r(T)) \tag{79}$$

$$\lambda_2(T) = 0. \tag{80}$$

The input stimulus current $i(t)$ can be removed by substitution using the stationarity condition

$$\frac{\partial H}{\partial i} = Ri(t) + \frac{\lambda_1(t)}{C} = 0, \tag{81}$$

and solving for $i(t)$ yields

$$i(t) = -\frac{1}{RC}\lambda_1(t). \tag{82}$$

Typically, a numerical solution to the two-point boundary value problem is computed using the MATLAB®routine *bvp4c*, yielding $i^*(t)$ for each choice of injected current stimulus and objective function constants P, Q, and R.

4.2 Nonlinear Analysis and Optimal Control

Sections 4.2.1 through 4.2.4 examine system dynamics of the four fundamental bifurcation types presented in [1] using nonlinear analysis and optimal control techniques presented in Chapter 3. As shown in Figure 12 of Chapter 3, location and classification of system equilibria can be achieved by two complementary techniques. In Section 4.2.1 the supercritical Andronov-Hopf bifurcation type is analyzed using both techniques to demonstrate their equivalence. In the remaining sections subcritical Andronov-Hopf, saddle-node, and saddle-node on invariant circle bifurcation types are investigated with techniques presented in Sections 3.1.1.1 and 3.1.2.1.

4.2.1 Super Critical Andronov-Hopf

Supercritical Andronov-Hopf bifurcations occur when a stable equilibrium becomes unstable, yielding a limit cycle attractor [1, p. 12]. The size of the limit cycle attractor increases as the injected current is increased beyond the bifurcation value.

Neuron models near a supercritical Andronov-Hopf bifurcation exhibit subthreshold oscillations and are thus categorized as resonators in the classification scheme presented by Izhikevich [1, p. 12]. This means that system trajectories, even with injected currents below the bifurcation value, will exhibit damped oscillation.

Neuron models near a supercritical Andronov-Hopf bifurcation do not exhibit coexistence of resting and repetitive spiking states [1].

During repetitive spiking the limit cycle attractor determines the size and shape of action potentials. Since the level of injected current determines the size of the limit cycle attractor in a supercritical Andronov-Hopf bifurcation, the resulting neuron model is capable of producing graded action potentials, as opposed to all or none spikes.

Parameterization and analysis of the reduced-order Hodgkin-Huxley model as shown in Table 3 will validate the expected system behaviors, quantify bifurcation values, and apply optimal control to compute reduced energy input stimuli capable of tracking a reference membrane voltage.

4.2.1.1 Fixed Point Location

Within this section location of the system fixed point will be determined using both the system nullclines and the derived function $f(v)$.

4.2.1.1.1 Fixed Point Location Using Nullclines

Using equations (63) and (64) for the nullclines, and varying the injected stimulus current I from $-100\,\mu\text{A/cm}^2$ to $100\,\mu\text{A/cm}^2$ by increments of $10\,\mu\text{A/cm}^2$, a family of curves is generated in Figure 23. Since the n-nullcline does not change it is represented by a single sigmoidal line on the plot. Each injected current value I produces a different curve for the v-nullcline.

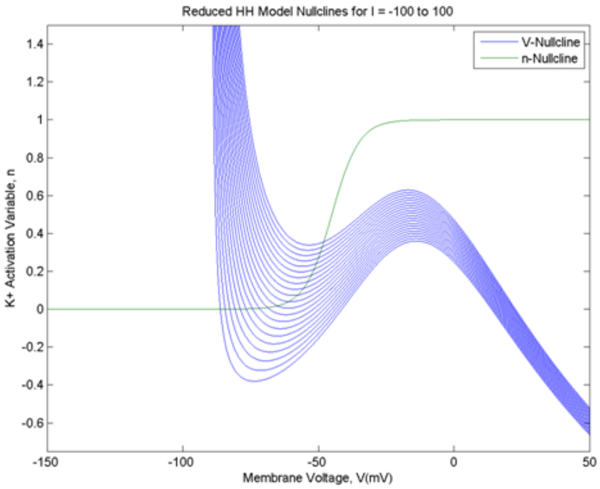

Figure 23: Supercritical Andronov-Hopf fixed point location using nullclines

Notice each v-nullcline intersects the n-nullcline at a single point in the phase plane for all considered values of I, indicating the presence of a single fixed point. The membrane voltage of fixed points range between approximately -85 to $-50\,\text{mV}$, and the gating variable ranges between 0 and 0.4.

Stability of the fixed point cannot be ascertained directly from the figure and requires further analysis per Section 4.2.1.2. For cases where the fixed point is stable, the value of the membrane voltage at the intersection of the nullclines is the resting membrane potential.

4.2.1.1.2 Fixed Point Location Using $f(v)$

Using equation (65) for $f(v)$ and the same range of injected current values, a family of curves is plotted in Figure 24. A fixed point of the system is indicated by each location where $f(v) = 0$.

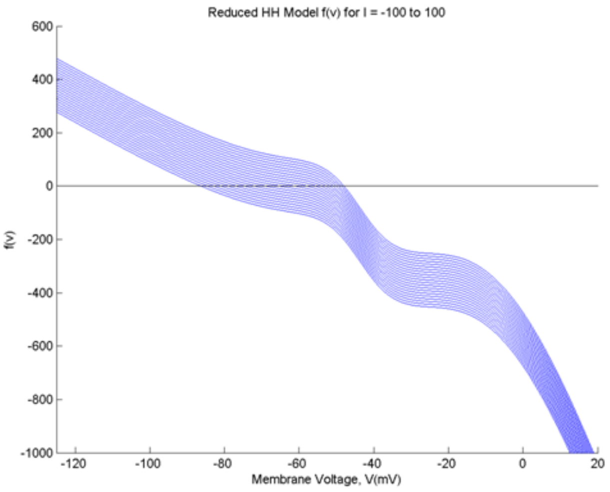

Figure 24: Supercritical Andronov-Hopf fixed point locations using derived function $f(v)$

Again, the system has a single fixed point for all considered values of I. Furthermore, since $f(v)$ is monotonic and the injected current translates the curve vertically, it is observable from Figure 24 that the system will have a single fixed point for all injected current values.

As in Figure 23, an approximate value for the membrane voltage of the system fixed point is directly observable in Figure 24. However, approximation of the gating variable n is not directly observable from Figure 24, and the value for membrane voltage must be back-substituted into equation (64) to estimate a value for n.

4.2.1.1.3 Comparison of Fixed Point Location Results

For each injected current level, the system fixed point location has been computed in two ways, by the intersection of the nullclines and by the root of $f(v)$. The primary difference between these two methods is that plotting the fixed point location using the intersection of the nullclines is only feasible with a reduced-order systems while the roots of $f(v)$ can be plotted for systems of any dimension, given an amenable structure to the state equations.

Both plots provide qualitative information regarding the number of fixed points and their approximate location. To verify the two techniques identify the same fixed point location for each injected current level the MATLAB®routine *fsolve* was used to compute the quantitative fixed point location. Table 4 shows that the values produced match for all injected current levels considered.

The approximate value of both state variables is directly observable on the phase plane in Figure 23. In contrast, when determining the system fixed point using $f(v)$, it is necessary to observe the value for membrane voltage, v, and back-substitute this value into equation (64) to determine the equilibrium value for n. The phase plane is also informative when studying system trajectories for determination of bifurcation type and application of the optimal control technique.

For the remainder of this dissertation, system fixed point location will be determined for all second-order models via intersection of the nullclines, and the (v, n) phase plane will be utilized. For higher-order models system, fixed point location will be determined by computing the roots of $f(v)$.

4.2.1.2 Fixed Point Classification

Within this section fixed points will be classified both graphically and according to eigenvalues of the linearized system.

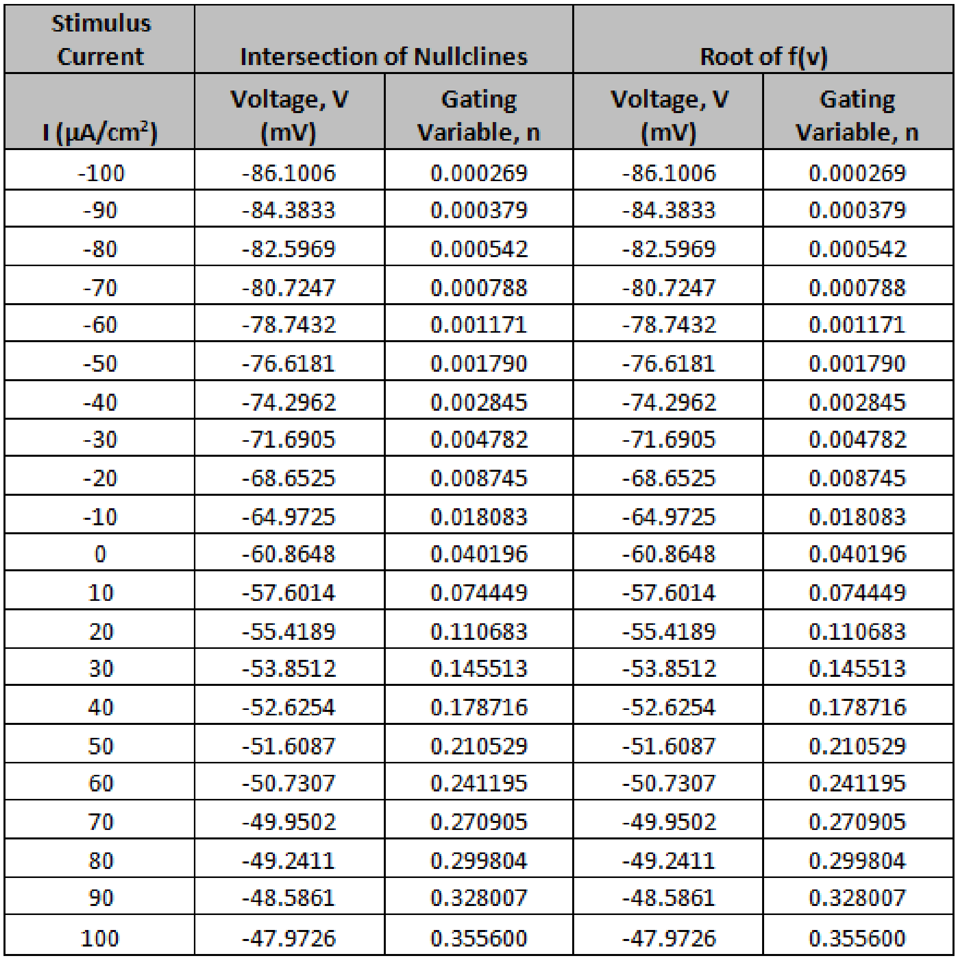

Stimulus Current	Intersection of Nullclines		Root of f(v)	
I (μA/cm^2)	Voltage, V (mV)	Gating Variable, n	Voltage, V (mV)	Gating Variable, n
-100	-86.1006	0.000269	-86.1006	0.000269
-90	-84.3833	0.000379	-84.3833	0.000379
-80	-82.5969	0.000542	-82.5969	0.000542
-70	-80.7247	0.000788	-80.7247	0.000788
-60	-78.7432	0.001171	-78.7432	0.001171
-50	-76.6181	0.001790	-76.6181	0.001790
-40	-74.2962	0.002845	-74.2962	0.002845
-30	-71.6905	0.004782	-71.6905	0.004782
-20	-68.6525	0.008745	-68.6525	0.008745
-10	-64.9725	0.018083	-64.9725	0.018083
0	-60.8648	0.040196	-60.8648	0.040196
10	-57.6014	0.074449	-57.6014	0.074449
20	-55.4189	0.110683	-55.4189	0.110683
30	-53.8512	0.145513	-53.8512	0.145513
40	-52.6254	0.178716	-52.6254	0.178716
50	-51.6087	0.210529	-51.6087	0.210529
60	-50.7307	0.241195	-50.7307	0.241195
70	-49.9502	0.270905	-49.9502	0.270905
80	-49.2411	0.299804	-49.2411	0.299804
90	-48.5861	0.328007	-48.5861	0.328007
100	-47.9726	0.355600	-47.9726	0.355600

Table 4: Fixed point locations

4.2.1.2.1 Fixed Point Classification for Two-Dimensional Systems

Qualitative information from Section 4.2.1.1 greatly informs the process of fixed point classification as it provides insight as to the number and approximate location of system fixed points for any given injected current level.

Using $fsolve$, the numerical solution for the location of the fixed point is computed. The values for the state variables, in this case v and n, are substituted into the Jacobian, allowing computation of eigenvalues according to equations (66) through (70).

Eigenvalues of the linearized system, evaluated at the location of a fixed point, are immensely informative regarding expected qualitative system behavior and stability of the fixed point. For two-dimensional systems, fixed points are readily classified using a graphical classification scheme once the eigenvalues have been computed [6, p. 137].

When classifying system fixed points via linearization, it is necessary to verify the linear system, with neglected higher-order terms, faithfully represents the original nonlinear system. As described in Section 3.1.2.1, graphical categorization of fixed points of two-dimensional systems is robust for saddles, nodes, and spirals. Further techniques are required for analysis of "borderline" cases [6, p. 151-155].

Analysis of the reduced-order Hodgkin-Huxley model proceeds with calculation of eigenvalues for the linearized system for each injected current value used to generate the family of curves in Section 4.2.1.1. Borderline cases, representing a bifurcation in system dynamics, are considered in Section 4.2.1.3.

After computing eigenvalues for the linearized system in the vicinity of the fixed point for each injected current level, the trace (τ) and determinant (Δ) for each fixed point is calculated as described in [6]. Namely,

$$\tau = \lambda_1 + \lambda_2 \tag{83}$$

and

$$\Delta = \lambda_1 * \lambda_2 \tag{84}$$

where λ_1 and λ_2 are the eigenvalues of the linearized two-dimensional system of equations. A single point is generated on the classification diagram for each fixed point at each injected current value. The plotted locus represents the varying classification of the system fixed point as the injected current is increased from $-100\,\mu\text{A/cm}^2$ to $100\,\mu\text{A/cm}^2$ by increments of $10\,\mu\text{A/cm}^2$.

The data point indicated with an asterisk denotes zero injected current. Bifurcations, or qualitative changes in system dynamics, occur when the classification of the fixed point transitions from one region of the classification diagram to another [6, p. 44]. In this case, one bifurcation occurs when the fixed point changes from a stable node to a stable spiral,

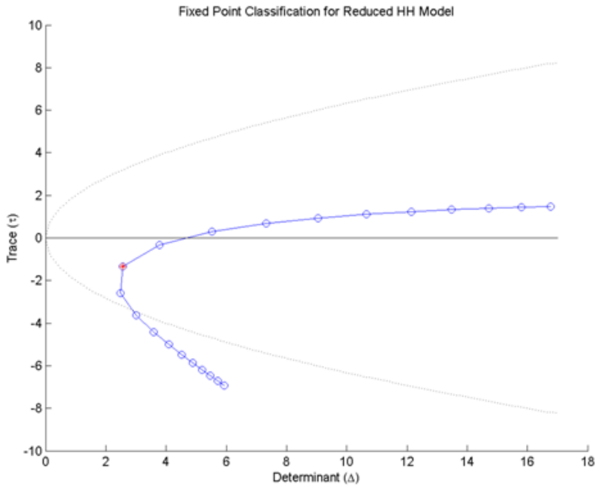

Figure 25: Graphical classification of reduced-order Hodgkin-Huxley supercritical Andronov-Hopf system fixed point

and another bifurcation occurs when the fixed point changes from a stable spiral to an unstable spiral.

The bifurcation of interest, as presented in [1], occurs as the injected current is increased from zero, corresponding to the transition from stable spiral to unstable spiral, along with the creation of a stable limit cycle attractor. Classification of the fixed point as a spiral is indicative of system dynamics which include oscillation, and is consistent with the description of the supercritical Andronov-Hopf bifurcation type as a resonator in [1].

For injected current values where the system fixed point is classified as a stable spiral, zero injected current and $10\,\mu\text{A/cm}^2$ as shown above, damped oscillations are expected. For injected currents, $20\,\mu\text{A/cm}^2$ and above undamped oscillations, or repetitive spiking, is produced with the size and shape of the action potentials determined by the limit cycle attractor. Since the size of the limit cycle attractor is related to the level of injected current, action potential size is expected to vary with injected current levels.

Inclusion of negative injected currents provides a second bifurcation of the system fixed point from stable spiral to stable node. The transition from spiral to node is expected to result in cessation of subthreshold membrane voltage oscillations.

Bifurcation points and verification of the described qualitative system behavior via time domain plots and phase plane trajectories will be demonstrated in Section 4.2.1.3.

The presented classification diagram, although incredibly informative, is not readily extended to higher-dimensional systems. Fortunately, investigation of the eigenvalues themselves, in parallel with the classification diagram, provides the ability to intuit system dynamics in a manner extensible to higher-dimensional system.

4.2.1.2.2 Fixed Point Classification for Higher-Dimensional Systems

Using the graphical classification diagram of the previous section, the fixed point is represented by a single point for each injected current level. When the fixed point is classified for higher-order systems, eigenvalues are plotted directly on the complex plain. For the second-order system currently under investigation, two eigenvalues, λ_1 and λ_2, are plotted for each injected current value.

Like the previous section, the plotted locus of eigenvalues corresponds to injected current increasing from $-100\,\mu\mathrm{A/cm^2}$ to $100\,\mu\mathrm{A/cm^2}$ by increments of $10\,\mu\mathrm{A/cm^2}$, with additional data points for injected current levels of $-12\,\mu\mathrm{A/cm^2}$, $-14\,\mu\mathrm{A/cm^2}$, $-16\,\mu\mathrm{A/cm^2}$, and $-18\,\mu\mathrm{A/cm^2}$. These values were added to clarify movement of the eigenvalues at the point where they break away from the real axis. In this region the eigenvalues are moving rapidly, and the addition of these injected current levels provides improved resolution. Again, the eigenvalues indicated with an asterisk denote zero injected current.

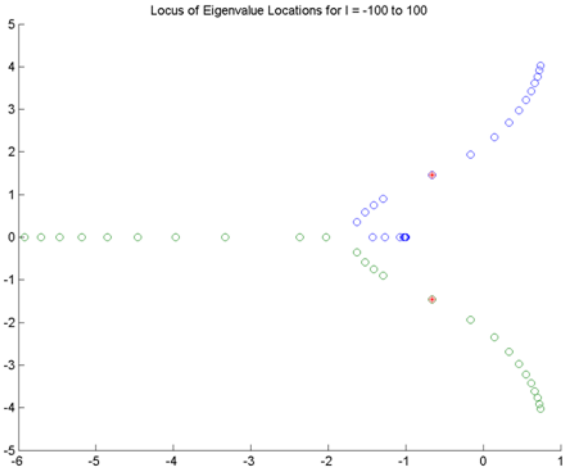

Figure 26: Classification of reduced-order Hodgkin-Huxley system fixed point using eigenvalues

With $I = -100\,\mu\mathrm{A/cm^2}$ the eigenvalues are purely real, and distributed distantly from each other on the real axis. As the injected current is increased, eigenvalues move toward each other until they collide and break away from the real axis. After breaking away from the real axis, the eigenvalues proceed away from the real axis and to the right, with the real part of the eigenvalues increasing. At some level of injected current, the imaginary pair of eigenvalues cross into the right hand plane.

Systems with purely real eigenvalues do not exhibit oscillation. In the case of the plot shown here, all of the purely real eigenvalues exist on the left hand plane. Thus, all injected current values which produce eigenvalues on the real axis correspond to system dynamics with stable fixed points, classified as stable nodes.

When eigenvalues appear in complex conjugate pairs, the system will exhibit oscillations. Less damped oscillations will be produced with greater imaginary content of the eigenvalues, or eigenvalues closer to the right hand plane. Once the real part of the complex conjugate pair of eigenvalues becomes positive the fixed point has become unstable.

4.2.1.2.3 Comparison of Fixed Point Classification Results

Graphical classification of the fixed point as presented in Figure 25 can be correlated with the trajectories of the eigenvalues on the complex plane as presented in Figure 26.

All injected current values which produce eigenvalues on the real axis, in the left-hand plane indicate system dynamics of stable fixed points without oscillation. This corresponds to the region of the graphical classifier described as stable nodes. For the reduced-order Hodgkin-Huxley model under investigation a stable node is produced for injected current values from $-100\,\mu\text{A/cm}^2$ to $-20\,\mu\text{A/cm}^2$.

Complex conjugate pair eigenvalues in the left-hand plane are representative of a stable fixed point and oscillatory dynamics. Using the graphical classifier, the presence of damped oscillation results in classification of the system fixed point as a stable node. For the reduced-order Hodgkin-Huxley model under investigation a stable spiral is produced for injected current values from $-10\,\mu\text{A/cm}^2$ to $10\,\mu\text{A/cm}^2$.

Complex conjugate pairs of eigenvalues in the right-hand plane exhibit undamped oscillation. However, unlike a linear system, the creation of a stable limit cycle attractor at the transition of the fixed point from stable to unstable prevents system trajectories from diverging. Thus, crossing into the right hand plane is related to the classification diagram where the trace (τ) is equal to zero. For injected current values of $20\,\mu\text{A/cm}^2$ or more eigenvalues exist in complex conjugate pairs in the right-hand plane, and are classified as unstable spirals. Pictorially, the results within the two figures can be correlated in the following manner.

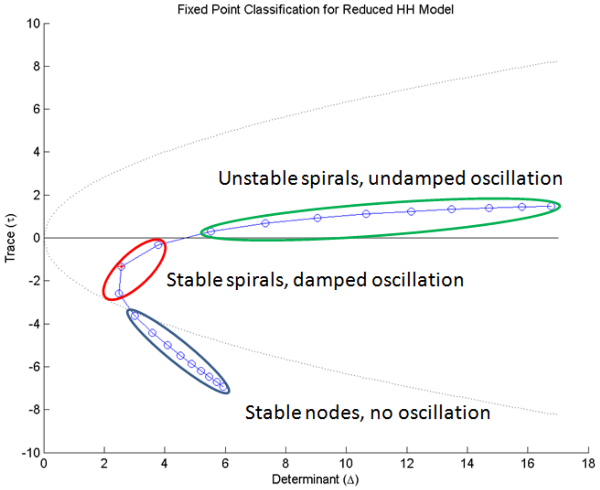

Figure 27: Categorization of reduced-order Hodgkin-Huxley system fixed points

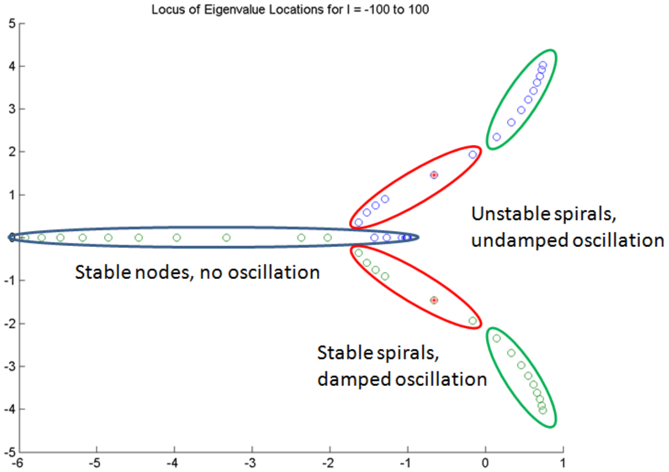

Figure 28: Eigenvalue categorization of reduced-order Hodgkin-Huxley system fixed points

Information gained about the stability of the fixed point for each injected current value can now be incorporated into Figures 23 and 24 from Section 4.2.1.1. Fixed point stability will be demarcated on the phase plane and the plot of $f(v)$ by filled and open dots where the fixed point is stable and unstable, respectively.

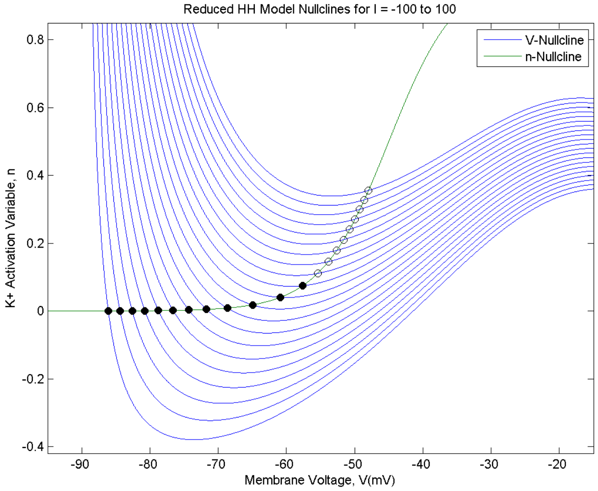

Figure 29: Supercritical Andronov-Hopf fixed point location and stability with nullclines

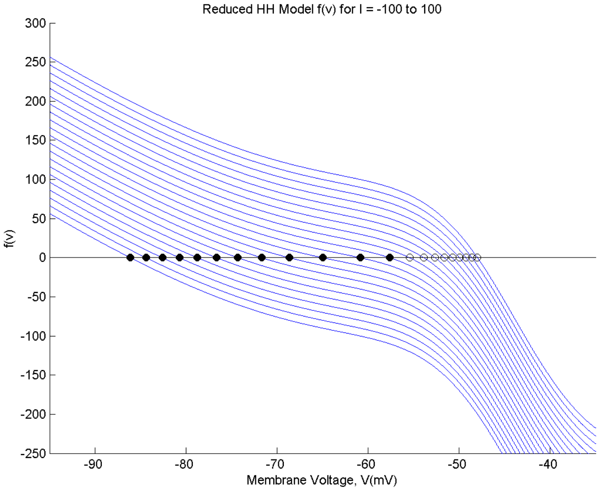

Figure 30: Supercritical Andronov-Hopf fixed point location and stability with derived function $f(v)$

4.2.1.3 Bifurcations

Information from Section 4.2.1.2 provides insight into the injected current levels for which qualitatively different system behaviors occur. Investigations related to bifurcation of the system fixed point in this section serves two purposes. One purpose is to demonstrate qualitatively different behaviors of the system using time domain plots along with the phase plane. The second purpose is to verify bifurcation type according to criteria provided in [1] which has been reproduced as Figure 26 in Chapter 3.

For example, investigation of Figure 31 indicates that three distinct classes behavior can be expected from the reduced-order Hodgkin-Huxley model using parameters selected to produce the supercritical Andronov-Hopf bifurcation type. From the graph, it is evident that at least three classes of behavior exist for injected current values below $-20\,\mu\text{A/cm}^2$, between $-10\,\mu\text{A/cm}^2$ and $10\,\mu\text{A/cm}^2$, and above $20\,\mu\text{A/cm}^2$. Using this information, injected current values will be selected which demonstrate the behavior of the system above and below any bifurcations.

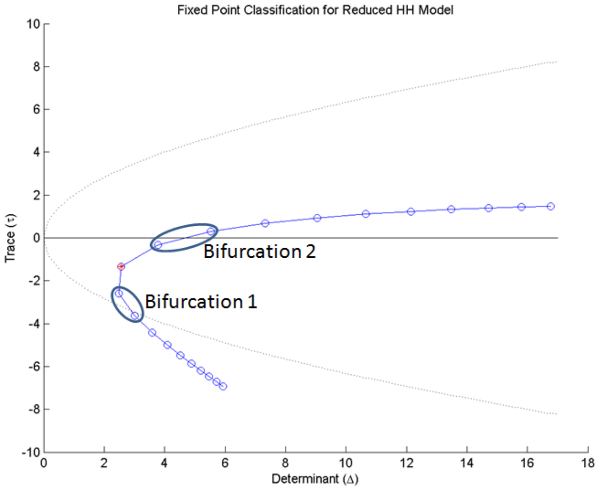

Figure 31: Bifurcations of the system fixed point as indicated by the graphical classifier

For the purposes of this dissertation, it is generally not necessary to determine the exact value of injected current at which a bifurcation of the fixed point occurs. Furthermore, when system dynamics at the bifurcation point are of interest, it must be verified that the linearized system is topologically equivalent to the original nonlinear system, as described in Section 3.1.3.

As an example, Section 4.2.1.3.1 demonstrates computation of the bifurcation point of the system. Sections 4.2.1.3.2 through 4.2.1.3.4 provide analysis of the three classes of behavior which are possible for the selected range of injected stimulus current.

4.2.1.3.1 Computation of System Bifurcation Points

When a more precise value of injected current at which the bifurcation occurs is required, $fsolve$ can be used to compute a numerical solution. Using the graphical classifier in Figure 31 or the locus of eigenvalues plotted in Figure 32 greatly informs this process, by providing initial conditions for use with $fsolve$.

As shown, there are two bifurcations which occur at different injected current levels. Bifurcation 1 occurs at some injected current value between $-10\,\mu\text{A/cm}^2$ and $-20\,\mu\text{A/cm}^2$. Bifurcation 2 occurs at some injected current value between $10\,\mu\text{A/cm}^2$ and $20\,\mu\text{A/cm}^2$. Bifurcation 2 of Figure 31 is a supercritical Andronov-Hopf bifurcation considered in [1].

For bifurcation 1, three equations must be satisfied simultaneously to find the bifurcation point. Namely, $\dot{v}$ must equal zero, $\dot{n}$ must equal zero, and the eigenvalues should cause the trace (τ) and determinant (Δ) to be equal to the borderline case between a stable node and a stable spiral. That is,

$$\tau^2 - 4\Delta = 0. \tag{85}$$

If an injected current value is found which satisfies all three of these conditions, then the value for v and n at which this occurs is a fixed point of the system, and the value of injected current is a bifurcation point. As described in Section 3.1.3, topological equivalence of the fixed point for linearized system is not guaranteed for boundaries between regions of the graphical classifier, and further investigation is required to confirm details of the system dynamics. Likewise for bifurcation 2 three equations must be satisfied simultaneously. In the case of the second bifurcation point $\dot{v}$ must equal zero, $\dot{n}$ must equal zero, and the trace (τ) must equal zero.

The fixed point classification diagram presented in [6] is not easily extensible to higher-dimensions. Fortunately, for the purposes of determining the bifurcation point, the same information can be gleaned from the locus of eigenvalues presented in Figure 32. Bifurcation 1 is the point at which the eigenvalues break away from the real axis. Bifurcation 2 is the point at which the eigenvalues loose stability, crossing into the right hand plane. These two conditions are when an eigenvalue, or the real part of the eigenvalues are equal to zero. Again, this is indicative of the point at which topological equivalence of the linearized system is not guaranteed to match that of the original nonlinear system.

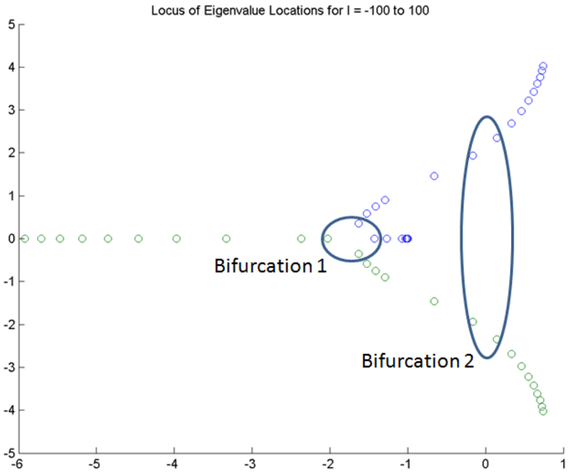

Figure 32: Bifurcations of the system fixed point as indicated by the locus of eigenvalues

For bifurcation 1 the value for the coordinates of the fixed point and injected current near the bifurcation point were given as initial conditions and $fsolve$ found a solution at $(v, n) \approx (-67.6723, 0.0106)$ with $I \approx -17.1356$. To verify this result the computed bifurcation value for the injected current will be used as an input, and the eigenvalues of the linearized system will be computed. The fixed point classification diagram predicts $\tau^2 - 4\Delta$ will equal zero, and the locus of eigenvalues predicts the two eigenvalues should be a repeated root with zero imaginary content.

As verified in MATLAB®, an injected current of $I \approx -17.1356$ produces a repeated pair of eigenvalues on the real axis at $\lambda_{1,2} \approx -1.684944 \pm 0i$. The imaginary content of the eigenvalues is zero out to the seventh decimal place with the present $fsolve$ configuration.

Using the computed eigenvalues $\tau \approx -3.36989$ and $\Delta \approx 2.83904$, which agrees with the boundary between a stable node and a stable spiral as computed by $\tau^2 - 4\Delta$.

For bifurcation 2 the value for the coordinates of the fixed point and injected current were given as initial conditions and $fsolve$ found a solution at $(v, n) \approx (-56.4815, 0.0914)$ and $I \approx 14.6590$. Again, to verify this result the computed bifurcation value for the injected current will be used as an input, and the eigenvalues of the linearized system will be computed. In this case, the fixed point classification diagram predicts the trace (τ) will equal zero, and the locus of eigenvalues predicts the two eigenvalues should be a complex conjugate pair with zero real content.

As verified in MATLAB®, an injected current of $I \approx 14.6590$ produces eigenvalues on the imaginary axis at $\lambda_{1,2} \approx 0 \pm 2.13748i$ and $\tau \approx 0$. Both the real part of the eigenvalues and the trace are approximately equal to zero to fourteen decimal places.

4.2.1.3.2 Supercritical Andronov-Hopf Dynamics in the Stable Spiral Region

Injected currents in the form of step inputs are used to investigate qualitatively different system dynamics. In each case the length of the simulation is 40 ms. The neuron model is initially quiescent at the resting membrane potential, followed by application of a step input at 10 ms.

Initial conditions for membrane voltage (v) and gating variable (n) were chosen by running a simulation with zero injected current, allowing any transients in the state variables to decay. This ensures a quiescent response prior to application of the step input. With the neuron model parameterized for the supercritical Andronov-Hopf bifurcation type, initial conditions are $v_0 \approx -60.8648\,\text{mV}$ and $n_0 \approx 0.0402$.

Three different injected current values of $10\,\mu\text{A/cm}^2$, $40\,\mu\text{A/cm}^2$, and $-40\,\mu\text{A/cm}^2$ were chosen to exemplify the three qualitatively different behaviors of the model neuron. As shown in Figures 31 and 32, and confirmed by computation of the bifurcation values in this section, these values demonstrate the different classification categories of the system fixed point. It is expected that any injected current values in the ranges $I > 14.6590\,\mu\text{A/cm}^2$, $-17.1356\,\mu\text{A/cm}^2 < I < 14.6590\,\mu\text{A/cm}^2$, and $I < -17.1356\,\mu\text{A/cm}^2$ would be sufficient.

For injected current values where $-17.1356\,\mu\text{A/cm}^2 < I < 14.6590\,\mu\text{A/cm}^2$, damped oscillations are expected based on fixed point classification as a stable spiral. Both time domain and phase plots are provided.

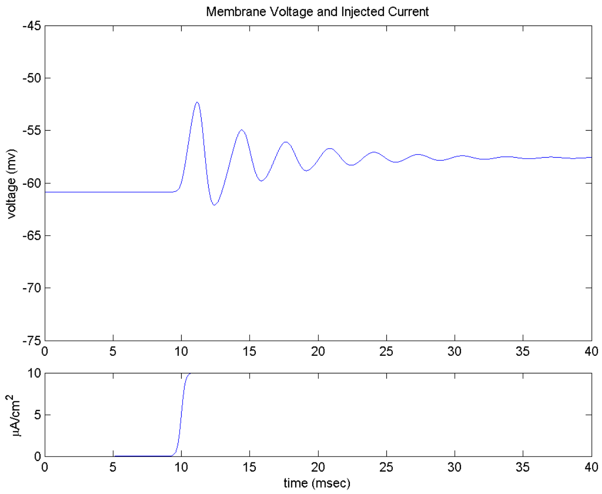

Figure 33: Supercritical Andronov-Hopf stable spiral time domain plot

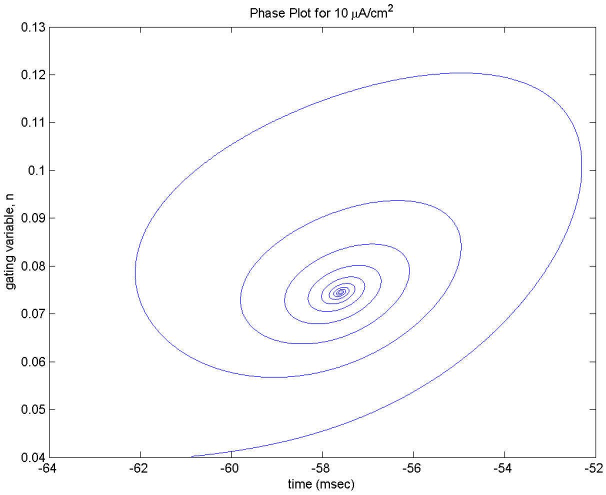

Figure 34: Supercritical Andronov-Hopf stable spiral phase plane

The time domain plot, showing both injected current and membrane voltage response, is a plot representative of what could be measured experimentally. Additional traces can be added to this plot, including current contributions for each ion accounted for by the model, any gating variables, and time dependent ionic conductance values. Some of these traces are accessible experimentally, which can aid in verification of modeled neuron dynamics.

Another way to depict the same information is through the phase plane. For two-dimensional systems the phase plane is particularly informative since repetitive spiking, directly related to the presence of a limit cycle, is very clearly depicted in the phase plane. In this case, the phase plane shows the system transitioning from one point in the phase plane to a second point in the phase plane. The path by which the system transitions between the two stable resting potentials is indicative of the naming convention provided by the fixed point classification diagram, a stable spiral [6].

Time is not explicitly indicated on the phase plane. Time is represented only by the speed at which the states are moving along the trajectory. This means that a resting membrane potential is actually only a single point on the phase plane. One means of displaying time along with the phase plane is to plot the trajectory in three-dimensions, allowing the simulation time to evolve along the vertical axis.

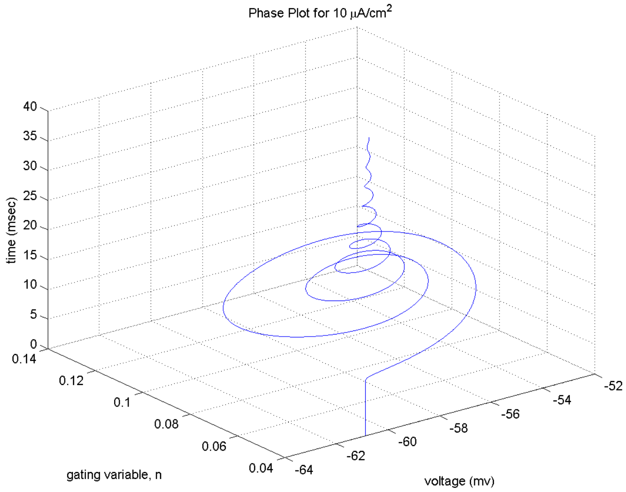

Figure 35: Supercritical Andronov-Hopf stable spiral phase plane plus time

Now the first 10 ms of the simulation, which was previously a single point in the phase plane, is represented by the purely vertical line at $v \approx -60.8648$. In the two-dimensional phase plot the largest oscillations dominate the figure. By including time as the third axis, it is evident that the system spends the vast majority of the simulation time in the immediate vicinity of the two stable fixed points.

When viewed directly from above, the three-dimensional phase plane reproduces the two-dimensional phase plane of Figure 34. Rotating Figure 35 to a different orientation it is possible to view only the voltage and time axes, allowing the three-dimensional picture to reproduce the time domain plot of Figure 33. When taken as a set, these three figures are extremely informative of the overall system state.

Furthermore, the behavior exhibited is exactly as predicted by the fixed point classification diagram and locus of eigenvalues. With higher-dimensional neuron models, it is not possible to succinctly depict system state graphically. By understanding the dynamics of reduced-order models graphically, it is possible to intuit system dynamics in higher-dimensions not extensible to graphical schemes.

4.2.1.3.3 Supercritical Andronov-Hopf Dynamics in the Unstable Spiral Region

For injected current values above $I \approx 14.6590\,\mu\text{A/cm}^2$, it is expected that the system fixed point becomes unstable, yielding a stable limit cycle attractor [1].

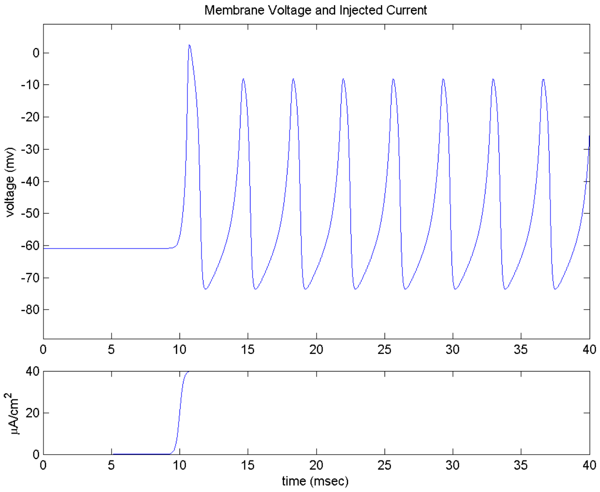

Figure 36: Supercritical Andronov-Hopf unstable spiral time domain plot

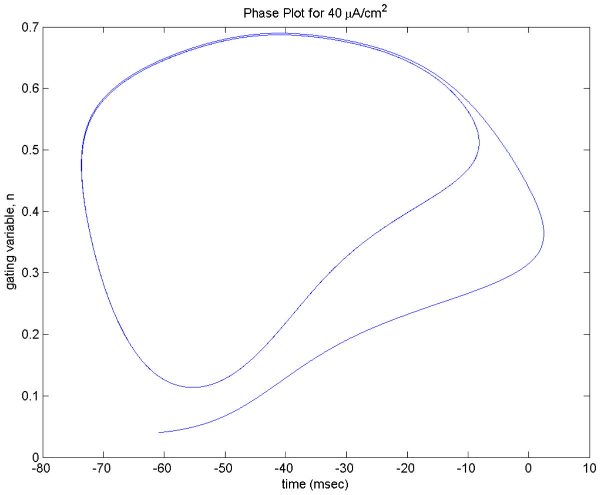

Figure 37: Supercritical Andronov-Hopf unstable spiral phase plane

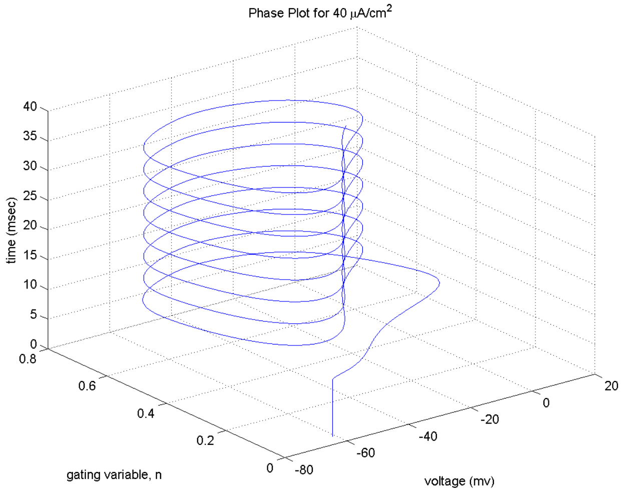

Figure 38: Supercritical Andronov-Hopf unstable spiral phase plane plus time

As expected, the first 10 ms of the simulation is still characterized by quiescence, and upon application of the step injected current the neuron model responds with an upswing in membrane voltage. However, rather than damped oscillation like the previous case, now the neuron model exhibits repetitive spiking. The limit cycle, displayed in the two-dimensional phase plane, determines the size and shape of the action potentials seen in the time domain. When plotted as a three-dimensional phase plot the limit cycle looks like a spring, coiling upward at a regular interval.

Again, the behavior exhibited is exactly as predicted by the fixed point classification diagram and locus of eigenvalues.

System behavior described thus far aligns with the bifurcation of interest in [1]. At the occurrence of a supercritical Andronov-Hopf bifurcation a single system fixed point looses stability, yielding a stable limit cycle attractor which changes size in relation to the amplitude of injected current [1, p. 15]. Plots for an injected current of $I = 20\,\mu\mathrm{A/cm}^2$ demonstrate a smaller limit cycle attractor.

From a neuroscience perspective, this behavior represents a neuron capable of repetitive spiking and encoding stimulus strength as graded action potentials.

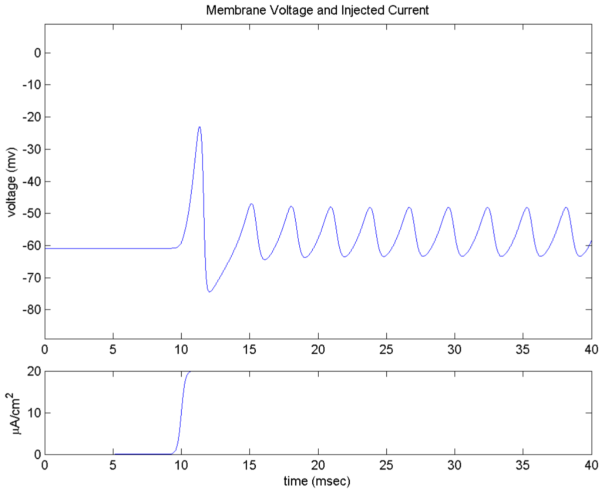

Figure 39: Supercritical Andronov-Hopf unstable spiral time domain plot, $I = 20\,\mu\text{A/cm}^2$

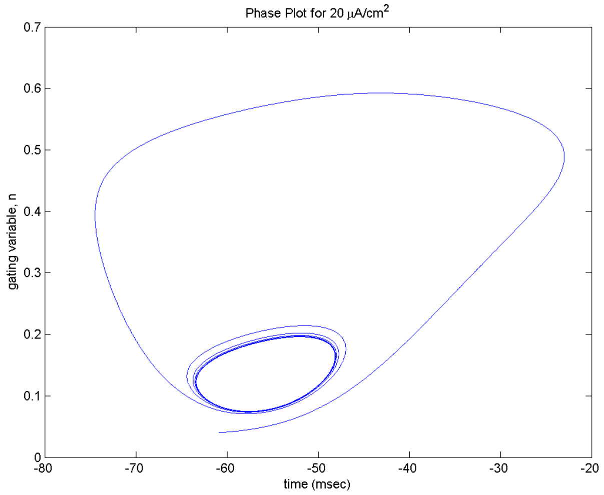

Figure 40: Supercritical Andronov-Hopf unstable spiral phase plane, $I = 20\,\mu\text{A/cm}^2$

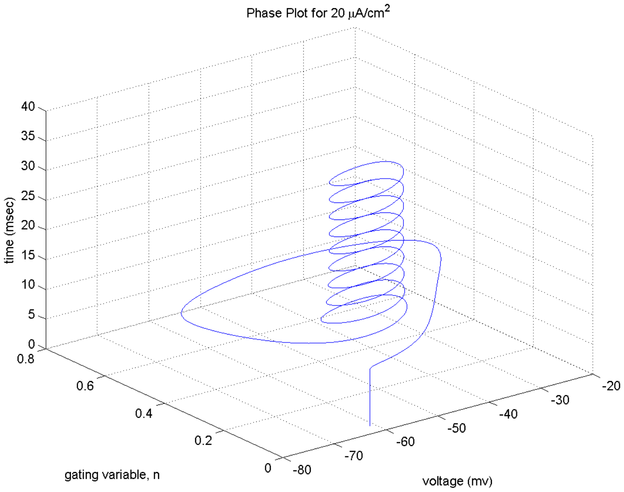

Figure 41: Supercritical Andronov-Hopf unstable spiral phase plane plus time, $I = 20\,\mu\text{A/cm}^2$

4.2.1.3.4 Supercritical Andronov-Hopf Dynamics in the Stable Node Region

As indicated by the fixed point classification diagram, another bifurcation of the fixed point is possible with negative injected current values. Negative injected current simply represents a reversal in direction of the electrical current. The transition should occur at all injected current levels less than $I \approx -17.1356\,\mu\text{A/cm}^2$.

According to the definition of a stable node, system trajectories should not exhibit oscillation. Included time domain and phase plots verify this expectation, without oscillations associated with system trajectories for positive injected current.

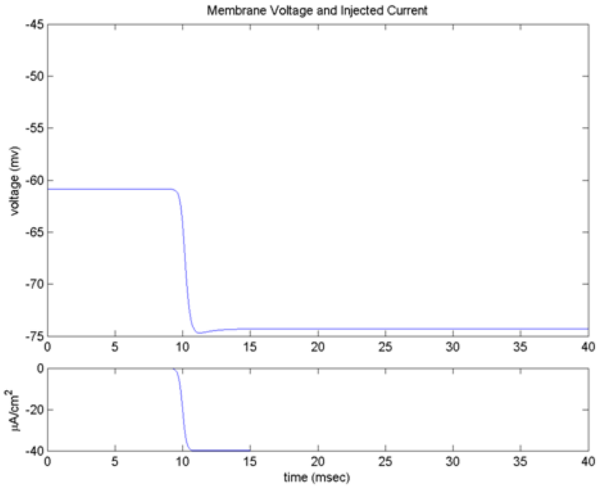

Figure 42: Supercritical Andronov-Hopf stable node time domain plot

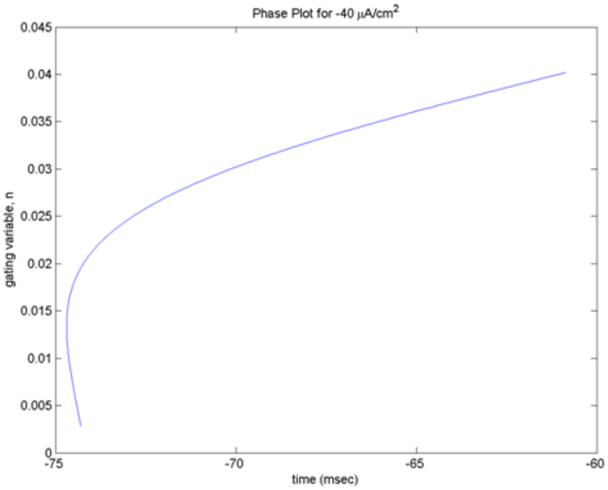

Figure 43: Supercritical Andronov-Hopf stable node phase plane

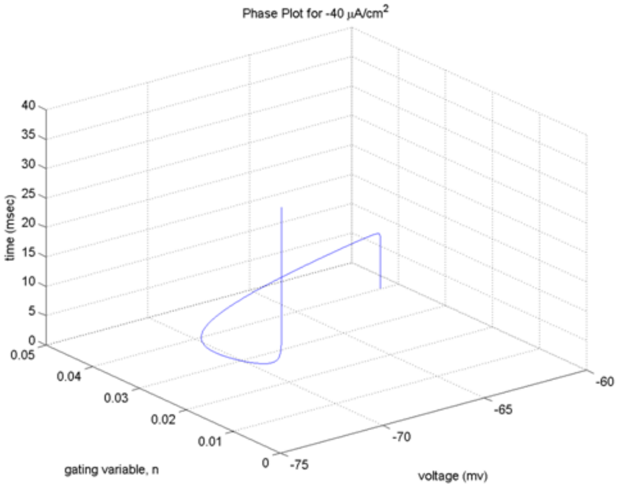

Figure 44: Supercritical Andronov-Hopf stable node phase plane plus time

There is a small amount of overshoot evident in the time domain plot. When the slope of the injected current step input is reduced, the overshoot vanishes, as depicted in Figure 45.

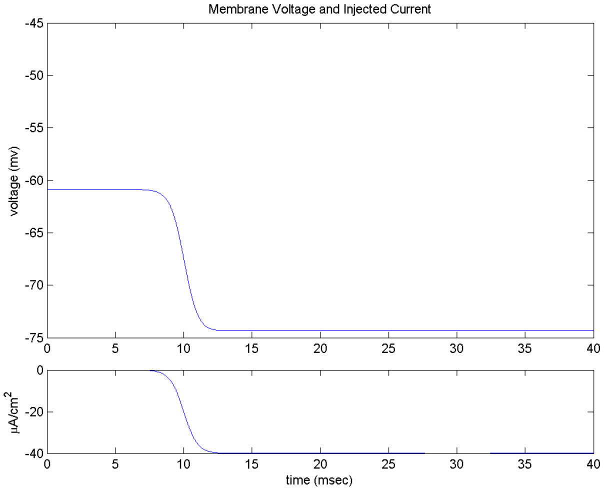

Figure 45: Supercritical Andronov-Hopf stable node time domain plot, without overshoot

The plotted results verify qualitative behaviors predicted in parallel by the fixed point classification diagram and the locus of eigenvalues. Two and three-dimensional phase plane plots, when viewed in conjunction with time domain plots, paint a thorough picture of system dynamics for two-dimensional systems, and establish sound intuition for higher-dimensional neuron models.

4.2.1.4 Optimal Control

In Sections 4.2.1.2 and 4.2.1.3, three qualitatively different system behaviors of the reduced-order Hodgkin-Huxley model, parameterized for a supercritical Andronov-Hopf bifurcation, were identified. In this section, optimal input stimuli will be computed for each category of system behavior.

4.2.1.4.1 Optimal Control of Supercritical Andronov-Hopf Dynamics in the Stable Spiral Region

Application of injected current $I = 10\,\mu\text{A/cm}^2$ results in system behavior identified as a stable spiral. Using the membrane voltage generated by a $I = 10\,\mu\text{A/cm}^2$ step input as the reference voltage, the optimal input stimuli is calculated for three different sets of values for P, Q, and R.

The first plot, with $P = Q = 1$ and $R = 10$, represents an emphasis on reduction of input stimuli energy at the expense of membrane voltage tracking accuracy. The third plot, with $P = Q = 1000$ and $R = 1$, represents the opposite end of the spectrum, emphasizing tracking accuracy. The remaining plot, with $P = Q = 100$, and $R = 1$, provides a balance of these two competing objectives.

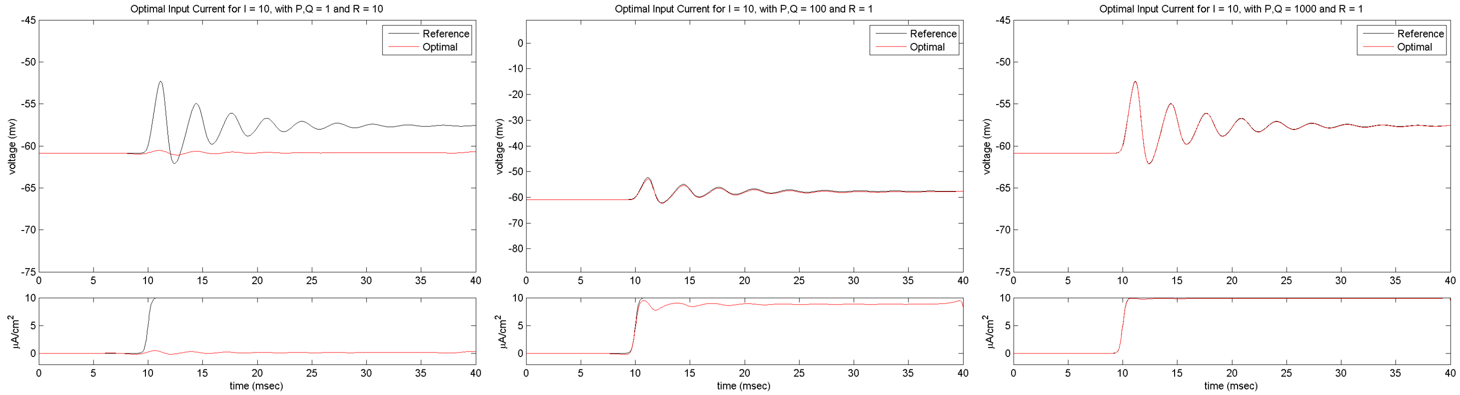

(a) $P = Q = 1,\ R = 10$

(b) $P = Q = 100,\ R = 1$

(c) $P = Q = 1000,\ R = 1$

Figure 46: Optimal control of supercritical Andronov-Hopf stable spiral

As shown in Figure 46a, the exaggerated emphasis on reduction of input stimuli energy results in a membrane voltage is hardly disturbed from rest. Figure 46b, with $P = Q = 100$ and $R = 1$, displays quite accurate tracking of the reference membrane potential, even with a steady state value of injected current that is reduced from the originally applied input. Further increasing emphasis on tracking in Figure 46c produces reduced error between the reference and optimally generated membrane potential at the expense of greater input stimuli energy. The same values of P, Q, and R will be used for computation of optimal input stimuli for unstable spiral and stable node dynamics of the reduced-order Hodgkin-Huxley model.

4.2.1.4.2 Optimal Control of Supercritical Andronov-Hopf Dynamics in the Unstable Spiral Region

Application of injected current $I = 40\,\mu\text{A/cm}^2$ results in system behavior identified as an unstable spiral. Bifurcation of the system fixed point, along with the birth of a limit cycle attractor, enables the neuron model to produce repetitive spiking behavior.

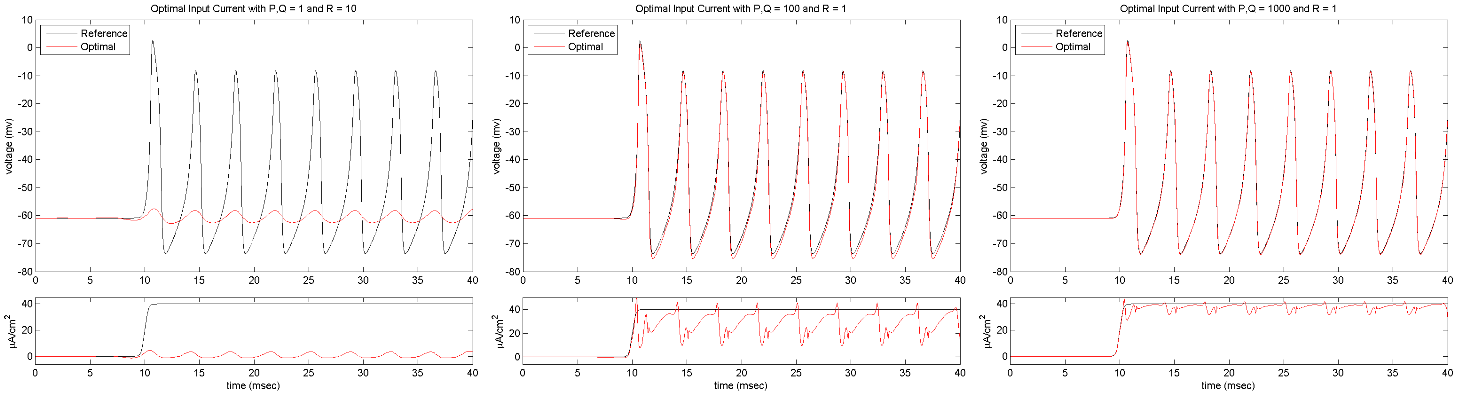

(a) $P = Q = 1,\ R = 10$ (b) $P = Q = 100,\ R = 1$ (c) $P = Q = 1000,\ R = 1$

Figure 47: Optimal control of supercritical Andronov-Hopf unstable spiral

Optimal inputs computed for a repetitively spiking reference membrane potential demonstrate "characteristic dips" which have been identified in previous publications [2, 3]. The dips are most noticeable when $P = Q = 100$ and $R = 1$, providing a marked decrease in the injected current 'energy' which clearly correlates with the generation of each action potential. That is, the optimal control methodology computes a reduced need for injected current once generation of an action potential is under-way.

Again, further improved accuracy of tracking can be achieved at the expense of stimulus energy with $P = Q = 1000$ and $R = 1$.

4.2.1.4.3 Optimal Control of Supercritical Andronov-Hopf Dynamics in the Stable Node Region

Application of injected current $I = -40\,\mu\text{A/cm}^2$ results in system behavior identified as a stable node.

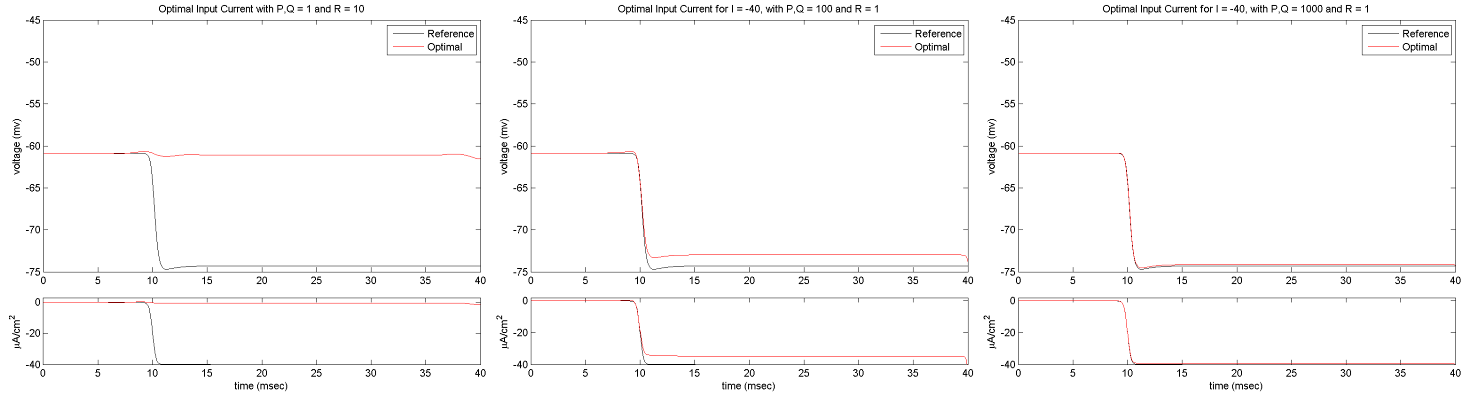

(a) $P = Q = 1,\ R = 10$

(b) $P = Q = 100,\ R = 1$

(c) $P = Q = 1000,\ R = 1$

Figure 48: Optimal control of supercritical Andronov-Hopf stable node

The third behavior, representative of a stable node, lacks any action potentials or oscillation. However, performance of the optimal input stimuli is similar to the previous two simulations. That is, when $P = Q = 1$ and $R = 10$ in Figure 48a, the neuron model is hardly disturbed from rest. When $P = Q = 100$ and $R = 1$, as seen in Figure 48b, a reduction of input stimulus energy is present, but tracking accuracy is lower than when $P = Q = 1000$ in Figure 48c.

The first and most important commonality across all computed inputs is that as the emphasis on tracking increases the optimal input current converges to more closely represent the original input signal. Furthermore, the trade-off between reduction of injected current energy and tracking accuracy has an asymptotic characteristic indicating a potential sweet spot for acceptable tracking accuracy with significantly reduced injected current energy.

4.2.1.5 Discussion of Supercritical Andronov-Hopf Bifurcation Dynamics

This section utilized a reduced-order Hodgkin-Huxley model with parameters selected for demonstration of supercritical Andronov-Hopf bifurcation dynamics [1]. The framework for nonlinear analysis and optimal control, presented as Figure 12 in Chapter 3, was the basis for investigating system dynamics.

For the remainder of this dissertation, one of two companion techniques will be utilized for locating and classifying system fixed points depending on the dimension of the neuron model. Within this section, the equality of these techniques was demonstrated.

The selected range of input stimuli produced three qualitatively different behaviors: stable spiral, unstable spiral, and stable node. For each behavior, system dynamics were investigated using the time domain as well as the phase plane. A spectrum of optimal input stimuli, ranging from emphasis on input ‘energy’ reduction to tracking accuracy, were computed injected current values representative of each qualitatively different behavior.

Section 4.1.2 demonstrated that, when required, it is often possible to compute the injected current value at the bifurcation point. As described in Section 3.1.3, the dynamics of the linearized system are not guaranteed to be topologically equivalent to those of the original nonlinear system when eigenvalues, or the real part of eigenvalues, are equal to zero, which is the case at both bifurcations investigated in this section.

In all cases, application of the optimal control technique to supercritical Andronov-Hopf dynamics of the reduced-order Hodgkin-Huxley model resulted in a consistent spectrum of results, ranging from reduced stimulus energy to tracking of the reference membrane voltage with a high degree of accuracy.

4.2.2 Subcritical Andronov-Hopf

Subcritical Andronov-Hopf bifurcations occur when an unstable limit cycle converges on a stable equilibrium, causing the fixed point to become unstable [1, p. 12].

Neuron models near a subcritical Andronov-Hopf bifurcation exhibit subthreshold oscillations, and are therefore resonators [1, p. 14]. System trajectories for inputs below the bifurcation value will exhibit damped oscillation. This is similar to system dynamics presented for supercritical Andronov-Hopf bifurcations.

Neuron models near a subcritical Adronov-Hopf bifurcation are bistable, exhibiting coexistence of resting and repetitive spike states [1]. This behavior is in contrast to the dynamics of the monostable supercritical Andronov-Hopf case. Bistability is often demonstrated via hysteresis, but is also brought out through appropriate selection of initial conditions. System behavior can be altered between rest and repetitive spiking through application of an appropriately timed transient pulse.

4.2.2.1 Fixed Point Location

Using equations (63) and (64) for the nullclines, and varying the injected stimulus current I from $-10\,\mu\text{A/cm}^2$ to $70\,\mu\text{A/cm}^2$ by increments of $5\,\mu\text{A/cm}^2$, a family of curves was generated in Figure 49. Since the n-nullcline did not change, it is represented by a single sigmoidal line on the plot. Each injected current value I produces a different curve for the v-nullcline.

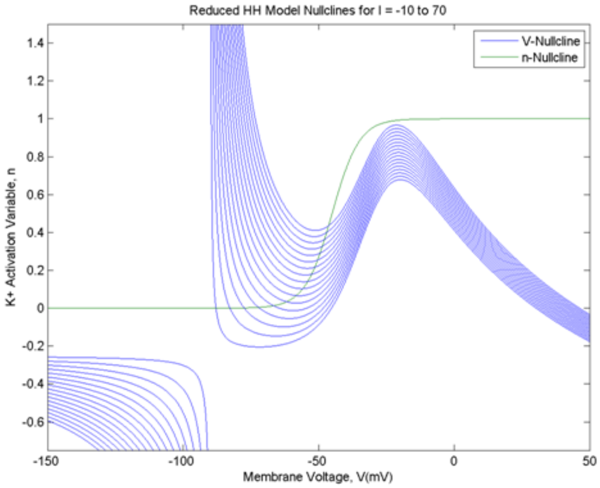

Figure 49: Subcritical Andronov-Hopf fixed point location using nullclines

Notice each v-nullcline intersects the n-nullcline at a single point in the phase plane for all considered values of I, indicating the presence of a single fixed point. The membrane voltage of fixed points range between approximately -85 to $-50\,\text{mV}$, and the gating variable ranges between 0 and 0.4.

Stability of the fixed point cannot be ascertained directly from the figure and requires further analysis per Section 4.2.2.2. For cases where the fixed point is stable, the value of the membrane voltage at the intersection of the nullclines is the resting membrane potential.

4.2.2.2 Graphical Fixed Point Classification

Using the approximate values for v and n from Section 4.2.2.1 as initial conditions, a numerical solution for the system fixed point is computed for each injected current value using $fsolve$. The values for the state variables are substituted into the Jacobian, allowing computation of eigenvalues according to equations (66) through (70).

After computing eigenvalues for the linearized system for each injected current level, the trace (τ) and determinant (Δ) are computed according to equations (83) and (84). These two values allow classification of the fixed point as shown in Figure 35, with a single point for each injected current value.

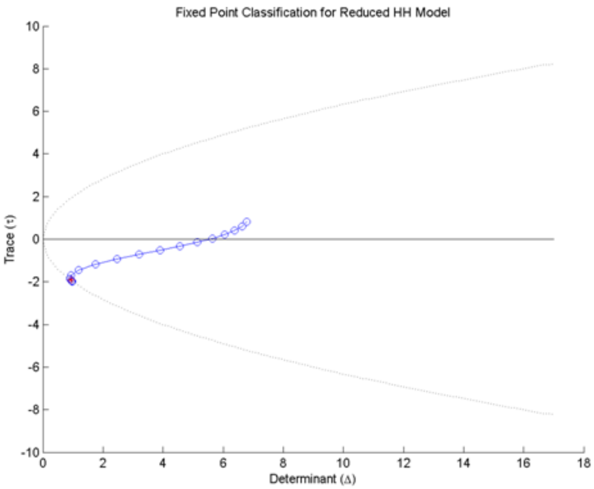

Figure 50: Graphical classification of reduced-order Hodgkin-Huxley subcritical Andronov-Hopf system fixed point

For negative and smaller injected current values, the fixed point classification clusters against the boundary between stable node and stable spiral regions. For values of injected current greater than approximately $50\,\mu\text{A}/\text{cm}^2$, a bifurcation of the fixed point has occurred, and the behavior is classified as an unstable spiral.

Information regarding stability of the fixed point can be added to each intersection of the nullclines as shown in Figure 51. Filled dots indicate a stable fixed point and open dots indicate an unstable fixed point for each injected current level.

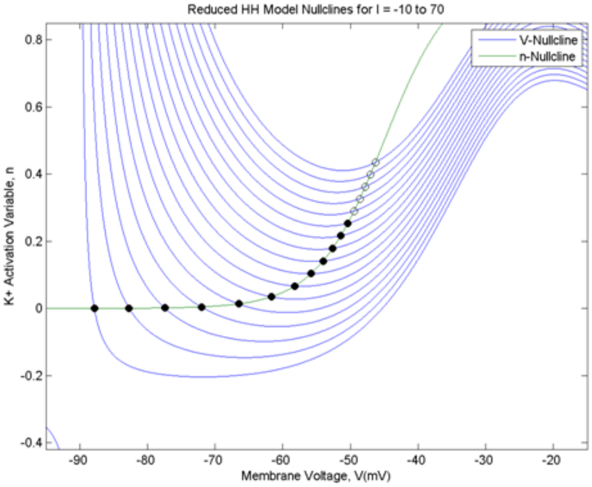

Figure 51: Subcritical Andronov-Hopf fixed point location and stability with nullclines

4.2.2.3 Bifurcations

Figure 50 reveals that injected current levels above 50 μA/cm^2 produce qualitative system behavior classified as an unstable spiral. Values between 0 μA/cm^2 and 45 μA/cm^2 produce behavior classified as a stable spiral.

As described in Chapter 3, when considering the major regions of Figure 50 no additional analysis is required to verify the linearized system is topologically equivalent to the original nonlinear system. Furthermore, if all eigenvalues are non-zero, with non-zero real parts, the linearized system is topologically equivalent to the nonlinear system.

Injected current values of 25 μA/cm^2 and 60 μA/cm^2 have been selected to demonstrate system dynamics for injected current levels above and below the subcritical Andronov-Hopf bifurcation.

4.2.2.3.1 Subcritical Andronov-Hopf Dynamics in the Stable Spiral Region

Injected currents in the form of step inputs are used to investigate qualitatively different system dynamics. In each case the length of the simulation is 40 ms. The neuron model is initially quiescent at the resting membrane potential, followed by application of a step input at 10 ms.

Initial conditions for membrane voltage (v) and gating variable (n) were chosen by running a simulation with zero injected current, allowing any transients in the state variables to decay. This ensures a quiescent response prior to application of the step input. With the neuron model parameterized for the subcritical Andronov-Hopf bifurcation type, initial conditions are $v_0 \approx -77.4513\,\mathrm{mV}$ and $n_0 \approx 0.0015$.

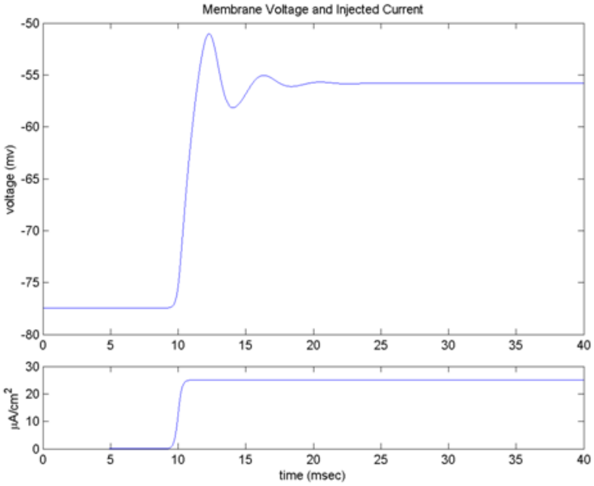

Figure 52: Subcritical Andronov-Hopf stable spiral time domain plot

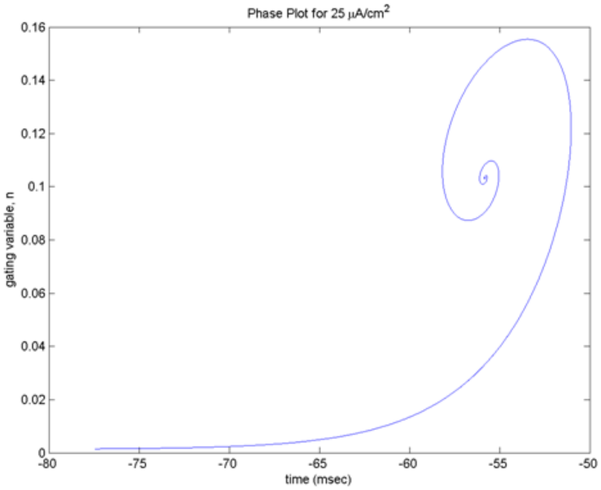

Figure 53: Subcritical Andronov-Hopf stable spiral phase plane

Figures 52 and 53 exhibit damped oscillations in the time domain and a collapsing spiral in the phase plane, consistent with expected behavior of a stable spiral. Figure 51 includes time as the vertical axis of the phase plane.

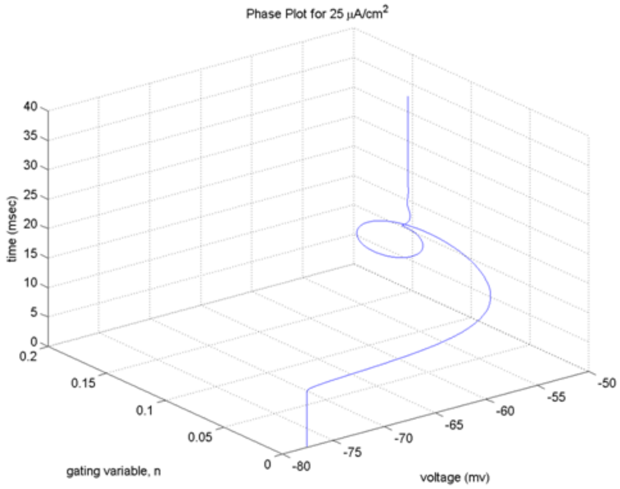

Figure 54: Subcritical Andronov-Hopf stable spiral phase plane plus time

The first 10 ms of the simulation are a purely vertical line, depicted in Figure 53 as a single point in the phase plane. The damped oscillation, a seeping arc in the phase plane, quickly decays to a steady state voltage, which agrees with the time domain plot of Figure 52 and the expected behavior for a stable spiral.

4.2.2.3.2 Subcritical Andronov-Hopf Dynamics in the Unstable Spiral Region

For injected current values above $I \approx 50\,\mu\text{A/cm}^2$, it is expected that the system fixed point becomes unstable, at which point the system trajectory approaches a stable limit cycle attractor [1]. A defining feature of the subcritical Andronov-Hopf dynamics is the coexistence of resting and repetitively spiking states. This is in contrast to the supercritical Andronov-Hopf case, where a bifurcation of the system fixed point births the stable limit cycle attractor.

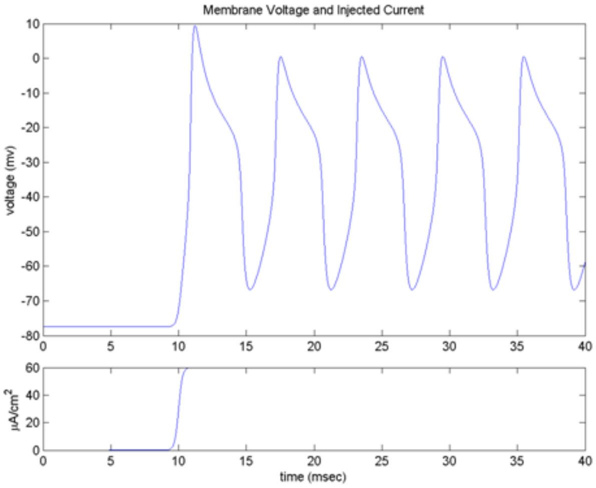

Figure 55: Subcritical Andronov-Hopf unstable spiral time domain plot

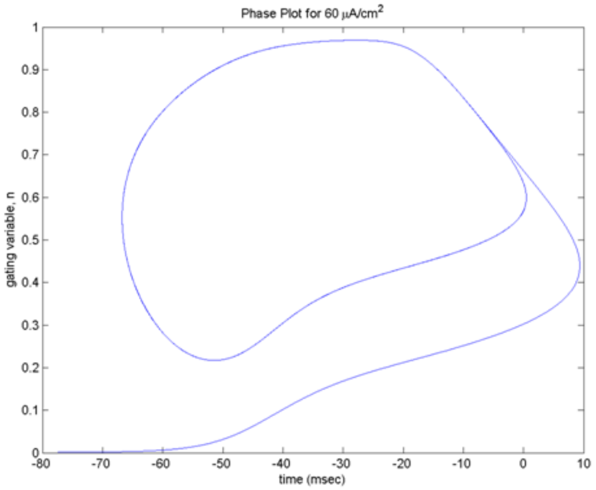

Figure 56: Subcritical Andronov-Hopf unstable spiral phase plane

Behavior depicted in Figures 55 and 56 is characteristic of a stable limit cycle attractor. Rather than damped oscillation as shown in Figures 52 and 53, application of an injected current of $65\,\mu\text{A/cm}^2$ causes loss of stability of the system fixed point, with the system trajectory following a stable limit cycle attractor.

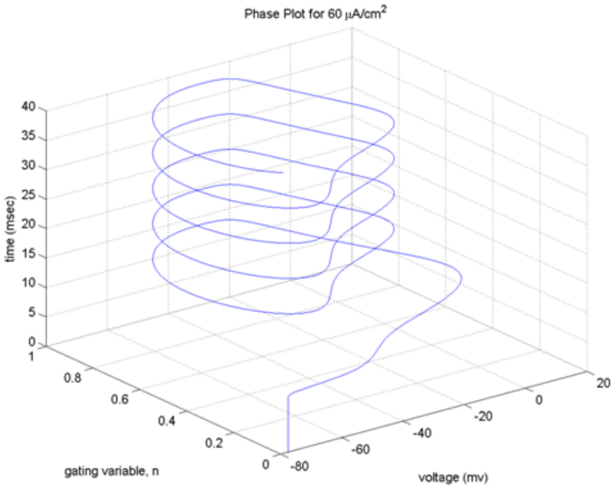

Figure 57: Subcritical Andronov-Hopf unstable spiral phase plane plus time

4.2.2.4 Optimal Control

In Sections 4.2.2.2 and 4.2.2.3, it was demonstrated that qualitatively different system behaviors could be induced when injected currents between $0\,\mu\text{A/cm}^2$ and $45\,\mu\text{A/cm}^2$ and above $50\,\mu\text{A/cm}^2$ are applied to the model neuron. For current values in the range $0 - 45\,\mu\text{A/cm}^2$, the system behavior was consistent with classification as a stable spiral. For values of injected current above $50\,\mu\text{A/cm}^2$, a bifurcation of the system fixed point occurs and behavior is consistent with classification as an unstable spiral, with characteristic limit cycle attractor, as expected for the subcritical Andronov-Hopf bifurcation. In this section optimal input stimuli will be computed for each category of system behavior.

4.2.2.4.1 Optimal Control of Subcritical Andronov-Hopf Dynamics in the Stable Spiral Region

Application of injected current $I = 25\,\mu\text{A/cm}^2$ results in system behavior identified as a stable spiral. Using the membrane voltage generated by a $I = 25\,\mu\text{A/cm}^2$ step input as the reference voltage, the optimal input stimuli is calculated for three different sets of values for P, Q, and R.

The first plot, with $P = Q = 1$ and $R = 10$, represents an emphasis on reduction of input stimuli energy at the expense of membrane voltage tracking accuracy. The third plot, with $P = Q = 1000$ and $R = 1$, represents the opposite end of the spectrum, emphasizing tracking accuracy. The remaining plot, with $P = Q = 100$ and $R = 1$, provides a balance of these two competing objectives.

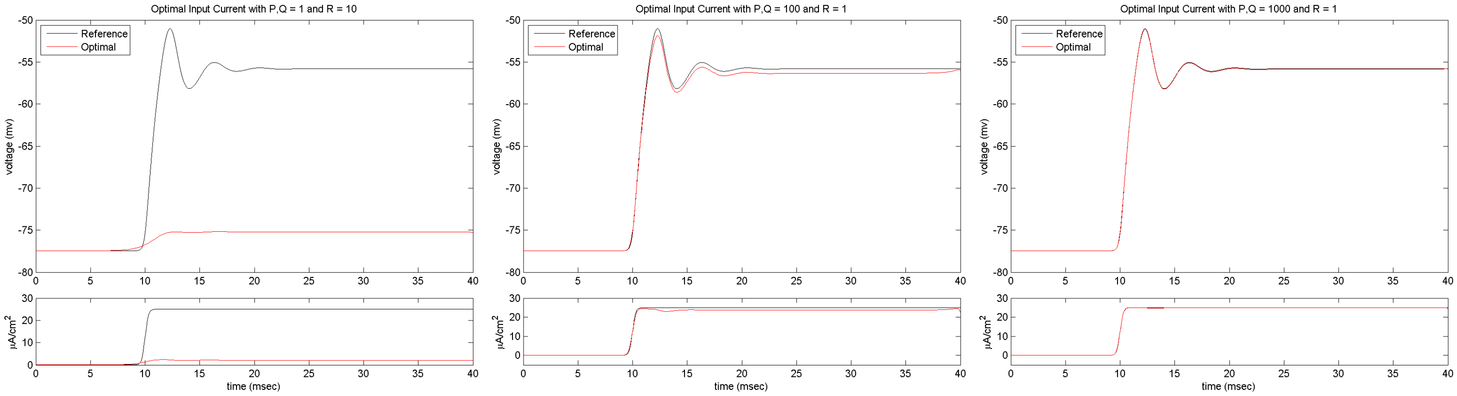

(a) $P = Q = 1,\ R = 10$

(b) $P = Q = 100,\ R = 1$

(c) $P = Q = 1000,\ R = 1$

Figure 58: Optimal control of subcritical Andronov-Hopf stable spiral

Figures 58a through 58c demonstrate a typical spectrum for application of the optimal control methodology, with an emphasis on reduced energy of input stimuli with relatively large values or R and improved tracking accuracy for large values of P and Q. Weighting terms of the objective function can be adjusted depending on the control objective.

4.2.2.4.2 Optimal Control of Subcritical Andronov-Hopf Dynamics in the Unstable Spiral Region

Application of injected current $I = 60\,\mu\text{A/cm}^2$ results in system behavior identified as an unstable spiral. The system fixed point loses of stability and the system trajectory approaches a coexistent stable limit cycle attractor.

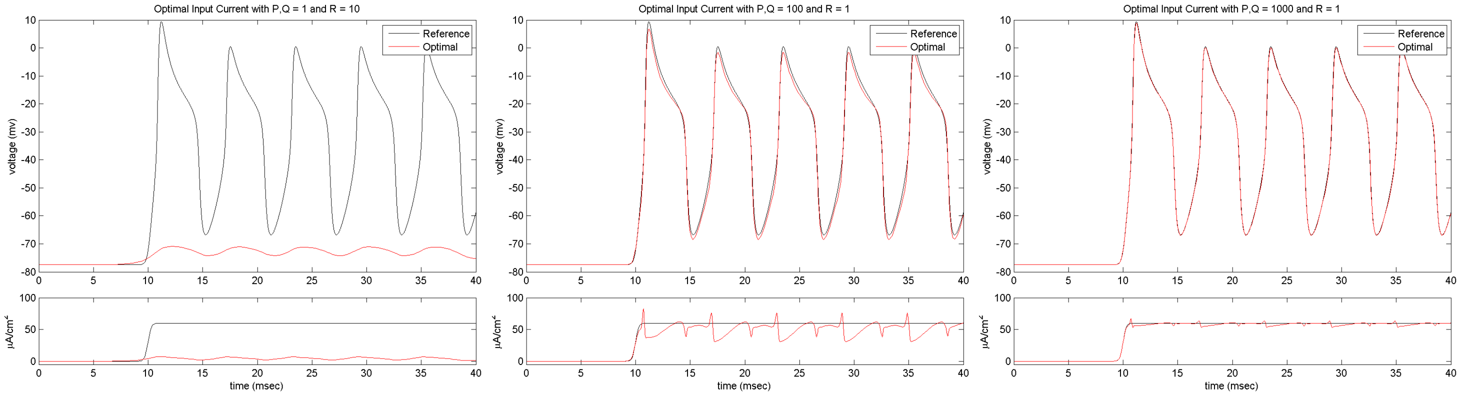

(a) $P = Q = 1,\ R = 10$ (b) $P = Q = 100,\ R = 1$ (c) $P = Q = 1000,\ R = 1$

Figure 59: Optimal control of subcritical Andronov-Hopf unstable spiral

Optimal inputs produce the expected range of behavior from energy reduction in Figure 59a to tracking accuracy in Figure 59c. As seen in Figure 59b, when simulations contain repetitive spiking "characteristic dips" in the optimal input current are often present as emphasis on tracking is reduced [2, 3]. The amplitude of these dips typically decreases, with the optimal current approaching the originally applied current, as emphasis on tracking is further increased.

4.2.2.5 Discussion of Subcritical Andronov-Hopf Bifurcation Dynamics

This section utilized a reduced-order Hodgkin-Huxley model with parameters selected for demonstration of subcritical Andronov-Hopf bifurcation dynamics [1]. Nonlinear analysis enables categorization of system fixed point behavior for a range of injected current values. It was determined that two classes of behavior, consistent with the subcritical Andronov-Hopf bifurcation type, could be elicited for ranges of injected input current between $0\,\mu\text{A/cm}^2$ and $45\,\mu\text{A/cm}^2$ and above $50\,\mu\text{A/cm}^2$.

Using injected input currents of $I = 25\,\mu\text{A/cm}^2$ and $I = 60\,\mu\text{A/cm}^2$ stable spiral and unstable spiral system dynamics were highlighted. The subcritical Andonrov-Hopf bifurcation occurs as a transition between these qualitatively different system behaviors.

Results were presented using time domain and phase plane plots, along with a three-dimensional portrayal of the phase plane to enable inclusion of time in the phase plane. A spectrum of optimal input currents was also computed for both stable and unstable spiral dynamics.

4.2.3 saddle-node

Saddle-node bifurcations occur when two fixed points, one stable and one unstable, converge and annihilate each other [1, p. 12]. When a saddle-node bifurcation occurs with the bifurcation parameter varied in the opposite direction, two fixed points, one stable and one unstable, appear and diverge away from each other. Thus, saddle-node bifurcations are responsible for creation and destruction of system fixed points [6, p. 45].

Since the stable fixed point involved in the saddle-node bifurcation is classified as a node, with purely real eigenvalues, subthreshold oscillations do not occur [1, p. 14].

When referring to the saddle-node bifurcation type in the context of the four bifurcations fundamental to neural behavior, the system is parameterized such that a third, unstable fixed point exists inside of a limit cycle attractor [1, p. 13]. Since the limit cycle attractor is coexistent with stable fixed point prior to the saddle-node bifurcation, neuron models defined as a saddle-node in this context are bistable. This also means system trajectories will transition from stable to repetitive spiking after the bifurcation.

As mentioned in Section 4.2.2, bistability is often demonstrated via hysteresis, but is also brought out through appropriate selection of initial conditions. System behavior can be altered between rest and repetitive spiking through application of an appropriately timed transient pulse.

4.2.3.1 Fixed Point Location

Using equations (63) and (64) for the nullclines, and varying the injected stimulus current I from $-80\,\mu\text{A/cm}^2$ to $100\,\mu\text{A/cm}^2$ by increments of $10\,\mu\text{A/cm}^2$, a family of curves is generated in Figure 60. Since the n-nullcline does not change it is represented by a single sigmoidal line on the plot. Each injected current value I produces a different curve for the v-nullcline.

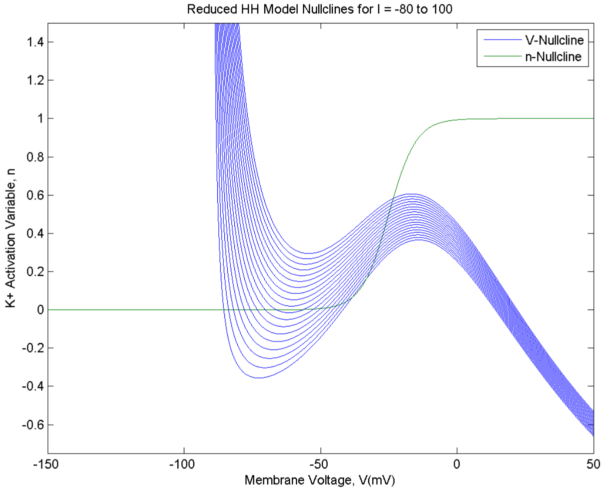

Figure 60: Saddle-node fixed point location using nullclines

Notice that the v-nullcline has a distinct local minimum. For values of injected current where $I \leq 0\,\mu\text{A/cm}^2$ there are three intersections of the nullclines for each trace. At some value of injected current between $I = 0\,\mu\text{A/cm}^2$ and $I = 10\,\mu\text{A/cm}^2$, the two fixed points just below $-50\,\text{mV}$ coalesce. For v-nullclines where the injected current is greater than or equal to $10\,\mu\text{A/cm}^2$ there is one intersection of the nullclines, corresponding to one fixed point, for each injected current value.

Stability of the fixed point cannot be ascertained directly from the figure and requires further analysis per Section 4.2.3.2. For cases where the fixed point is stable, the value of the membrane voltage at the intersection of the nullclines is the resting membrane potential.

4.2.3.2 Graphical Fixed Point Classification

Using the approximate values for v and n from Section 4.2.3.1 as initial conditions, a numerical solution for the system fixed point is computed for each injected current value using $fsolve$. The values for the state variables are substituted into the Jacobian, allowing computation of eigenvalues according to equations (66) through (70).

After computing eigenvalues for the linearized system for each injected current level the trace (τ) and determinant (Δ) are computed according to equations (83) and (84). These two values allow classification of each fixed point as shown in Figure 61. Three sets of points are plotted on the bifurcation diagram, one for each fixed point. Each data point on the diagram represents the classification of a given fixed point for a single injected current value. Each point containing an asterisk indicates zero injected current.

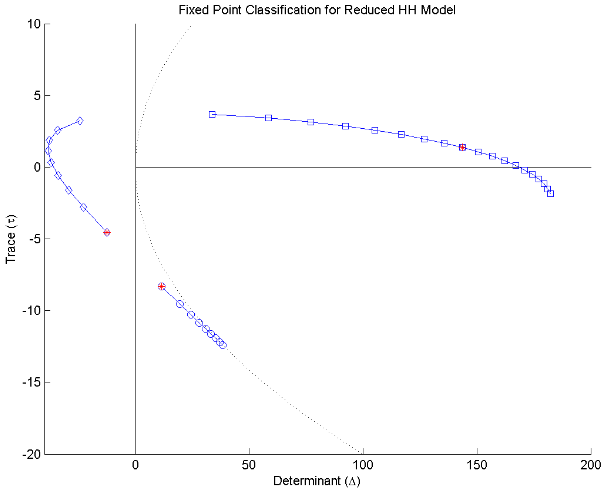

Figure 61: Graphical classification of reduced-order Hodgkin-Huxley saddle-node system fixed point

Since the fixed point classified as a saddle point coalesces with the fixed point classified as a stable node, the traces for these fixed points does not exist for injected current values above $0\,\mu\text{A/cm}^2$. For the range of injected current values shown, $-80\,\mu\text{A/cm}^2$ to $0\,\mu\text{A/cm}^2$, one fixed point is classified as a stable node and the second fixed point is classified as a saddle point.

The third fixed point is classified as an unstable spiral for injected current values from $-80\,\mu\text{A/cm}^2$ to $40\,\mu\text{A/cm}^2$. A bifurcation of this fixed point does occur at higher injected current values, but will not be considered as a part of the neural dynamics.

Information regarding stability of the fixed point can be added to each intersection of the nullclines as shown in Figure 62. Filled dots indicate a stable fixed point and open dots indicate an unstable fixed point for each injected current level.

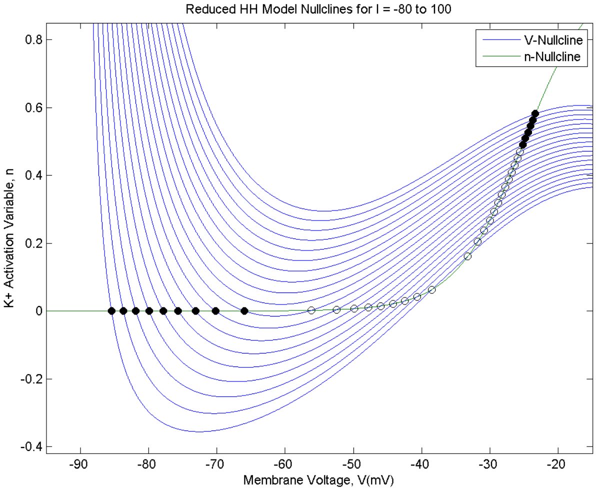

Figure 62: Saddle-node fixed point location and stability with nullclines

4.2.3.3 Bifurcations

Figure 61 reveals that for injected current levels between $-80\,\mu\text{A/cm}^2$ and $0\,\mu\text{A/cm}^2$, classification of the three system fixed points is robust to the major regions of the classification diagram, with one saddle point, one stable node, and one unstable spiral. Additionally, the fixed point classified as an unstable spiral does not undergo a bifurcation for injected currents up to $40\,\mu\text{A/cm}^2$.

As described in Chapter 3, when considering the major regions of Figure 61 no additional analysis is required to verify the linearized system is topologically equivalent to the original nonlinear system. Furthermore, if all eigenvalues are non-zero, with non-zero real parts, the linearized system is topologically equivalent to the nonlinear system.

For consistency with analysis of other bifurcation types it is desirable to determine two positive injected current values, one below and one above the bifurcation of interest. Since the bifurcation of interest occurs between $0\,\mu\text{A/cm}^2$ and $10\,\mu\text{A/cm}^2$, further investigation is required to determine a positive injected current value below the bifurcation current. As shown in Figure 63, an injected current value of $3\,\mu\text{A/cm}^2$ satisfies this criteria.

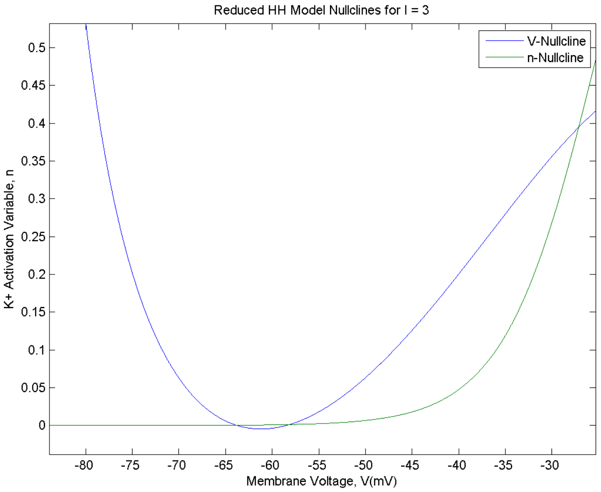

Figure 63: Saddle-node nullcline plot, $I = 3\,\mu\text{A/cm}^2$

Injected current values of $3\,\mu\text{A/cm}^2$ and $10\,\mu\text{A/cm}^2$ have been selected to demonstrate system dynamics for injected current levels above and below the saddle-node bifurcation.

4.2.3.3.1 saddle-node Dynamics in the Stable Node Region

Injected currents in the form of step inputs are used to investigate qualitatively different system dynamics. In each case, the length of the simulation is 40 ms. The neuron model is initially quiescent at the resting membrane potential, followed by application of a step input at 10 ms.

Initial conditions for membrane voltage (v) and gating variable (n) were chosen by running a simulation with zero injected current, allowing any transients in the state variables to decay. This ensures a quiescent response prior to application of the step input. With the neuron model parameterized for the saddle-node bifurcation type, initial conditions are $v_0 \approx -65.9529\,\text{mV}$ and $n_0 \approx 0.00027$.

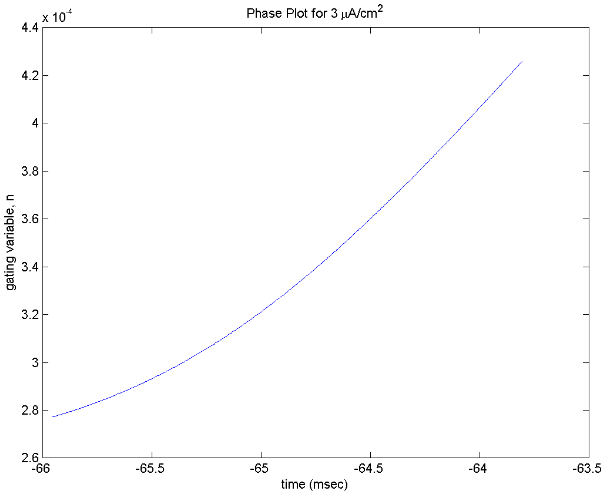

Figure 64: Saddle-node stable node time domain plot

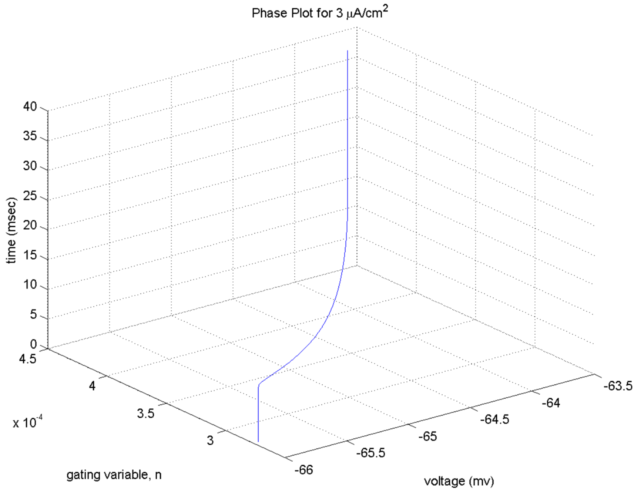

Figure 65: Saddle-node stable node phase plane

Figures 64 and 65 exhibit a change from one resting potential to another without oscillation, consistent with expected behavior of a stable node. Figure 66 includes time as the vertical axis of the phase plane.

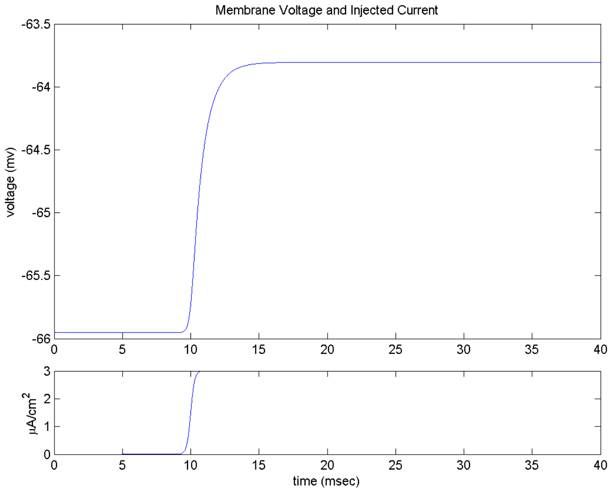

Figure 66: Saddle-node stable node phase plane plus time

The first 10 ms of the simulation are a purely vertical line, depicted in Figure 65 as a single point in the phase plane. The state of the model transitions from one stable point to another by an exponential, without overshoot in both the time and phase plane, which agrees with the time domain plot of Figure 64 and the expected behavior for a stable node.

4.2.3.3.2 saddle-node Dynamics in the Unstable Spiral Region

For injected current values at or above $I \approx 10\,\mu\text{A/cm}^2$, it is expected that the unstable saddle point and stable node coalesce, at which point the system trajectory approaches a stable limit cycle attractor [1]. A defining feature of the saddle-node dynamics is the coexistence of resting and repetitively spiking states.

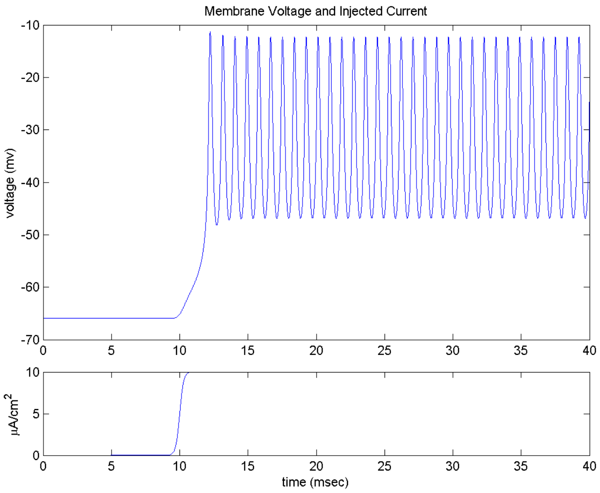

Figure 67: Saddle-node unstable spiral time domain plot

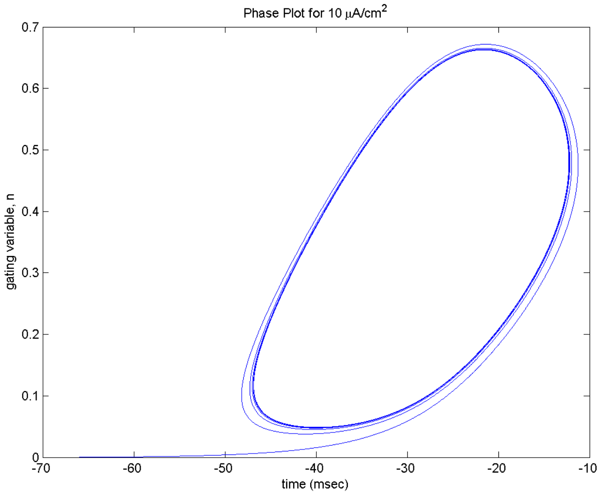

Figure 68: Saddle-node unstable spiral phase plane

Behavior depicted in Figures 67 and 68 is characteristic of a stable limit cycle attractor. Rather than the exponential transition from one stable resting potential to another as shown in Figures 64 and 65 application of an injected current of $10\,\mu\text{A/cm}^2$ causes annihilation of the stable fixed point, resulting in the system trajectory transitioning to the limit cycle attractor.

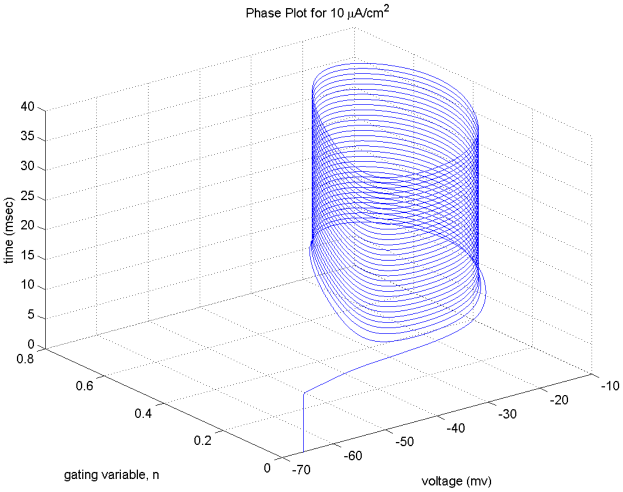

Figure 69: Saddle-node unstable spiral phase plane plus time

Although qualitatively similar to other bifurcation types, notice the higher spike frequency of the saddle-node dynamics.

4.2.3.4 Optimal Control

In Sections 4.2.3.2 and 4.2.3.3, it was demonstrated that qualitatively different system behaviors could be induced when injected currents between $-80\,\mu\mathrm{A/cm}^2$ and $3\,\mu\mathrm{A/cm}^2$, and at or above $10\,\mu\mathrm{A/cm}^2$ are applied to the model neuron. For current values in the range $-80\,\mu\mathrm{A/cm}^2$ to $3\,\mu\mathrm{A/cm}^2$ the system behavior was consistent with classification as a stable node. For values of injected current at or above $10\,\mu\mathrm{A/cm}^2$ a bifurcation of the stable system fixed point occurs and behavior is consistent with classification as an unstable spiral, with characteristic limit cycle attractor, as expected for the saddle-node bifurcation. In this section, optimal input stimuli will be computed for each category of system behavior.

Due to the high spike frequency, the simulation time has been reduced from 40 ms to 20 ms to better depict inter-spike oscillations, or 'characteristic dips', present in the optimal injected current signal.

4.2.3.4.1 Optimal Control of saddle-node Dynamics in the Stable Node Region

Application of injected current $I = 3\,\mu\text{A/cm}^2$ results in system behavior identified as a stable node. Using the membrane voltage generated by a $I = 3\,\mu\text{A/cm}^2$ step input as the reference voltage, the optimal input stimuli is calculated for three different sets of values for P, Q, and R.

The first plot, with $P = Q = 1$ and $R = 10$, represents an emphasis on reduction of input stimuli energy at the expense of membrane voltage tracking accuracy. The third plot, with $P = Q = 1000$ and $R = 1$, represents the opposite end of the spectrum, emphasizing tracking accuracy. The remaining plot, with $P = Q = 100$ and $R = 1$, provides a balance of these two competing objectives.

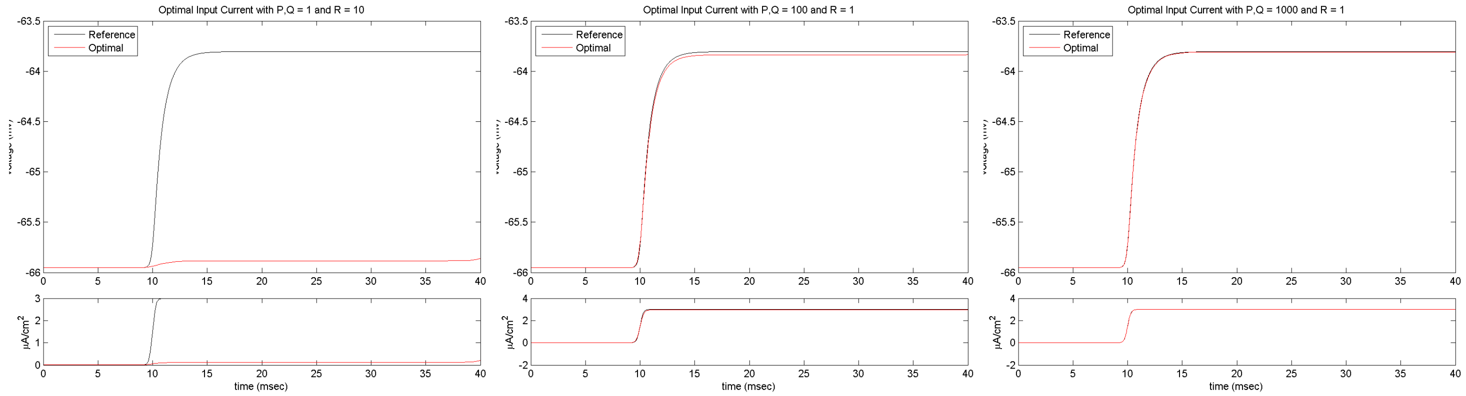

(a) $P = Q = 1,\ R = 10$

(b) $P = Q = 100,\ R = 1$

(c) $P = Q = 1000,\ R = 1$

Figure 70: Optimal control of saddle-node stable node

Figures 70a through 70c demonstrate a typical spectrum for application of the optimal control methodology, with an emphasis on reduced energy of input stimuli with relatively large values or R and improved tracking accuracy for large values of P and Q. Weighting terms of the objective function can be adjusted depending on the control objective.

4.2.3.4.2 Optimal Control of saddle-node Dynamics in the Unstable Spiral Region

Application of injected current $I = 10\,\mu\text{A/cm}^2$ results in system behavior identified as an unstable spiral. The saddle point and stable node fixed points coalesce and the system trajectory approaches a coexistent limit cycle attractor.

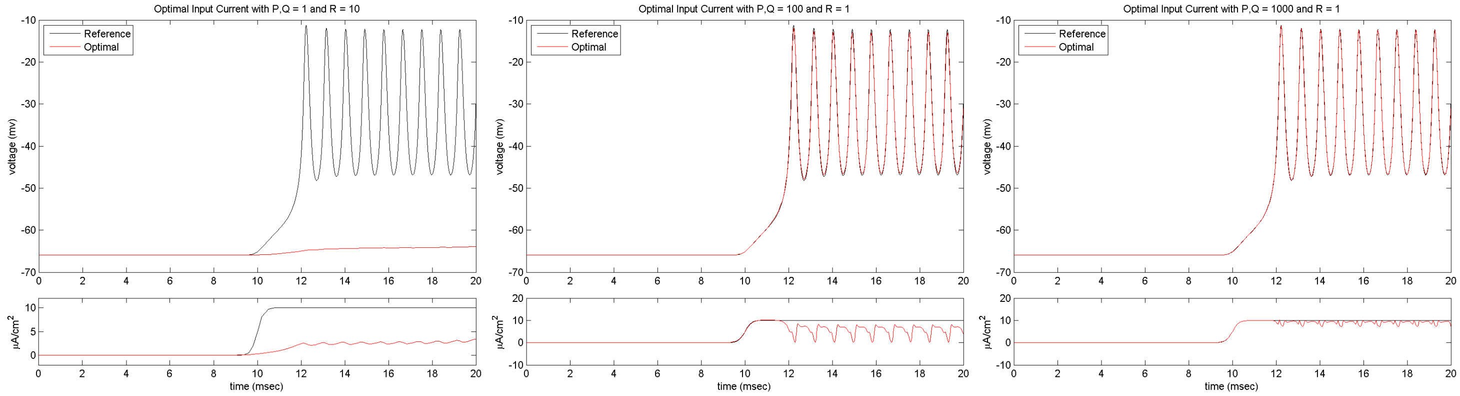

(a) $P = Q = 1,\ R = 10$ (b) $P = Q = 100,\ R = 1$ (c) $P = Q = 1000,\ R = 1$

Figure 71: Optimal control of saddle-node unstable spiral

Optimal inputs produce the expected range of behavior from energy reduction to tracking accuracy. As seen in Figure 71b, when simulations contain repetitive spiking, "characteristic dips" in the optimal input current are often present as emphasis on tracking is reduced [2, 3]. The amplitude of these dips typically decreases, with the optimal current approaching the originally applied current, as emphasis on tracking is further increased.

4.2.3.5 Discussion of saddle-node Bifurcation Dynamics

This section utilized a reduced-order Hodgkin-Huxley model with parameters selected for demonstration of saddle-node bifurcation dynamics [1]. Nonlinear analysis enables categorization of system fixed point behavior for a range of injected current values. It was determined that two classes of behavior, consistent with the saddle-node bifurcation type, could be elicited for ranges of injected input current between $-80\,\mu\text{A/cm}^2$ and $3\,\mu\text{A/cm}^2$ and at or above $10\,\mu\text{A/cm}^2$.

Using injected input currents of $I = 3\,\mu\text{A/cm}^2$ and $I = 10\,\mu\text{A/cm}^2$, stable node and unstable spiral system dynamics were highlighted. The saddle-node bifurcation occurs as a transition between these qualitatively different system behaviors.

Results were presented using time domain and phase plane plots, along with a three-dimensional portrayal of the phase plane to enable inclusion of time in the phase plane. A spectrum of optimal input currents were also computed for both stable node and unstable spiral dynamics.

4.2.4 saddle-node on Invariant Circle

The saddle-node on invariant circle bifurcation type exhibits the same bifurcation characteristics as the saddle-node of Section 4.2.3. Two fixed points, one stable and one unstable, converge and annihilate each other [1, p. 12]. The main difference is that in this case, the two fixed points exist on an invariant circle, which becomes a limit cycle attractor. This is different from the system dynamics of Section 4.2.3 where the limit cycle coexists with the stable fixed point and can thus exhibit bistable behavior.

Since the stable fixed point involved in the saddle-node bifurcation is classified as a node, with purely real eigenvalues, subthreshold oscillations do not occur [1, p. 14].

saddle-node on invariant circle system dynamics, in the context of neural behavior, have a third, unstable fixed point inside the invariant circle [1, p. 13]. Since the stable fixed point exists on the invariant circle, this bifurcation type does not exhibit bistability.

4.2.4.1 Fixed Point Location

Using equations (63) and (64) for the nullclines, and varying the injected stimulus current I from $-80\,\mu\text{A/cm}^2$ to $100\,\mu\text{A/cm}^2$ by increments of $10\,\mu\text{A/cm}^2$, a family of curves is generated in Figure 72. Since the n-nullcline does not change it is represented by a single sigmoidal line on the plot. Each injected current value I produces a different curve for the v-nullcline.

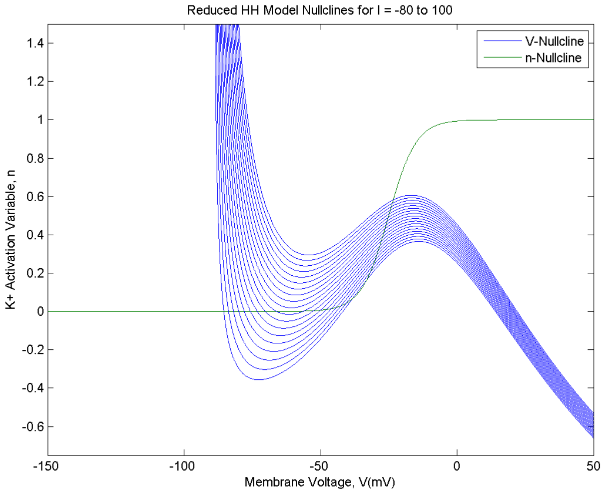

Figure 72: Saddle-node on invariant circle fixed point location using nullclines

Notice that the v-nullcline has a distinct local minimum. For values of injected current where $I \leq 0\,\mu\text{A/cm}^2$, there are three intersections of the nullclines for each trace. At some value of injected current between $I = 0\,\mu\text{A/cm}^2$ and $I = 10\,\mu\text{A/cm}^2$, the two fixed points just below $-50\,\text{mV}$ coalesce. For v-nullclines where the injected current is greater than or equal to $10\,\mu\text{A/cm}^2$, there is one intersection of the nullclines, corresponding to one fixed point, for each injected current value.

Stability of the fixed point cannot be ascertained directly from the figure and requires further analysis per Section 4.2.4.2. For cases where the fixed point is stable, the value of the membrane voltage at the intersection of the nullclines is the resting membrane potential.

4.2.4.2 Graphical Fixed Point Classification

Using the approximate values for v and n from Section 4.2.4.1 as initial conditions, a numerical solution for the system fixed point is computed for each injected current value using $fsolve$. The values for the state variables are substituted into the Jacobian, allowing computation of eigenvalues according to equations (66) through (70).

After computing eigenvalues for the linearized system for each injected current level, the trace (τ) and determinant (Δ) are computed according to equations (83) and (84). These two values allow classification of each fixed point as shown in Figure 73. Three sets of points are plotted on the bifurcation diagram, one for each fixed point. Each data point on the diagram represents the classification of a given fixed point for a single injected current value. Each point containing an asterisk indicates zero injected current.

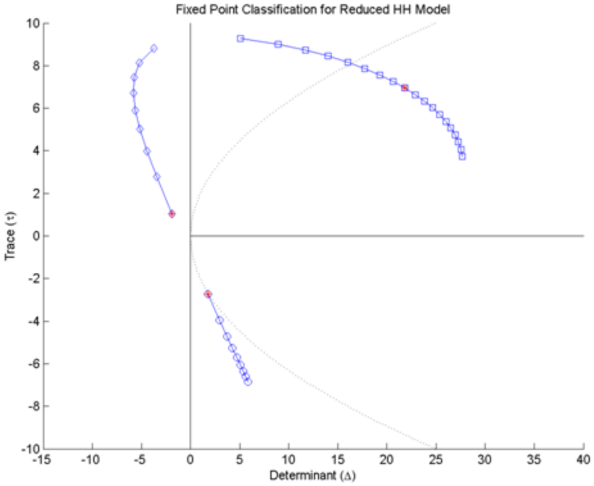

Figure 73: Graphical classification of reduced-order Hodgkin-Huxley saddle-node on invariant circle system fixed point

Since the fixed point classified as a saddle point coalesces with the fixed point classified as a stable node, the traces for these fixed points does not exist for injected current values above $0\,\mu\text{A/cm}^2$. For the range of injected current values shown, $-80\,\mu\text{A/cm}^2$ to $0\,\mu\text{A/cm}^2$, one fixed point is classified as a stable node and the second fixed point is classified as a saddle point.

The third fixed point is classified as an unstable node for injected current values from $-80\,\mu\text{A/cm}^2$ to $-40\,\mu\text{A/cm}^2$. A bifurcation of this fixed point occurs between $-40\,\mu\text{A/cm}^2$ and $-50\,\mu\text{A/cm}^2$. For all injected current values considered where $I \geq -50\,\mu\text{A/cm}^2$, the fixed point is classified as an unstable spiral. Since all injected current values chosen for analysis are greater than $-50\,\mu\text{A/cm}^2$, this bifurcation will not be considered as a part of the neural dynamics.

Information regarding stability of the fixed point can be added to each intersection of the nullclines as shown in Figure 74. Filled dots indicate a stable fixed point and open dots indicate an unstable fixed point for each injected current level.

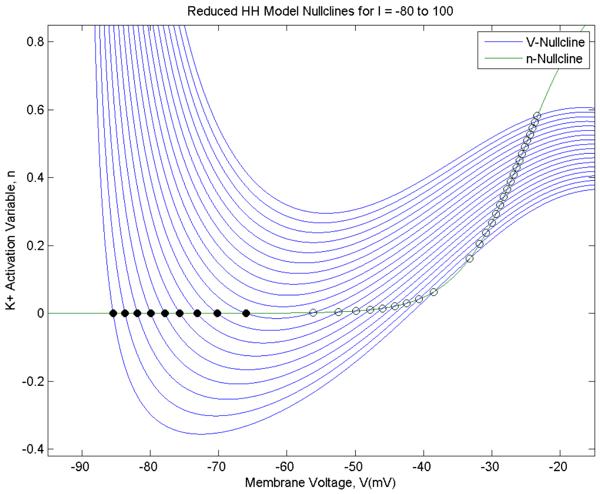

Figure 74: Saddle-node on invariant circle fixed point location and stability with nullclines

4.2.4.3 Bifurcations

Figure 73 reveals that for injected current levels between $-80\,\mu\text{A/cm}^2$ and $0\,\mu\text{A/cm}^2$, classification of saddle point and stable node fixed points is robust to the major regions of the classification diagram. Additionally, the fixed point classified as an unstable spiral does not undergo a bifurcation for injected currents above $-50\,\mu\text{A/cm}^2$.

As described in Chapter 3, when considering the major regions of Figure 73, no additional analysis is required to verify the linearized system is topologically equivalent to the original nonlinear system. Furthermore, if all eigenvalues are non-zero, with non-zero real parts, the linearized system is topologically equivalent to the nonlinear system.

For consistency with analysis of other bifurcation types, it is desirable to determine two positive injected current values, one below and one above the bifurcation of interest. Since the bifurcation of interest occurs between $0\,\mu\text{A/cm}^2$ and $10\,\mu\text{A/cm}^2$, further investigation is required to determine a positive injected current value below the bifurcation current. As shown in Figure 75, an injected current value of $3\,\mu\text{A/cm}^2$ satisfies this criteria.

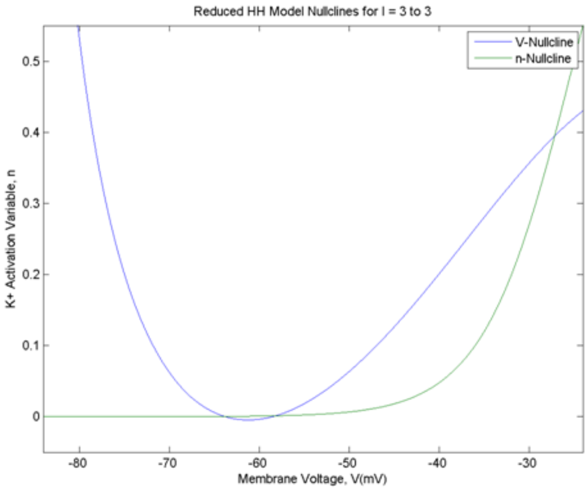

Figure 75: Saddle-node on invariant circle nullclines plot, $I = 3\,\mu\text{A/cm}^2$

Injected current values of $3\,\mu\text{A/cm}^2$ and $10\,\mu\text{A/cm}^2$ have been selected to demonstrate system dynamics for injected current levels above and below the saddle-node bifurcation.

4.2.4.3.1 saddle-node on Invariant Circle Dynamics in the Stable Node Region

Injected currents in the form of step inputs are used to investigate qualitatively different system dynamics. In each case, the length of the simulation is 40 ms. The neuron model is initially quiescent at the resting membrane potential, followed by application of a step input at 10 ms.

Initial conditions for membrane voltage (v) and gating variable (n) were chosen by running a simulation with zero injected current, allowing any transients in the state variables to decay. This ensures a quiescent response prior to application of the step input. With the neuron model parameterized for the saddle-node on invariant circle bifurcation type, initial conditions are $v_0 \approx -65.9529\,\mathrm{mV}$ and $n_0 \approx 0.00027$.

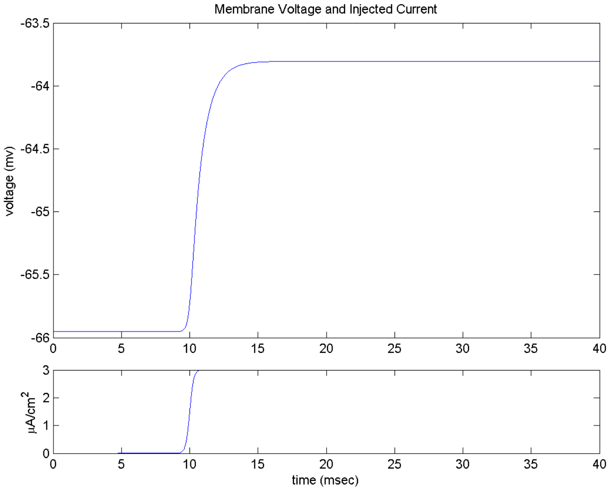

Figure 76: Saddle-node on invariant circle time domain plot

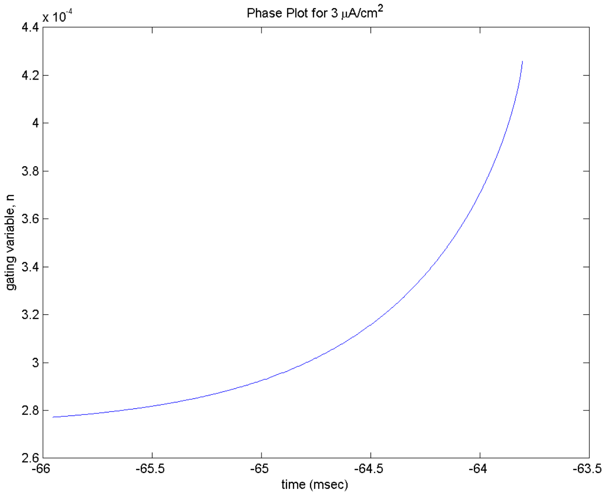

Figure 77: Saddle-node on invariant circle phase plane

Figures 76 and 77 exhibit a change from one resting potential to another without oscillation, consistent with expected behavior of a stable node. Figure 78 includes time as the vertical axis of the phase plane.

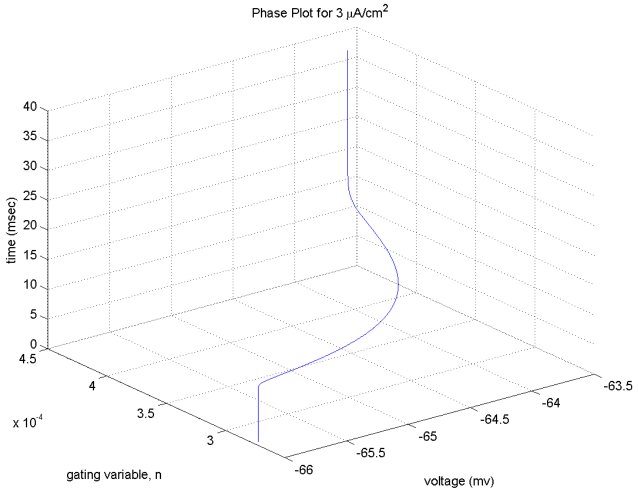

Figure 78: Saddle-node on invariant circle phase plane plus time

The first 10 ms of the simulation are a purely vertical line, depicted in Figure 77 as a single point in the phase plane. The state of the model transitions from one stable point to another by an exponential, without overshoot in both the time and phase plane, which agrees with the time domain plot of Figure 76 and the expected behavior for a stable node.

4.2.4.3.2 saddle-node on Invariant Circle Dynamics in the Unstable Spiral Region

For injected current values at or above $I \approx 10\,\mu\text{A/cm}^2$, it is expected that the unstable saddle point and stable node coalesce, at which point the invariant circle becomes a stable limit cycle attractor [1].

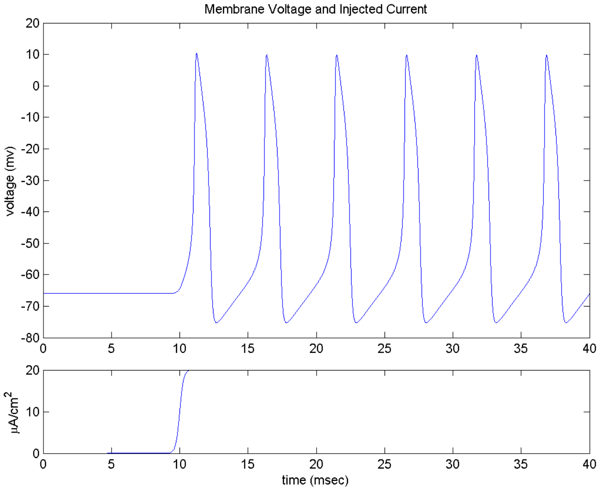

Figure 79: Saddle-node on invariant circle time domain plot

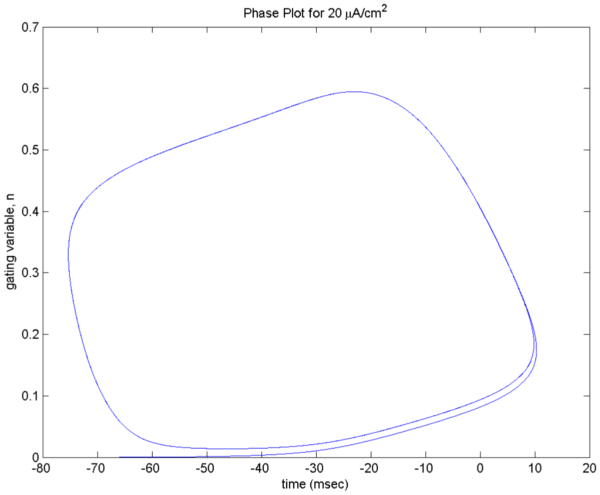

Figure 80: Saddle-node on invariant circle phase plane

Behavior depicted in Figures 79 and 80 is characteristic of a stable limit cycle attractor. Rather than the exponential transition from one stable resting potential to another as shown in Figures 76 and 77, application of an injected current of $10\,\mu\mathrm{A/cm}^2$ causes annihilation of the stable fixed point, resulting in repetitively spiking behavior after the invariant circle becomes a limit cycle attractor.

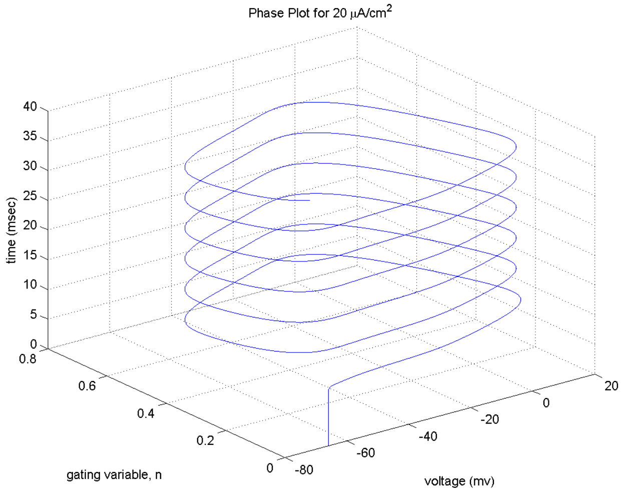

Figure 81: Saddle-node on invariant circle phase plane plus time

4.2.4.4 Optimal Control

In Sections 4.2.4.2 and 4.2.4.3, it was demonstrated that qualitatively different system behaviors could be induced when injected currents between $-50\,\mu\text{A/cm}^2$ and $3\,\mu\text{A/cm}^2$ and at or above $10\,\mu\text{A/cm}^2$ are applied to the model neuron. For current values in the range $-50\,\mu\text{A/cm}^2$ to $3\,\mu\text{A/cm}^2$, the system behavior was consistent with classification as a stable node. For values of injected current at or above $10\,\mu\text{A/cm}^2$, a bifurcation of the stable system fixed point occurs and behavior is consistent with classification as an unstable spiral, with characteristic limit cycle attractor, as expected for the saddle-node on invariant circle bifurcation. In this section, optimal input stimuli will be computed for each category of system behavior.

4.2.4.4.1 Optimal Control of saddle-node on Invariant Circle Dynamics in the Stable Node Region

Application of injected current $I = 3\,\mu\text{A/cm}^2$ results in system behavior identified as a stable node. Using the membrane voltage generated by a $I = 3\,\mu\text{A/cm}^2$ step input as the reference voltage, the optimal input stimuli is calculated for three different sets of values for

P, Q, and R.

The first plot, with $P = Q = 1$, and $R = 10$, represents an emphasis on reduction of input stimuli energy at the expense of membrane voltage tracking accuracy. The third plot, with $P = Q = 1000$, and $R = 1$, represents the opposite end of the spectrum, emphasizing tracking accuracy. The remaining plot, with $P = Q = 100$ and $R = 1$, provides a balance of these two competing objectives.

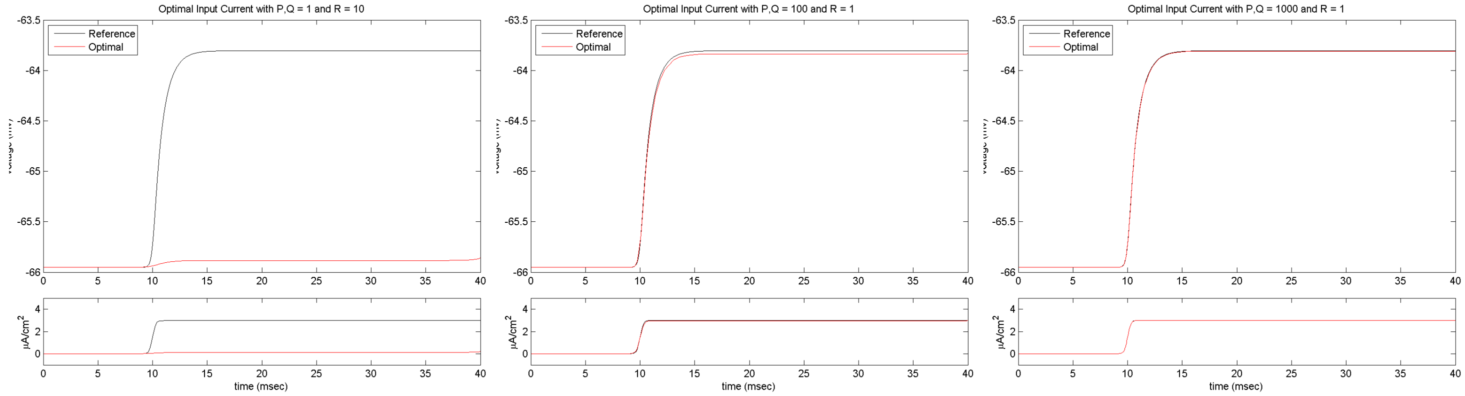

(a) $P = Q = 1,\ R = 10$

(b) $P = Q = 100,\ R = 1$

(c) $P = Q = 1000,\ R = 1$

Figure 82: Optimal control of saddle-node on invariant circle stable node

Figures 82a through 82c demonstrate a typical spectrum for application of the optimal control methodology, with an emphasis on reduced energy of input stimuli with relatively large values or R and improved tracking accuracy for large values of P and Q. Weighting terms of the objective function can be adjusted depending on the control objective.

4.2.4.4.2 Optimal Control of saddle-node on Invariant Circle Dynamics in the Unstable Spiral Region

Application of injected current $I = 20\,\mu\text{A/cm}^2$, results in system behavior identified as an unstable spiral. The saddle point and stable node fixed points coalesce and the invariant circle becomes a limit cycle attractor.

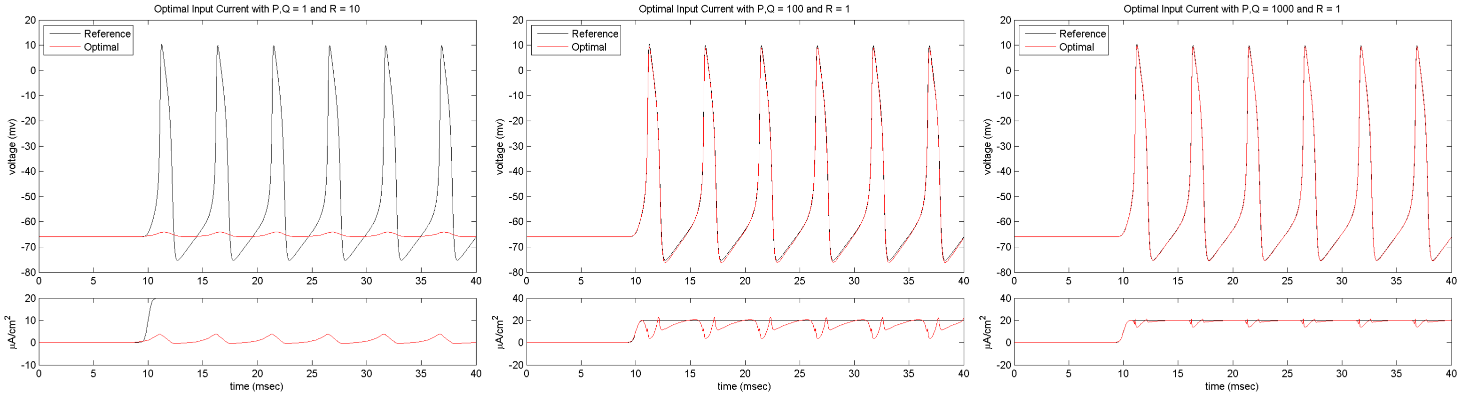

(a) $P = Q = 1,\ R = 10$ (b) $P = Q = 100,\ R = 1$ (c) $P = Q = 1000,\ R = 1$

Figure 83: Optimal control of saddle-node on invariant circle unstable spiral

Optimal inputs produce the expected range of behavior from energy reduction to tracking accuracy. As seen in Figure 83b, when simulations contain repetitive spiking, "characteristic dips" in the optimal input current are often present as emphasis on tracking is reduced [2, 3]. The amplitude of these dips typically decreases, with the optimal current approaching the originally applied current, as emphasis on tracking is further increased.

4.2.4.5 Discussion of saddle-node on Invariant Circle Bifurcation Dynamics

This section utilized a reduced-order Hodgkin-Huxley model with parameters selected for demonstration of saddle-node on invariant circle bifurcation dynamics [1, p. 17]. Nonlinear analysis enables categorization of system fixed point behavior for a range of injected current values. It was determined that two classes of behavior, consistent with the saddle-node on invariant circle bifurcation type, could be elicited for ranges of injected input current between $-50\,\mu\text{A/cm}^2$ and $3\,\mu\text{A/cm}^2$ and at or above $10\,\mu\text{A/cm}^2$.

Using injected input currents of $I = 3\,\mu\text{A/cm}^2$ and $I = 20\,\mu\text{A/cm}^2$, stable node and unstable spiral system dynamics were highlighted. The saddle-node on invariant circle bifurcation occurs as a transition between these qualitatively different system behaviors.

Results were presented using time domain and phase plane plots, along with a three-dimensional portrayal of the phase plane to enable inclusion of time in the phase plane. A spectrum of optimal input currents were also computed for both stable node and unstable spiral dynamics.

5 Classical Hodgkin-Huxley Model

This chapter applies the nonlinear analysis and optimal control techniques depicted in Chapter 3, Figure 12 to the classical Hodgkin-Huxley neuron model defined in Section 2.2.

Since it is a fourth-order model, the function $f(v)$ will be used to locate system fixed points and eigenvalues will be used to classify stability. This is in contrast to the second-order model of Chapter 4, where nullclines were used to locate the fixed point and the graphical classifier was used to describe fixed point stability and localized behavior.

Section 5.1 defines the neuron model, provides derivation of $f(v)$, and defines the Hamiltonian with associated state and co-state equations. Section 5.2 demonstrates nonlinear analysis and optimal control of the classical Hodgkin-Huxley model, along with case studies that highlight dynamics specific to the model.

5.1 Model Definition

Following Chapter 3, Figure 12, this section corresponds to the first row of the figure, definition of the conductance-based neuron model. This includes definition of the classical Hodgkin-Huxley model and all symbolic equations required for nonlinear analysis and optimal control techniques.

5.1.1 Classical Hodgkin-Huxley Model Definition

The classical Hodgkin-Huxley model has the same ionic currents as the reduced-order model of Chapter 4. Like the reduced-order model, the classical Hodgkin-Huxley model consists of persistent potassium current, transient sodium current, ohmic leak current, injected stimulus current, and cellular membrane capacitance. The difference between the reduced-order and classical model is the means by which sodium channel activation is modeled. In the classical model, two state variables are dedicated to activation and inactivation of sodium channel conductance. The reduced model approximates this behavior with an instantaneous voltage dependent activation function $m_\infty(v)$.

Presented as Figure 5 in Chapter 2, an equivalent circuit for the neuron model is reproduced here for completeness.

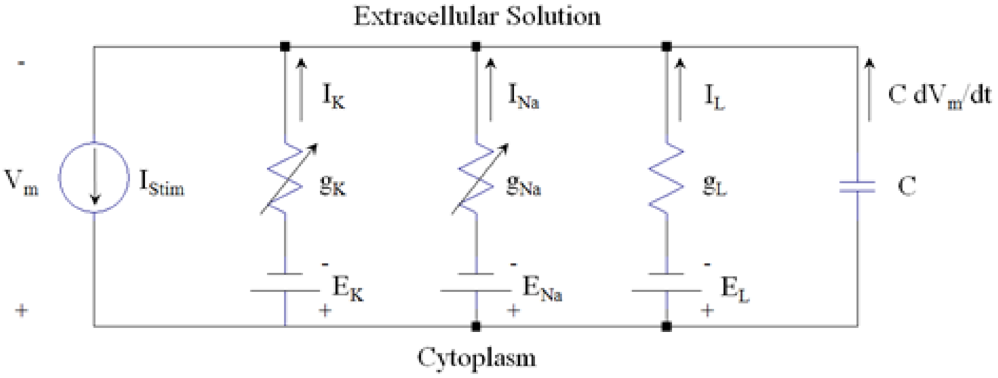

Figure 84: Equivalent circuit of the classical Hodgkin-Huxley neuron model

Differential equations for the classical Hodgkin-Huxley model are

$$C\dot{V} = I_{Stim} - g_K n^4(V_m - E_K) - g_{Na}m^3h(V_m - E_Na) - g_L(V_m - E_L), \tag{86}$$

$$\dot{n} = \alpha_n(V)(1-n) - \beta_n(V)n, \tag{87}$$

$$\dot{m} = \alpha_m(V)(1-m) - \beta_m(V)m, \text{ and} \tag{88}$$

$$\dot{h} = \alpha_h(V)(1-h) - \beta_h(V)h, \tag{89}$$

with ancillary functions defined in Section 2.2.2 [1, p. 37][38].

Modulation of potassium and sodium conductance values is achieved using gating variables n, m, and h. Parameters were chosen to reproduce the classical Hodgkin-Huxley model [1, p. 37]. Parameters chosen in [4] produce qualitatively similar behavior over the region of interest. Parameter values are provided in Table 5.

The injected current stimulus I is varied to demonstrate bifurcations in system dynamics.

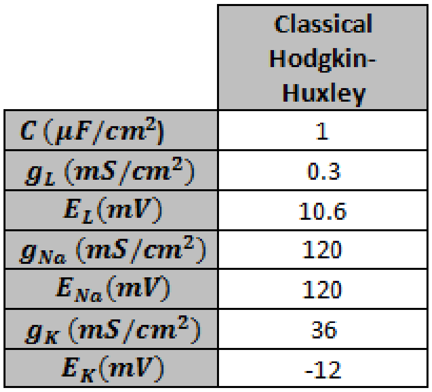

	Classical Hodgkin-Huxley
$C\ (\mu F/cm^2)$	1
$g_L\ (mS/cm^2)$	0.3
$E_L (mV)$	10.6
$g_{Na}\ (mS/cm^2)$	120
$E_{Na} (mV)$	120
$g_K\ (mS/cm^2)$	36
$E_K (mV)$	-12

Table 5: Classical Hodgkin-Huxley model parameters [1, p. 37]

5.1.2 Derivation of $f(v)$

The form of equations (86) through (89) make it possible to derive a single function, $f(v)$, the roots of which are system fixed points. The function $f(v)$ is obtained by setting equations (87) through (89) equal to 0 and solving for the associated gating variable. The result is substituted into equation (86) yielding

$$f(v) = \frac{1}{C}(I - g_K n_\infty(v)^4(V - E_K) - g_{Na} m_\infty(v)^3 h_\infty(v)(V - E_{Na}) - g_L(V - E_L)) \quad (90)$$

with $n_\infty(v)$, $m_\infty(v)$, and $h_\infty(v)$ representing steady state values for each gating variable as described by equations (32). The function $f(v)$ will be plotted for each injected current value, with the roots of the function indicating the location of the system fixed point.

Once the membrane voltage of the system fixed point is found using $f(v)$ the value for v can be back substituted into $n_\infty(v)$, $m_\infty(v)$, and $h_\infty(v)$. This yields the value for all state variables at the system fixed point.

5.1.3 System Linearization

Once the number and location of system fixed points has been determined, they can be classified according to their localized behavior. Classification of system fixed points proceeds as described in Section 3.1.2, beginning with linearization of the phase plane using the system Jacobian [Str].

For the classical Hodgkin-Huxley model the Jacobian is

$$\begin{bmatrix} \dot{V} \\ \dot{n} \\ \dot{m} \\ \dot{h} \end{bmatrix} = \begin{bmatrix} \frac{\partial f_1}{\partial V} & \frac{\partial f_1}{\partial n} & \frac{\partial f_1}{\partial m} & \frac{\partial f_1}{\partial h} \\ \frac{\partial f_2}{\partial V} & \frac{\partial f_2}{\partial n} & \frac{\partial f_2}{\partial m} & \frac{\partial f_2}{\partial h} \\ \frac{\partial f_3}{\partial V} & \frac{\partial f_3}{\partial n} & \frac{\partial f_3}{\partial m} & \frac{\partial f_3}{\partial h} \\ \frac{\partial f_4}{\partial V} & \frac{\partial f_4}{\partial n} & \frac{\partial f_4}{\partial m} & \frac{\partial f_4}{\partial h} \end{bmatrix} \begin{bmatrix} V \\ n \\ m \\ h \end{bmatrix} \tag{91}$$

where for $\dot{V} = f_1()$, $\dot{n} = f_2()$, $\dot{m} = f_3()$, and $\dot{h} = f_4()$.

As described in Section 3.1.2.2, classification of behavior in the immediate vicinity of system fixed points is described based on the location of eigenvalues of the Jacobian.

Values from Table 5 for the model parameters, the injected current value, and the location of the system fixed point are substituted into the Jacobian, allowing computation of eigenvalues. The eigenvalues for each injected current value are plotted on the complex plane to predict localized system behavior.

5.1.4 Objective Function Definition

The objective function, previously published in [2], is

$$J[i(t)] = \frac{P}{2}(v(T) - r(T))^2 + \frac{Q}{2}\int_0^T (v(t) - r(t))^2 dt + \frac{R}{2}\int_0^T (i(t))^2 dt. \tag{92}$$

A user prescribed balance between tracking error and minimization of ‘energy’ is used in the computation of the optimal input current $i^*(t)$. Making P and Q large with respect to R penalizes differences between the chosen reference signal $r(t)$ and the computed membrane voltage $v(t)$, resulting in a solution which emphasizes tracking accuracy. Conversely, a large value for R, in comparison to P and Q, emphasizes a solution which seeks to minimize the ‘energy’ content of $i^*(t)$, likely at the expense of reduced agreement between reference and membrane potential signals.

The Hamilton associated with equation (92) is

$$\begin{aligned} H(v,n,m,h,\lambda_1,\lambda_2,\lambda_3,\lambda_4) &= \frac{Q}{2}(v(t)-r(t))^2 + \frac{R}{2}(i(t))^2 \\ &+ \frac{\lambda_1(t)}{C}(i(t) - g_K n(t)^4(v(t)-E_K) - g_{Na}m(t)^3h(t)(v(t)-E_{Na}) - g_L(v(t)-E_L)) \\ &+ \frac{\lambda_2(t)}{\tau_n}(n_\infty(v)-n(t)) + \frac{\lambda_3(t)}{\tau_m}(m_\infty(v)-m(t)) \\ &+ \frac{\lambda_4(t)}{\tau_h}(h_\infty(v)-h(t)) \end{aligned} \tag{93}$$

where λ_1, λ_2, λ_3 and λ_4 are the co-state variables. Following [46, p. 134], the “Continuous Nonlinear Optimal Controller with Function of Final State Fixed” yields

$$\begin{aligned} \dot{v} &= \frac{\partial H}{\partial \lambda_1} \\ &= \frac{1}{C}[i(t) - g_K n(t)^4(v(t)-E_K) - g_{Na}m(t)^3h(t)(v(t)-E_{Na}) - g_L(v(t)-E_L)] \end{aligned} \tag{94}$$

$$\dot{n} = \frac{\partial H}{\partial \lambda_2} = \frac{1}{\tau_n}[n_\infty(v) - n(t)] \tag{95}$$

$$\dot{m} = \frac{\partial H}{\partial \lambda_3} = \frac{1}{\tau_m}[m_\infty(v) - m(t)] \tag{96}$$

$$\dot{h} = \frac{\partial H}{\partial \lambda_4} = \frac{1}{\tau_h}[h_\infty(v) - h(t)] \tag{97}$$

$$\begin{aligned} \dot{\lambda}_1 = -\frac{\partial H}{\partial v} &= -Q(v(t)-r(t)) \\ &+ \frac{\lambda_1(t)}{C}(g_K n(v)^4 + g_{Na}m(v)^3h(v) + g_L) \\ &- \lambda_2(t)(\frac{\partial \alpha_n(v)}{\partial v}(1-n) - \frac{\partial \beta_n(v)}{\partial v}(n)) \\ &- \lambda_3(t)(\frac{\partial \alpha_m(v)}{\partial v}(1-m) - \frac{\partial \beta_m(v)}{\partial v}(m)) \\ &- \lambda_4(t)(\frac{\partial \alpha_h(v)}{\partial v}(1-h) - \frac{\partial \beta_h(v)}{\partial v}(h)) \end{aligned} \tag{98}$$

$$\dot{\lambda}_2 = -\frac{\partial H}{\partial n} = \frac{\lambda_1(t)}{C}(4g_K n(v)^3)(v(t) - E_K) + \lambda_2(t)(\alpha_n(v) + \beta_n(v)) \tag{99}$$

$$\dot{\lambda}_3 = -\frac{\partial H}{\partial m} = \frac{\lambda_1(t)}{C}(3g_{Na} m(v)^2 h(v))(v(t) - E_{Na}) + \lambda_3(t)(\alpha_m(v) + \beta_m(v)) \tag{100}$$

$$\dot{\lambda}_4 = -\frac{\partial H}{\partial h} = \frac{\lambda_1(t)}{C}(3g_{Na} m(v)^3)(v(t) - E_{Na}) + \lambda_4(t)(\alpha_h(v) + \beta_h(v)) \tag{101}$$

with boundary conditions

$$v(0) = v_0 \tag{102}$$

$$n(0) = n_0 \tag{103}$$

$$m(0) = m_0 \tag{104}$$

$$h(0) = h_0 \tag{105}$$

$$\lambda_1(T) = P(v(T) - r(T)) \tag{106}$$

$$\lambda_2(T) = 0 \tag{107}$$

$$\lambda_3(T) = 0 \tag{108}$$

$$\lambda_4(T) = 0 \tag{109}$$

The input stimulus current $i(t)$ can be removed by substitution using the stationarity condition,

$$\frac{\partial H}{\partial i} = Ri(t) + \frac{\lambda_1(t)}{C} = 0, \tag{110}$$

and solving for $i(t)$ yields

$$i(t) = -\frac{1}{RC}\lambda_1(t). \tag{111}$$

Typically a numerical solution to the two-point boundary value problem is computed using the MATLAB$^{®}$routine *bvp4c*, yielding $i^*(t)$ for each choice of injected current stimulus and objective function constants P, Q, and R.

5.2 Nonlinear Analysis and Optimal Control

Sections 5.2.1 through 5.2.4 examine system dynamics using nonlinear analysis and optimal control techniques presented in Chapter 3. Since the classical Hodgkin-Huxley model is a fourth-order system, techniques presented for higher-order models will be used. Specifically, fixed point locations will be computed using a derived function $f(v)$ and localized behavior will be classified according to the eigenvalues of the linearized system in the immediate vicinity of system fixed points.

5.2.1 Fixed Point Location Using $f(v)$

Using equation (90) for $f(v)$, the injected stimulus current I is varied from $2\,\mu\text{A/cm}^2$ to $15\,\mu\text{A/cm}^2$. Plotting $f(v)$ for each value of I generates the family of curves plotted in Figure 85. A fixed point of the system is indicated by each location where $f(v) = 0$.

Since each curve for $f(v)$ has a single root, the system has a single fixed point for all considered values of I. Furthermore, since $f(v)$ is monotonic and the injected current translates the curve vertically, it is observable from Figure 85 that the system will have a single fixed point for all injected current values.

An approximate value for the membrane voltage of the system fixed point is directly observable in Figure 85, and can be computed using $fsolve$ to find the root of $f(v)$ for each injected current value. The value computed for v is then back-substituted into $n_\infty(v)$, $m_\infty(v)$, and $h_\infty(v)$ to find the values of the remaining state variables at the system fixed point.

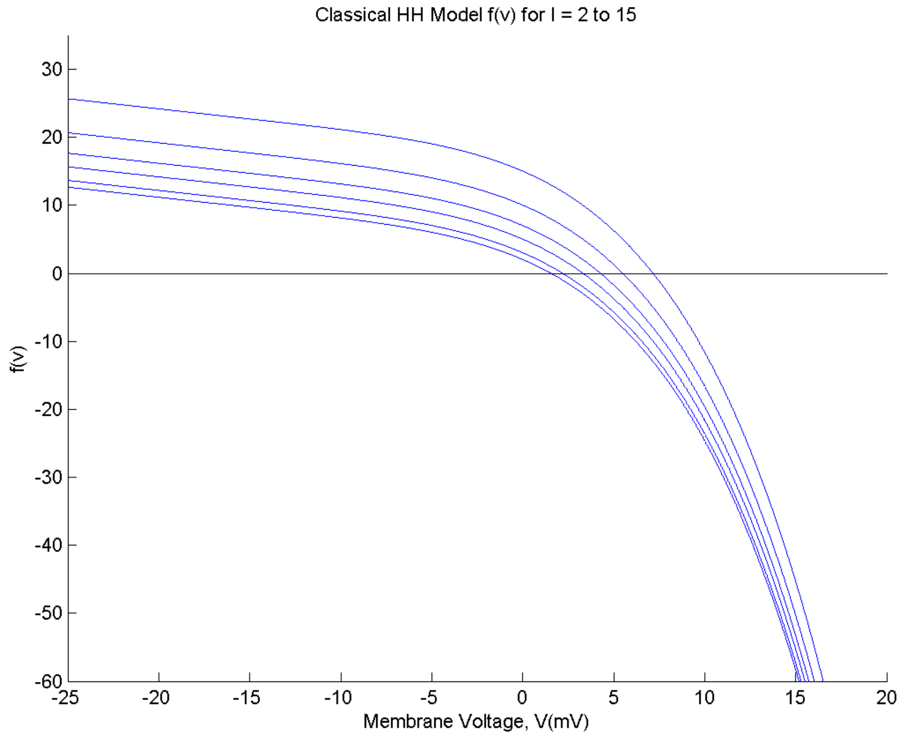

Figure 85: Classical Hodgkin-Huxley fixed point location using derived function $f(v)$

Stability of the fixed point cannot be ascertained directly from the figure and requires further analysis per Section 5.2.2.

5.2.2 Fixed Point Classification Using Eigenvalues

Within this section, fixed points will be classified according to eigenvalues of the linearized system. Qualitative information from Section 5.2.1 greatly informs the process of fixed point classification as it provides insight as to the number and approximate location of system fixed points for any given injected current level.

Using $fsolve$, the numerical solution for the location of the fixed point is computed. The values for the state variables, in this case v, n, m, and h, are substituted into the Jacobian, allowing computation of eigenvalues according to equation (91).

When classifying system fixed points via linearization, it is necessary to verify the linear system, with neglected higher-order terms, faithfully represents the original nonlinear system. See Section 3.1.2.1 for further details.

Analysis of the classical Hodgkin-Huxley model proceeds with calculation of eigenvalues for the linearized system for each injected current value used to generate the family of curves in Section 5.2.1.

Each eigenvalue is plotted directly on the complex plane for each injected current value from $2\,\mu\mathrm{A/cm}^2$ to $15\,\mu\mathrm{A/cm}^2$. The chosen injected current values are $I = 2, 3, 5, 7$, and $15\,\mu\mathrm{A/cm}^2$. The data point indicated with an asterisk denotes an injected current of $2\,\mu\mathrm{A/cm}^2$.

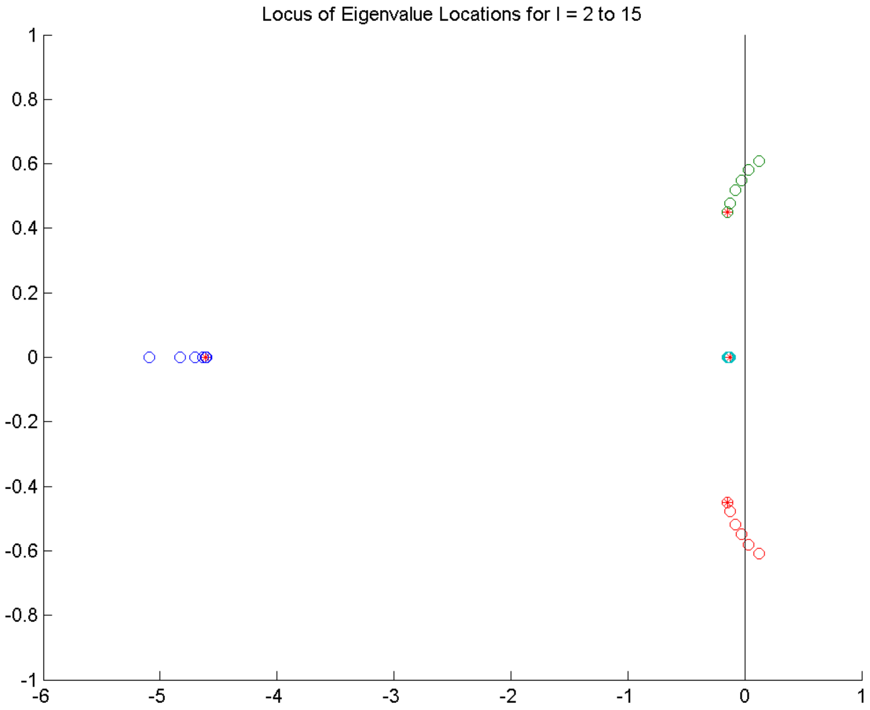

Figure 86: Classification of classical Hodgkin-Huxley model fixed points using eigenvalues

Figure 86 shows that for all selected injected current values, there are two eigenvalues on the real axis and a pair of complex conjugate eigenvalues. For some injected current value between $5\,\mu\text{A/cm}^2$ and $7\,\mu\text{A/cm}^2$, the system fixed point becomes unstable based on movement into the right hand plane by the complex conjugate pair of eigenvalues, indicating a bifurcation of the system fixed point.

Information gained about the stability of the fixed point for each injected current value can now be incorporated into Figure 85 from Section 5.2.1. Fixed point stability will be indicated on the plot of $f(v)$ by filled and open dots where the fixed point is stable and unstable, respectively.

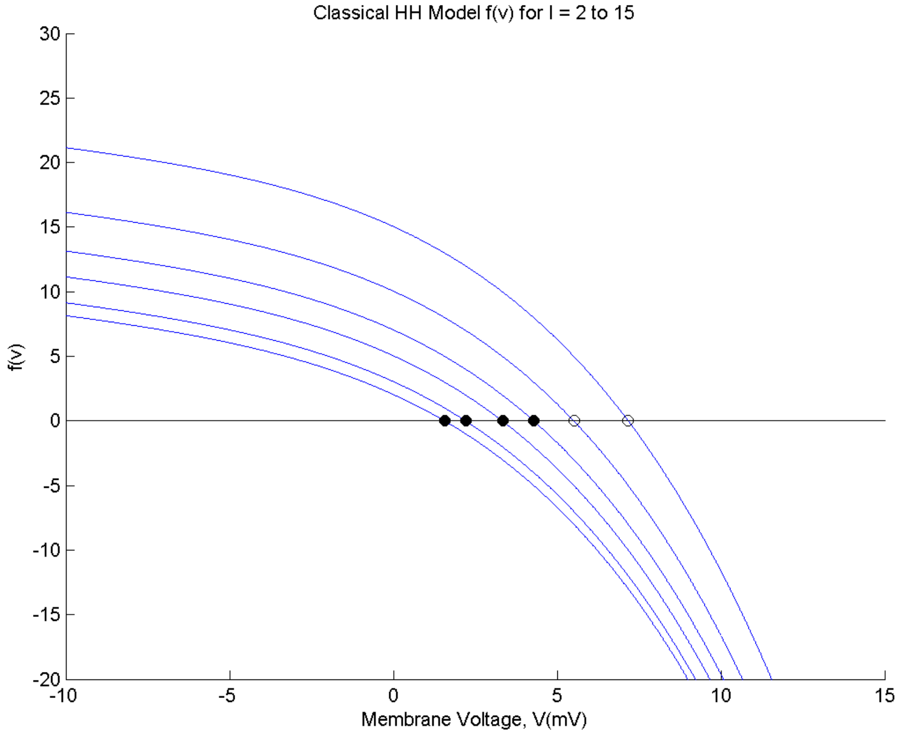

Figure 87: Classical Hodgkin-Huxley fixed point location and stability with derived function $f(v)$

5.2.3 Bifurcations

Information from Section 5.2.2 provides insight into the injected current levels for which qualitatively different system behaviors occur, especially related to the number and stability of system fixed points. However, bifurcation dynamics can exist, especially in higher-order nonlinear systems, which are not related to changes in the stability and number of system fixed points.

The classical Hodgkin-Huxley model is known to exhibit the inactive, single spike, and repetitive spiking behavior depending on the applied input stimulus [52]. When model parameters are set according to Table 6 it was found in [52, 4] that the transition to repetitive spiking occurs when $I \approx 6.44\,\mu\mathrm{A/cm}^2$ and the system fixed point loses stability when the stimulus current is further increased.

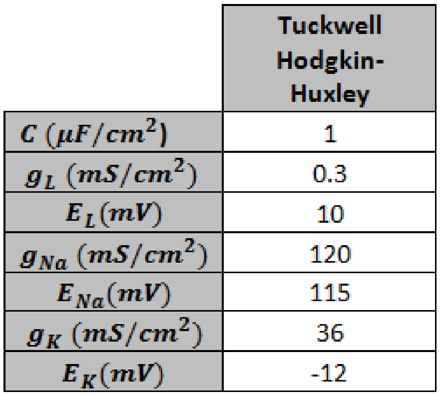

	Tuckwell Hodgkin-Huxley
$C\ (\mu F/cm^2)$	1
$g_L\ (mS/cm^2)$	0.3
$E_L (mV)$	10
$g_{Na}\ (mS/cm^2)$	120
$E_{Na} (mV)$	115
$g_K\ (mS/cm^2)$	36
$E_K (mV)$	-12

Table 6: Classical Hodgkin-Huxley model parameters [4]

The bifurcation dynamics published in [4] have been qualitatively verified with the classical Hodgkin-Huxley parameters shown in Table 5, and in this section, system dynamics will be illustrated using time domain plots for each injected current level.

Injected currents in the form of step inputs are used to investigate qualitatively different system dynamics. In each case the length of the simulation is 80 ms. The neuron model is initially quiescent at the resting membrane potential, followed by application of a step input at 15 ms.

Initial conditions for membrane voltage, v and gating variables n, m, and h were chosen by running a simulation with zero injected current, allowing any transients in the state variables to decay. This ensures a quiescent response prior to application of the step input. With the neuron model parameterized according to 5 initial conditions are $v_0 \approx 0.04626\,\mathrm{mV}$,

$n_0 \approx 0.3184$, $m_0 \approx 0.0532$, and $h_0 \approx 0.5944$.

Injected current values of $I = 2, 3, 5, 7$, and $15\,\mu\text{A/cm}^2$ were chosen to exemplify the qualitatively different behaviors of the model neuron.

5.2.3.1 Dynamics in the Inactive Region

When a step current of $I = 2\,\mu\text{A/cm}^2$ is applied, the model neuron remains inactive, exhibiting subthreshold oscillations.

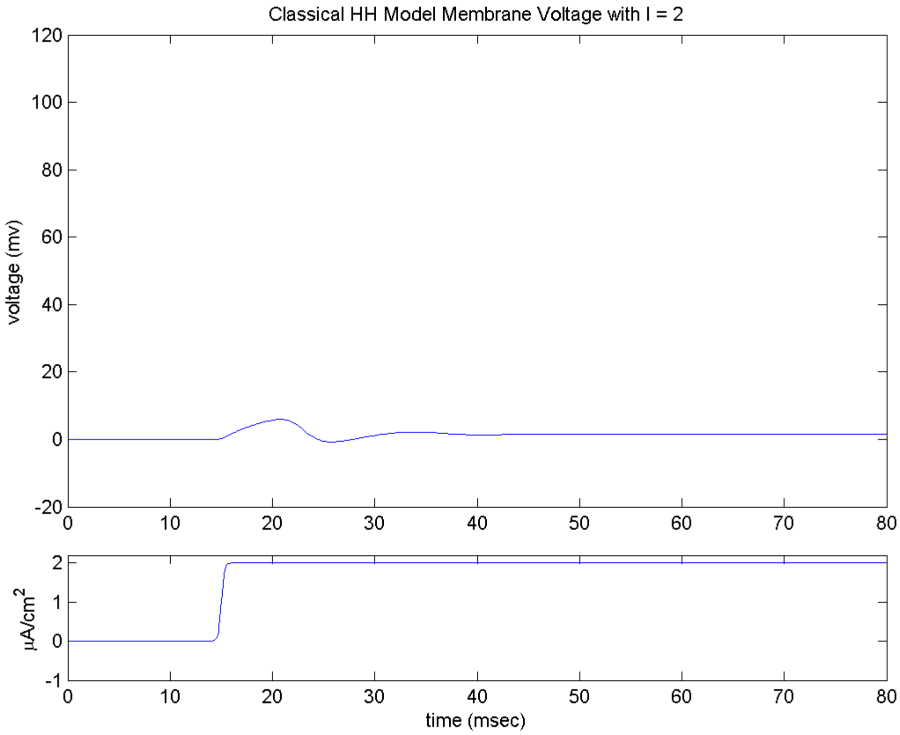

Figure 88: Classical Hodgkin-Huxley model, inactive response, $I = 2\,\mu\text{A/cm}^2$

The time domain plot, showing both injected current and membrane voltage response, is a plot representative of what could be measured experimentally. Additional traces can be added to this plot, including current contributions for each ion accounted for by the model, any gating variables, and time dependent ionic conductance values. Some of these traces are accessible experimentally, which can aid in verification of modeled neuron dynamics.

5.2.3.2 Dynamics in the Single Spike Region

Application of an injected current of $I = 3\,\mu\text{A/cm}^2$ results in a single action potential. Increasing the injected current to $I = 5\,\mu\text{A/cm}^2$ does not qualitatively change the response of the model neuron, but subthreshold oscillations following the action potential become pronounced.

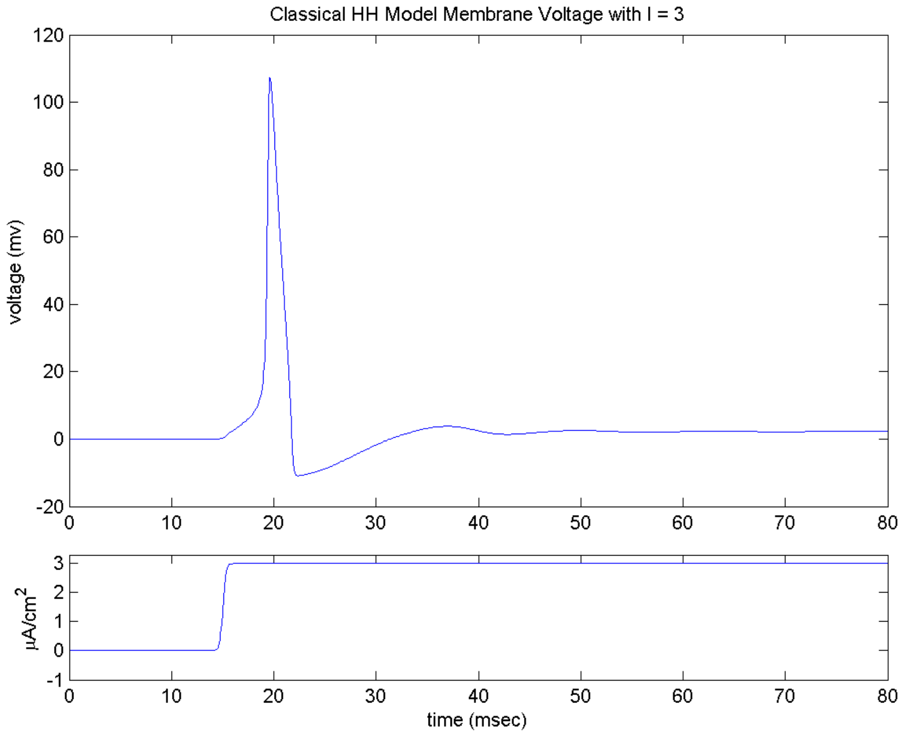

Figure 89: Classical Hodgkin-Huxley model, single spike response, $I = 3\,\mu\text{A/cm}^2$

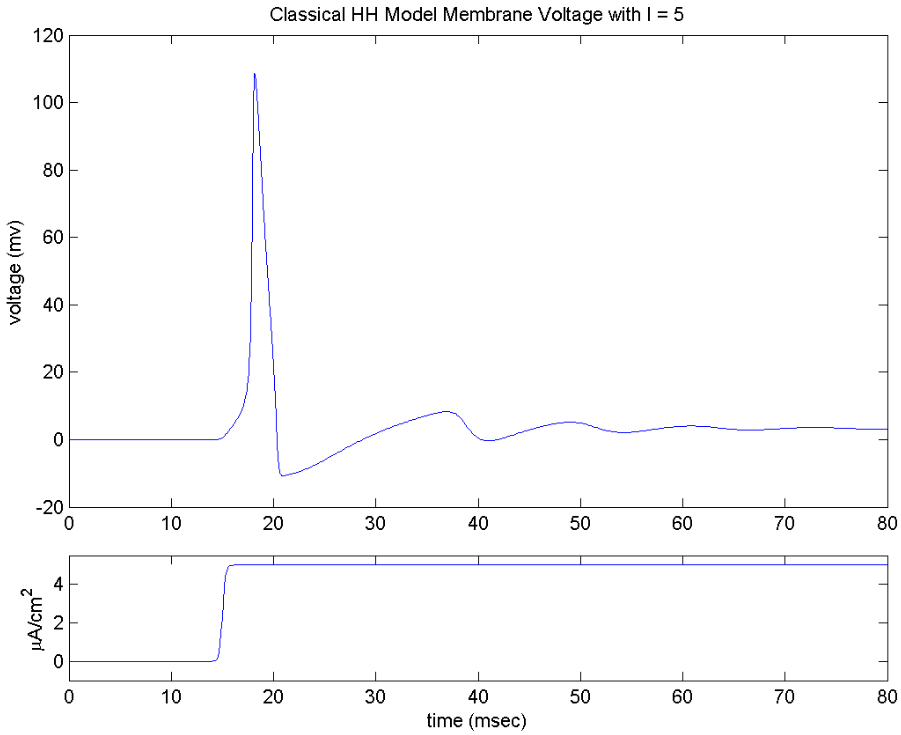

Figure 90: Classical Hodgkin-Huxley model, single spike response, $I = 5\,\mu\text{A/cm}^2$

Defining the neural response in terms of all or none spikes with a unique threshold has been largely replaced by the concept of action potentials as a dynamical response [1, 52]. However, when the boundary between qualitatively different behaviors is sufficiently narrow, as in the classical Hodgkin-Huxley model, the concept of threshold remains useful for practical discussion.

5.2.3.3 Dynamics in the Repetitive Spiking Region

Application of an injected current of $I = 7\,\mu\text{A/cm}^2$ results in repetitive spiking. Raising the injected current further to $I = 10\,\mu\text{A/cm}^2$ and $I = 15\,\mu\text{A/cm}^2$ results in an increased spike frequency. Referring back to Figure 87, the system fixed point loses stability in the injected current range of $6\,\mu\text{A/cm}^2 < I < 10\,\mu\text{A/cm}^2$, which qualitatively agrees with the analysis of [4].

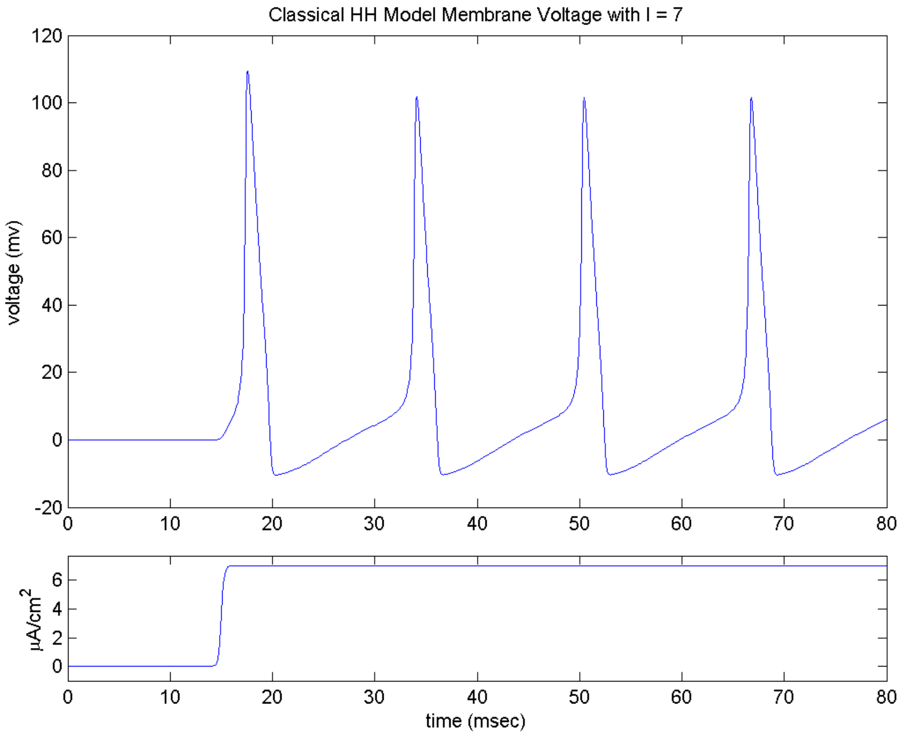

Figure 91: Classical Hodgkin-Huxley model, repetitive spiking response, $I = 7\,\mu\mathrm{A}/\mathrm{cm}^2$

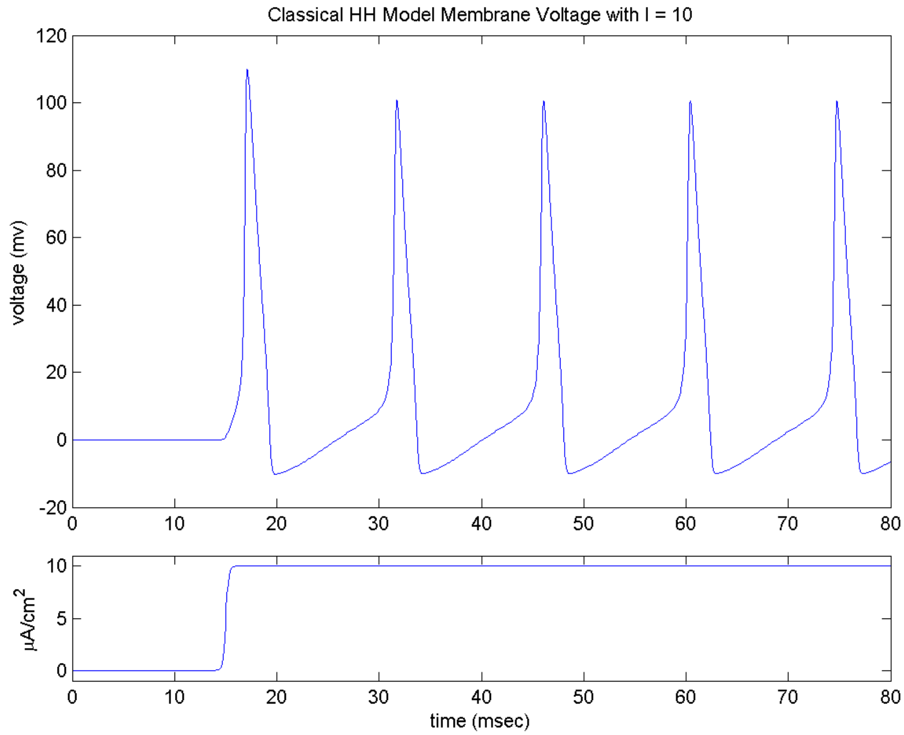

Figure 92: Classical Hodgkin-Huxley model, repetitive spiking response, $I = 10\,\mu\mathrm{A}/\mathrm{cm}^2$

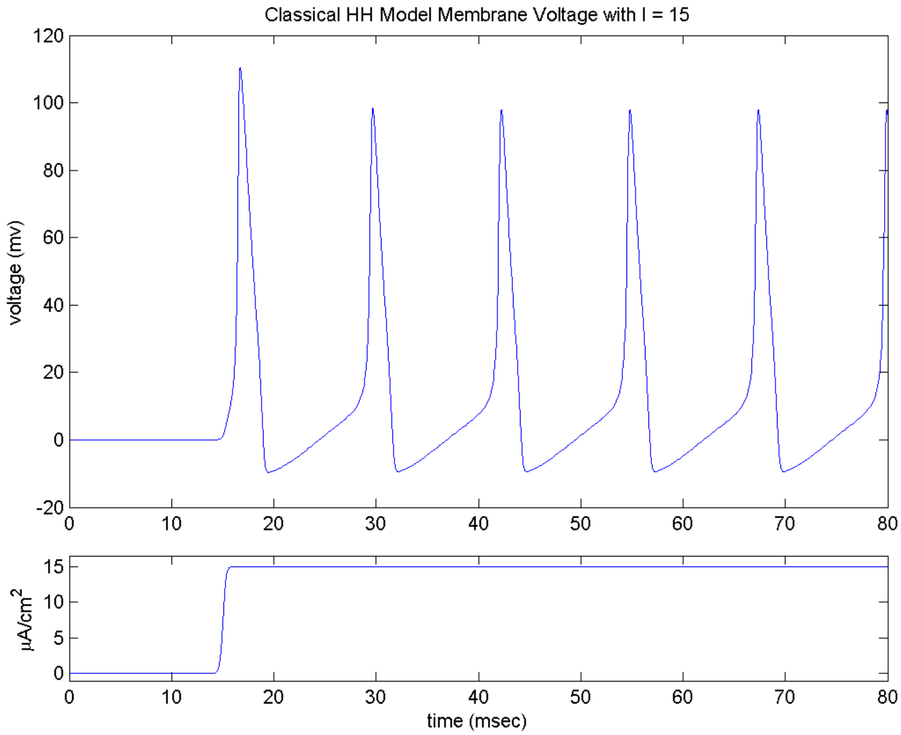

Figure 93: Classical Hodgkin-Huxley model, repetitive spiking response, $I = 15\,\mu\mathrm{A/cm}^2$

The threshold between “single spike” and “repetitive spiking” regions, much like the concept of unique threshold for a single action potential, is not an all or none transition. Carefully chosen injected current values can cause the neuron model to exhibit a finite number of action potentials. An injected current of $I = 5.15\,\mu\mathrm{A/cm}^2$, for example, causes the neuron model to elicit two action potentials as shown in Figure 94.

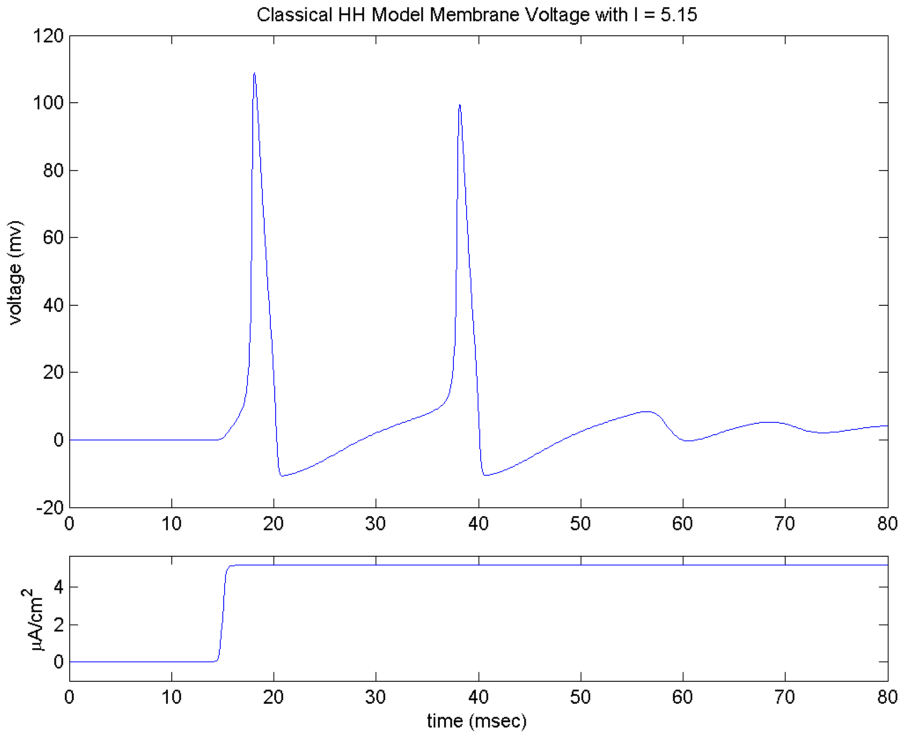

Figure 94: Classical Hodgkin-Huxley model, multiple spike response, $I = 5.15\,\mu\text{A/cm}^2$

The plotted results verify qualitative behaviors published in [4] and predicted by the locus of eigenvalues.

5.2.4 Optimal Control

In Sections 5.2.2 and 5.2.3, three qualitatively different system behaviors of the classical Hodgkin-Huxley model were identified. These behaviors were the inactive, single spike, and repetitive spiking regions. In this section, optimal input stimuli will be computed for each category of system behavior.

5.2.4.1 Optimal Control in the Inactive Region

Application of a step current of $I = 2\,\mu\text{A/cm}^2$ results in system behavior identified as the inactive region [52]. No action potential is generated, and the membrane potential exhibits subthreshold oscillations. Using the membrane voltage generated by a $I = 2\,\mu\text{A/cm}^2$ step input as the reference voltage, the optimal input stimuli is calculated for three different sets of values for P, Q, and R.

The first plot, with $P = Q = 1$, and $R = 10$, represents an emphasis on reduction of input stimuli energy at the expense of membrane voltage tracking accuracy. The third plot, with $P = Q = 1000$, and $R = 1$, represents the opposite end of the spectrum, emphasizing tracking accuracy. The remaining plot, with $P = Q = 100$ and $R = 1$, provides a balance of these two competing objectives.

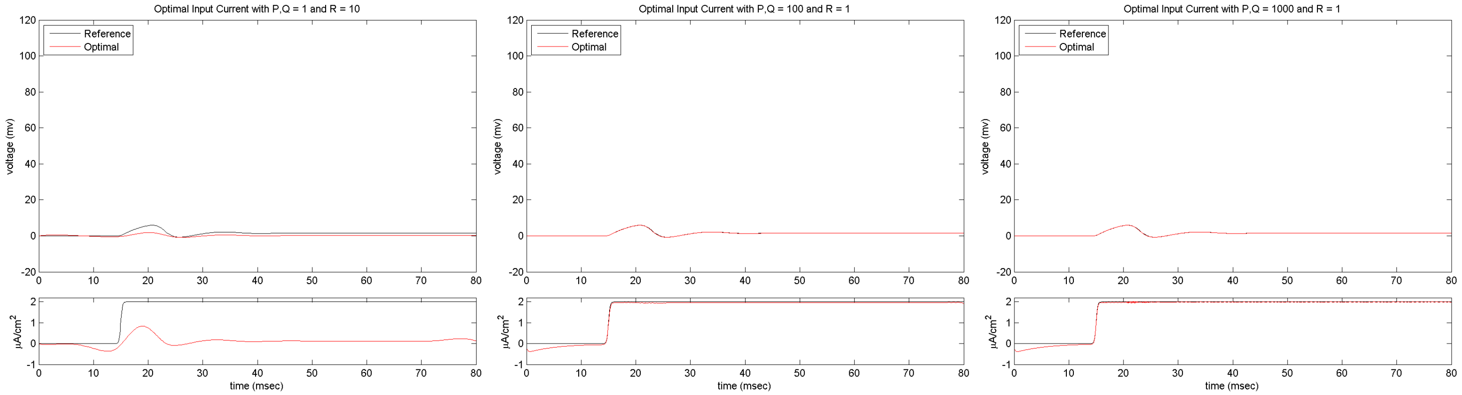

(a) $P = Q = 1,\ R = 10$

(b) $P = Q = 100,\ R = 1$

(c) $P = Q = 1000,\ R = 1$

Figure 95: Optimal control in the inactive region

As shown in Figure 95a, the exaggerated emphasis on reduction of input stimuli energy results in a membrane voltage is hardly disturbed from rest. Figure 95b, with $P = Q = 100$, and $R = 1$, displays quite accurate tracking of the reference membrane potential, but the optimal input current closely resembles the original input current. Further increasing emphasis on tracking in Figure 95c produces results which are not qualitatively different than those of Figure 95b.

The same values of P, Q, and R will be used for computation of optimal input stimuli for single spike and repetitive spiking regions of the classical Hodgkin-Huxley model.

5.2.4.2 Optimal Control in the Single Spike Region

Application of injected current $I = 3\,\mu\text{A/cm}^2$ results in system behavior identified as the single spike region [52]. Using the membrane voltage generated by a $I = 3\,\mu\text{A/cm}^2$ step input as the reference voltage, the optimal input stimuli is calculated for three different sets of values for P, Q, and R.

The first plot, with $P = Q = 1$, and $R = 10$, represents an emphasis on reduction of input stimuli energy at the expense of membrane voltage tracking accuracy. The third plot, with $P = Q = 1000$, and $R = 1$, represents the opposite end of the spectrum, emphasizing tracking accuracy. The remaining plot, with $P = Q = 100$ and $R = 1$, provides a balance of these two competing objectives.

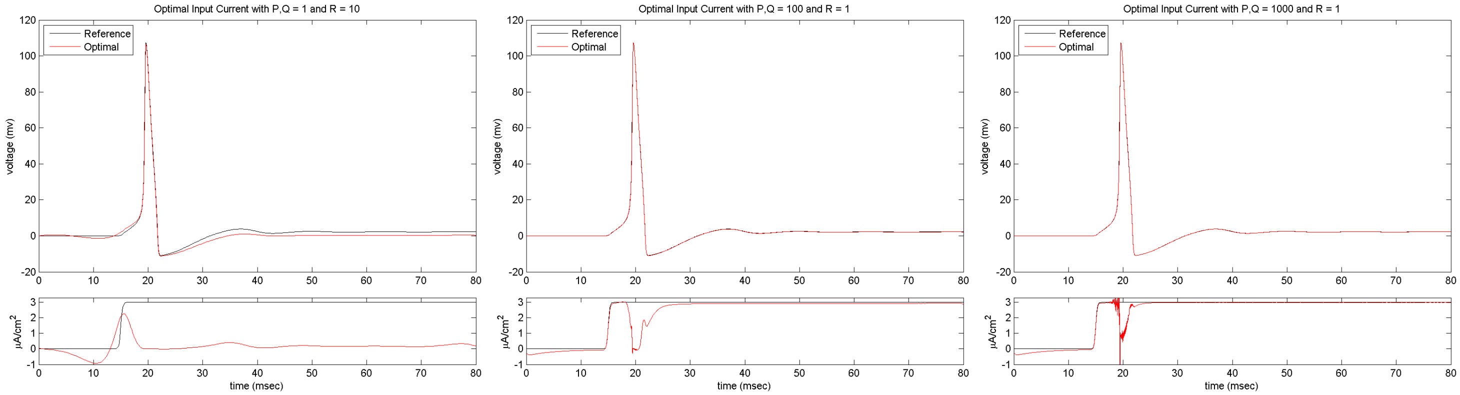

(a) $P = Q = 1,\ R = 10$

(b) $P = Q = 100,\ R = 1$

(c) $P = Q = 1000,\ R = 1$

Figure 96: Optimal control in the single spike region

As shown in Figure 96a, even with an exaggerated emphasis on reduction of input stimuli energy the membrane voltage still tracks the reference signal reasonably well. An action potential is generated, with noticeable errors existing mostly in the oscillations after in the range of $25 - 55\,\mathrm{ms}$. Figure 96b, with $P = Q = 100$, and $R = 1$, displays quite accurate tracking of the reference membrane potential over the entire simulation interval with a marked characteristic dip during the course of the action potential. Further increasing emphasis on tracking in Figure 96c produces further reduced error between the reference and optimally generated membrane potential at the expense of greater input stimuli energy. A dip in the input stimulus still exists during action potential generation, but in other regions of the simulation interval the optimal input current $i^*(t)$ closely resembles the original input current $i(t)$.

5.2.4.3 Optimal Control in the Repetitive Spiking Region

Application of injected current $I = 7\,\mu\mathrm{A/cm}^2$ results in system behavior identified as the repetitive spiking region [52]. Using the membrane voltage generated by a $I = 7\,\mu\mathrm{A/cm}^2$ step input as the reference voltage, the optimal input stimuli is calculated for three different sets of values for P, Q, and R. As described in [4] birth of a limit cycle attractor, enables the neuron model to produce repetitive spiking behavior.

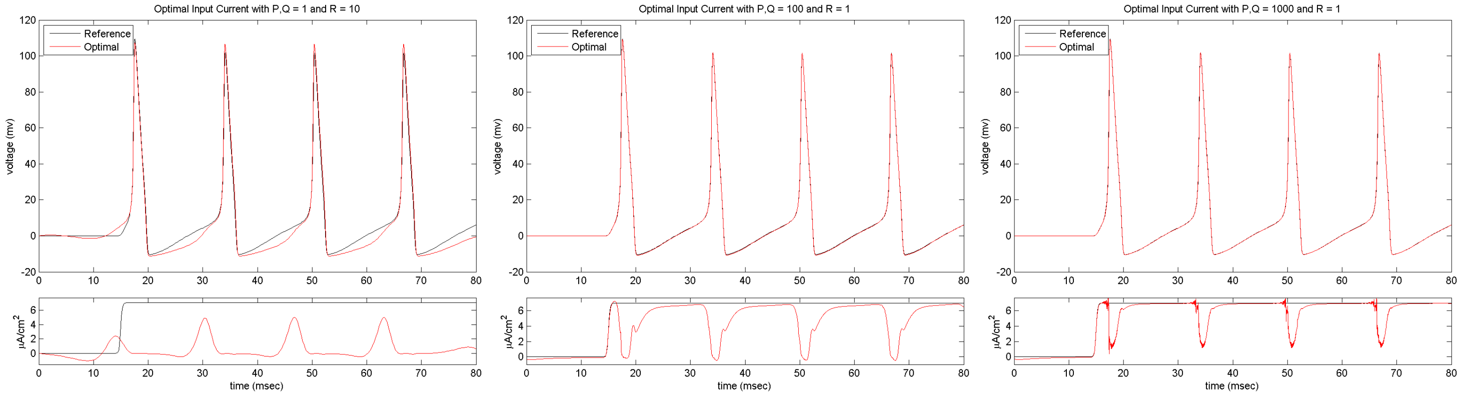

(a) $P = Q = 1,\ R = 10$ (b) $P = Q = 100,\ R = 1$ (c) $P = Q = 1000,\ R = 1$

Figure 97: Optimal control in the repetitive spiking region

For Figure 97a, notice that the first 20 ms of the optimal input current very closely resembles the optimal input current computed for the single spike case in Figure 96a. For the remainder of the simulation interval, a continued reduction in input stimulus amplitude exists, but unlike Figure 96a, small appropriately timed pulses of current enable generation of action potentials which track the reference membrane voltage. Noticeable error is present between action potentials.

Characteristic dips in the optimal input current have been identified in previous publications [2, 3], and are prominent in both Figure 97b and 97c. The dips provide a marked decrease in the injected current 'energy' which clearly correlates with the generation of each action potential.

Looking at Figures 97a through 97c as a set reveals that tracking is quite accurate during each action potential in all cases. Emphasizing reference membrane voltage tracking with higher values of P and Q has the greatest impact on portions of the simulation interval outside of the action potentials.

5.2.5 Case Studies

Within this section, two additional case studies are performed to highlight characteristics of optimal input stimulus signals computed for the classical Hodgkin-Huxley model. The first case study in Section 5.2.5.1 investigates differences in optimal input stimuli when pulse width of the original reference signal is varied. The second case study in Section 5.2.5.2 investigates differences in the optimal input stimuli when amplitude of the original reference signal is varied. In both case studies the stimulus signal generates a response from the single spike region [4].

5.2.5.1 Case Study 1 - Pulse Width Study

Within this case study, two different input stimuli were selected of equal amplitude and different pulse widths. Both signals elicit a single action potential from the classical Hodgkin-Huxley model. Using the membrane voltage generated by each input stimulus as the reference signal $r(t)$, the optimal input stimuli $i^*(t)$ is calculated for three different sets of values for P, Q, and R.

The first plot, with $P = Q = 1$, and $R = 10$, represents an emphasis on reduction of input stimuli energy at the expense of membrane voltage tracking accuracy. The third plot, with $P = Q = 100$, and $R = 1$, represents the opposite end of the spectrum, emphasizing tracking accuracy. The remaining plot, with $P = Q = 10$ and $R = 1$, provides a balance of these two competing objectives.

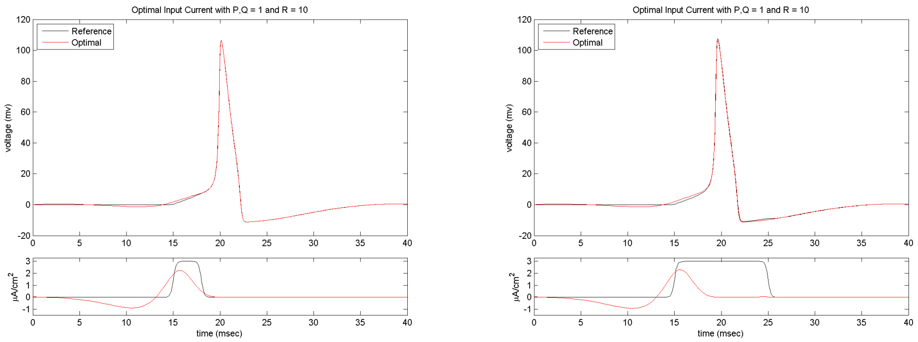

(a) (b)

Figure 98: Optimal control pulse width case study, $P = Q = 1$, $R = 10$

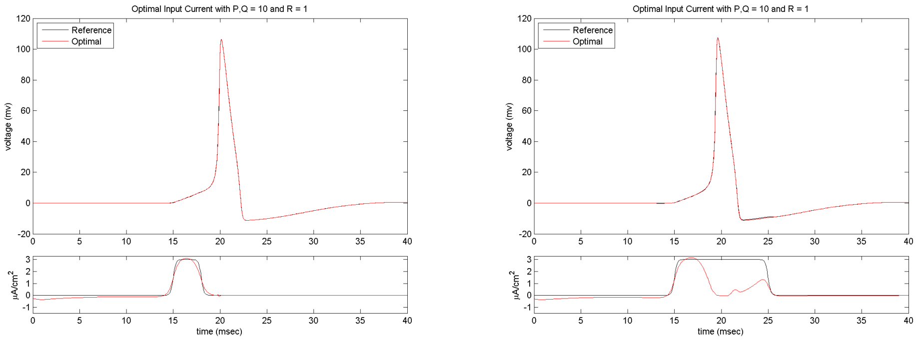

(a) (b)

Figure 99: Optimal control pulse width case study, $P = Q = 10$, $R = 1$

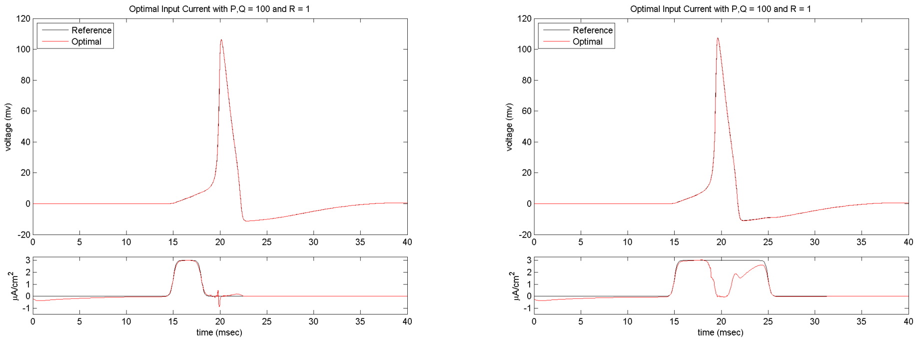

(a) (b)

Figure 100: Optimal control pulse width case study, $P = Q = 100$, $R = 1$

For Figures 98 through 100, all of the left-hand plots represent simulations with an input stimulus of $I = 3\,\mu\text{A/cm}^2$ and a stimulus duration of 3 ms. Right-hand plots in Figures 98 through 100 represent simulations with an input stimulus of $I = 3\,\mu\text{A/cm}^2$ and a stimulus duration of 10 ms. In all cases, a single action potential is generated. Qualitatively, the plots are very similar with a small difference in the shape and timing of the action potential between $15 - 18$ ms.

The most striking feature of the set of simulations is that optimal input stimuli are nearly identical in Figure 98a and 98b and the optimal stimuli more closely represent the original input stimulus in Figure 100. Figure 101 depicts the optimal input stimulus of for the 10 ms pulse width input when $P = Q = 1000$ and $R = 1$.

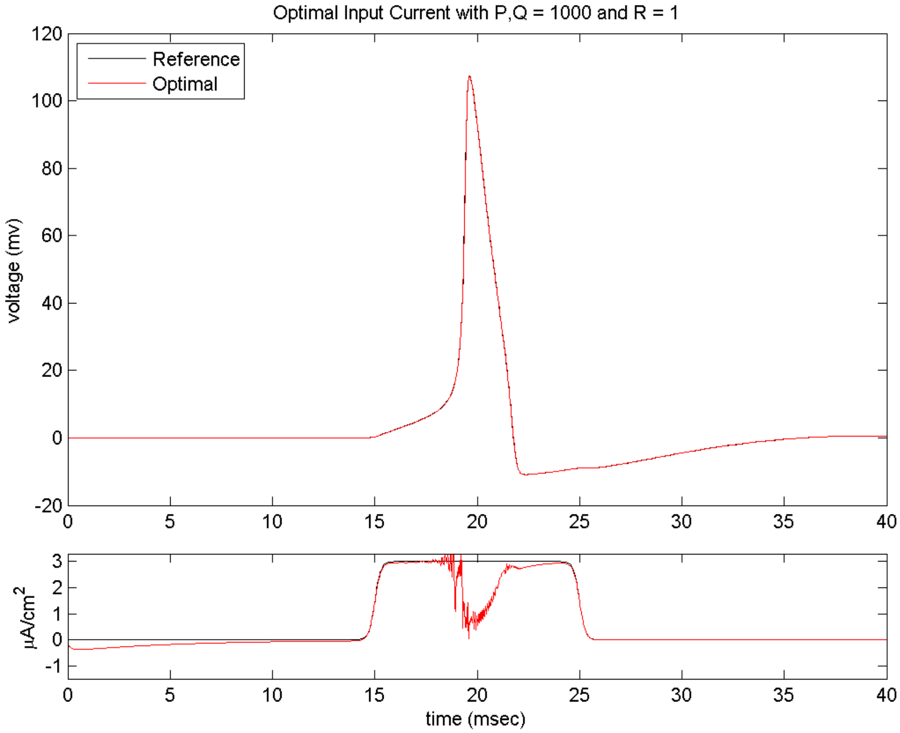

Figure 101: Optimal control pulse width case study, $P = Q = 1000$, $R = 1$

When the values chosen for P, Q, and R emphasize reduction in input stimulus amplitude, the computed optimal input stimulus is capable of recreating the qualitative features of the reference signal $r(t)$, and the resulting $i^*(t)$ is independent of the originally applied pulse width. When the values chosen for P, Q, and R emphasize accurate tracking of the reference signal $r(t)$, the resulting optimal input stimulus is effected by small differences in the reference signal, and the optimal input stimulus recaptures general characteristics of the original input signal, along with a characteristic dip in $i^*(t)$. Figures 102a through 102c further highlight these characteristics by plotting the membrane voltage and optimal stimulus current for each set of values P, Q, and R on a single plot.

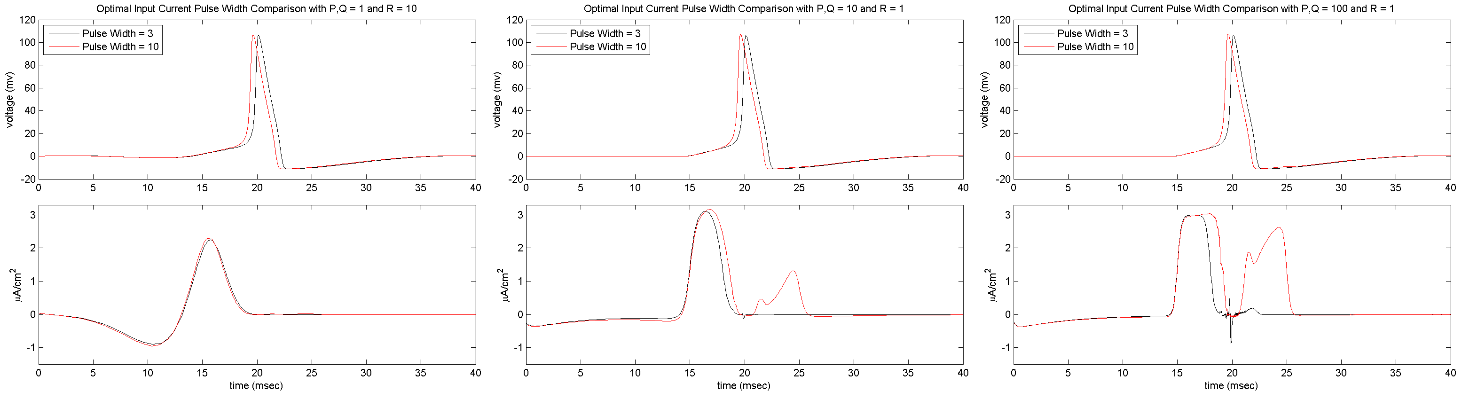

(a) $P = Q = 1,\ R = 10$ (b) $P = Q = 10,\ R = 1$ (c) $P = Q = 100,\ R = 1$

Figure 102: Optimal control pulse width input comparison

5.2.5.2 Case Study 2 - Pulse Amplitude Study

Within this case study, two different input stimuli were selected of different amplitude and equal pulse widths. Both signals elicit a single action potential from the classical Hodgkin-Huxley model. Using the membrane voltage generated by each input stimulus as the reference signal $r(t)$, the optimal input stimuli $i^*(t)$ is calculated for three different sets of values for P, Q, and R.

The first plot, with $P = Q = 1$, and $R = 10$, represents an emphasis on reduction of input stimuli energy at the expense of membrane voltage tracking accuracy. The third plot, with $P = Q = 100$, and $R = 1$, represents the opposite end of the spectrum, emphasizing tracking accuracy. The remaining plot, with $P = Q = 10$ and $R = 1$, provides a balance of these two competing objectives.

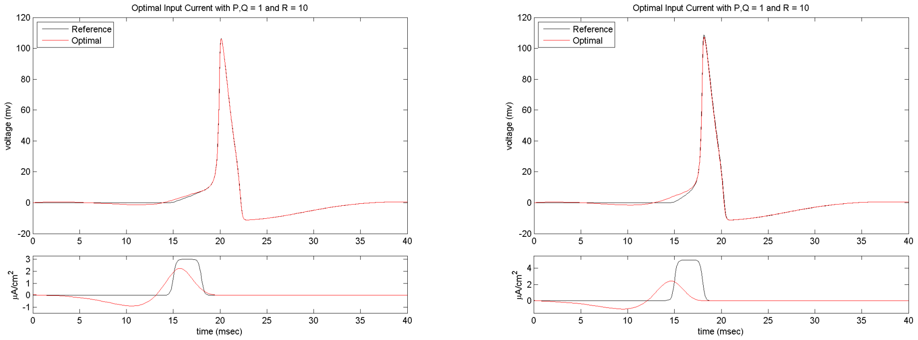

(a) (b)

Figure 103: Optimal control pulse amplitude case study, $P = Q = 1$, $R = 10$

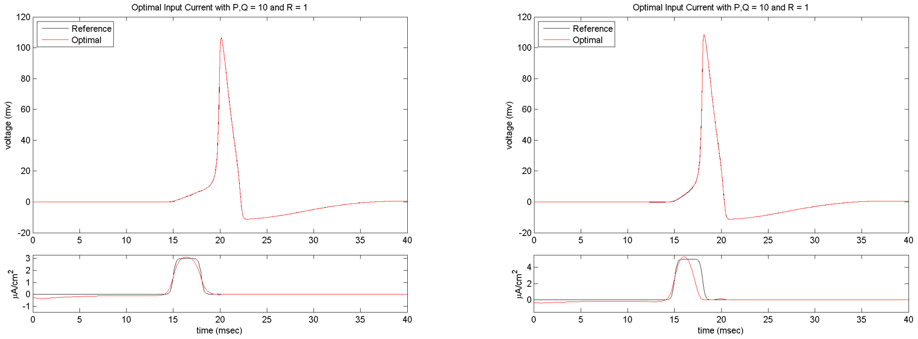

(a) (b)

Figure 104: Optimal control pulse amplitude case study, $P = Q = 10$, $R = 1$

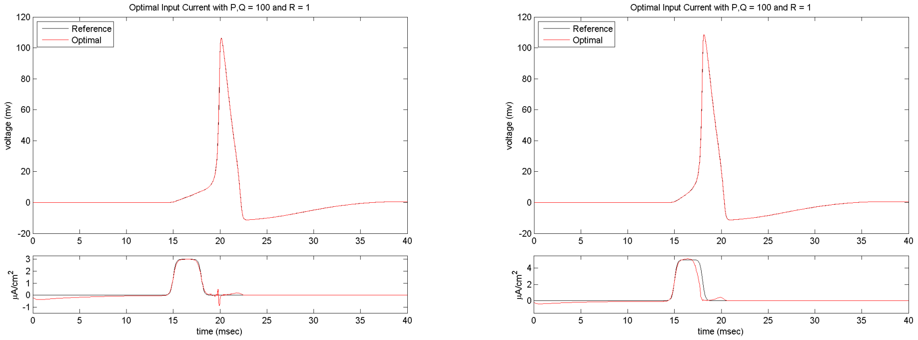

(a) (b)

Figure 105: Optimal control pulse amplitude case study, $P = Q = 100$, $R = 1$

For Figures 103 through 105 all of the left-hand plots represent simulations with an input stimulus of $I = 3\,\mu\text{A/cm}^2$ and a stimulus duration of 3 ms. Right-hand plots in Figures 103 through 105 represent simulations with an input stimulus of $I = 5\,\mu\text{A/cm}^2$ and a stimulus duration of 3 ms. In all cases a single action potential is generated. Qualitatively the plots are very similar with a small difference in the shape and timing of the action potential between $15 - 18$ ms.

Optimal input stimuli are nearly identical in Figure 103a and 103b and the optimal stimuli more closely represent the original input stimulus in Figure 105. These results mirror those found in the pulse width case study in Section 5.2.5.1.

When the values chosen for P, Q, and R emphasize reduction in input stimulus amplitude, the computed optimal input stimulus is capable of recreating the qualitative features of the reference signal $r(t)$, and the resulting $i^*(t)$ is independent of the originally applied pulse amplitude. When the values chosen for P, Q, and R emphasize accurate tracking of the reference signal $r(t)$, the resulting optimal input stimulus is effected by small differences in the reference signal, namely timing of the action potential, and the optimal input stimulus recaptures features of the original input signal.

Figures 106a through 106c further highlight these findings by plotting the membrane voltage and optimal stimulus current for each set of values P, Q, and R on a single plot.

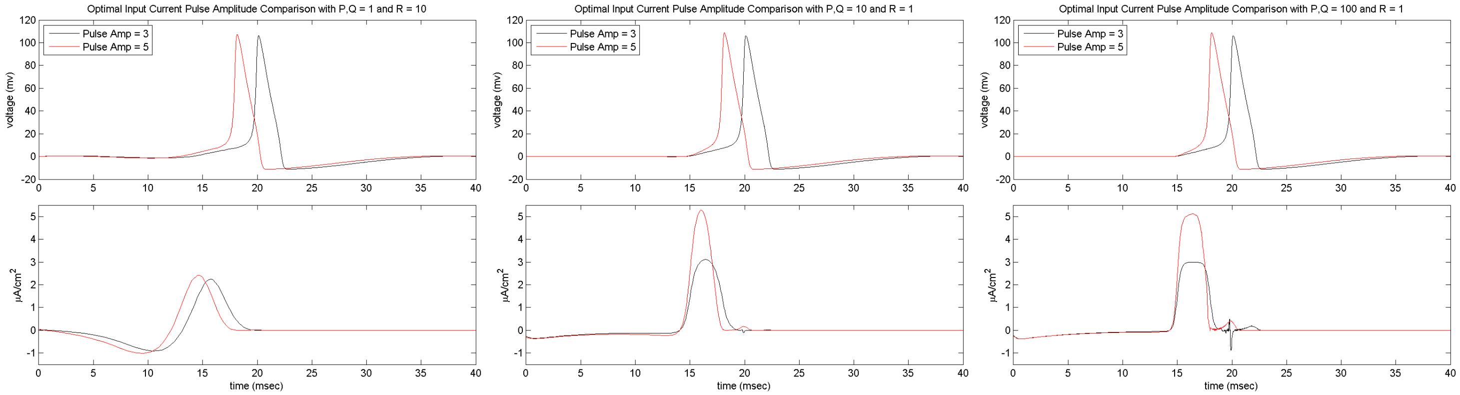

(a) $P = Q = 1,\ R = 10$

(b) $P = Q = 10,\ R = 1$

(c) $P = Q = 100,\ R = 1$

Figure 106: Optimal control pulse amplitude input comparison

The most noticeable difference between the plotted signals in Figures 106a through 106c is the apparent time shift between the action potentials. The action potential computed as a result of the larger amplitude input stimulus occurs approximately $2 - 3\,\text{ms}$ earlier in the simulation.

In Figure 106a, the optimal input stimuli emphasizing reduced stimulus amplitude are very similar, with a time shift between the two input stimuli. In Figures 106b and 106c the time shift becomes less noticeable as the optimal stimuli more closely represent the originally applied input stimuli.

In Section 5.2.5.1, as emphasis on reference signal tracking was increased, the optimal input signal recovered the wider pulse width of the originally applied input signal. Here as tracking accuracy is emphasized the optimal input signal more closely approximates the original input stimulus amplitude.

5.2.6 Discussion of Results

This section utilized the classical Hodgkin-Huxley model with parameters selected according to [1, p. 38]. The framework for nonlinear analysis and optimal control, presented as Figure 12 in Chapter 3, was the basis for investigating system dynamics.

The selected range of input stimuli produced three qualitatively different behaviors: inactive, single spike, and repetitive spiking [4]. A spectrum of optimal input stimuli were computed, ranging from emphasis on input ‘energy’ reduction to tracking accuracy, for injected current values representative of each qualitatively different behavior. Resulting bifurcation dynamics qualitatively agree with previously published dynamics [4, 52]. Minor quantitative differences are a result of different parameter values selected for E_L and E_Na as shown in Tables 5 and 6.

Two case studies demonstrated the commonality and divergence of computed optimal input stimuli when the originally applied input stimulus pulse width and amplitude are varied. The first and most important commonality across all computed inputs is that as emphasis on tracking increases the optimal input current $i^*(t)$ more closely represents the original input signal, with characteristic dips at the occurrence of action potentials. Conversely, Figures 102a and 106a demonstrate that as energy reduction is emphasized the computed signals for $i^*(t)$ become increasingly similar, demonstrating a lack of dependence on the pulse width or amplitude of the originally applied input stimulus.

Another interesting characteristic of all simulations which emphasized energy reduction, where $P = Q = 1$, and $R = 10$, is the presence of a negative pre-pulse dip in the optimal input stimulus. The general form of the solution is reminiscent of input signals applied to exhibit post inhibitory rebound spikes or negative pre-step values often applied experimentally [1, p. 5, 52, 96, 243, 252]. This type of behavior was not witnessed in any of the reduced-order solutions, regardless of bifurcation type or values chosen for P, Q, and R.

Also, for all simulations presented as the trade-off between reduction of injected current energy and tracking accuracy is varied, an asymptotic characteristic indicates that through appropriate choice of P, Q, and R values, a sweet spot will exist for an acceptable balance of tracking accuracy and input stimulus energy reduction can be found.

In summary, the optimal input stimulus calculation technique has sufficient generality to capture qualitative system dynamics with a marked reduction in input stimulus energy, along with enough fidelity to recover nuanced changes in the reference signal when tracking accuracy is emphasized. As an example, reference Figures 100b and 101 in the $22 - 25\,\mathrm{ms}$ time frame. Although there is not a noticeable difference between the membrane potentials in Figure 100a and 100b, further emphasis on tracking accuracy enables the wider input pulse to be recovered.

6 Experimental Feasibility

This chapter presents results which demonstrate experimental feasibility of the "Reduced Energy Input Stimulus Discovery Method" [2, 3]. Single cell intracellular stimulation and recordings using sharp microelectrodes enables injection of stimulus currents and measurement of resulting neuron membrane voltages. Experiments were conducted in neurons from the central nervous system (CNS) of the leech *Hirudo verbana*.

Prior to performing the experiment the reduced-order Hodgkin-Huxley type model of Chapter 4 was configured based on a qualitative estimate of the bifurcation type. A smooth input current pulse was applied in simulation to generate a single action potential and sets of optimal input current stimuli were computed for the modeled neuron.

Using sharp microelectrode recording techniques a non-smooth input current stimulus pulse was applied to neurons of the leech sufficient to generate an action potential. The amplitude and width of the experimentally applied pulse were used to scale the set of time-varying input stimuli which are optimal for the model neuron.

The scaled optimal input current stimuli was applied to the neuron. The resulting experimentally obtained membrane voltage waveform was compared to the original membrane voltage which was obtained in response to the square wave input stimulus.

The results demonstrate experimental feasibility of the "Reduced Energy Input Stimulus Discovery Method", largely merging the theoretical approach published in [2, 3] and electrophysiology techniques performed at the rig. Specifically, the feasibility of computing and applying time-varying current stimuli which are optimal for the modeled neuron to biological neurons is validated. The last step not completed here is to use experimentally measured membrane voltages for the computation of optimal currents.

Some parameters of the experimental preparation are unique to each trial. Resting potential of the cell, resistance of the microelectrode, and the presence of any leakage currents resulting from sharp microelectrode recording are examples of variables not incorporated into this feasibility study.

This chapter proceeds as follows: An overview of the setup required to perform the experiment is provided in Section 6.1, including rationale for selection of the experimental preparation, electrophysiology rig configuration, and application of the optimal control technique. Section 6.2 provides results from the feasibility analysis, describing the experimental method and results. Results of the experiment are discussed in Section 6.3.

6.1 Experiment Setup

This section describes preparatory work required prior to performing the feasibility study. An overview is provided, including why the nervous system of the leech *Hirudo verbana* was selected for this study, configuration of the electrophysiology rig, and computation of reduced energy optimal input stimuli.

6.1.1 Experiment Preparation

The leech *Hirudo verbana* was the focus of this feasibility study for the following reasons:

1. leeches possess a well-documented, segmentally organized, and consistent nervous system [53];
2. leeches exhibit complex behaviors; and
3. local expertise is available via the John Jellies laboratory [54, 7, 55].

Figure 107: Leech *Hirudo verbana*. Photograph: John Jellies. Image appears in [7] and is ©2014 The Company of Biologists Ltd.

The nervous system of the leech *Hirudo verbana* is organized in repeated segments, with each segment containing a ganglion with approximately 200 neurons. Ganglia are the small white spheres along the nerve cord at the center of the animal shown in Figure 108. Segments 9, 10, and 11 in the mid-body region of the leech will be utilized for this experiment. Figure 109 depicts three mid-body segments and the ventral nerve cord after removal.

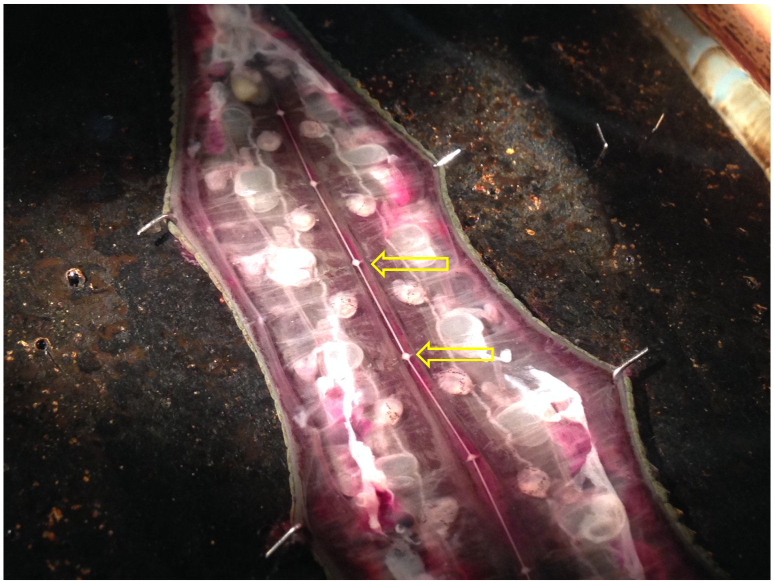

Figure 108: Exposed nervous system of the leech. Photograph: John Jellies.

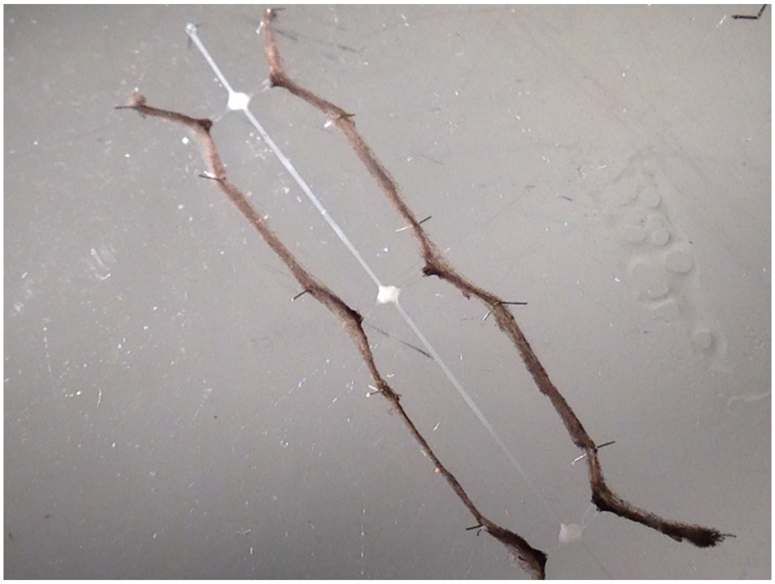

Figure 109: Three mid-body ganglia and ventral nerve cord. Photograph: John Jellies.

Once the dissection and removal of mid-body ganglia are complete, the dish containing the experimental preparation is transferred to the microscope stand on the rig. P, N, and

T-cells are primary mechanosensory neurons, which are identifiable within each ganglion. A broad range of functionality is exhibited by P, N, and T-cells, ranging from low-threshold phasic response in T-cells to high-threshold tonic behavior in N-cells.

Since the model parameters were set a priori based on known properties of P and N-cells reliable identification of these cells in each preparation is essential. Future experiments will require sufficient sample size to exhibit statistical significance of the results prior to publication. The preparation is sufficiently robust to withstand experimentation on the rig upwards of one hour. This allows time for any required computations in the simulation environment. Repeatability and robustness of the leech preparation is an essential feature for this feasibility study.

6.1.2 Electrophysiology Rig

An electrophysiology rig has been assembled to support experimental application of the “Reduced Energy Input Stimulus Discovery Method” by Western Michigan University faculty [2, 3]. The main functional requirements for the rig is the capability to apply arbitrary injected stimulus currents and the ability to measure membrane voltage using sharp microelectrodes.

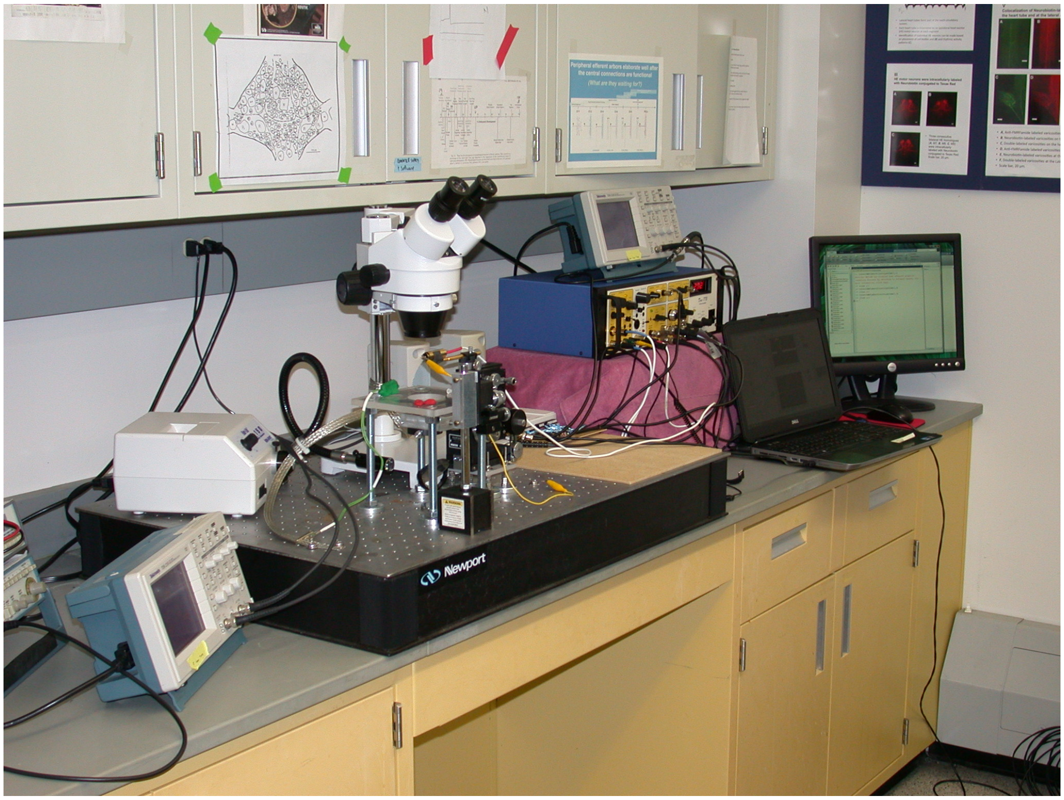

Figure 110: Electrophysiology rig utilized in the described experiments

Figure 110 shows the rig which is composed of the following components:

- Laptop computer running a custom graphical user interface built using LabVIEW®software;
- National Instruments (NI) USB 6211 Multifunction data acquisition (DAQ) unit;
- Tektronix Dual Channel Oscilloscopes;
- World Precision Instruments (WPI) Duo 773 Electrometer;
- Audio Speakers;
- Anti-vibration table;
- Microscope with light source; and a
- Micromanipulator.

A graphical user interface (GUI) provides (1) specification of current stimuli, and (2) acquisition and visualization of neuron stimulus and response signals. The laptop computer interfaces to the NI 6211 via standard universal serial bus (USB). The NI 6211 connects to the oscilloscope and the WPI Duo 773 using coaxial cables. The WPI Duo 773 is connected to audio speakers and the microelectrode head stage. The micromanipulator and microscope are somewhat isolated from vibration using an anti-vibration table. The microscope and light source enable visualizing the preparation. Figure 111 provides a block diagram of the described connections.

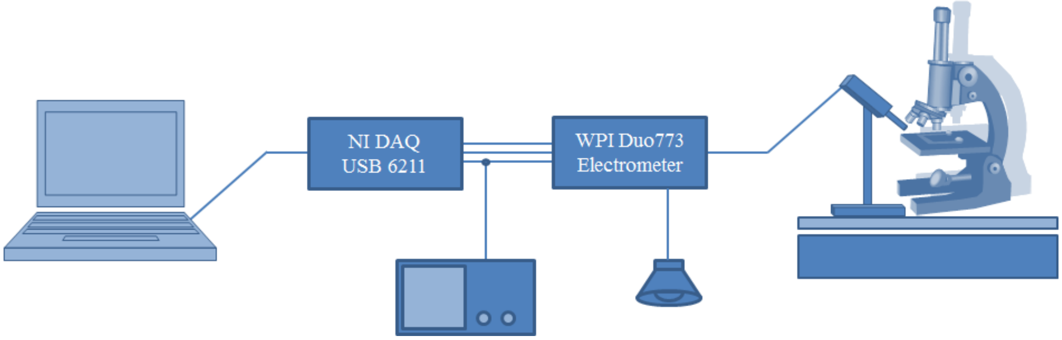

Figure 111: Electrophysiology rig block diagram

Visualization and control of electrical signals is accomplished using a GUI on the laptop. The GUI serves three purposes. It provides a convenient interface for the user while working at the rig, reads data files produced by MATLAB®simulations which are the time varying input stimulus signals, and controls the NI USB 6211 which is the electrical interface to the rig.

The NI USB 6211 is used to:

1. Generate a voltage signal proportional to the desired input current stimulus signal with sensitivity 1 nA/20 mV;
2. Monitor the actual stimulation current delivered by the WPI Duo 773;
3. Monitor the neuron membrane voltage at a rate of 40kHz; and
4. Generate a trigger signal.

Oscilloscopes provide additional monitoring of these key signals. The WPI Duo 773 interfaces with the neuron via the head stage and sharp microelectrode.

The membrane voltage measured by the WPI Duo 773 is fed back into the NI USB 6211. Analog signals applied to the NI USB 6211 are sampled at a rate of 40 kHz and transmitted to the laptop over USB for storage.

6.1.3 Application of Optimal Control Technique

Qualitative properties of the P and N-cells were assessed according to Table 1 of Chapter 3 to determine which of the four fundamental bifurcation types presented in [1] reasonably describe the behavior of these cell types. Using a a reduced-order Hodgkin-Huxley type model and known neurocomputational properties of leech P and N-cells, it was determined that the transition from rest to a single action potential could be modeled by the saddle node on invariant circle bifurcation type. Section 4.2.4 provides a theoretical description of the nonlinear analysis and optimal control of the saddle node on invariant circle bifurcation type.

Prior to performing the experiment, a set of reference and optimal injected stimulus current waveforms were computed. Three different pulse widths were chosen, and in all cases the pulse amplitude was sufficient to generate a single action potential in the model cell. The three cases are a pulse with duration of 5 ms with amplitude of $6\,\mu\text{A/cm}^2$, 10 ms with amplitude of $5\,\mu\text{A/cm}^2$, and 20 ms with amplitude of $4.75\,\mu\text{A/cm}^2$. For each of these three input signals, a set of three optimal injected currents were generated with emphasis ranging from energy reduction to tracking accuracy. Pre-computed waveforms are included as Figures 112 through 114.

While closed-loop application of the "Reduced Energy Input Stimulus Discovery Method" is the ultimate goal, this set of pre-computed waveforms provided a preliminary assessment of experimental feasibility [2, 3]. Previous experiments with P and N-cell types reveals that the timing of the action potential varies with the choice of stimulus pulse width and amplitude. The three pre-computed input signals provide a qualitative range of behavior. Short duration 5 ms pulses provide an action potential occurring near the falling edge of the stimulus pulse. The 10 ms pulse results in a slightly longer membrane depolarization prior to the action potential with a peak nearly coincident with the falling edge of the stimulus pulse. Lastly, a longer 20 ms pulse causes the cell to fire an action potential during the stimulus pulse. Experimentally obtained stimulus response pairs were qualitatively analyzed to determine the best match for the timing of the action potential in relation to the square wave stimulus pulse.

The pre-computed optimal injected current stimuli were used in an experimental setting as follows. After establishing a reliable sharp microelectrode recording for a cell, a non-smooth injected current pulse was applied. The injected current pulse amplitude was increased gradually until a single action potential was reliably received. Next, timing of the injected current pulse in relation to the action potential, as measured by the WPI Duo 773, are observed. It was qualitatively determined which of the pre-computed signals most accurately represented timing of the experimentally recorded action potential.

After determining which pulse width to use, the smooth injected current pulse of the pre-computed waveform is scaled in time and amplitude to match the experimentally applied injected current stimulus. The scale factor between the square wave pulses was used as a baseline for scaling the pre-computed optimal input stimulus $i^*(t)$ as shown in Figures 112 through 114.

This approach results in determining a square wave pulse with sufficient in amplitude to generate an action potential, and then applying a family of optimal injected stimuli. If the resulting membrane voltage of the cell approximates the originally recorded action potential, the utility of the optimal stimuli has been experimentally demonstrated.

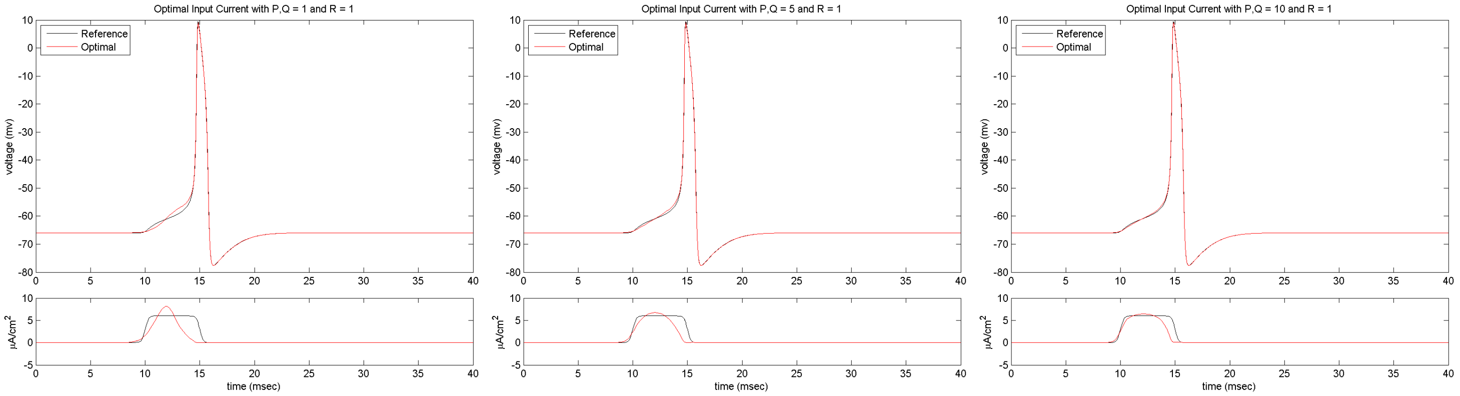

(a) $P = Q = 1,\ R = 1$

(b) $P = Q = 5,\ R = 1$

(c) $P = Q = 10,\ R = 1$

Figure 112: Optimal input stimuli with $6\,\mu\mathrm{A/cm}^2$ and $5\,\mathrm{ms}$ pulse width

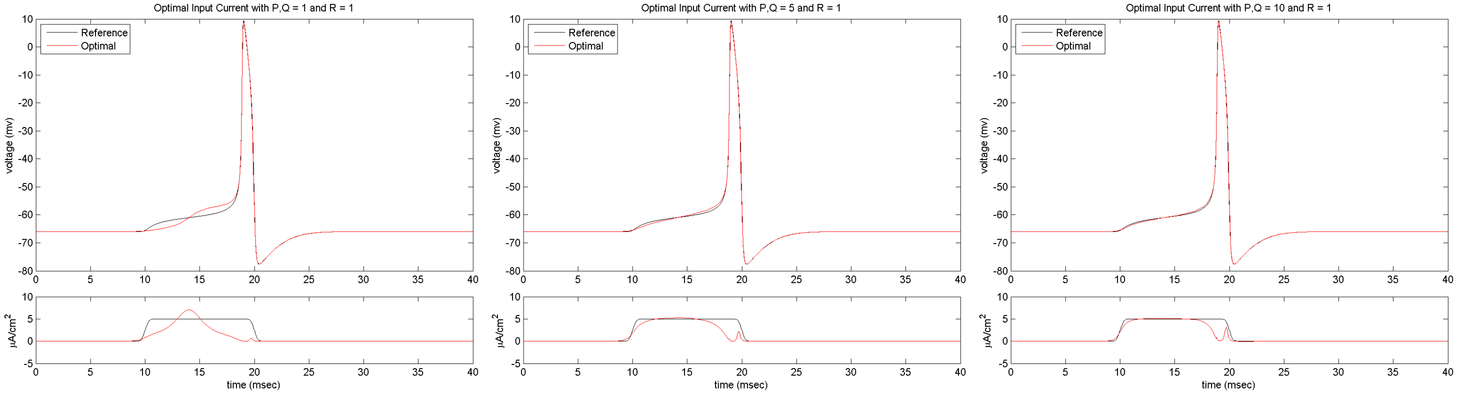

(a) $P = Q = 1 \quad , R = 1$ (b) $P = Q = 5 \quad , R = 1$ (c) $P = Q = 10, \ R = 1$

Figure 113: Optimal input stimuli with $5\,\mu\mathrm{A/cm}^2$ and $10\,\mathrm{ms}$ pulse width

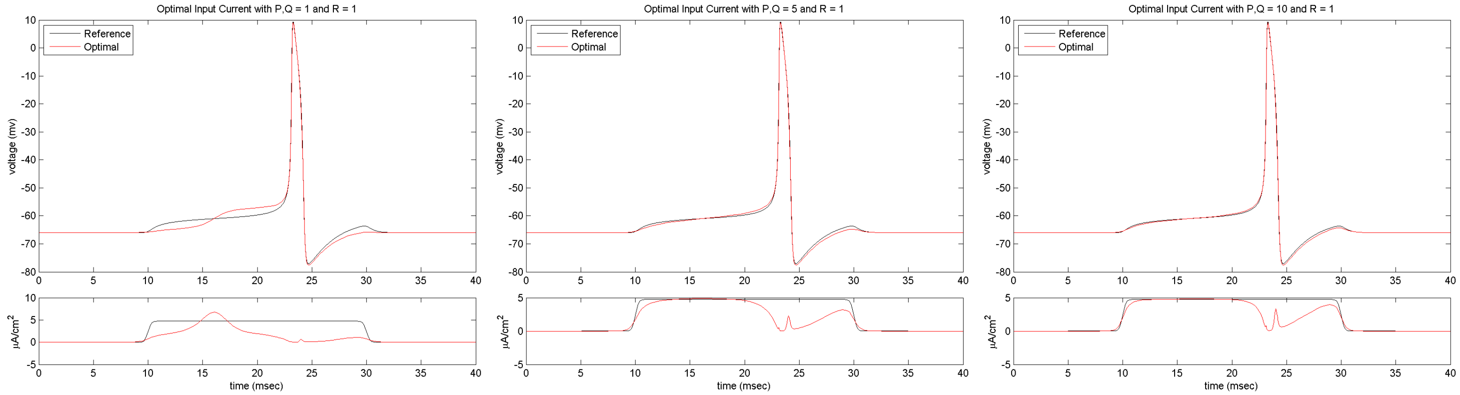

(a) $P = Q = 1,\ R = 1$

(b) $P = Q = 5,\ R = 1$

(c) $P = Q = 10,\ R = 1$

Figure 114: Optimal input stimuli with $4.75\,\mu\mathrm{A/cm}^2$ and $20\,\mathrm{ms}$ pulse width

6.1.4 Experiment Overview

The following steps were followed to conduct the described experiment:

1. Leech Preparation

   A leech is dissected, exposing the nervous system, as shown in Figure 108. The mid-body portion of the nervous system is removed and pinned into a separate dish, in saline solution, for use on the electrophysiology rig, as shown in Figure 109.

2. Microelectrode Preparation

   Using a Sutter Flaming-Brown micropipette puller, a sharp microelectrode is pulled to approximately 50 MΩ, and backfilled with 4 M potassium acetate.

3. Microelectrode Balance

   The micropipette is then installed on the head stage, with a sodium chloride coated sliver wire immersed in the potassium acetate inside the micropipette. The position and angle of the head stage is adjusted and the microelectrode is lowered into the saline solution on the microscope stage.

   The WPI Duo 773 is used to balance the electrode, and resistance is verified between 40 and 60 MΩ.

4. Poke Cell

   Using the microscope and micromanipulator, the microelectrode is positioned and inserted into the selected P or N-cell. Before stimulating the neuron, a good seal between the midcroelectrode and cell membrane and the resting membrane potential were verified.

5. Stimulate Neuron with a Non-Smooth Current Pulse

   Apply a stimulus current to the neuron, beginning with a moderate pulse width and low pulse amplitude of approximately 25 ms and 0.5 nA. Gradually increase the amplitude until an action potential is generated by the neuron.

6. Scale Optimal Input Stimuli

   Use a MATLAB®script and the values for pulse width and amplitude from step 5 to scale the pre-computed optimal input stimuli. The output of the MATLAB®script is a range of optimal input stimuli with differing emphasis on tracking accuracy and input stimulus energy reduction and uniform sample times that are able to be read by LabVIEW®for transmission to the USB 6211 and application to the target tissue.

7. Apply Scaled Optimal Input Stimuli to Neuron

   First, determine the pulse width which most accurately aligns the action potential with the square wave stimulus pulse as compared to the experimental results in step 5. Using the 5, 10, or 20 ms pulse apply optimal input stimulus which most emphasizes tracking, $P = Q = 10$, $R = 1$. Verify the neuron still generates an action potential.

   If the neuron consistently fires action potentials, apply the optimal input stimulus where $P = Q = 5$, $R = 1$, and verify the neuron still fires and action potential.

   If the neuron consistently fires action potentials, apply the optimal input stimulus where $P = Q = 1$, $R = 1$, and verify the neuron still fires and action potential.

8. Compare Recorded Membrane Voltages

   To compare the presence and timing of action potentials, the recorded data was compared on a single plot using MATLAB®.

6.2 Experimental Feasibility Analysis Results

This section describes the experiment conducted to analyze the feasibility of applying reduced energy optimal injected stimuli to P and N-cell neuron types in the leech central nervous system. An overview of the experimental results are provided.

The results presented within this section were recorded from one P-cell and one N-cell within a leech mid-body ganglion. Steps 1 through 3 of Section 6.1.4 were performed for the preparation. Next step 4 was performed for an identified P-cell. Results from the P-cell are presented in Section 6.2.1. Following application of baseline and optimal input stimuli to the P-cell, an N-cell was identified and steps 4 through 7 were repeated. Results from the N-cell are presented in Section 6.2.2.

6.2.1 Experimental Results in Leech P-Cell

Before applying optimal input stimuli, it is necessary to identify a square wave stimulus pulse which is of sufficient amplitude to generate an action potential as described in step 5 of Section 6.1.4. A plot containing 16 injected current stimulus and response traces is shown in Figure 115. As shown in Figure 116, timing of individual action potentials is quite consistent within the baseline data set.

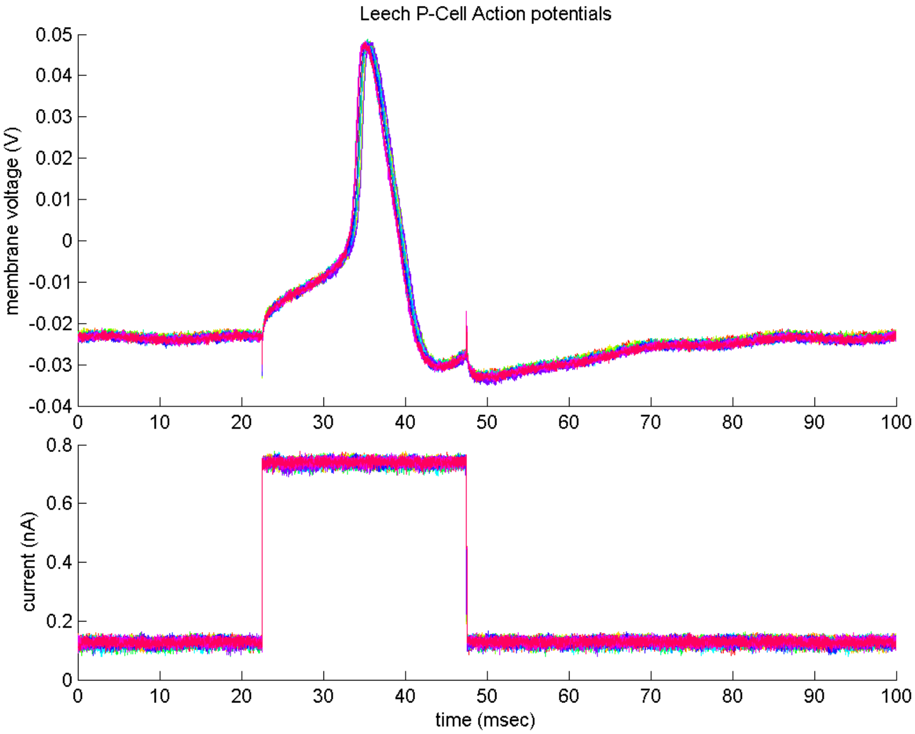

Figure 115: Leech P-cell action potentials and input current stimuli (Baseline: Non-smooth current pulse)(16 curves)

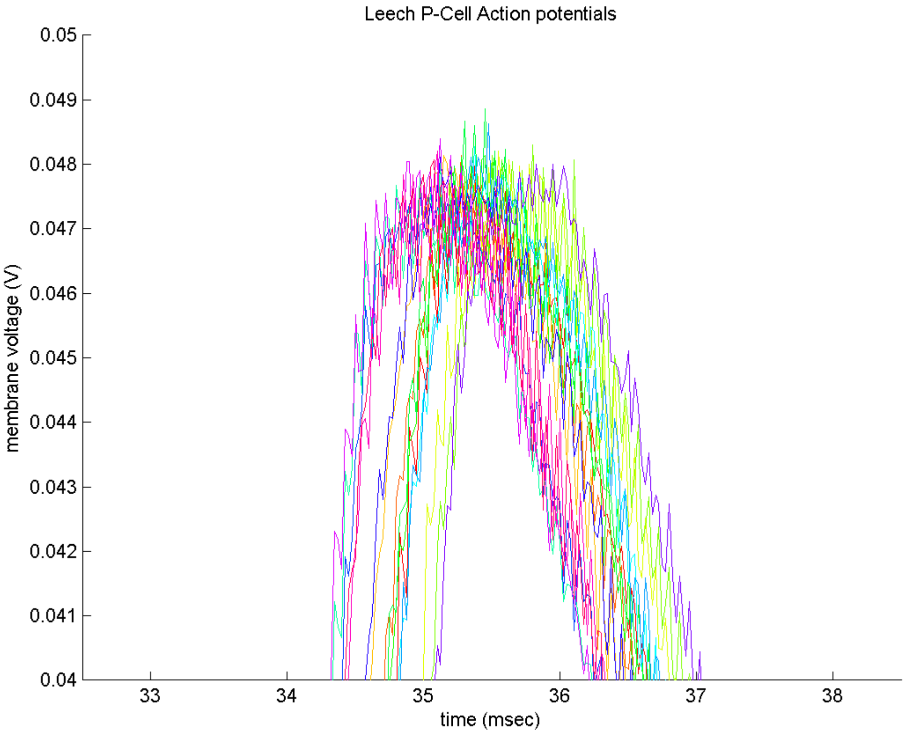

Figure 116: Leech P-cell peak action potential timing variation (Baseline: Non-smooth current pulse)(16 curves)

The original stimulus pulse is approximately 0.75 nA and has a duration of approximately 25 ms. The amplitude and duration of the injected stimulus is used to scale a predefined set of optimal input stimuli signals. Three sets of optimal input stimuli were generated for 5 ms, 10 ms, and 20 ms pulse widths. Time alignment between the original injected stimulus current and the resulting action potential was observed. Then, pre-computed optimal input stimuli having similar time alignment from the 10 ms and 20 ms waveform sets were applied to the P-cell under investigation.

6.2.1.1 Application of 10 ms Optimal Injected Currents in Leech P-Cell

To verify the scaling of optimal input signals, a 10 ms pulse was applied to the P-cell as pictured in Figure 117. The plot consists of 7 injected current stimulus and response traces.

Again the timing of individual action potentials is quite consistent.

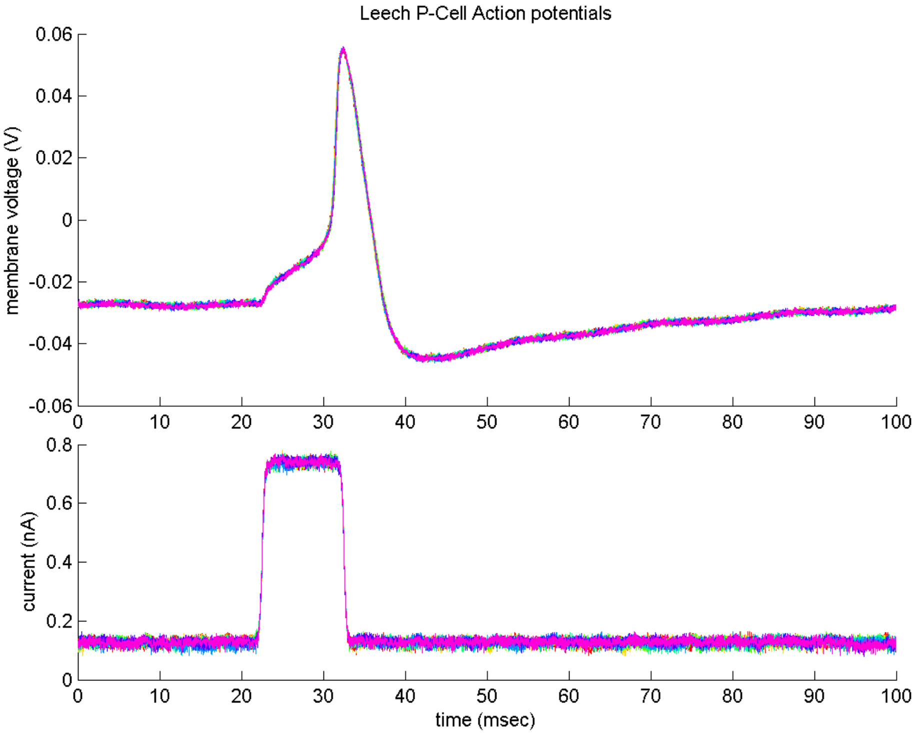

Figure 117: Leech P-cell action potentials and reference input current stimuli (Smooth 10 ms reference current pulse)(7 curves)

Application of an optimal injected current with $P = Q = 5$ and $R = 1$ is shown in Figure 118. The plot consists of 14 injected current stimulus and response traces.

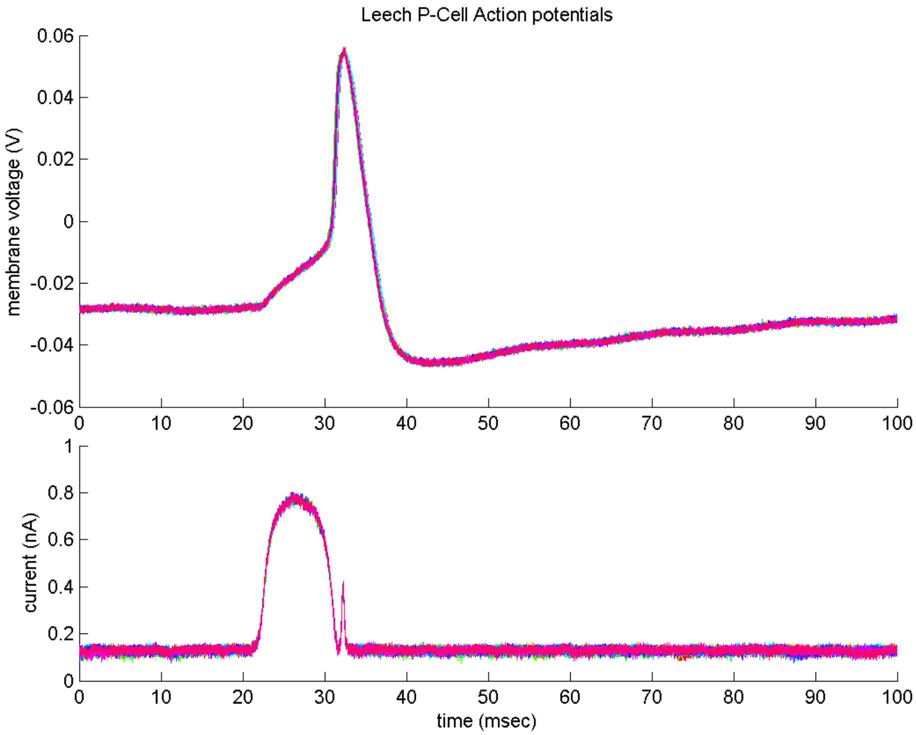

Figure 118: Leech P-cell action potentials and 10 ms optimal input current stimuli (Low energy reduction with $P = Q = 5$ and $R = 1$)(14 curves)

Application of an optimal injected current with $P = Q = 1$ and $R = 1$ is shown in Figure 119. The plot consists of 18 injected current stimulus and response traces. Even with a significantly reduced energy content between the 10 ms non-smooth current pulse and the optimal injected current in Figure 119, the neuron generates a consistently timed action potential in all cases. However, there is a change in the shape of the membrane potential around 30 ms preceding the action potential. This change represents a lack of tracking between the original membrane potential and the response to the neuron to the optimal input current.

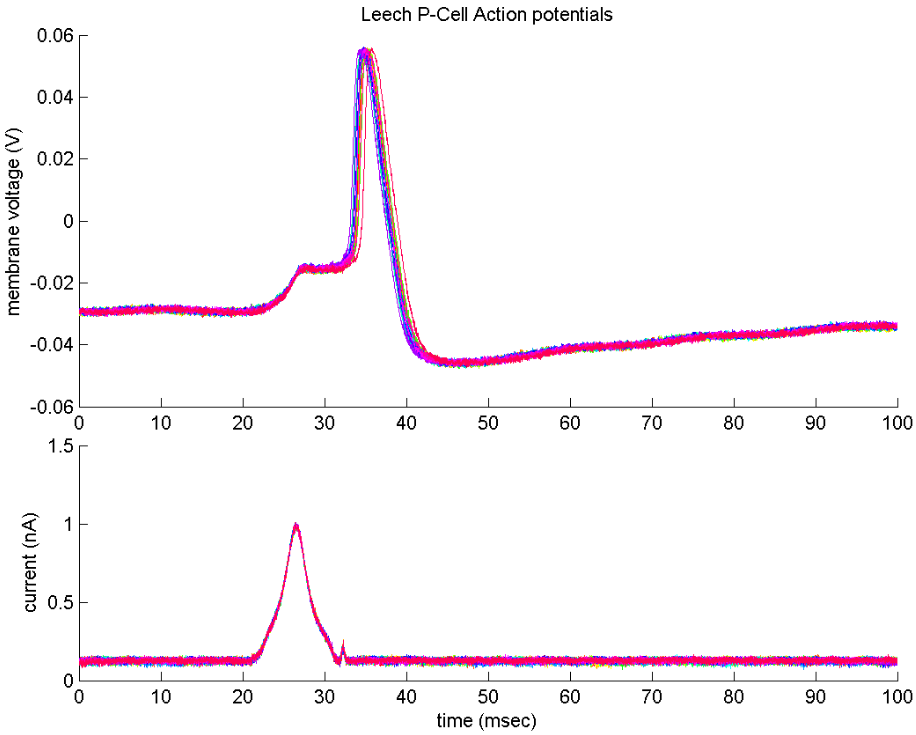

Figure 119: Leech P-cell action potentials and 10 ms optimal input current stimuli (High energy reduction with $P = Q = 1$ and $R = 1$)(18 curves)

Comparing the results plotted in Figures 117 through 119 to each other provides an experimental example of the trade-off between membrane voltage tracking accuracy and input stimulus energy reduction. Figure 120 plots the 10 ms square wave stimulus and response as the reference signal, as compared to the optimal 10 ms stimulus with $P = Q = 5$ and $R = 1$. Figure 121 plots the 10 ms square wave stimulus and response as the reference signal, as compared to the optimal 10 ms stimulus with $P = Q = 1$ and $R = 1$.

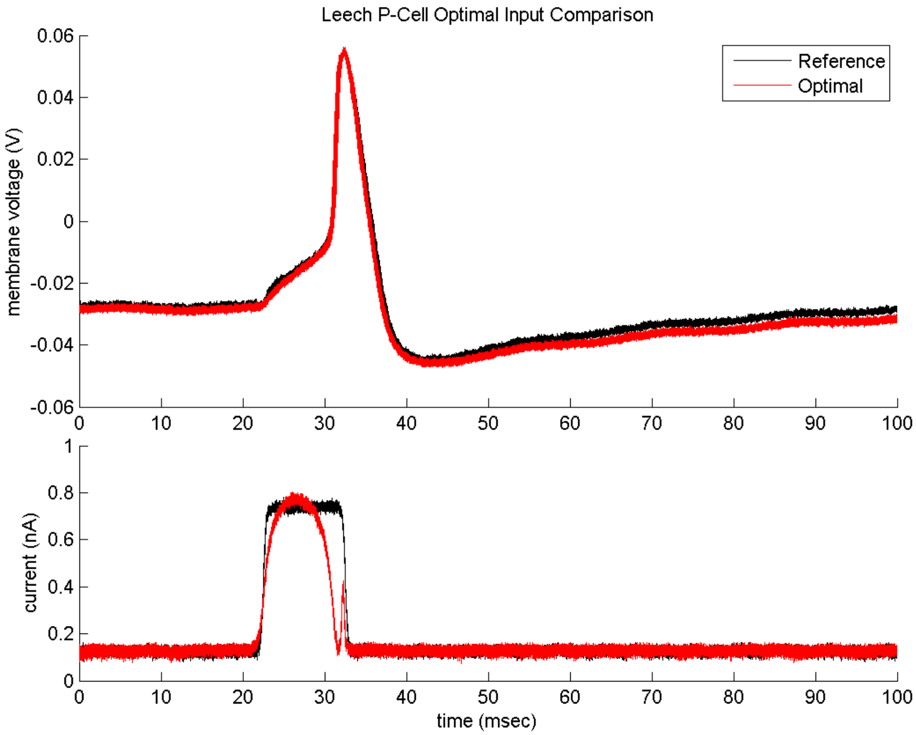

Figure 120: Reference vs. low energy reduction case with $P = Q = 5$ and $R = 1$

Within Figure 120, the reference data is the set of 7 traces presented in Figure 117. The optimal data is the set of 14 traces presented in Figure 118. As shown in Figure 120, there is very little difference between the membrane voltage response to reference and optimal input stimulus signals. A slight difference is noticeable in the membrane potentials immediately before and after the action potential, but action potential timing is well aligned between the two data sets.

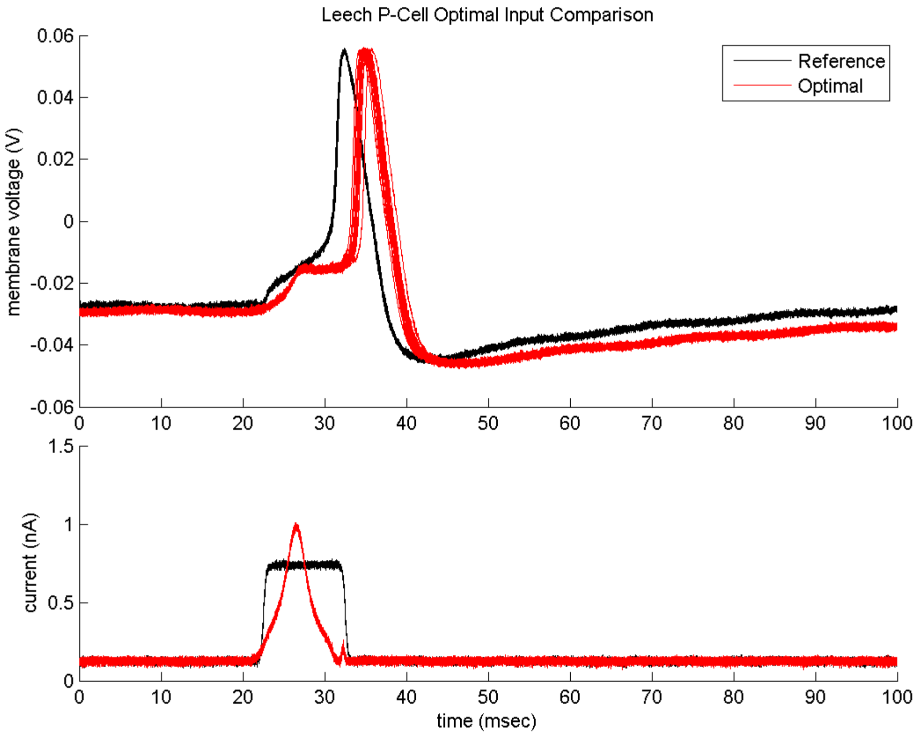

Figure 121: Reference vs. high energy reduction case with $P = Q = 1$ and $R = 1$

Within Figure 121, the reference data is the set of 7 traces presented in Figure 117. The optimal data is the set of 18 traces presented in Figure 119. As shown in Figure 121, the main difference between the membrane voltage response to reference and optimal input stimulus signals is in timing of the action potentials. A noticeable difference in the membrane voltage waveform preceding the action potential results in delayed action potential timing in response to the optimal input stimulus. However, it is noteworthy that in all cases, the neuron still exhibits an action potential in response to the optimal input stimulus.

6.2.1.2 Application of 20 ms Optimal Injected Currents in Leech P-Cell

After application of the optimal waveforms presented in Section 6.2.1.1, optimal waveforms related to the 20 ms pulse width were applied to the same P-cell. Figure 122 corresponds to application of an optimal input stimulus with 20 ms pulse width, $P = Q = 10$

and $R = 1$. Figure 123 corresponds to application of an optimal input stimulus with 20 ms pulse width, $P = Q = 5$ and $R = 1$. Viability of the P-cell became questionable before application of the case with $P = Q = 1$ and $R = 1$ was performed.

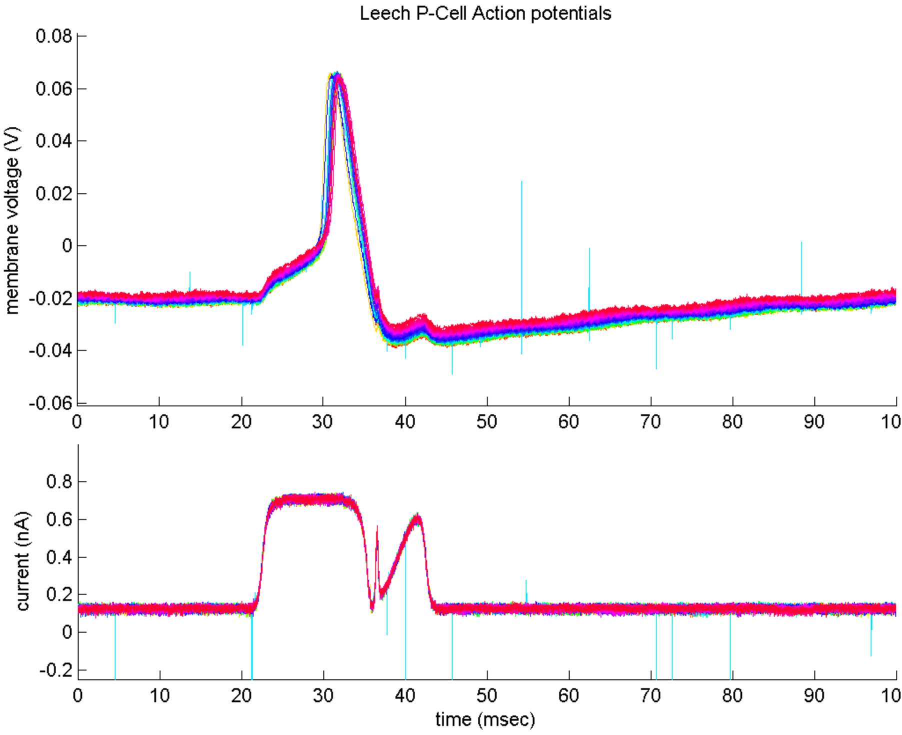

Figure 122: Leech P-cell action potentials and 20 ms optimal input current stimuli (Lowest energy reduction with $P = Q = 10$ and $R = 1$)(29 curves)

Figure 122 consists of 29 injected current stimulus and response traces. Again, timing of all action potentials is consistent. Ideally, if the experiment design was more closely linked with the preparation of this trial, the dip in the optimal stimulus current at approximately 37 ms would be more closely timed with the arrival of the action potential. However, the shape of the action potential, including the membrane potential before the action potential and the depolarization corresponding with the increased stimulus current at 40 ms, does resemble the theoretical reference membrane potential presented in Figure 114c.

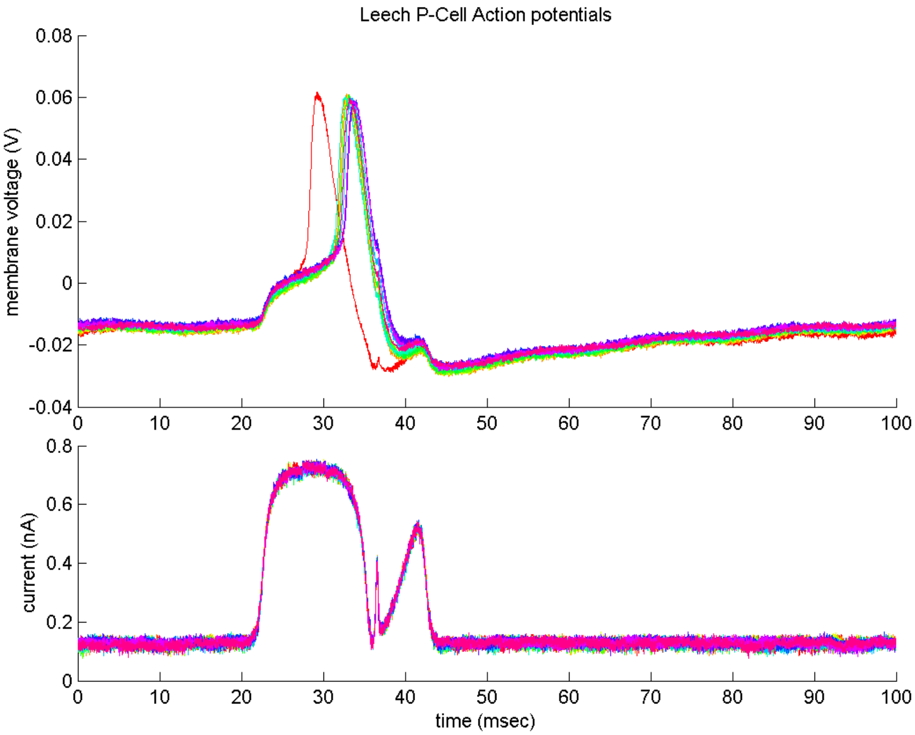

Figure 123: Leech P-cell action potentials and 20 ms optimal input current stimuli (Low energy reduction with $P = Q = 5$ and $R = 1$)(11 curves)(Note outlier)

Figure 123 consists of 11 injected current stimulus and response traces. The optimal input stimulus represents a further reduction in energy at the expense of membrane potential tracking accuracy. Notice that one action potential occurred outside the consistent arrival time of the other 10 traces. However, in Figure 123, the action potential is more closely aligned with the characteristic dip in the optimal input stimulus. Also, the shape of the 10 action potential waveforms does resemble that shown in Figure 114b.

6.2.2 Experimental Results in Leech N-Cell

Steps 4 and 5 were conducted in an identified N-cell within a leech mid-body ganglion. Scaled optimal input signals of a 20 ms pulse were applied to the N-cell, as pictured in Figures 124 through 126. Figure 124 represents application of an optimal input stimulus with $P = Q = 10$ and $R = 1$, an emphasis on tracking the reference membrane potential.

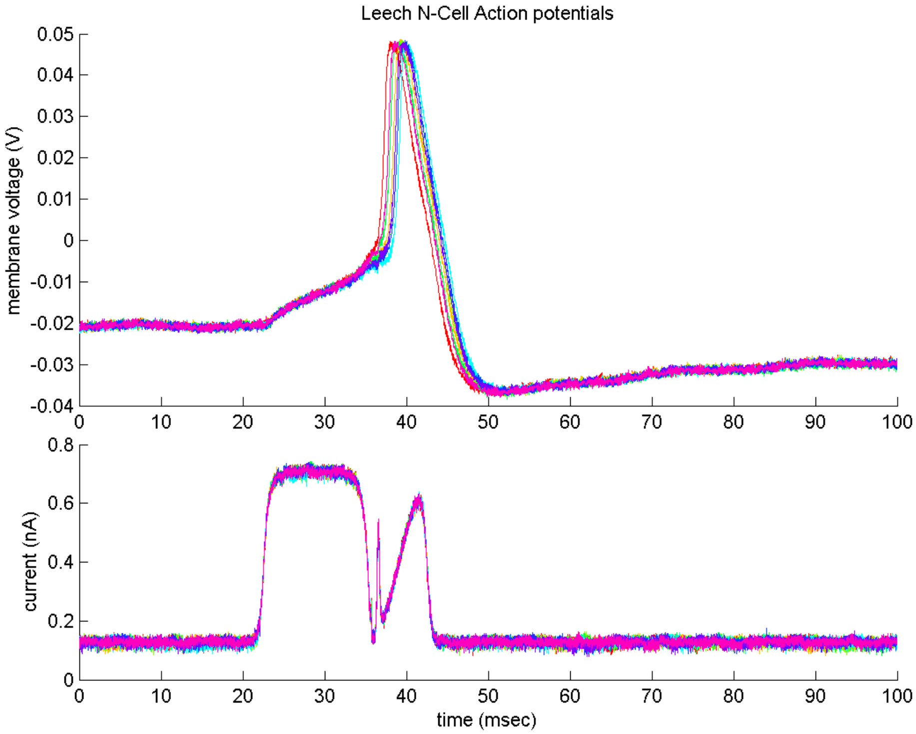

Figure 124: Leech N-cell action potentials and 20 ms optimal input current stimuli (Lowest energy reduction with $P = Q = 10$ and $R = 1$)(8 curves)

Figure 124 consists of 8 injected current stimulus and response traces. Timing of individual action potentials is quite consistent and even with the open-loop nature of the experiment, the action potential is consistent with the characteristic dip in the optimal input stimulus.

Figure 125 represents application of an optimal input stimulus with $P = Q = 5$ and $R = 1$, a reduced emphasis on tracking the reference membrane potential with greater emphasis on reduction in input stimulus energy, consisting of 8 injected current stimulus and response traces. Notice the significant variation in action potential timing.

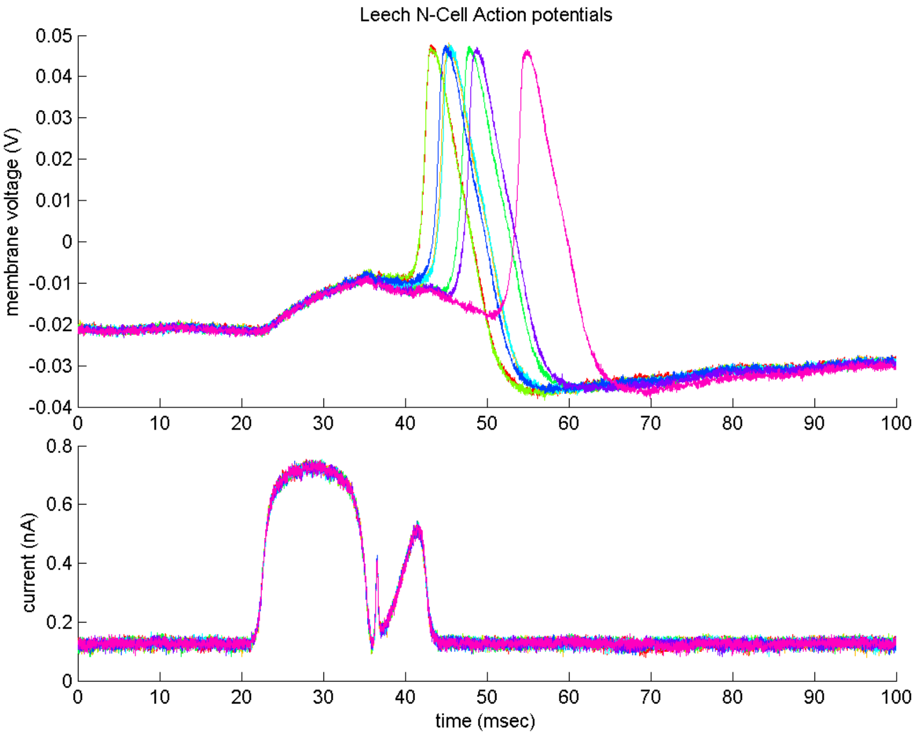

Figure 125: Leech N-cell action potentials and 20 ms optimal input current stimuli (Low energy reduction with $P = Q = 5$ and $R = 1$)(8 curves)

Figure 126 represents application of an optimal input stimulus with $P = Q = 1$ and $R = 1$, an emphasis on reduction in input stimulus energy, consisting of 11 injected current stimulus and response traces. In all cases, the neuron does not fire an action potential in response to the optimal input stimulus. Still, lack of subthreshold oscillations is a key observation when attempting to classify the bifurcation dynamics of the cell under investigation.

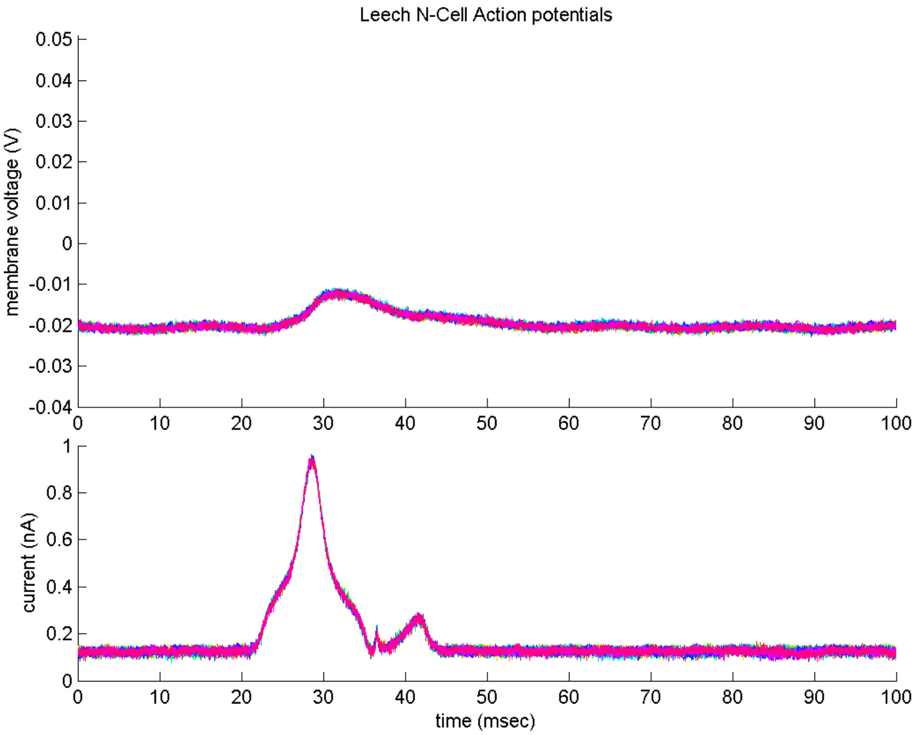

Figure 126: Leech N-cell action potentials and 20 ms optimal input current stimuli (High energy reduction with $P = Q = 1$ and $R = 1$)(11 curves)

6.3 Discussion of Results

The results presented in this chapter demonstrate feasibility of the “Reduced Energy Input Stimulus Discovery Method” in P and N-cell of the leech central nervous system [2, 3]. Results for the P-cell present greater agreement between reference and optimal membrane potentials over a wider range of objective functions. However, as demonstrated in Chapter 4, when emphasis on reduction of input stimulus energy is increased the theoretical results of all four bifurcation types lacked action potentials in the repetitive spiking cases.

Results of the experiment confirm application of optimal control based techniques at the rig is a feasible approach. The leech P and N-cells provide a robust and reliable preparation for the experiment. The technique holds promise for investigating the biophysical basis of functionality in the nervous system that integrates mathematical modeling, optimally balancing competing performance objectives, and relation to bifurcations of system fixed points fundamental to neurocomputation.

7 Conclusions

This chapter provides an overview of results, recommendations for further application and extension of the developed optimal control technique, and a discussion of the contributions of this work.

7.1 Results

The pioneering work of Hodgkin and Huxley is foundational to biophysically-based neuron models [1, p. 320][10, p. 41]. It has been demonstrated in [1] that a reduced-order conductance-based model is capable of producing the four bifurcation types fundamental to many neurocomputational properties. If dynamics under investigation depend upon additional ionic currents or activation properties, conductance-based models can be extended or modified to include the behavior of interest [3, 40].

Optimal control theory provides a mathematical framework for maximization or minimization of performance objectives. For the investigations presented in this dissertation, an objective function was developed which balances two competing criteria: tracking a reference membrane voltage and reducing the squared input stimulus current 'energy'. A framework has been provided which facilitates application of the technique to conductance-based neuron models and provides guidance for interpretation of results.

The technique has been applied to the reduced-order conductance-based model of [1] which was also published in [2]. Within this dissertation, the technique has also been applied to the classical Hodgkin-Huxley model and a previous publication demonstrated its utility in a higher-order conductance-based model [3]. Reduced-order models offer facilitated analysis and reduced computation times while higher-order models enable incorporation of neural dynamics that may be of interest in specific investigations.

When applying this method, choice of the order of the model, as well as parameter value selection, should be considered carefully taking into account the dynamics of interest and computation time of the simulation. Increased complexity of the model comes at the expense of increased simulation time and more complex analysis of model results. If experimental application is needed at the rig, the simulation time needs to be considered preparation viability.

Application of the "Reduced Energy Input Stimulus Discovery Method" in theoretical simulations was successful in all cases, which included a variety of neuron responses [2, 3]. Emphasis on tracking accuracy increased the match between optimal input stimulus current and the original input stimulus. As reduction of input stimulus energy is emphasized it is common to see the resulting membrane potential track the original reference membrane potential to a lesser degree. How rapidly and dramatically the resulting and reference membrane potential diverge depends on the model dynamics. In all cases, when comparing original stimuli to optimal input stimulus currents, an optimal input with noticeably reduced energy has been found which enables acceptable membrane voltage tracking accuracy. Models with a more defined threshold tend to enable accurate tracking of the reference membrane potential with a greater reduction of input stimulus energy. The membrane voltage response of the classical Hodgkin-Huxley model in Chapter 5 is particularly striking. Figure 96a of Section 5.2.4.2 demonstrates that for the case with greatest emphasis on energy reduction, the "Reduced Energy Input Stimulus Discovery Method" computes a negative going prepulse which enables exceptionally accurate tracking of the reference membrane voltage with a dramatic decrease in input stimulus energy [2, 3]. It is interesting that this is essentially a mathematical discovery of a technique researchers commonly use at the rig to investigate the ability of neurons to fire post inhibitory rebound action potentials [1, p. 5]. The presence of 'characteristic dips' in the optimal injected stimulus current is another feature which is common to all repetitive spiking simulations within this dissertation.

A feasibility study has been conducted using neurons in the central nervous system of the leech *Hirudo verbana.* The reduced-order conductance-based model presented in [1] was used in the feasibility study. Model parameters were selected to cause a saddle node on invariant circle bifurcation of the system fixed point based on known properties of the cells under investigation. It was found that application of optimal input stimuli were capable of driving a neuron to fire action potentials in a manner consistent with the theoretical approach. In the leech P-cell, action potentials of consistent timing were produced for the two selected performance indices applied with a 10 ms pulse width, as well as two selected performance indices with a 20 ms pulse width. Application of optimal injected stimulus signals into leech N-cell produced results which demonstrated consistent timing when tracking of reference membrane potential was emphasized, reduced consistency with increased emphasis on reduction in input stimulus energy, and no action potentials when emphasis on energy reduction was highest.

7.2 Contributions of this Work

Contributions of this work, including those presented within this dissertation are as follows:

- Successful implementation of the Reduced Energy Input Stimulus Discovery Method by using a membrane voltage naturally produced by the neuron model as the reference signal to be tracked. This enabled convergence of the boundary value problem solver required for practical application of this method [2].

- Extension of the Reduced Energy Input Stimulus Discovery Method to a sixth-order conductance-based Hodgkin-Huxley type model [3].

- Application of the Reduced Energy Input Stimulus Discovery Method to the classical Hodgkin-Huxley model (Chapter 5). The case studies of Section 5.2.5 are of particular interest. Reference Figures 103 through 105. When reduction of input stimulus current energy is emphasized, the optimal input stimuli in these two cases are remarkably similar to each other. Yet, even with very little difference between the two reference membrane potentials, the optimal control algorithm has sufficient fidelity to recover the original, wider pulse width when tracking accuracy is emphasized, as highlighted in Figure 97c.

- The “Reduced Energy Input Stimulus Discovery Method” substantiates use of negative going pre-pulse injected currents is similar to waveforms used by electrophysiologists for investigation of post inhibitory rebound spikes [2, 3]. The underlying systems dynamics of the classical Hodgkin-Huxley model which cause optimal input current stimuli of this shape warrant further investigation since this characteristic is not present in the reduced-order models.

- The steps required for nonlinear system analysis and application of optimal control to Hodgkin-Huxley type conductance-based neuron models has been organized into a coherent framework, as summarized in Figure 12 of Chapter 3. The approach presented in this dissertation extends previous work by providing phase plane and eigenvalue analysis for classification of system fixed points and controlling initial transients of the state variables for improved presentation of results.

- Utilizing smoothed input current pulses extended previously published results which was essential for the transition to experimental applicability of the technique. A set of simulations including smooth input current pulses was the initial point of discussion for design of the experiment leading toward the demonstrated experimental feasibility of the technique as presented in Chapter 6. The utility of pre-computed wave forms along with a non-smooth current pulse was an essential simplification for initial application of optimal input current stimuli, and resulted in successful demonstration within neurons of the leech.

- Merging of theoretical simulations with preliminary experimental trials. Successful application of the technique results in a spectrum of results ranging from accurate reference membrane voltage tracking at one end reduction of input stimulus energy is at the other. The technique is effective for reduced-order models and is extensible to higher-order models. The conductance-based neuron models have sufficient fidelity to respond to small changes in post action potential membrane voltage levels while maintaining broad features of the neuron dynamics in energy reduction cases. A preliminary study has confirmed the experimental feasibility of using optimal injected current stimuli to drive neurons within the leech central nervous system to fire action potentials very similar to those produced using standard smooth input current pulses.

7.3 Future Work

Two directions to extend this work are to refine experimental techniques and investigate other objective functions.

7.3.1 Refined Experimental Techniques

The method used for the experimental feasibility study was a preliminary effort to demonstrate the application of this technique in a laboratory setting. Further refinement is required to streamline application of the technique.

Refining the experimental protocol primarily relates to "closing the loop" on more of the experimental variables. More specifically, rather than using pre-computed, scaled versions of the reference membrane potentials and optimal input stimuli it, would be a dramatic improvement in the technique to use the actual recorded membrane potential as the reference signal as the input to the reduced stimulus computation.

More tightly closing the loop in the experimental setting does not comprise continual incorporation of all experimental variables. Remembering the "pipe dream" described in [1, p. 20] can aid in deciding which variables are of significance. Variables which do not relate to the dynamical behavior of interest should be disregarded.

The electrophysiology rig employed for use in this dissertation is highly customizable in terms of application of electrical signals and graphical user interface. A more pragmatic aspect of refining the experimental techniques is related to automation of the routine aspects of the experiment. A simple example from this dissertation is that the number of traces captured for each trial was based simply on how long the rig was allowed to run. It would be simple to add a small number of buttons to the graphical interface to automate application and recording of 10 stimulus pulses. Additional features of this type which are aligned with the experiment of interest will promote simplified and consistent application of the technique.

7.3.2 Development of Additional Objective Functions

Using the Reduced Energy Input Stimulus Discovery Method" presented in this dissertation enabled demonstration of the feasibility of using optimal control with conductance-based neuron models [2, 3]. The objective function developed within this dissertation only represents a single application of a more general method. Development of different objective functions will allow investigation of other neural system functionality.

Developing objective functions which seek to optimize the activity of gating variables seems particularly promising since many disorders of the nervous system relate to improper function of a set of ion channels or neurorecpetors. Likewise, many pharmaceuticals which seek to alleviate neural conditions modify neural receptor or ion channel behavior. Optimization of performance indices related to gating variables and ion conductance could elucidate the biophysical basis of neural disorders and pharmacological treatments in this area of study.

7.4 Conclusions

The feasibility of this technique in an experimental setting, combined with the generality of its approach, is a novel and promising combination of theoretical and experimental techniques from the fields of neurobiology, control systems, and optimal control theory.

References

[1] E. M. Izhikevich, *Dynamical Systems in Neuroscience: The Geometry of Excitability and Bursting*, The MIT Press, Cambridge, MA, 2007.

[2] M. Ellinger, M. E. Koelling, D. A. Miller, F. L. Severance, and J. Stahl, "Exploring optimal current stimuli that provide membrane voltage tracking in a neuron model", *Biological Cybernetics*, vol. 104, no. 3, pp. 185–195, 2011.

[3] M. E. Koelling, D. A. Miller, M. Ellinger, F. L. Severance, and J. Stahl, "Current stimuli that provide membrane voltage tracking in a six dimensional neuron model", *Journal of Dynamic Systems, Measurement, and Control*, vol. 135, no. 4, July 2013.

[4] H. C. Tuckwell, J. Jost, and B. S. Gutkin, "Inhibition and modulation of rhythmic neuronal spiking by noise", *Phys. Rev. E*, vol. 80, 2009.

[5] M. Ellinger, "Acquisition and analysis of biological neural network action potential sequences", Master's thesis, Western Michigan University, Kalamazoo, MI, 2009.

[6] S. H. Strogatz, *Nonlinear Dynamics and Chaos*, Perseus Books Publishing, LLC, 1994.

[7] J. Jellies, "Detection and selective avoidance of near ultraviolet radiation by an aquatic annelid: the medicinal leech", *The Journal of Experimental Biology*, vol. 217, pp. 974–985, 2014.

[8] John G. Nicholls, A. Robert Martin, Bruce G. Wallace, and Paul A. Fuchs, *From Neuron to Brain*, Sinauer, fourth edition edition, 2001.

[9] Peter Dayan and L. F. Abbott, *Theoretical Neuroscience, Computational and Mathematical Modeling of Neural Systems*, Computational Neuroscience. The MIT Press, 2005.

[10] Steven J. Schiff, *Neural Control Engineering, The Emerging Intersection between Control Theory and Neuroscience*, Computational Neuroscience. The MIT Press, 2012.

[11] P. Danzl, A. Nabi, and J. Moehlis, "Charge-balanced spike timing control for phase models of spiking neurons", *Discrete and Continuous Dynamical Systems*, vol. 28, no. 4, pp. 1413–1435, December 2010.

[12] P. Gorzelic, S. J. Schiff, and A. Sinha, "Model-based rational feedback controller design for closed-loop deep brain stimulation of Parkinson's disease", *Journal of Neural Engineering*, vol. 10, no. 2, 2013.

[13] E. Waltz, "Spinal stimulation gets paralyzed patients moving: Implanted electrodes can reach where the brain cannot", *IEEE Spectrum*, October 2013, Available online http://spectrum.ieee.org/biomedical/devices/spinal-stimulation-gets-paralyzed-patients-moving.

[14] D. A. Miller, M. E. Koelling, J. Jellies, and C. L. Linn, *Experimental validation of optimal control current stimuli for tracking leech neuron membrane voltages*, National Science Foundation proposal (unfunded), 2014.

[15] D. Tuninetti and D. Graupe, "Adaptive closed-loop control of deep brain stimulation for movement disorders", *National Science Foundation*, 2011, Miller NSF Grant 10.

[16] B. Hille, *Ion Channels of Excitable Membranes*, Sinauer, second edition, 1992.

[17] C. W. Huang, J. J. Tsai, C. C. Huang, and S. N. Wu, "Experimental and simulation studies on the mechanisms of levetiracetam-mediated inhibition of delayed-rectifier potassium current (KV3.1) : Contribution to the firing of action potentials", *Journal of Physiology and Pharmacology*, vol. 60 (4), pp. 37–47, 2009.

[18] D. K. Mohan, P. Molnar, and J. J. Hickman, "Toxin detection based on action potential shape analysis using a realistic mathematical model of differentiated NG108-15 cells", *Biosensors and Bioelectronics*, vol. 21, pp. 1804–1811, 2006.

[19] F. Rieke, D. Warland, R. de Ruyter van Steveninck, and W. Bialek, *Spikes: Exploring the Neural Code*, The MIT Press, Cambridge, MA, paperback edition, 1999.

[20] A. Nabi, T. Stigen, J. Moehlis, and T. Netoff, "Minimum energy control for *in vitro* neurons", *Journal of Neural Engineering*, vol. 10, no. 3, June 2013.

[21] H. Markram, "The blue brain project", *Nature Reviews Neuroscience*, vol. 7, pp. 153–160, February 2006, Website: www.nature.com/reviews/neuro.

[22] C. Daniel Meliza, M. Kostuk, H. Huang, A. Nogaret, D. Margoliash, and H. D. I. Abarbanel, "Estimating parameters and predicting membrane voltages with conductance-based neuron models", *Biological Cybernetics*, vol. 108, pp. 495–516, 2014.

[23] B. Sengupta, M. Stemmler, S. B. Laughlin, and J. E. Niven, "Action potential energy efficiency varies among neuron types in vertebrates and invertebrates", *PLoS Comput Biol*, vol. 6, no. 7, e1000840 2010.

[24] K. Harmon, "Earlier model of human brain's energy usage underestimated its efficiency", *Scientific American*, September 2009, Available at scientificamerican.com.

[25] J. E. Niven and S. B. Laughlin, "Energy limitation as a selective pressure on the evolution of sensory systems", *The Journal of Experimental Biology*, vol. 211, pp. 1792–1804, 2008.

[26] D. Atwell and S. B. Laughlin, "An energy budget for signaling in the grey matter of the brain", *Journal of Cerebral Blood Flow and Metabolism*, vol. 21, no. 10, pp. 1133–1145, 2001.

[27] A. T. Winfree, *The Geometry of Biological Time*, Springer-Verlag, 1980.

[28] J. Moehlis, E. Shea-Brown, and H. Rabitz, "Optimal inputs for phase models of spiking neurons", *Journal of Computational and Nonlinear Dynamics*, vol. 1, no. 4, pp. 358–367, October 2006.

[29] P. A. Tass, "Effective desynchronization by means of double-pulse phase resetting", *Europhysics Letters*, vol. 53, no. 1, pp. 15–21, 2000.

[30] J. Anyalebechi, M. E. Koelling, and D. A. Miller, "Computation of reduced energy input current stimuli for neuron phase models", in *Proc. of the Intl. Conf. of the IEEE Engineering in Medicine and Biology Society*, 2014.

[31] G. Ullah and S. J. Schiff, "Tracking and control of neuronal Hodgkin-Huxley dynamics", *Physical Review E*, vol. 79, no. 4, April 2009.

[32] S. Freeman, *Biological Science*, Pearson Education, third edition, 2008.

[33] W. O. Friesen and J. A. Friesen, *NeuroDynamix II*, Oxford University Press, second edition, 2009.

[34] A.L. Hodgkin, A.F. Huxley, and B. Katz, "Measurement of current-voltage relations in the membrane of the giant axon of *Loligo*", *The Journal of Physiology*, vol. 116, pp. 424–448, 1952.

[35] A.L. Hodgkin and A.F. Huxley, "Current carried by sodium and potassium ions through the membrane of the giant axon of *Loligo*", *The Journal of Physiology*, vol. 116, pp. 449–472, 1952.

[36] A.L. Hodgkin and A.F. Huxley, "The components of membrane conductance in the giant axon of *Loligo*", *The Journal of Physiology*, vol. 116, pp. 473–496, 1952.

[37] A.L. Hodgkin and A.F. Huxley, "The dual effect of membrane potential on sodium conductance in the giant axon of *Loligo*", *The Journal of Physiology*, vol. 116, pp. 497–506, 1952.

[38] A.L. Hodgkin and A.F. Huxley, "A quantitative description of membrane current and its application to conduction and excitation in nerve", *The Journal of Physiology*, vol. 117, pp. 500–544, 1952.

[39] L.F. Abbott, "Lapicques introduction of the integrate-and-fire model neuron (1907)", *Brain Research Bulletin*, vol. 50, no. 5/6, pp. 303–304, 1999.

[40] R.E. Plant and M. Kim, "Mathematical description of a bursting pacemaker neuron by a modification of the hodgkin-huxley equations", *Biophysical Journal*, vol. 16, pp. 227–244, 1976.

[41] J. Guckenheimer and R.A. Oliva, "Chaos in the hodgkin-huxley model", *SIAM Journal on Applied Dynamical Systems*, vol. 1, no. 1, pp. 105–114, 2002.

[42] C. Meunier and I. Segev, "Playing the devil's advocate: is the Hodgkin-Huxley model useful?", *Trends in Neurosciences*, vol. 25, no. 11, pp. 558–563, 2002.

[43] F.L. Severance, *System modeling and simulation, An introduction*, John Wiley & Sons, Ltd., 2001.

[44] A.R. Willms, "An improved parameter estimation method for hodgkin-huxley models", *Journal of Comutational Neuroscience*, vol. 6, pp. 145–168, 1999.

[45] R.F. Stengel, *Optimal Control and Estimation*, Dover Publications, 1994.

[46] F. L. Lewis and V. L. Syrmos, *Optimal Control*, John Wiley & Sons, Inc., 2nd edition, 1995.

[47] L. F. Shampine, J. Kierzenka, and M. W. Reichelt, *Solving Boundary Value Problems for Ordinary Differential Equations in MATLAB with bvp4c*, Downloaded from http://www.mathworks.com, still available January 2013.

[48] N.P. Hale, "A sixth-order extension to the MATLAB bvp4c software of J. Kierzenka and L. Shampine", Master's thesis, Imperial College London, 2006.

[49] MathWorks, Inc., "Vectorization", http://www.mathworks.com/help/matlab/matlab_prog /vectorization.html?refresh=true, accessed May, 2015.

[50] MathWorks, Inc., "bvpset", http://www.mathworks.com/help/matlab/ref/bvpset.html, accessed May, 2015.

[51] MathWorks, Inc., "profile", http://www.mathworks.com/help/matlab/ref/profile.html, accessed May, 2015.

[52] W. Gerstner and W. M. Kistler, *Spiking Neuron Models. Single Neurons, Populations, Plasticity*, Cambridge University Press, August 2002, Book in HTML format: http://lcn.epfl.ch/ gerstner/SPNM/SPNM.html.

[53] K. J. Muller, J. G. Nicholls, and G. S. Stent, editors, *Neurobiology of the Leech*, Cold Spring Harbor Laboratory Press, 2010, http://www.amazon.com/Neurobiology-Leech-Kenneth-J-Muller/dp/1936113090.

[54] J. Jellies, "Which way is up? Asymmetric spectral input along the dorsal-ventral axis influences postural responses in an amphibious annelid", *Journal of Comparative Physiology A*, vol. 200, pp. 923–938, 2014.

[55] J. Jellies and D. Kueh, "Centrally patterned rhythmic activity integrated by a peripheral circuit linking multiple oscillators", *Journal of Comparative Physiology A*, vol. 198, no. 8, pp. 567–582, 2012.